# Modelling of Large-scale Folds and Ice Streams in Polar Ice Sheets

**Dissertation**

der Mathematisch-Naturwissenschaftlichen Fakultät

der Eberhard Karls Universität Tübingen

zur Erlangung des Grades eines

Doktors der Naturwissenschaften

(Dr. rer. nat.)

vorgelegt von

Yu Zhang

aus Hubei / China

Tübingen

2024

Gedruckt mit Genehmigung der Mathematisch-Naturwissenschaftlichen Fakultät der Eberhard Karls Universität Tübingen.

| | |
|---|---|
| Tag der mündlichen Qualifikation: | 18.02.2025 |
| Dekan: | Prof. Dr. Thilo Stehle |
| 1. Berichterstatter/-in: | Prof. Dr. Paul D. Bons |
| 2. Berichterstatter/-in: | Prof. Dr. Ilka Weikusat |
| 3. Berichterstatter/-in: | Prof. Dr. Nanna B. Karlsson |

# Erklärung

Ich erkläre hiermit, dass ich die zur Promotion eingereichte Arbeit selbständig verfasst, nur die angegebenen Quellen und Hilfsmittel benutzt und wörtlich oder inhaltlich übernommene Stellen als solche gekennzeichnet habe. Ich erkläre, dass die Richtlinien zur Sicherung guter wissenschaftlicher Praxis der Universität Tübingen (Beschluss des Senats vom 25.5.2000) beachtet wurden. Ich versichere an Eides statt, dass diese Angaben wahr sind und dass ich nichts verschwiegen habe. Mir ist bekannt, dass die falsche Abgabe einer Versicherung an Eides statt mit Freiheitsstrafe bis zu drei Jahren oder mit Geldstrafe bestraft wird.

Tübingen, 1. Dec 2024

## Abstract

Satellite and airborne sensors have provided detailed data on ice surface flow velocities, englacial structures of ice sheets and bedrock elevations. These data give insight into the flow behaviour of ice sheets and glaciers. One significant structural phenomenon observed is large-scale folds (over 100 m in amplitude) in the englacial stratigraphy in polar ice sheets. A large population of folds is located at ice streams, where the flow is distinctly faster than in the surroundings and bound by the marginal shear zones (known as shear margins), such as the over 500 km long Northeast Greenland Ice Stream (NEGIS). Fast-flowing ice streams drain most of the inland ice from the Antarctic and Greenland ice sheets. However, there is no consensus yet on how these folds and ice streams form.

Ice in ice sheets is a ductile material, i.e., it can flow as a thick viscous fluid with a power-law rheology. Furthermore, ice is significantly anisotropic in its flow properties due to its crystallographic preferred orientation. By incorporating an anisotropic, non-linear viscosity and evolving c-axis orientations of ice crystals, this thesis mainly uses the particle-in-cell full-Stokes code Underworld2 to simulate ice flow in three-dimensional large-scale ice-sheet models.

The simulated folds with anisotropic ice show complex patterns on a bumpy bedrock, and are classified into three types: large-scale folds (fold amplitudes >100 m), small-scale folds (fold amplitudes <<100 m, wavelength <<km) and recumbent basal-shear folds. The results indicate that ice anisotropy amplifies the perturbations in ice layers (mainly due to bedrock topography) into large-scale folds during flow. Density differences between the warm deep ice and cold ice above may enhance fold amplification.

The ice stream models show that ice streams and their shear margins can form solely due to the anisotropic rheology of ice and evolving crystallographic orientations. A fully developed, fast-flowing ice stream can form in only 1000–2000 years by internal ice anisotropy, even without external forcing such as basal melting. As the ice stream evolves, new shear margins establish and subdivide the flow into tributaries. Shear margins continue to migrate along with the ice flow, forming new margins as the system develops further. Dominant tributaries, such as NEGIS, can extend inland, nearly reaching the ice divide, within another 1000–2000 years.

Hence, this thesis stresses the importance of evolving ice anisotropy in large-scale ice-sheet models to more accurately predict future ice-sheet evolution and sea-level rise during global climate change.

# Zusammenfassung

Satelliten- und Luftbildsensoren haben detaillierte Daten über die Fließgeschwindigkeiten an der Eisoberfläche, die glazialen Strukturen der Eisschilde und die Topographie des Eisuntergrundes geliefert. Diese Daten geben Aufschluss über das Fließverhalten von Eisschilden und Gletschern. Ein bedeutendes strukturelles Phänomen, das beobachtet wurde, sind großflächige Falten (mit einer Amplitude von über 100 m) in der englazialen Stratigraphie der polaren Eisschilde. Eine große Anzahl von Falten befindet sich in Eisströmen, die deutlich schneller fließen als die Umgebung und die durch marginale Scherzonen begrenzt sind, wie z. B. der über 500 km lange Northeast Greenland Ice Stream (NEGIS). Schnell fließende Eisströme tragen erheblich zum Massenverlust des Inlandeises der antarktischen und grönländischen Eisschilde bei. Es besteht jedoch noch wenig Konsens darüber, wie diese Falten und Eisströme entstehen.

Eis in Eisschilden ist ein duktiles Material, d. h. es kann als dickflüssiges viskoses Fluid mit einer Rheologie nach dem Potenzgesetz fließen. Darüber hinaus sind die Fließeigenschaften von Eis aufgrund seiner kristallographischen Vorzugsorientierung erheblich anisotrop. Unter Einbeziehung einer anisotropen, nichtlinearen Viskosität und sich entwickelnder c-Achsen-Orientierungen der Eiskristalle wird in dieser Arbeit hauptsächlich der „particle-in-cell full-Stokes code" Underworld2 zur Simulation des Eisflusses in dreidimensionalen großräumigen Eisschildmodellen verwendet.

Die simulierten Falten mit anisotropem Eis zeigen komplexe Muster auf einer variablen Bodentopographie und werden in drei Typen eingeteilt: großskalige Falten (Faltenamplituden >100 m), kleinskalige Falten (Faltenamplituden <<100 m, Wellenlänge <<km) und liegende basale Scherfalten. Die Ergebnisse deuten darauf hin, dass die Anisotropie des Eises die Störungen in den Eisschichten (hauptsächlich aufgrund der Topographie des Untergrunds) während des Fließens zu großräumigen Falten verstärkt. Dichteunterschiede zwischen dem warmen tiefen Eis und dem kalten darüberliegendem Eis können das Faltenwachstum verstärken.

Die Eisstrommodelle zeigen, dass Eisströme und ihre Scherzonen allein aufgrund der anisotropen Rheologie des Eises und der sich entwickelnden kristallographischen Orientierungen entstehen können. Ein voll entwickelter, schnell fließender Eisstrom kann sich in nur 1000–2000 Jahren durch interne Eisanisotropie bilden, auch ohne äußere Einflüsse wie

basales Schmelzen. Während sich der Eisstrom entwickelt, bilden sich neue Scherzonen, die den Eisstrom in Nebenströme unterteilen. Die Scherzonen wandern mit dem Eisstrom und bilden neue Scherzonen, mit voranschreitender Entwicklung des Eisstromsystems. Dominante Nebenströme wie NEGIS können sich innerhalb von weiteren 1000–2000 Jahren ins Landesinnere ausdehnen und fast bis zur Eisscheide propagieren.

Daher wird in dieser Arbeit die Bedeutung der Entwicklung der Eisanisotropie in großräumigen Eisschildmodellen betont, um die künftige Entwicklung der Eisschilde und den Anstieg des Meeresspiegels während des globalen Klimawandels genauer vorherzusagen.

## Acknowledgements

First and foremost, I would like to thank Prof. Paul Bons for giving me the opportunity to pursue my PhD studies in the Structural Geology group at Tübingen. Paul has a lot of new ideas and guides me to the cutting-edge research. Paul is also full of energy and supports me on the icy and rocky science way. His patience and understanding are important as well when I was struggling with problems in my modelling. I would also like to thank his friendly help on my life during those corona time.

Thanks to Prof. Ilka Weikusat, my second supervisor at AWI, Helmholtz Centre for Polar and Marine Research, for co-supervising my PhD proposal and manuscripts, the Glaciology course, and discussions at AWI-Tübingen seminars. Thanks also to Till Sachau and Steven Franke, who are also like supervisors to me. Till taught me the Underworld code, helped me set up initial models, and solved lots of problems during model running, without whom I would not finish my modelling. Steven helped me a lot on the manuscript writing. I benefit from his experiences on ice sheets and geophysical observations. I also respect his efficiency on every work.

I would also like to thank my colleagues in Tübingen: Yuanbang Hu, Tamara de Riese, Isaac Naaman, Kyra Streng, He Tian, Dongsheng Cao, Yuzhen Fu, Dian Li, Oliver Vonderschmidt, Willi Kappler, Catherine Bauer, and also members from Prof. Reinhard Drews' group and Prof. Todd Ehlers' group. Thanks for all of your help on my research and life here. Thanks also to colleagues from AWI and AWI-Tübingen seminars: Daniela Jansen, Maria-Gema Llorens, Enrique Gomez-Rivas, Eloi González-Esvertit, Julien Westhoff, Nicolas Stoll, Johanna Kerch, etc. Special thanks to Haibin Yang, one of the Underworld developers from Prof. Louis Moresi's group (Australian National University), for his help on my code scripts. Special thanks to people I met on field trips in Spain and scientific conferences such as EGU and DRT, for discussions and inspirations to my research.

Many thanks to China Scholarship Council (CSC) for financially supporting my PhD project. Many thanks to my teachers and schoolmates from Peking University and Yangtze University, Prof. Jianghai Li, Prof. Zhicheng Zhang, Zhonglan Liu, Yi Luo, Kang Xie and Haijing Jiao, for their help on my PhD and scholarship application.

Finally, I want to thank my friends here in Tübingen for those funny and relaxing moments. I want to thank my family for cultivating my character of perseverance and never giving up, and for supporting me in every aspect of my life all these years.

# Table of Contents

# Chapter 1

# Introduction

## 1. Background

### 1.1 Ice flow and structural phenomena

Ice in ice sheets mainly exhibits properties of the ductile material, i.e. it can flow as a thick viscous fluid. The increased flow of ice from the polar ice sheets into the oceans is one of the main factors that causes global sea-level rise. The Antarctic and Greenland ice sheets store vast amounts of fresh water. Ice is continuously added to their surface by snow precipitation. At the same time, ice flows under its own weight towards the ice sheet front. The ice sheets currently lose mass, as more ice is lost by melting and flowing into the oceans than is added by precipitation. Satellite and airborne sensors have provided detailed data on ice surface flow velocities, englacial structures of ice sheets and bedrock elevations. These data give insight into the flow behaviour of ice sheets and glaciers.

Ice streams are zones where the flow is distinctly faster than in the surrounding ice, found in both Antarctic and Greenland ice sheets (GrIS) (Hughes, 1977; Bentley, 1987; Fahnestock et al., 1993). A well-developed ice stream is bound by the marginal shear zones, known as shear margins, separating the fast and slow flowing ice. The North-East Greenland Ice Stream (NEGIS; Fig. 1), for example, extends for over 500 km from central GrIS ice divide to its outlets, with flow velocities 5-10x higher than in its surroundings (Fahnestock et al., 1993). The drainage basin of NEGIS is about 16% of the total area of GrIS (Hvidberg et al., 2020). Fast-flowing ice streams drain most of the inland ice from Antarctic and Greenland ice sheets, and play an important role in the mass balance of ice sheets (Khan et al., 2014, 2022), which are associated with climate change (Larsen et al., 2018) and will cause sea-level rise through accelerating ice discharge (Mouginot et al., 2015).

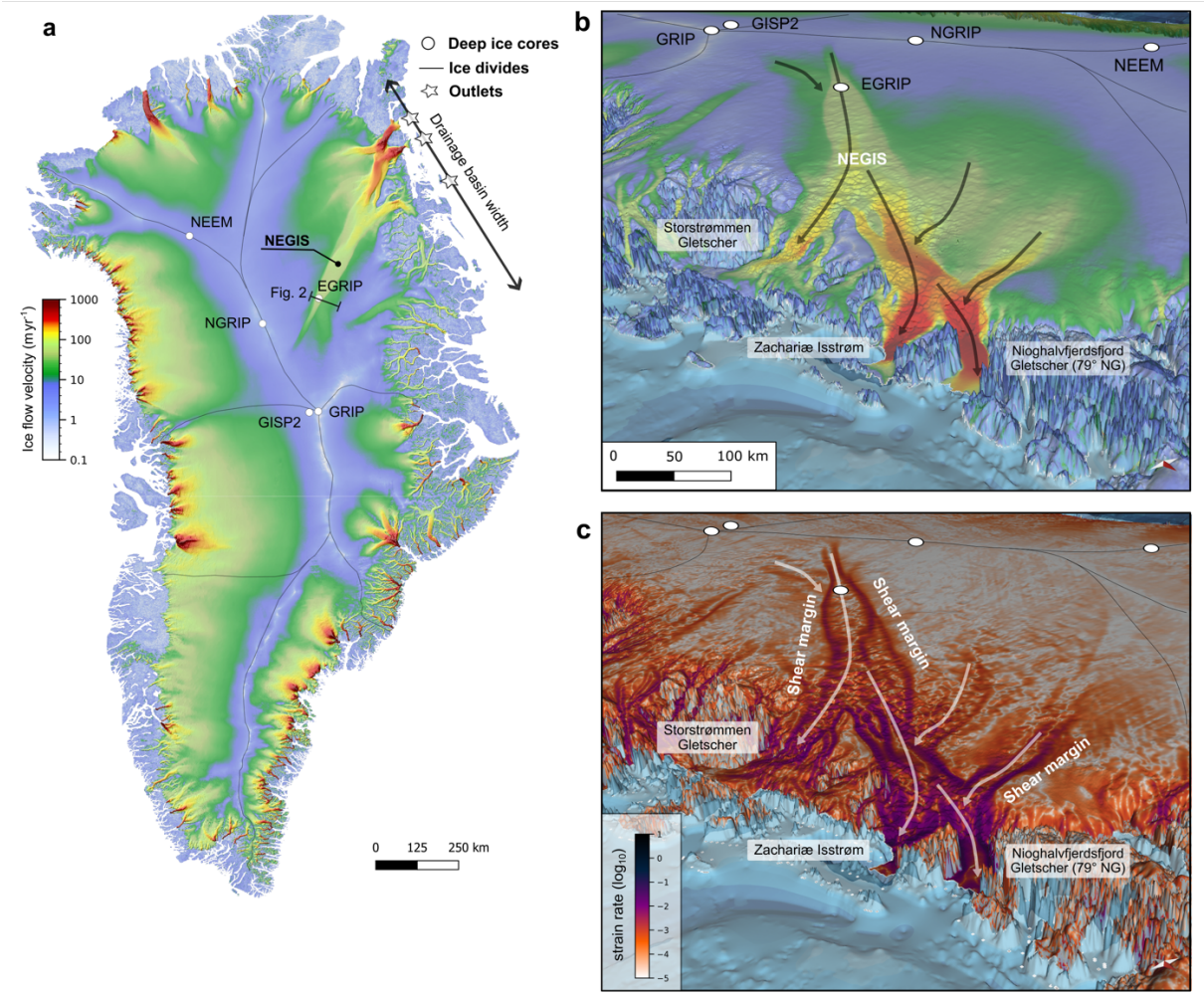


Fig. 1. Overview of the Greenland's ice flow. (a) Surface velocity of the Greenland ice sheet. (b, c) Close-up of NEGIS and its coastal outlets, showing surface flow velocity (b), and strain rates (c). The surface velocity and strain rate data are from Joughin et al. (2018), and visualized by Steven Franke with the open-source code QGIS (QGIS Development Team, 2024).

In addition, airborne radio-echo sounding (RES) data reveal internal layering and large-scale folding (up to >100 m, sometimes even 1 km fold amplitude) on the bumpy bedrock, such as in several regions of GrIS (Fig. 2) (NEEM community members, 2013; Bell et al., 2014; Wolovick et al., 2014; MacGregor et al., 2015; Panton and Karlsson, 2015; Bons et al., 2016; Leysinger-Vieli et al., 2018; Franke et al., 2022a, 2022b). Large-scale folds appear both within ice streams and in regions of slow-moving ice. Fold amplitudes usually reach their maximum in the middle of the ice column or just below, gradually decrease towards the

upper layers and flatten at the ice surface. Studies of past and present ice dynamics (Franke et al., 2022a) and of basal conditions (Wolovick et al., 2014; Leysinger-Vieli et al., 2018) need to include mechanisms to generate folds to be robust. Fold geometry can be used to date the establishment of shear margins of ice streams (see Chapter 4, Jansen et al., 2024) and is needed to unravel ice stratigraphy in ice cores that penetrate folded ice (NEEM community members, 2013).

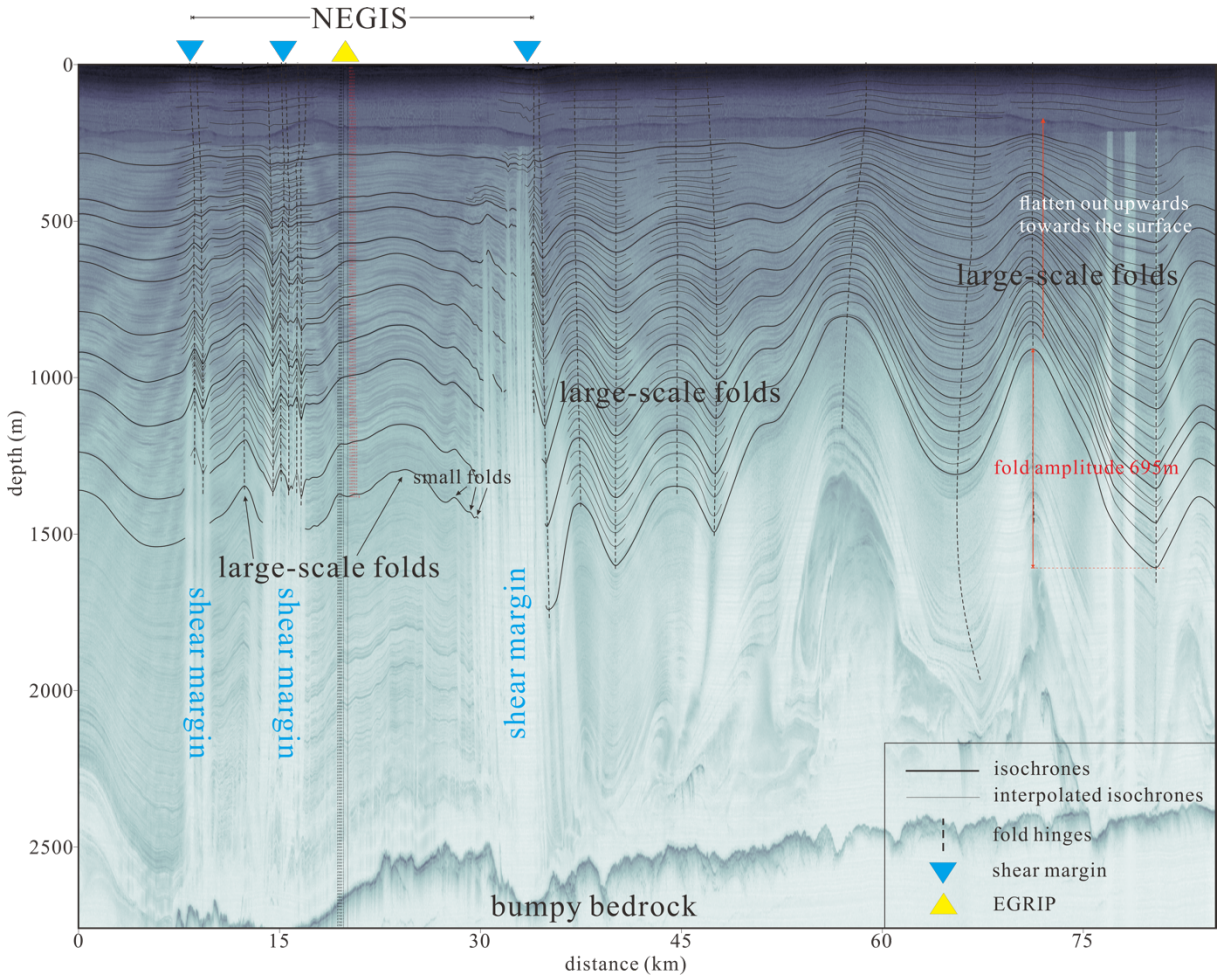


Fig. 2. Radar profile (position in Fig. 1) across the NEGIS and the EGRIP drill site (East Greenland Ice-Core Project) showing large-scale folds and shear margins. These internal layers were traced by Yu Zhang, and the final published version (combined with other co-authors) and radar data source can be found in Chapter 4 (Jansen et al., 2024).

## 1.2 Geothermal heat flux

The geothermal heat flux has an impact on ice in ice sheets. Due to the geothermal heat flux (or strain heating; Rogozhina et al., 2011), ice temperature increases with depth: upper "cold ice" has a high viscosity and density, while the lower "warm ice" has a lower viscosity and also has a lower density due to thermal expansion (Hills et al., 2017; Robin, 1955). The geothermal heat flux is suggested elevated in Northeast Greenland and usually attributed to the trail of the Iceland plume (Rogozhina et al., 2016; Martos et al., 2018; Artemieva, 2019). Rogozhina et al. (2016) propose that the Iceland hotspot left a 400 km wide, roughly NW–SE-oriented swath of elevated geothermal heat flux across Greenland as the crust there was positioned above the hotspot 35–80 Myr ago. The elevated geothermal heat flux in the trail reaches values of the order of 100 mW $m^{-2}$. But it should also be noted that for example, Colgan's model does not show an area of elevated heat flow that might be interpreted as remnant from the Icelandic plume track (Colgan et al., 2022).

## 1.3 Ice anisotropy rheology

The important ice properties are anisotropic, non-linear rheology and evolving c-axis orientations. Ice in the interior of ice sheets is generally assumed to flow as a non-linear viscous material, due to deformation by dislocation creep (Glen, 1955; Weertman, 1983; Budd and Jacka, 1989). The classical Glen's flow law treats ice as a purely incompressible, isotropic, non-Newtonian fluid, with a viscosity determined by a power law relation between strain rate ($\dot{\varepsilon}$) and stress ($\sigma$):

$$\dot{\varepsilon} = A\sigma^n \tag{1}$$

where $A$ and $n$ are constants. The stress exponent $n$ is dimensionless, in the range from one to five which are obtained from observations on natural ice flows (borehole deformation measurements, ice flow velocities, etc.; Hutter, 1983; Pettit & Waddington, 2003; Cuffey & Kavanaugh, 2011; Gillet-Chaulet et al., 2011) and laboratory experiments on polycrystalline ice aggregates (Glen, 1955; Weertman, 1983; Goldsby & Kohlstedt, 2001; Treverrow et al., 2012). The exact value of the stress exponent of ice under Earth conditions is uncertain and most literatures invariably assume that $n = 3$. Recent studies on both the Greenland and Antarctic ice sheets suggest a higher $n = 4$ (Bons et al., 2018; Ranganathan and Minchew, 2024).

Polycrystalline ice crystal (Ih) deformed in the laboratory (e.g., Kamb, 1972; Qi et al., 2017, 2019) and in nature (e.g., Gow and Williamson, 1976; Hudleston, 1977; Thorsteinsson et al., 1999; Weikusat et al., 2017a, 2017b; Ershadi et al., 2022) is strongly anisotropic, because it deforms much more easily parallel to its crystallographic basal plane than perpendicular to it along crystal's c-axis (Duval et al., 1983; Pimienta and Duval, 1987), which during deformation leads to a preferred alignment of the crystal orientations, known as crystallographic preferred orientation (CPO) (Budd and Jacka, 1989) (Fig. 3). This anisotropic rheology has significant implications for ice flow.

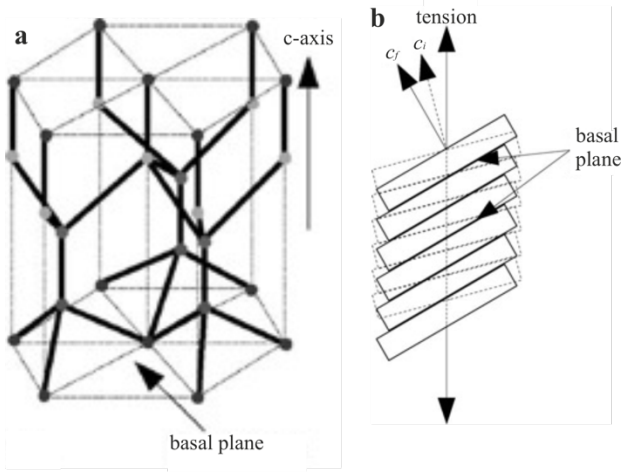


Fig. 3. Crystal of ice Ih: (a) hexagonal structure of the lattice of oxygen atoms and (b) the c-axis rotation of a grain undergoing tension (from Fig. 1a and Fig. 2 of Gillet-Chaulet et al., 2006).

# 2 Mechanisms: basal conditions vs. ice anisotropy

## 2.1 Formation of large-scale folds

Several mechanisms and models have been proposed to explain the formation of large-scale folds in ice sheets. Bell et al. (2014) and Leysinger-Vieli et al. (2018) suggest that refreezing meltwater adds material to the ice base and elevates the overlying stratigraphy and influences basal ice deformation. Alternatively, Wolovick et al. (2014) suggest that variable slip rates due to “traveling slippery patches” can create large-scale folds. Furthermore, Krabbendam (2016) proposes the basal temperate (melting) ice layer may be locally thickened by internal deformation of folding or thrusting over a bedrock high. These models mainly focus on basal ice and bed conditions, which may apply to individual fold cases but seem inadequate to explain the presence of folds throughout the GrIS, especially in the NE of the ice sheet. Additionally, these models are purely 2D along-flow models and no predictions have been published for their 3D geometry. However, especially when considering the margins of ice streams, the three-dimensional geometries of folds show that fold axes are sub-parallel or at a small angle to the flow direction (Bons et al., 2016; Franke et al., 2022a, 2023).

Hudleston (2015) proposes that irregularities in primary ice stratification can be kinematically amplified in convergent flow by horizontal shortening and without the requirement of rheological contrast in the ice. Thorsteinsson and Waddington (2002) invoke anisotropy as a cause of fold initiation near ice-sheet centers considering the initial layer disturbance relative to the extensile flow regime, and anisotropy is also well-studied in the development of small-scale folds in ice cores (Alley et al., 1997; Jansen et al., 2016) and anisotropic materials (Kocher et al. 2008; Ran et al., 2019) (see Chapter 6). Bons et al. (2016) suggest that mechanical anisotropy and convergent flow cause large-scale folding. This hypothesis has so far not been tested with numerical simulations.

## 2.2 Formation of ice streams and shear margins

The formation of a large-scale ice stream like NEGIS, or in other words the establishment of the ice stream's shear margins, is controversial as well. Bedrock topography or subglacial geology (Anandakrishnan et al., 1998) does not appear to be the main control on the location, shape and size of NEGIS (Joughin et al., 2001; Franke et al., 2021, 2022a). Regional

variations in the geothermal flux have been suggested beneath GrIS (Fahnestock et al., 2001; Rogozhina et al., 2016), but the heat flux needed to sustain NEGIS (Smith-Johnsen et al., 2020) is unrealistically high and geologically unfeasible (Artemieva, 2019; Colgan et al., 2022) (see Chapter 5, Bons et al., 2021). Other studies suggest self-organizing shear margins, due to subglacial meltwater channeling (Christianson et al., 2014; Kyrke-Smith et al., 2015; Elsworth & Suckale, 2016), and shear heating and resulting softening of the ice (Perol and Rice, 2015; Holschuh et al., 2019). However, no model has so far been able to test whether ice stream initiation can solely result from the evolving internal properties of the ice itself, without relying on external forcing.

In 1988, Alley found convergent flow causes c-axes to rotate toward a vertical plane transverse to flow (Alley, 1988). Recent airborne radar data reveal ice fabric variation across ice streams in Antarctic and Greenland ice sheets, which causes directional softening of shear margins (Young et al., 2021; Jordan et al., 2022; Gerber et al., 2023). Microseismic data show shearing is close to ten times more easily along the ice flow direction than across flow due to ice fabric (Smith et al., 2017). Numerical simulations of ice-crystal fabric prove easy-glide crystallographic basal planes would rotate towards the shear plane (Lilien et al., 2021; Llorens et al., 2022). These studies reveal: (i) The easy-glide crystallographic basal planes would rotate towards the shear plane, and become parallel to the shear margins; (ii) The shear margins are effectively softened for shearing along these basal planes. Despite decades of research and the importance of ice streams for (changing) mass balance, the full effect of ice anisotropy on the ice-stream formation has not yet been numerically modelled.

## 3. Objectives of this thesis

Taking observations from Northeast Greenland as an example, this thesis aims to the formation and evolution of the two important structural phenomena in polar ice sheets by numerical modelling: 1) large-scale englacial folds; 2) ice streams and the shear margins, to improve our understanding of the flow behaviour of ice sheets and better predict future ice-sheet development and sea-level rise. NEGIS and its shear margins are observed through the ice flow velocity data and the processed strain rate data from Joughin et al. (2018), available at the National Snow and Ice Data Center: https://nsidc.org/data/nsidc-0670/, combined with the bed elevation data of the Northeast Greenland (Morlighem et al., 2017). Englacial folded layers are traced through internal reflection horizons on the airborne radargrams. The radio-echo sounding data are from AWI's EGRIP-NOR-2018 survey and CReSIS Data Products (Franke et al., 2022a, 2022b). The vertical shear margin planes can also be indicated by bright stripes on radargrams.

Here are several general objectives of this thesis:

I. ***Information on the fold and ice stream history.*** Folding of stratigraphy causes a change in vertical position of layers, either upwards (anticlines) or downwards (synclines) relative to the undisturbed layer level. To determine the amplitude-depth curves, as many layers in a radargram as possible will be manually traced for anticline-syncline pairs. Axial planes are constructed as lines that connect the fold hinges. Ages of layers will be derived from tracing to or correlating layers at the EGRIP drill site where ages are known as a function of depth (Mojtabavi et al., 2020). Fold deformation stages can then be analysed by the amplitude-age data of folded layers along each fold hinge. A folding event leads to a steady increase in fold amplitude with depth in all layers older than the folding event. Every change in the amplitude-age trend represents a folding event. This will give information on fold evolution periods, which would also be connected with shear margin establishment / ice stream formation.

II. ***Fold classification and formation mechanisms.*** This thesis will investigate several factors on fold growth with 3D ice-sheet models, such as rheological anisotropy of ice, vertical gradients of viscosity and density, and bedrock topography. Different fold types may appear in the modeling. Ice anisotropy will be particularly studied for

large-scale fold formation, like its influence on those small-scale folds. A full growth process of large-scale folding is also expected to be demonstrated with modeling.

III. ***Evolving ice anisotropy and shear margin establishment.*** The important hypothesis is to be proved through modelling that in the convergent ice flow, c-axes would rotate toward a vertical plane transverse to flow. A shear zone (margin) is then expected to be seen due to the localized shearing in the vertical plane.

IV. ***Past and future evolution of a typical ice stream.*** A full evolution process of an ice stream will be modelled. Different model boundary conditions will be compared. How the ice stream changes its shape and position is expected to be observed. Indications for future ice-stream development would be concluded.

# 4. Full-Stokes Geodynamics code Underworld2

## 4.1 Code suitability

The full-Stokes software "Underworld2" (Beucher et al., 2022) was originally designed and developed for modelling and tracking internal deformation in Geodynamics processes. The solution in Underworld is based on the Stokes equation of slow flow of a Newtonian incompressible fluid:

$$\frac{\partial \tau_{ij}}{\partial x_j} - \frac{\partial P}{\partial x_i} + \rho g_i = 0 \quad (1)$$

$$\frac{\partial v_i}{\partial x_i} = 0 \quad (2)$$

Here $\tau_{ij}$ is the deviatoric stress tensor, $P$ the pressure, $g$ the gravitational acceleration and v the velocity.

Underworld2 is specifically optimized for our case. Some of the advantages are (i) tracking of material "particles" during deformation and (ii) local fabric evolution can be coupled to the local rheological anisotropy. Underworld2 uses the material point method (MPM), which is related to the better-known particle-in-cell method (Moresi et al., 2003). MPM uses an Eulerian finite-element mesh to calculate the incremental development of the velocity field and other field variables, such as temperature and pressure, while Lagrangian material points ("particles") carry the density, viscosity, lattice orientation, and other relevant local material parameters. This code is already well established in complex geodynamic modeling with a full-Stokes solution for isotropic and anisotropic elasto–visco–plastic materials (Moresi & Mühlhaus, 2006; Sharples et al., 2016). The software has also passed the usual benchmark tests for full-Stokes ice sheet models of Pattyn et al. (2008) (Sachau et al., 2022).

## 4.2 Anisotropy in Underworld2

Here we used the dislocation creep component of the composite flow law of Goldsby and Kohlstedt (2001). The flow law has two parameterizations, one for high and one for low temperature, and the parameters used are those modified by Kuiper (Kuiper et al., 2020) to

ensure no discontinuity at the transition temperature (–11 °C). The strain rate ($\dot{\varepsilon}_{i,j}$) is proportional to the deviatoric stress ($\tau_{ij}$) to the power $n$:

$$\dot{\varepsilon}_{i,j} = A_0 \mathrm{e}^{\frac{-Q}{R(T+273)}} {\tau_{II}}^{\mathrm{n}-1} \tau_{ij} \tag{3}$$

where $A_0$ is the material parameter, $Q$ the activation energy, $R$ the gas constant and $\tau_{\mathrm{II}}$ the second invariant of the deviatoric stress tensor $\tau_{ij}$. The power-law viscosity of ice (general viscosity $\eta_1$, Pa · s) is then derived from temperature ($T$, °C) and strain rate ($\dot{\varepsilon}_{i,j}$, $\mathrm{yr}^{-1}$) (Sachau et al., 2022)

$$\eta_1 = \frac{1}{2} \left(A_0 \mathrm{e}^{\frac{-Q}{R(T+273)}}\right)^{\frac{-1}{n}} \cdot {\dot{\varepsilon}_{II}}^{\frac{1-n}{n}} \tag{4}$$

where $\dot{\varepsilon}_{II}$ is the second invariant of the strain rate tensor. Note the unit conversion of stress and time. The stress exponent was set to $n$ = 4 based on experimental results (Goldsby and Kohlstedt, 2001) and studies on both the Greenland and Antarctic ice sheets (Bons et al., 2018; Ranganathan and Minchew, 2024).

The c-axis orientation of the ice crystal is stored for each particle in Underworld2. It is represented as a dimensionless unit vector ($c_x$, $c_y$, $c_z$). In our model, the initial c-axis directions of ice particles are perpendicular to the local layer orientation with a Gaussian random distribution with a standard deviation of $\pm 5°$ (Fig. 4). The c-axes rotate in the flow field according to the symmetric deformation-rate tensor $D$ and the skew-symmetric rotation-rate tensor $W$

$$D = \frac{1}{2}(L + L^{\mathrm{T}}) \tag{5}$$

$$W = \frac{1}{2}(L - L^{\mathrm{T}}) \tag{6}$$

where $L$ is the velocity gradient tensor (see detailed c-axis rotation equations in Appendix B in Sharples et al., 2016). Note that this routine does not include other processes, such as recrystallization, that may affect c-axis orientations (Qi et al., 2019; Lilien et al., 2021; Richards et al., 2021).

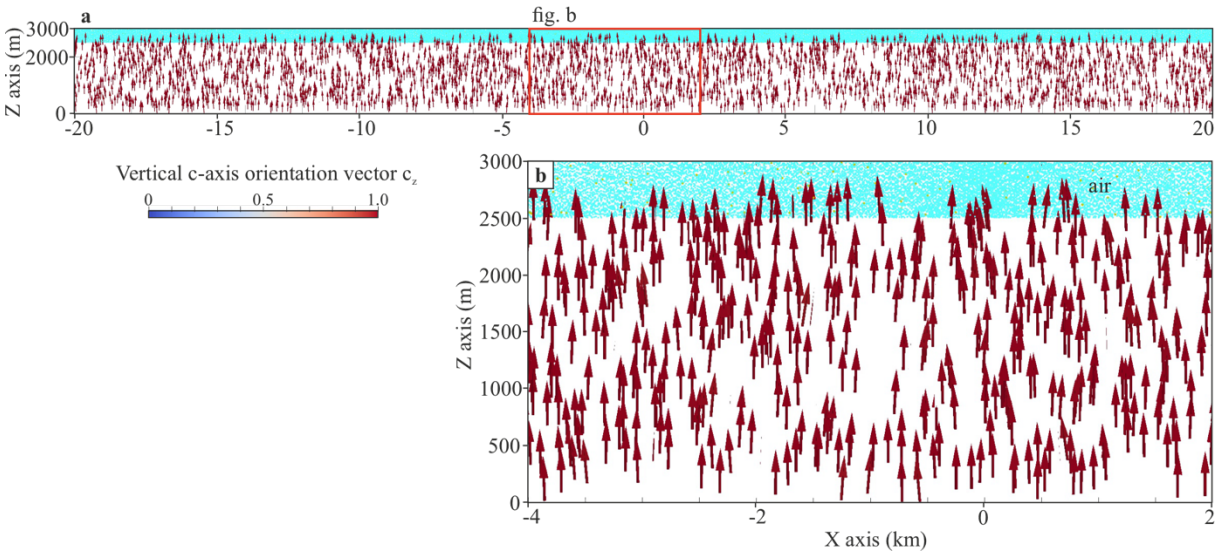


Fig. 4. C-axis orientations (arrows) of ice particles (from Chapter 3). Arrow colors represent vertical vectors, with deep red being vertical (1.0).

The anisotropy of the ice crystal is modelled as transverse isotropy, which is a common practice in numerical modeling (Gillet-Chaulet et al., 2005; Martín et al., 2009). Transverse isotropic viscosity is defined by two viscosity values: a general viscosity $\eta_1$ (Pa · s) and a second viscosity $\eta_2$ (Pa · s). $\eta_1$ is set proportional to $\eta_2$:

$$\eta_1 = k\eta_2 \tag{7}$$

where *k* represents the rheological anisotropy parameter. The general viscosity $\eta_1$ represents the maximum value for shortening or stretching parallel to the c-axis maximum, and the second viscosity $\eta_2$ is the minimum value for shearing along the plane perpendicular to the c-axis maximum (crystallographic basal plane).

## 4.3 Boundary conditions

This thesis starts from the semi-2D models for large-scale fold formation in a 3D convergent flow (Fig. 5). The model comprises four main material layers: air, cold ice (–30 ℃), warm ice (–30 to –3 ℃), and bedrock, and 10 internal marker horizons to track the deformation. Internal horizons are progressively shortened by lateral inflows (x-axis). Outflow in the y-direction, compensates the inflow to maintain a constant ice volume. As the main interest is

in the ice-layer geometry in the vertical x-z-plane, and to maximize the resolution of the model, its width in the y-direction (500 m) is much smaller than in the x-direction (25 km), which makes the model close to the ice divide and near upstream part of an ice stream. Further away from the ice divide, horizontal flow velocities are much higher and bedrock-parallel shear rates are thus also higher. The strain-rate softening results in a decrease in effective viscosity. The value of $A_0$ is then reduced for the effective viscosity to model the ice further downstream from the divide. Three different bed conditions are tested: (i) a free-slip bottom boundary without a bedrock, (ii) a 1000 m thick bedrock layer with a flat surface to which the ice is frozen, and (iii) the same as (ii), but with an undulating bedrock surface with bumps of variable wavelengths and amplitudes.

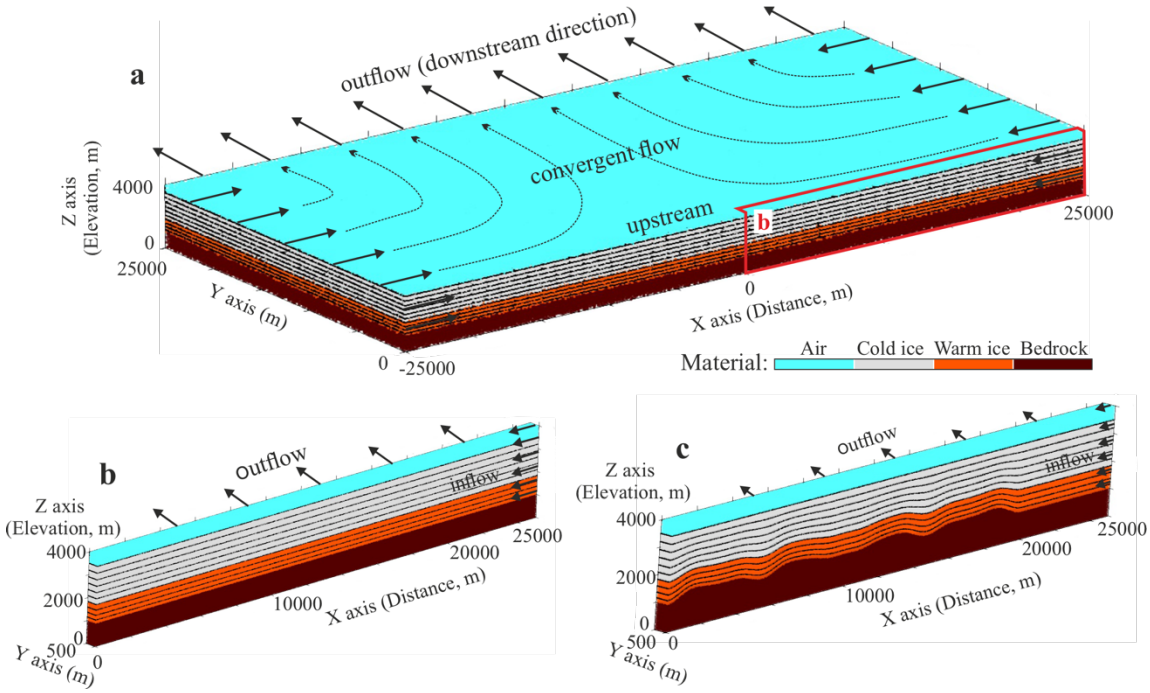


Fig. 5. Initial fold model from Chapter 2 (Zhang et al., 2024). (a) 3D view of the initial model with convergent ice flow; (b) the adapted semi-2D model to enable a higher model resolution (see location in a) and (c) with bedrock bumps.

The ice-stream model (Fig. 6) is a 3D extension along the outflow direction of the convergent flow in the fold model. Basic model setup consists of a rectangular box (40 × 50 km, and 3 km height) where ice can leave the system at one 10 km wide outlet gate only, mimicking the

general drainage basin configuration in NE Greenland (Fig. 1). To maintain a constant ice volume, ice precipitates on the surface and flows into the modeling domain from the left and right boundaries of the model. Ice does not flow into the system from the back side of the model that thus represents the ice divide. This thesis performs several model runs to explore the effect of varying boundary conditions, such as zero or free slip at the ice base, symmetry or asymmetry of inflow from the sides, and varying anisotropies.

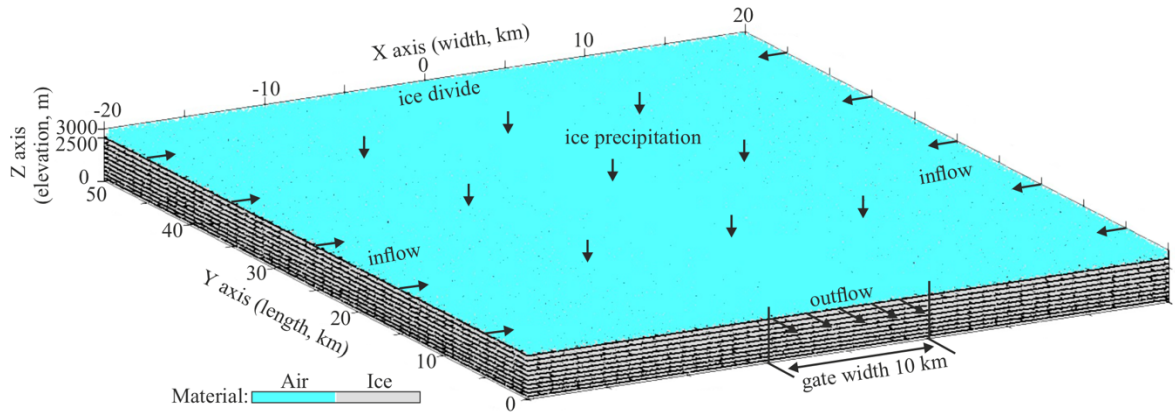


Fig. 6. 3D view of the initial ice-stream model from Chapter 3.

# 5. Framework and main outcome of this thesis

## 5.1 Framework of the thesis and introduction of chapters

This thesis is composed of a collection of publications in recognised scientific journals. Some of the publications are already published, and others are currently in review. In Chapter 1, the whole scientific background of this thesis is explained. Chapters 2 and 3 are the core parts of this thesis, where the modelling work of large-scale folds and ice streams is presented. Realistic observations of folds and shear margins are shown in Chapter 4, which are the model basis and provide time-scale constrain for model running. Chapter 5 and Chapter 6 are other related work to support the ice stream and fold mechanisms.

- ***Chapter 1 Introduction***. This chapter introduces the general background, debates on fold and ice stream mechanisms, objectives of the thesis, the numerical modelling method, the framework, main conclusions and future perspectives.

- ***Chapter 2 Formation mechanisms of large-scale folding in Greenland's ice sheet***. Radio-echo sounding (RES) shows large-scale englacial stratigraphic folds are ubiquitous in Greenland's ice sheet. However, there is no consensus yet on how these folds form. Here, we use the full-Stokes code Underworld2 to simulate ice movements in three-dimensional convergent flow, mainly considering ice anisotropy due to a crystallographic preferred orientation, vertical viscosity and density gradients in ice layers, and bedrock topography.

- ***Chapter 3 Rapid ice stream formation due to mechanical anisotropy***. Fast-flowing ice streams drain most of the inland ice from Antarctic and Greenland ice sheets and it is fundamental to model them correctly to better project sea-level rise. However, the formation mechanism of ice streams which lack topographic steering and the development of their shear margins are still controversial. Here, we apply the full-Stokes code Underworld2 to simulate anisotropic ice flow in 3D large-scale ice-sheet models. By incorporating an anisotropic, non-linear viscosity and evolving c-axis orientations into our model, we are able to simulate the formation and behavior of ice streams under realistic, internally driven conditions, providing new insights into the fundamental processes governing ice stream dynamics.

- ***Chapter 4 Shear margins in upper half of Northeast Greenland Ice Stream were established two millennia ago***. Here we present a 3-dimensional analysis of the folding and advections of its stratigraphic horizons. We use isochronous radar reflections as passive tracers of ice deformation to reveal the history of NEGIS over the past few thousand years.

- ***Chapter 5 Comment on "Exceptionally high heat flux needed to sustain the Northeast Greenland Ice Stream" by Smith-Johnsen et al.(2020)***. Smith-Johnsen et al. (2020) model the effect of a potential hotspot on the Northeast Greenland Ice Stream (NEGIS). Here we argue an exceptionally high heat flux (970 mW $m^{-2}$) used in Smith-Johnsen's NEGIS model would be unique in the world and is incompatible with known geological processes that can raise the heat flux. There must thus be other possible mechanisms for NEGIS formation.

- ***Chapter 6 Folding due to anisotropy in ice, from drill core-scale cloudy bands to km-scale internal reflection horizons***. Folds in ice sheets are observed on the cm-scale in cloudy bands in drill cores and on the km-scale in radargrams. We address the question of the folding mechanism for these folds, by analysing the power spectra of fold trains to obtain the amplitude as a function of wavelength signal. These folds are not identical to the classical Biot-type (Biot, 1957) buckle folds due to a rheological contrast between layers. This chapter combines studies of large-scale and small-scale folds and provides strong substance to our large-scale fold modelling.

- ***Appendix***. The appendix attaches the example code scripts of modelling of large-scale folds and ice streams separately. Full-scripts can be accessed through Zenodo (large-scale folds, https://doi.org/10.5281/zenodo.11396618; ice streams, https://doi.org/10.5281/zenodo.13925401).

## 5.2 Outcome and main conclusions

The main results of this thesis are preliminary shown here by two cases of the modelling (details in Chapters 2 and 3):

For the scenario with a bumpy bedrock topography in the anisotropic ice model, the initial ice layers on bedrock bumps start to evolve into large-scale folds up to 300 m amplitude in 2000–3000 years with additional small folds in between (Fig. 7). The model in Fig. 8 has the same settings, but we reduced the value of $A_0$ to model the ice further downstream from the divide. Folds here can reach over 500 m (to 987 m) in amplitude in only 1000 years, indicating the buoyancy effect of the lowermost warmer and strain-rate softened ice.

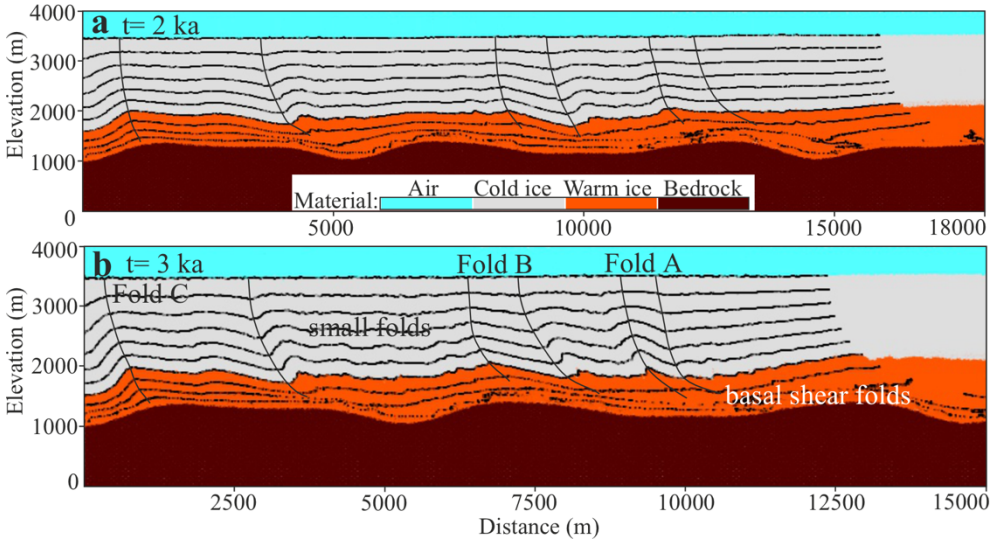


Fig. 7. Snapshots of the anisotropic ice model (near ice divide) with bedrock topography with 400 m tall bumps after (a) 2000 years and (b) 3000 years (full published results can be found in Chapter 2, Zhang et al., 2024).

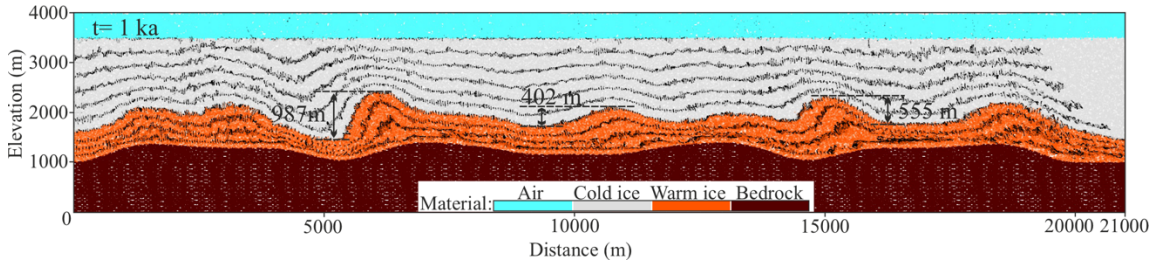


Fig. 8. Layer geometry snapshots after 1000 years of the anisotropic ice model with adapted $A_0$ value for softness in ice viscosities (near downstream) (full published results can be found in Chapter 2, Zhang et al., 2024).

The ice stream model in Fig. 9 has a zero velocity at the base of the ice sheet, simulating ice that is frozen to the bedrock. Ice first shows convergent flow towards the outlet gate. The convergent flow is asymmetric when the left inflow flux is twice as large as the right one. This effectively simulates a ca. 700 km wide drainage basin where the outflow gate is not centered in the middle, as is the case in the NE Greenland drainage basin of NEGIS (Fig. 1).

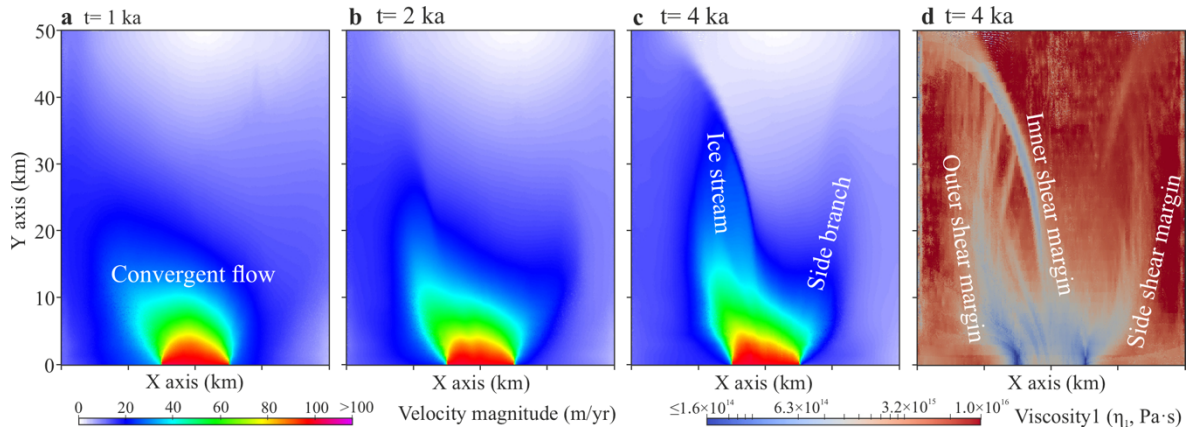


Fig. 9. Results of the NEGIS-type ice stream after 1000 years (a), 2000 years (b), and 4000 years (c) (full results can be found in Chapter 3). General viscosities $\eta_1$ from the ice surface at 4000 years (d) show shear margins with localized softening.

Conclusions of this thesis are mainly obtained from radargram observations and analysis, large-scale fold modelling, and numerical simulations of ice streams and shear margins, including formation mechanisms and evolution processes of folds and ice streams:

1) ***Geological time scale***. According to the amplitude-age trends of large-scale folds deprived from radargrams perpendicular to NEGIS, folds well outside of NEGIS and inside NEGIS show amplitudes that already start to increase from zero at the surface, which indicates currently active fold amplification. Folds inside and adjacent to the shear margins show amplitudes are close to zero in layers younger than 2 kyrs BP, signifying that these folds stopped growing by about 2 kyrs at the latest when shear margins in the upstream region of NEGIS were established. The onset of folding is the age where the amplitude-depth trend reaches a steady slope and, hence, the age for layers older than ca 3.5-4 kyrs BP. Some amplitude-age trends of folds inside and

outside NEGIS also show bends at other ages, such as ca. 5-6 kyrs and ca. 8 kyrs, which suggests that the ice sheet here experienced multiple folding events over time.

2) ***Large-scale folding mechanisms***. Motivated by observations of folds in radargrams of the GrIS, our modeling results within few thousand years show that: Large-scale folds can form in convergent ice flow, mainly controlled by its rheological anisotropy. This anisotropy is due to the CPO. Anisotropy amplifies existing undulations in the ice stratigraphy due to bedrock topography or processes at the ice-bed interface. Buoyancy of the deepest and warmest ice in anticlinal cores can significantly enhance fold amplifications where ice is effectively weakened by strain-rate softening due to the power-law rheology of ice. As observed in ice sheets, large-scale fold amplitudes are highest in the middle of the ice column or just below. Meanwhile, near-base fold patterns are more complex and often result in recumbent folds due to the bedrock constraint.

3) ***Anisotropy on all-scale folds***. According to our large-scale fold study and observations of small-scale folds in cloudy bands in the EGRIP drill core, rheological variations within ice layers appear to not play a significant role. Biot-type buckle folds due to rheological contrasts between layers have a characteristic length scale, related to the layer thickness and the rheological contrast between the isotropic layers, which are not cases of small-scale and large-scale folds in ice sheets with no length scale that are expected due to anisotropy. Combining the small-scale and large-scale folds in ice sheets resulted in a self-affine trend where largest folds are relatively flat, which can be caused by additional boundary conditions, such as vertical flattening and bedrock irregularities, that modify the anisotropy-induced folds on the large scale.

4) ***Shear margin establishment***. The rotation of c-axes, an inherent material behavior that is implemented in Underworld2, is the primary mechanism for the formation of shear margins, and, hence, ice streams in our simulations. C-axis rotations cause the directional alignment of the easy-glide crystallographic basal planes towards the vertical shear-margin plane, making the ice effectively softer. Shear zones usually form in pairs that bound the ice stream that can now flow much faster. Our models show that shear-induced CPO change by itself is enough to establish shear margins and an ice stream like NEGIS if the drainage is constrained by a relatively narrow outflow gate. Without ice anisotropy, shear margins and an ice stream cannot be

established under our model conditions. Bedrock topography, bedrock sliding, elevated geothermal heat flux, or shear heating may still play a role as additional or modifying factors, or in the further development of the ice stream as shear heating affects the shear margins formed due to CPO rotation.

5) ***Ice stream evolution***. Our model results reinforce the understanding, that ice streams initiate and evolve primarily by the formation and movement of shear margins in relation to the location of outlet gates within the drainage basin. We demonstrate that ice anisotropy can initiate a proto ice stream draining ice towards the outlet(s) in approximately 1000 to 2000 years. As the ice stream evolves, newly shear margins establish and subdivide the flow into tributaries depending on inland flow environments. Shear margins continue to migrate along with the ice flow, forming new margins as the system develops further. Dominant tributaries, such as NEGIS, can extend inland, nearly reaching the ice divide. Radar observations constrain the timing of when the shear margins of NEGIS fully developed to about 2000 years before present, and our simulations suggest that the lead-up time to this state was another 1000–2000 years. This would allocate the overall initiation of NEGIS to about 3–4 ka BP at the end of the warm phase that caused the retreat of the glaciers at the outlets in NE Greenland.

## 6. Future perspectives

This thesis applies an evolving anisotropy in large-scale ice-sheet modelling with respect to folds and ice streams, which can better explain ice-flow dynamics of ice sheets and provide indications to future ice research:

1) In our fold modelling, an improved implementation of ice anisotropy and basal shearing can result in high-strain-rate areas where the power-law ice would be softened, even when frozen to the bed. This indicates that ice sheets could be more unstable when suddenly triggered to flow by external forcings, such as climate change, ice-sheet geometry changes or tectonic events.

2) Our ice-stream modelling indicates that future ice stream evolution will likely involve continuous geometry and position changes due to shear margin migration, occurring on a thousand-year timescale. These systems are sensitive to shifts in ice mass, which alter inland ice flows, potentially leading to the emergence of new tributaries, or their shutdown. Additionally, abrupt changes at the ice sheet front, such as variations in basal conditions, could result in the rapid formation of new ice streams and shear margins.

3) Our most important finding is that internal ice anisotropy alone can drive ice stream formation and evolution on a time scale of only thousands of years, without external forcing by, for example, basal melting, shear heating or bedrock topography. This underscores the dynamic nature of ice streams, with their evolving margins and tributaries, and must be considered in future projections of ice sheet stability under climate change scenarios.

There are also some model limitations and unsolved scientific problems needed more work in the future:

1) ***Buoyancy effect between folded layers***. Our fold simulations indicate that fold amplification can be significantly enhanced to form tall 'plume-like' folds, when the overall flow velocity is sufficiently high to reduce the effective viscosity enough to allow the rise of warm, buoyant ice in anticlinal cores. However, there is a need to constrain the effective viscosity of flowing ice since we simplify the calculation of the near-downstream ice viscosity. In addition, it deserves more work to carefully

constrain and find a balance between the negative vertical strain rates from surface accumulation, the increased horizontal stretching rate (outflow) and the buoyancy effect through viscosity changes, etc. For example, the syn-sedimentation experiments for salt diapir growth are good indications (eg., Fuchs et al., 2011; and publications during my PhD period of my master work, Zhang et al., 2020, 2021), where 'fold' patterns would be different from the way of 'surface accumulation', layer thickness, external forcing, etc.

2) ***Influence of a changeable outlet environment on ice-stream formation and evolution***. We define a fixed outlet boundary condition (width & a low outflow velocity). However, the real velocities at the NEGIS front are variable through space and time and can reach up to more than 1000 m/yr (Khan et al., 2022). Our ice viscosities near the ice front or downstream are possibly higher than reality. It deserves more future work to improve the outlet settings according to geological observations, and model an ice stream's respond to a changeable outlet environment.

3) ***Ice stream and its tributaries in a muti-outlets system***. To maximize the model resolution and accuracy of the anisotropy code, we scale down the horizontal model size and set only one outlet gate. The real NEGIS, for example, has three main outlet glaciers at present. There is a need to investigate how an ice stream and its tributaries evolve (formation, shifts, and cessation) in a dynamic muti-outlets system. This would help to rebuild the history of ice streams and ice sheets, especially where the old ice streams were found (Franke et al., 2022a; Tabone et al., 2024), and to predict their future developments.

4) ***Other influencing factors on ice-stream evolution: variable ice precipitation through time and space, shear heating and basal melting***. Variable ice precipitation and surface accumulation may change the inland ice flow environment related to evolution of an ice stream and especially its tributaries. The dynamic nature of ice streams may accelerate when processes such as basal melting or shear heating are additionally involved. These are important to be considered in the ice-stream evolution with a longer geological time.

## References

Anandakrishnan, S., Blankenship, D. D., Alley, R. B., & Stoffa, P. L. (1998). Influence of subglacial geology on the position of a West Antarctic ice stream from seismic observations. *Nature*, 394, 62–65. https://doi.org/10.1038/27889

Artemieva, I. M. (2019). Lithosphere thermal thickness and geothermal heat flux in Greenland from a new thermal isostasy method. *Earth-Science Reviews*, 188, 469–481. https://doi.org/10.1016/j.earscirev.2018.10.015

Alley, R. B., Gow, A. J., Meese, D. A., Fitzpatrick, J. J., Waddington, E. T., & Bolzan, J. F. (1997). Grain-scale processes, folding, and stratigraphic disturbance in the GISP2 ice core. *Journal of Geophysical Research: Oceans*, 102(C12), 26819–26830. https://doi.org/10.1029/96JC03836

Alley, R. B. (1988). Fabrics in polar ice sheets: development and prediction. *Science*, 240(4851), 493–495. doi:10.1126/science.240.4851.493

Bell, R. E., Tinto, K., Das, I., Wolovick, M., Chu, W., Creyts, T. T., et al. (2014). Deformation, warming and softening of Greenland's ice by refreezing meltwater. *Nature Geoscience*, 7(7), 497–502. https://doi.org/10.1038/ngeo2179

Bentley, C. R. (1987). Antarctic Ice Streams: A review. *Journal of Geophysical Research: Solid Earth*, 92(B9), 8843–8858. https://doi.org/10.1029/JB092iB09p08843

Beucher, R., Giordani, J., Moresi, L., Mansour, J., Kaluza, O., Velic, M., et al. (2022). Underworld2: Python Geodynamics Modelling for Desktop, HPC and Cloud (v2.14.1b) [Software]. Zenodo. https://doi.org/10.5281/zenodo.7455999

Biot, M. A. (1957). Folding instability of a layered viscoelastic medium under compression. *Proceedings of the Royal Society of London. Series A. Mathematical and Physical Sciences*, 242(1231), 444-454. https://doi.org/10.1098/rspa.1957.0187

Bons, P. D., de Riese, T., Franke, S., Llorens, M. G., Sachau, T., Stoll, N., Weikusat, I., Westhoff, J., & Zhang, Yu (2021). Comment on "Exceptionally high heat flux needed to sustain the Northeast Greenland Ice Stream" by Smith-Johnsen et al.(2020). *The Cryosphere*, 15(5), 2251–2254. https://doi.org/10.5194/tc-15-2251-2021

Bons, P. D., Jansen, D., Mundel, F., Bauer, C. C., Binder, T., Eisen, O., et al. (2016). Converging flow and anisotropy cause large-scale folding in Greenland's ice sheet. *Nature communications*, 7(1), 11427. https://doi.org/10.1038/ncomms11427

Bons, P. D., Kleiner, T., Llorens, M. G., Prior, D. J., Sachau, T., Weikusat, I., & Jansen, D. (2018). Greenland Ice Sheet: Higher nonlinearity of ice flow significantly reduces estimated basal motion. *Geophysical Research Letters*, 45(13), 6542–6548. https://doi.org/10.1029/2018GL078356

Budd, W. F., & Jacka, T. H. (1989). A review of ice rheology for ice sheet modelling. *Cold regions science and technology*, 16(2), 107–144. https://doi.org/10.1016/0165-232X(89)90014-1

Christianson, K., Peters, L. E., Alley, R. B., Anandakrishnan, S., Jacobel, R. W., Riverman, et al. (2014). Dilatant till facilitates ice-stream flow in northeast Greenland. *Earth and Planetary Science Letters*, 401, 57–69. https://doi.org/10.1016/j.epsl.2014.05.060

Colgan, W., Wansing, A., Mankoff, K., Lösing, M., Hopper, J., Louden, K., et al. (2021). Greenland geothermal heat flow database and map (version 1). *Earth System Science Data*, 14, 2209–2238. https://doi.org/10.5194/essd-14-2209-2022

Cuffey, K. M., & Kavanaugh, J. L. (2011). How nonlinear is the creep deformation of polar ice? A new field assessment. *Geology*, 39, 1027–1030. https://doi.org/10.1130/G32259.1

Duval, P., Ashby, M. F., & Anderman, I. (1983). Rate-controlling processes in the creep of polycrystalline ice. *The Journal of Physical Chemistry*, 87(21), 4066–4074. https://doi.org/10.1021/j100244a014

Elsworth, C. W., & Suckale, J. (2016). Rapid ice flow rearrangement induced by subglacial drainage in West Antarctica. *Geophysical Research Letters*, 43(22), 11697–11707. https://doi.org/10.1002/2016GL070430

Ershadi, M. R., Drews, R., Martín, C., Eisen, O., Ritz, C., Corr, H., et al. (2022). Polarimetric radar reveals the spatial distribution of ice fabric at domes and divides in East Antarctica. *The Cryosphere*, 16(5), 1719–1739. https://doi.org/10.5194/tc-16-1719-2022

Fahnestock, M. A., Bindschadler, R. A., Kwok, R., & Jezek, K. C. (1993). Greenland ice sheet surface properties and ice dynamics from ERS-1 SAR imagery. *Science*, 262(5139), 1530–1534. doi:10.1126/science.262.5139.1530

Fahnestock, M. A., Joughin, I., Scambos, T. A., Kwok, R., Krabill, W. B., & Gogineni, S. (2001). Ice-stream-related patterns of ice flow in the interior of northeast Greenland. *Journal of Geophysical Research: Atmospheres*, 106(D24), 34035–34045. https://doi.org/10.1029/2001JD900194

Franke, S., Jansen, D., Beyer, S., Neckel, N., Binder, T., Paden, J., & Eisen, O. (2021). Complex basal conditions and their influence on ice flow at the onset of the Northeast Greenland Ice Stream. *Journal of Geophysical Research: Earth Surface*, 126(3), e2020JF005689. https://doi.org/10.1029/2020JF005689

Franke, S., Bons, P. D., Westhoff, J., Weikusat, I., Binder, T., Streng, K., et al. (2022a). Holocene ice-stream shutdown and drainage basin reconfiguration in northeast Greenland. *Nature Geoscience*, 15(12), 995–1001. https://doi.org/10.1038/s41561-022-01082-2

Franke, S., Jansen, D., Binder, T., Paden, J. D., Dörr, N., Gerber, T. A., et al. (2022b). Airborne ultra-wideband radar sounding over the shear margins and along flow lines at the onset region of the Northeast Greenland Ice Stream. *Earth System Science Data*, *14*(2), 763–779. https://doi.org/10.5194/essd-14-763-2022

Franke, S., Bons, P. D., Streng, K., Mundel, F., Binder, T., Weikusat, I., et al. (2023). Three-dimensional topology dataset of folded radar stratigraphy in northern Greenland. *Scientific Data*, *10*(1), 525. https://doi.org/10.1038/s41597-023-02339-0

Fuchs, L., Schmeling, H., & Koyi, H. (2011). Numerical models of salt diapir formation by down-building: the role of sedimentation rate, viscosity contrast, initial amplitude and wavelength. *Geophysical journal international*, 186(2), 390–400. https://doi.org/10.1111/j.1365-246X.2011.05058.x

Gillet-Chaulet, F., Gagliardini, O., Meyssonnier, J., Zwinger, T., & Ruokolainen, J. (2006). Flow-induced anisotropy in polar ice and related ice-sheet flow modelling. *Journal of non-newtonian fluid mechanics*, 134(1–3), 33–43. https://doi.org/10.1016/j.jnnfm.2005.11.005

Gillet-Chaulet, F., Hindmarsh, R. C. A., Corr, H. F. J., King, E. C., & Jenkins, A. (2011). In-situ quantification of ice rheology and direct measurement of the Raymond Effect at Summit,

Greenland using a phase-sensitive radar. Geophysical Research Letters, 38, L24503. https://doi.org/10.1029/2011GL049843

Glen, J. W. (1955). The creep of polycrystalline ice. *Proceedings of the Royal Society of London. Series A. Mathematical and Physical Sciences*, 228(1175), 519–538. https://doi.org/10.1098/rspa.1955.0066

Goldsby, D. L., & Kohlstedt, D. L. (2001). Superplastic deformation of ice: Experimental observations. *Journal of Geophysical Research: Solid Earth*, 106(B6), 11017–11030. https://doi.org/10.1029/2000JB900336

Gow, A. J., & Williamson, T. (1976). Rheological implications of the internal structure and crystal fabrics of the West Antarctic ice sheet as revealed by deep core drilling at Byrd Station. *Geological Society of America Bulletin*, 87(12), 1665–1677. https://doi.org/10.1130/0016-7606(1976)87<1665:RIOTIS>2.0.CO;2

Hills, B. H., Harper, J. T., Humphrey, N. F., & Meierbachtol, T. W. (2017). Measured horizontal temperature gradients constrain heat transfer mechanisms in Greenland ice. *Geophysical Research Letters*, 44(19), 9778–9785. https://doi.org/10.1002/2017GL074917

Holschuh, N., Lilien, D. A., & Christianson, K. (2019). Thermal weakening, convergent flow, and vertical heat transport in the Northeast Greenland Ice Stream shear margins. *Geophysical Research Letters*, 46(14), 8184–8193. https://doi.org/10.1029/2019GL083436

Hudleston, P.J. (1977). Progressive Deformation and Development of Fabric Across Zones of Shear in Glacial Ice. *In: Saxena, S.K., Bhattacharji, S., Annersten, H., Stephansson, O. (eds) Energetics of Geological Processes. Springer, Berlin, Heidelberg*. https://doi.org/10.1007/978-3-642-86574-9_7

Hudleston, P. J. (2015). Structures and fabrics in glacial ice: A review. *Journal of Structural Geology*, 81, 1–27. https://doi.org/10.1016/j.jsg.2015.09.003

Hughes, T. (1977). West Antarctic ice streams. *Reviews of Geophysics*, 15(1), 1–46. https://doi.org/10.1029/RG015i001p00001

Hutter, K. (1983). Theoretical glaciology; material science of ice and the mechanics of glaciers and ice sheets. *D. Reidel Publishing Co., Dordrecht, Terra Scientific Publishing Co*, Tokyo.

Hvidberg, C. S., Grinsted, A., Dahl-Jensen, D., Khan, S. A., Kusk, A. J., Andersen, K., et al. (2020). Surface velocity of the Northeast Greenland Ice Stream (NEGIS): assessment of interior velocities derived from satellite data by GPS. *The Cryosphere*, 14(10), 3487–3502. https://doi.org/10.5194/tc-14-3487-2020

Jansen, D., Llorens, M. G., Westhoff, J., Steinbach, F., Kipfstuhl, S., Bons, P. D., et al. (2016). Small-scale disturbances in the stratigraphy of the NEEM ice core: observations and numerical model simulations. *The Cryosphere*, 10(1), 359–370. https://doi.org/10.5194/tc-10-359-2016

Jansen, D., Franke, S., Bauer, C. C., Binder, T., Dahl-Jensen, D., Eichler, J., Eisen, O., Hu, Y., Kerch, J., Llorens, M. G., Miller, H., Neckel, N., Paden, J., de Riese, T., Sachau, T., Stoll, N., Weikusat, I., Wilhelms, F., Zhang, Yu, & Bons, P. D. (2024). Shear margins in upper half of Northeast Greenland Ice Stream were established two millennia ago. *Nature Communications*, 15(1), 1193. https://doi.org/10.1038/s41467-024-45021-8

Joughin, I., Fahnestock, M., MacAyeal, D., Bamber, J. L., & Gogineni, P. (2001). Observation and analysis of ice flow in the largest Greenland ice stream. *Journal of*

*Geophysical Research: Atmospheres*, 106(D24), 34021–34034. https://doi.org/10.1029/2001JD900087

Joughin, I. A. N., Smith, B. E., & Howat, I. M. (2018). A complete map of Greenland ice velocity derived from satellite data collected over 20 years. *Journal of Glaciology*, 64(243), 1–11. https://doi.org/10.1017/jog.2017.73

Kamb, B. (1972). Experimental recrystallization of ice under stress. *Geophysical Monograph Series*, 16, 211–241.

Kocher, T., Mancktelow, N. S., & Schmalholz, S. M. (2008). Numerical modelling of the effect of matrix anisotropy orientation on single layer fold development. *Journal of Structural Geology*, 30(8), 1013–1023. https://doi.org/10.1016/j.jsg.2008.04.006

Khan, S., Kjær, K., Bevis, M., Bamber, J. L., Wahr, J., Kjeldsen, K. K., et al. (2014). Sustained mass loss of the northeast Greenland ice sheet triggered by regional warming. *Nature Climate Change*, 4(4), 292–299. https://doi.org/10.1038/nclimate2161

Khan, S. A., Choi, Y., Morlighem, M., Rignot, E., Helm, V., Humbert, A., et al. (2022). Extensive inland thinning and speed-up of Northeast Greenland Ice Stream. *Nature*, 611(7937), 727–732. https://doi.org/10.1038/s41586-022-05301-z

Krabbendam, M. (2016). Sliding of temperate basal ice on a rough, hard bed: creep mechanisms, pressure melting, and implications for ice streaming. *The Cryosphere*, 10(5), 1915–1932. https://doi.org/10.5194/tc-10-1915-2016

Kuiper, E. J. N., De Bresser, J. H., Drury, M. R., Eichler, J., Pennock, G. M., & Weikusat, I. (2020). Using a composite flow law to model deformation in the NEEM deep ice core, Greenland–Part 2: The role of grain size and premelting on ice deformation at high homologous temperature. *The Cryosphere*, 14(7), 2449–2467. https://doi.org/10.5194/tc-14-2449-2020

Kyrke-Smith, T. M., Katz, R. F., & A. C. Fowler. (2015). Subglacial hydrology as a control on emergence, scale, and spacing of ice streams. *Journal of Geophysical Research: Earth Surface*, 120(8), 1501–1514. https://doi.org/10.1002/2015JF003505

Larsen, N. K., Levy, L. B., Carlson, A. E., Buizert, C., Olsen, J., Strunk, A., et al. (2018). Instability of the Northeast Greenland Ice Stream over the last 45,000 years. *Nature Communications*, 9(1), 1872. https://doi.org/10.1038/s41467-018-04312-7

Leysinger Vieli, G. M., Martin, C., Hindmarsh, R. C. A., & Lüthi, M. P. (2018). Basal freeze-on generates complex ice-sheet stratigraphy. *Nature Communications*, 9(1), 4669. https://doi.org/10.1038/s41467-018-07083-3

Lilien, D. A., Rathmann, N. M., Hvidberg, C. S., & Dahl-Jensen, D. (2021). Modeling Ice-Crystal Fabric as a Proxy for Ice-Stream Stability. *Journal of Geophysical Research: Earth Surface*, 126(9), e2021JF006306. https://doi.org/10.1029/2021JF006306

Llorens, M. G., Griera, A., Bons, P. D., Weikusat, I., Prior, D., Gomez-Rivas, E., et al. (2022). Can changes in deformation regimes be inferred from crystallographic preferred orientations? *The Cryosphere*, 16(5), 2009–2024. https://doi.org/10.5194/tc-16-2009-2022

Martos, Y. M., Jordan, T. A., Catalán, M., Jordan, T. M., Bamber, J. L., & Vaughan, D. G. (2018). Geothermal heat flux reveals the Iceland hotspot track underneath Greenland. *Geophysical research letters*, 45, 8214–8222. https://doi.org/10.1029/2018GL078289,

MacGregor, J. A., Fahnestock, M. A., Catania, G. A., Paden, J. D., Prasad Gogineni, S., Young, S. K., et al. (2015). Radiostratigraphy and age structure of the Greenland Ice Sheet.

*Journal of Geophysical Research: Earth Surface*, 120(2), 212–241. https://doi.org/10.1002/2014JF003215

Martín, C., Gudmundsson, G. H., Pritchard, H. D., & Gagliardini, O. (2009). On the effects of anisotropic rheology on ice flow, internal structure, and the age-depth relationship at ice divides. *Journal of Geophysical Research: Earth Surface*, 114(F4). https://doi.org/10.1029/2008JF001204

Moresi, L., Dufour, F., & Mühlhaus, H. B. (2003). A Lagrangian integration point finite element method for large deformation modeling of viscoelastic geomaterials. *Journal of computational physics*, 184(2), 476–497. https://doi.org/10.1016/S0021-9991(02)00031-1

Moresi, L., & Mühlhaus, H. B. (2006). Anisotropic viscous models of large-deformation Mohr–Coulomb failure. *Philosophical Magazine*, 86(21–22), 3287–3305. https://doi.org/10.1016/S0021-9991(02)00031-1

Mojtabavi, S., Wilhelms, F., Cook, E., Davies, S., Sinnl, G., Skov Jensen, M., et al. (2019). A first chronology for the East Greenland Ice-core Project (EGRIP) over the Holocene and last glacial termination. *Climate of the Past Discussions*, 2019, 1–22. https://doi.org/10.5194/cp-16-2359-2020

Morlighem, M., Williams, C. N., Rignot, E., An, L., Arndt, J. E., Bamber, J. L., et al. (2017). BedMachine v3: Complete bed topography and ocean bathymetry mapping of Greenland from multibeam echo sounding combined with mass conservation. *Geophysical research letters*, 44(21), 11–051. https://doi.org/10.1002/2017GL074954

Mouginot, J., Rignot, E., Scheuchl, B., Fenty, I., Khazendar, A., Morlighem, M., et al. (2015). Fast retreat of zachariæ isstrøm, northeast Greenland. *Science*, 350, 1357–1361 doi:10.1126/science.aac7111

NEEM community members. (2013). Eemian interglacial reconstructed from a Greenland folded ice core. *Nature*, 493, 489–494. https://doi.org/10.1038/nature11789

Panton, C., & Karlsson, N. B. (2015). Automated mapping of near bed radio-echo layer disruptions in the Greenland Ice Sheet. *Earth and Planetary Science Letters*, 432, 323–331. https://doi.org/10.1016/j.epsl.2015.10.024

Pattyn, F., Perichon, L., Aschwanden, A., Breuer, B., De Smedt, B., Gagliardini, O., et al. (2008). Benchmark experiments for higher-order and full-Stokes ice sheet models (ISMIP–HOM). *The Cryosphere*, 2(2), 95–108. https://doi.org/10.5194/tc-2-95-2008

Pettit, E. C., & Waddington, E. D. (2003). Ice flow at low deviatoric stress. *Journal of Glaciology*, 49, 359–369. https://doi.org/10.3189/172756503781830584

Perol, T., Rice, J. R. (2015). Shear heating and weakening of the margins of West Antarctic ice streams. *Geophysical Research Letters*, 42(9), 3406–3413. https://doi.org/10.1002/2015GL063638

Pimienta, P., Duval, P., & Lipenkov, V. Y. (1987). Mechanical behavior of anisotropic polar ice. *The Physical Basis Of Ice Sheet Modeling (Proceedings Of The Vancouver Symposium, August 1987)*, 170, 57–66.

QGIS Development Team. (2024). QGIS Geographic Information System. Open Source Geospatial Foundation Project. http://qgis.osgeo.org

Qi, C., Goldsby, D. L., & Prior, D. J. (2017). The down-stress transition from cluster to cone fabrics in experimentally deformed ice. *Earth and Planetary Science Letters*, 471, 136–147. https://doi.org/10.1016/j.epsl.2017.05.008

Qi, C., Prior, D. J., Craw, L., Fan, S., Llorens, M. G., Griera, A., et al. (2019). Crystallographic preferred orientations of ice deformed in direct-shear experiments at low temperatures. *The Cryosphere*, 13(1), 351–371. https://doi.org/10.5194/tc-13-351-2019

Ran, H., de Riese, T., Llorens, M. G., Finch, M. A., Evans, L. A., Gomez-Rivas, E., et al. (2019). Time for anisotropy: The significance of mechanical anisotropy for the development of deformation structures. *Journal of Structural Geology*, 125, 41–47. https://doi.org/10.1016/j.jsg.2018.04.019

Ranganathan, M., & Minchew, B. (2024). A modified viscous flow law for natural glacier ice: Scaling from laboratories to ice sheets. *Proceedings of the National Academy of Sciences*, 121(23), e2309788121. https://doi.org/10.1073/pnas.2309788121

Richards, D. H., Pegler, S. S., Piazolo, S., & Harlen, O. G. (2021). The evolution of ice fabrics: A continuum modelling approach validated against laboratory experiments. *Earth and Planetary Science Letters*, 556, 116718. https://doi.org/10.1016/j.epsl.2020.116718

Robin, G. D. Q. (1955). Ice movement and temperature distribution in glaciers and ice sheets. *Journal of glaciology*, 2(18), 523-532. https://doi.org/10.3189/002214355793702028

Rogozhina, I., Martinec, Z., Hagedoorn, J. M., Thomas, M., & Fleming, K. (2011). On the long-term memory of the Greenland Ice Sheet. *Journal of Geophysical Research: Earth Surface*, 116(F1). https://doi.org/10.1029/2010JF001787

Rogozhina, I., Petrunin, A. G., Vaughan, A. P. M., Steinberger, B., Johnson, J. V., Kaban, M. K. R., et al. (2016). Melting at the base of the Greenland ice sheet explained by Iceland hotspot history. *Nature Geoscience*, 9, 366–369. https://doi.org/10.1038/ngeo2689

Sachau, T., Yang, H., Lang, J., Bons, P. D., & Moresi, L. (2022). ISMIP-HOM benchmark experiments using Underworld. *Geoscientific Model Development*, 15(23), 8749–8764. https://doi.org/10.5194/gmd-15-8749-2022

Smith, E. C., Baird, A. F., Kendall, J. M., Martín, C., White, R. S., Brisbourne, A. M., & Smith, A. M. (2017). Ice fabric in an Antarctic ice stream interpreted from seismic anisotropy. *Geophysical Research Letters*, 44(8), 3710–3718. https://doi.org/10.1002/2016GL072093

Smith-Johnsen, S., de Fleurian, B., Schlegel, N., Seroussi, H., & Nisancioglu, K. (2020). Exceptionally high heat flux needed to sustain the Northeast Greenland Ice Stream. *The Cryosphere*, 14(3), 841–854. https://doi.org/10.5194/tc-14-841-2020

Sharples, W., Moresi, L. N., Velic, M., Jadamec, M. A., & May, D. A. (2016). Simulating faults and plate boundaries with a transversely isotropic plasticity model. *Physics of the Earth and Planetary Interiors*, 252, 77–90. https://doi.org/10.1016/j.pepi.2015.11.007

Tabone, I., Robinson, A., Montoya, M., & Alvarez-Solas, J. (2024). Holocene thinning in central Greenland controlled by the Northeast Greenland Ice Stream. *Nature communications*, 15(1), 6434. https://doi.org/10.1038/s41467-024-50772-5

Thorsteinsson, T., Waddington, E. D., Taylor, K. C., Alley, R. B., & Blankenship, D. D. (1999). Strain-rate enhancement at Dye 3, Greenland. *Journal of Glaciology*, 45(150), 338-345. https://doi.org/10.3189/002214399793377185

Thorsteinsson, T., & Waddington, E. D. (2002). Folding in strongly anisotropic layers near ice-sheet centers. *Annals of Glaciology*, 35, 480–486. https://doi.org/10.3189/172756402781816708

Treverrow, A., Budd, W. F., Jacka, T. H., & Warner, R. C. (2012). The tertiary creep of polycrystalline ice: experimental evidence for stress-dependent levels of strain-rate enhancement. *Journal of Glaciology*, 58(208), 301-314. https://doi.org/10.3189/2012JoG11J149

Weertman, J. (1983). Creep deformation of ice. *Annual Review of Earth and Planetary Sciences*, 11, 215–240

Weikusat, I., Kuiper, E. J. N., Pennock, G. M., Kipfstuhl, S., & Drury, M. R. (2017a). EBSD analysis of subgrain boundaries and dislocation slip systems in Antarctic and Greenland ice. *Solid Earth*, 8(5), 883–898. https://doi.org/10.5194/se-8-883-2017

Weikusat, I., Jansen, D., Binder, T., Eichler, J., Faria, S. H., Wilhelms, F., ... & Kleiner, T. (2017b). Physical analysis of an Antarctic ice core—towards an integration of micro-and macrodynamics of polar ice. *Philosophical Transactions of the Royal Society A: Mathematical, Physical and Engineering Sciences*, 375(2086), 20150347. https://doi.org/10.1098/rsta.2015.0347

Wolovick, M. J., Creyts, T. T., Buck, W. R., & Bell, R. E. (2014). Traveling slippery patches produce thickness-scale folds in ice sheets. *Geophysical Research Letters*, 41(24), 8895–8901. https://doi.org/10.1002/2014GL062248

Zhang, Yu, Li, J., Lei, Y., Yang, M., & Cheng, P. (2020). 3D simulations of salt tectonics in the Kwanza Basin: Insights from analogue and Discrete-Element numerical modeling. *Marine and Petroleum Geology*, 122, 104666. https://doi.org/10.1016/j.marpetgeo.2020.104666

Zhang, Yu, Li, J., & Cheng, P. (2021). Comparison of Salt Structure Deformation Periods of Conjugated Salt Basins in Central Segment of South Atlantic. *Earth Science*, 46(6), 2218–2229. http://www.earth-science.net/article/doi/10.3799/dqkx.2020.033

Zhang, Yu, Sachau, T., Franke, S., Yang, H., Li, D., Weikusat, I., & Bons, P. D. (2024). Formation mechanisms of large-scale folding in Greenland's ice sheet. *Geophysical Research Letters*, 51(16), e2024GL109492. https://doi.org/10.1029/2024GL109492

## Contributions to scientific publications

***Chapter 2***

**Zhang, Yu,** Sachau, T., Franke, S., Yang, H., Li, D., Weikusat, I., & Bons, P. D. (2024). Formation mechanisms of large-scale folding in Greenland's ice sheet. Published in *Geophysical Research Letters*, 51(16), e2024GL109492. doi:10.1029/2024GL109492

This paper is mainly based on numerical simulations of Zhang. The general idea for this paper comes from the original PhD-project proposal by supervisors Bons and Weikusat. Authors Zhang, Sachau, Yang, and Li developed the Underworld2 scripts and setups of the numerical simulations. Franke made the maps of northern Greenland and radar profiles. Zhang wrote the original manuscript, which was edited by the other authors.

***Chapter 3***

**Zhang, Yu,** Franke, S., Sachau, T., Jansen, D., Yang, H., Li, D., Hu, Y., Weikusat, I., & Bons, P. D. Rapid ice stream formation due to mechanical anisotropy. Submitted to *Science Advances* (Note that the final manuscript may deviate slightly from the version provided in the thesis).

This manuscript is mainly based on numerical simulations of Zhang. The general idea for this manuscript comes from the original PhD-project proposal by supervisors Bons and Weikusat. Authors Zhang, Sachau, Yang, Li, and Hu developed the Underworld2 scripts and setups of the numerical simulations. Franke and Jansen made the maps of surface velocity and strain analysis of NEGIS and its shear margins. Zhang wrote the original manuscript, which was edited by the other authors.

***Chapter 4***

Jansen, D., Franke, S., Bauer, C. C., Binder, T., Dahl-Jensen, D., Eichler, J., Eisen, O., Hu, Y., Kerch, J., Llorens, M. G., Miller, H., Neckel, N., Paden, J., de Riese, T., Sachau, T., Stoll, N., Weikusat, I., Wilhelms, F., **Zhang, Yu,** & Bons, P. D. (2024). Shear margins in upper

half of Northeast Greenland Ice Stream were established two millennia ago. Published in *Nature Communications*, 15(1), 1193. doi:10.1038/s41467-024-45021-8

Jansen, Franke, and Bons are the lead authors. Jansen conceived the idea of folds dragged into the ice stream, while Bons conceived the method to date folding events. Zhang contributed to tracing folded ice layers on radargrams and analysing the amplitude-depth/age data. Other authors also contributed to collecting and processing the radar data, fold layer tracing and analyses, constructing the 3D model and stratigraphic surface, the ELLE + VPFFT folding simulations, and the strain and ice fabric analyses. All authors participated in writing and discussing the final results.

***Chapter 5***

Bons, P. D., de Riese, T., Franke, S., Llorens, M. G., Sachau, T., Stoll, N., Weikusat, I., Westhoff, J., & **Zhang, Yu** (2021). Comment on "Exceptionally high heat flux needed to sustain the Northeast Greenland Ice Stream" by Smith-Johnsen et al.(2020). Published in *The Cryosphere*, 15(5), 2251–2254. doi:10.5194/tc-15-2251-2021

Bons provided the initial idea and concept of the paper, which was discussed and written jointly by Zhang and all authors.

***Chapter 6***

Bons, P. D., Hu, Y., Llorens, M. G., Franke, S., Stoll, N., Weikusat, I., Westhoff, J., & **Zhang, Yu.** Folding due to anisotropy in ice, from drill core-scale cloudy bands to km-scale internal reflection horizons. Submitted to *The Cryosphere* (Note that the final manuscript may deviate slightly from the version provided in the thesis).

Bons conceived the study, performed most analyses, and wrote the manuscript. Hu, Llorens, and Zhang carried out numerical simulations and contributed to modelling efforts. Westhoff, Stoll and Weikusat acquired and processed visual stratigraphy data. Franke processed and contributed radar data. All authors jointly contributed to the discussion of results and reviewed the manuscript.

# Chapter 2

## Formation mechanisms of large-scale folding in Greenland's ice sheet

**Yu Zhang[1], Till Sachau[1], Steven Franke[1,2], Haibin Yang[3], Dian Li[1,4], Ilka Weikusat[1,2], and Paul D. Bons[1,5]**

[1]Department of Geosciences, Tübingen University, Tübingen, Germany.

[2]Alfred Wegener Institute, Helmholtz Centre for Polar and Marine Research, Bremerhaven, Germany.

[3]School of Earth Sciences, Zhejiang University, Hangzhou, China.

[4]College of Earth and Planetary Science, Chengdu University of Technology, Chengdu, China.

[5]School of Earth Science and Resources, China University of Geosciences (Beijing), Beijing, China.

Published in Geophysical Research Letters, 2024, 51(16), e2024GL109492. doi:10.1029/2024GL109492

This is an author version of the manuscript. The fulltext (copy-edited publishers version) can be accessed at: https://doi.org/10.1029/2024GL109492

## Abstract

Radio-echo sounding (RES) shows large-scale englacial stratigraphic folds are ubiquitous in Greenland's ice sheet. However, there is no consensus yet on how these folds form. Here, we use the full-Stokes code Underworld2 to simulate ice movements in three-dimensional convergent flow, mainly considering ice anisotropy due to a crystallographic preferred orientation, vertical viscosity and density gradients in ice layers, and bedrock topography. Our simulated folds show complex patterns and are classified into: large-scale folds (>100 m amplitude), small-scale folds (<<100 m) and basal-shear folds. The amplitudes of large-scale folds tend to be at their maximum in the middle of the ice column or just below, in accordance with observations in RES data. We conclude that ice anisotropy amplifies the perturbations in ice layers (mainly due to bedrock topography) into large-scale folds during flow. Density differences between the warm deep ice and cold ice above may enhance fold amplification.

## Plain Language Summary

Polar ice sheets are composed of compacted former snow layers deposited at the ice surface. If not distorted or deformed, these layers are flat or adapt to the underlying bedrock topography. However, vertical radar scans of Greenland's ice sheet show large-scale folds of up to hundreds of meters in height. To investigate how these large-scale folds form, we set up a three-dimensional numerical ice-sheet model and simulate fold growth. Our modeling emphasizes the distinctive physical properties of ice required for fold formation, notably its anisotropy (the direction dependency of the flow strength) and power-law rheology (when ice becomes softer with increasing strain rate). These findings help to better explain ice flow dynamics.

## 1. Introduction

Airborne radio-echo sounding (RES) data reveal internal layering and large-scale folding (up to >100 m, sometimes even 1 km fold amplitude) on the bumpy bedrock in several regions of Greenland's ice sheet (GrIS, Figure 1) (Bell et al., 2014; Bons et al., 2016; Franke et al., 2022a, 2022b; Jansen et al., 2024; Leysinger-Vieli et al., 2018; MacGregor et al., 2015; NEEM community members, 2013; Panton and Karlsson, 2015; Wolovick et al., 2014).

Large-scale folds appear both within ice streams and in regions of slow-moving ice. Fold amplitudes usually reach their maximum in the middle of the ice column or just below, gradually decrease towards the upper layers and flatten at the ice surface. Studies of past and present ice dynamics (Franke et al., 2022a) and of basal conditions (Leysinger-Vieli et al., 2018; Wolovick et al., 2014) need to include mechanisms to generate folds to be robust. Fold geometry can be used to date the establishment of shear margins of ice streams (Jansen et al., 2024) and is needed to unravel ice stratigraphy in ice cores that penetrate folded ice (NEEM community members, 2013).

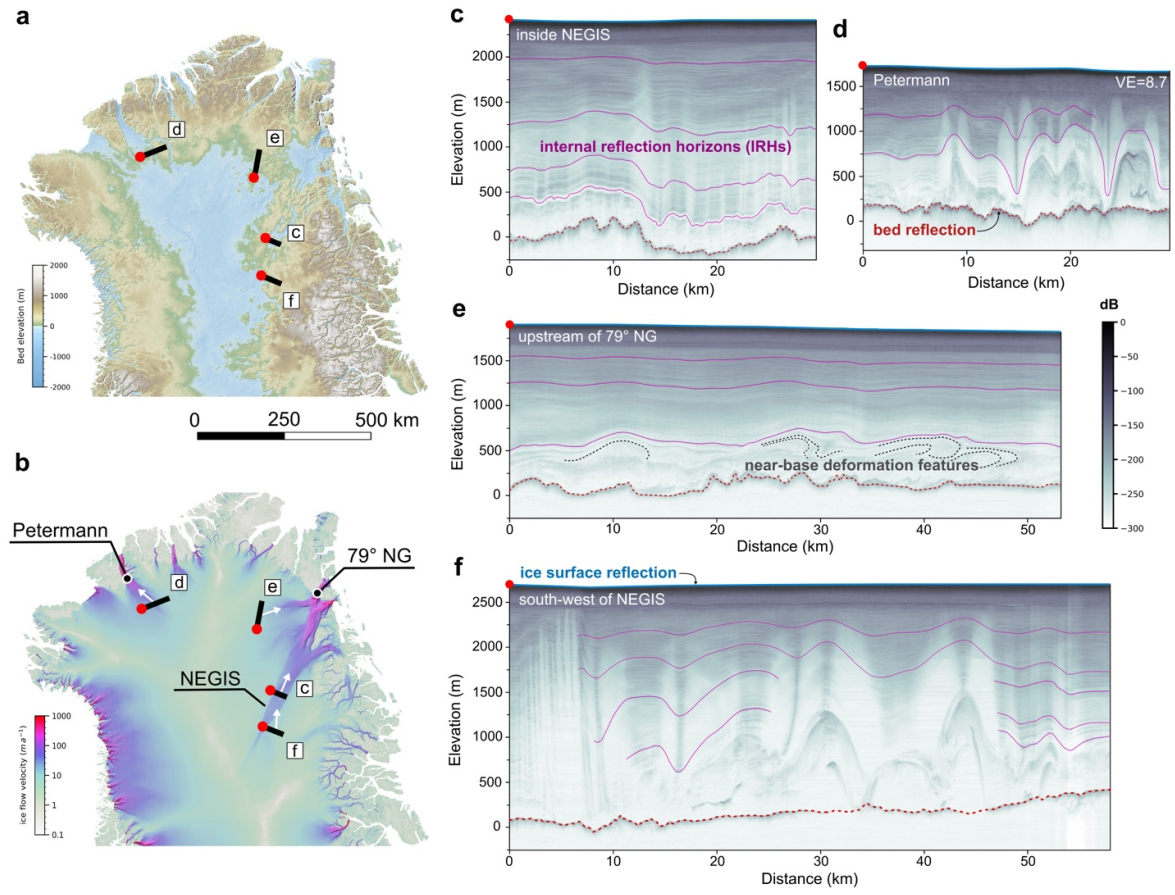


Fig. 1. Overview of the northern Greenland ice sheet and radio-echo sounding (RES) profiles: (a) bedrock topography (Morlighem et al., 2017) and location of RES profiles; (b) ice surface flow velocity (Joughin et al., 2018) and the average flow direction relative to the profiles (white arrows); (c-f) RES images (Franke et al., 2022a, 2022b) showing englacial folds (c) in the central North-East Greenland Ice Stream (NEGIS), (d) at the Petermann ice stream, (e) upstream of the 79° North Glacier (Nioghalvfjerdsbrae), and (f) in the upstream region of the NEGIS. Note the strong vertical exaggeration (8.7x) in the RES-profiles.

Several mechanisms and models have been proposed to explain the formation of folds in ice sheets. Bell et al. (2014) and Leysinger-Vieli et al. (2018) suggest that refreezing meltwater adds material to the ice base and elevates the overlying stratigraphy and influences basal ice deformation. Alternatively, Wolovick et al. (2014) suggest that variable slip rates due to "traveling slippery patches" can create large-scale folds. Furthermore, Krabbendam (2016) proposes the basal temperate (melting) ice layer may be locally thickened by internal deformation of folding or thrusting over a bedrock high. These models mainly focus on basal ice and bed conditions, which may apply to individual fold cases but seem inadequate to explain the presence of folds throughout the GrIS, especially in the NE of the ice sheet. Additionally, these models are purely 2D along-flow models and no predictions have been published for their 3D geometry. However, especially when considering the margins of ice streams, the three-dimensional geometries of folds show that fold axes are sub-parallel or at a small angle to the flow direction (Bons et al., 2016; Franke et al., 2022a, 2023).

Hudleston (2015) proposes that irregularities in primary ice stratification can be kinematically amplified in convergent flow by horizontal shortening and without the requirement of rheological contrast in the ice. Thorsteinsson and Waddington (2002) invoke anisotropy as a cause of fold initiation near ice-sheet centers considering the initial layer disturbance relative to the extensile flow regime, and anisotropy is also well-studied in the development of small-scale folds in ice cores (Alley et al., 1997; Jansen et al., 2016) and anisotropic materials (Kocher et al. 2008; Ran et al., 2019). Bons et al. (2016) and Jansen et al. (2024) suggest that mechanical anisotropy and convergent flow cause large-scale folding. This hypothesis has so far not been tested with numerical simulations.

Three properties of ice or ice sheets are significant for the modeling of flow in ice sheets: (1) The viscoplastic deformation of ice Ih (hexagonal ice) results essentially from dislocation glide parallel to the crystallographic basal plane (Gillet-Chaulet et al., 2006). The crystallographic preferred orientation (CPO) in ice sheets is typically a vertical alignment of the crystals' c-axes, which are perpendicular to the easy-glide basal planes. As a result, the ice becomes significantly anisotropic in its flow properties (Duval et al., 1983). (2) Ice temperature increases with depth: upper "cold ice" has a high viscosity and density, while the lower "warm ice" has a lower viscosity and also has a lower density due to thermal expansion (Robin, 1955; Rogozhina et al., 2011). Hughes (2009) proposes the thermal convection hypothesis and the possibility of fold formation. (3) Ice layers are initially not necessarily

perfect sheets with constant thickness. The irregularities may come from the ice divides (Thorsteinsson and Waddington, 2002), variable basal processes (Leysinger-Vieli et al., 2018; Wolovick et al., 2014), and more generally the underlying bedrock topography (Figure 1c; Hudleston, 2015). In addition, not all layering is necessarily strained original stratigraphy. Layers could be created by the deformation process, especially when strain is high (Jennings and Hambrey, 2021). Taking these considerations into account, we here use the full-Stokes software "Underworld2" (Beucher et al., 2022; Sachau et al., 2022) to investigate the development of folds in 3D convergent flow. We investigate particularly the factors rheological anisotropy of ice, vertical gradients of viscosity and density, and bedrock topography.

## 2. Method

The basic model design is shown in Figure 2a (detailed parameters in Text S1, Table S1 and Figures S1-S2 in Supporting Information SI). The model comprises four main material layers: air (500 m), cold ice (1667 m;  -30 °C), warm ice (833 m; -30 to -3 °C), and bedrock, and 10 internal marker horizons to track the deformation. Internal horizons are progressively shortened by lateral inflows (x-axis) of 5 m/yr. To reduce computing time, our model (Figure 2b) thus consists of one half of a convergent zone (Figure 2a), as, for example, envisaged by Bons et al. (2016) for the inlet area of the Petermann Glacier. Outflow in the y-directon, compensates the inflow to maintain a constant ice volume. As the main interest is in the ice-layer geometry in the vertical x-z-plane, and to maximize the resolution of the model, its width in the y-direction (500 m) is much smaller than in the x-direction (25 km). A 25 x 25 km model is shown in Figures S7-S8 in Supporting Information SI for comparison.

The non-linear viscous ice rheology used is the dislocation creep component of the Goldsby & Kohlstedt (2001) composite flow law. The flow law has two parameterizations, one for high and one for low temperature, and the parameters used are those modified by Kuiper et al. (2020) to ensure no discontinuity at the transition temperature (-11 °C). The power-law viscosity of ice (isotropic viscosity $\eta_1$, Pa · s) is derived from temperature (T, °C) and strain rate ($\dot{\varepsilon}_{ij}$, $\mathrm{yr}^{-1}$). Underworld2 is a particle-in-cell model and the local c-axis orientations are stored for each particle. Initial c-axis orientations of ice particles are perpendicular to the local layer orientation with a Gaussian random distribution with a standard deviation of $\pm 5°$. As the simulation progresses, the c-axes rotate in the flow field (Sharples et al., 2016). The

anisotropy of the ice crystal is modeled as transverse isotropic (Martín et al., 2009; Sharples et al., 2016) by two viscosity values: a maximum value $\eta_1$ (Pa · s) for shortening or stretching parallel to the c-axis maximum, and a minimum viscosity $\eta_2$ (Pa · s) for shearing along the plane perpendicular to the c-axis maximum. We define the intensity of anisotropy with the anisotropy parameter k = $\eta_1/\eta_2$.

Seven models are discussed here to explore the effect of the ice anisotropy, viscosity and density, and bed conditions on large-scale folding. Three different bed conditions are tested: (i) a free-slip bottom boundary without a bedrock (Figures 2c-2f), (ii) a 1000 m thick bedrock layer with a flat surface to which the ice is frozen (Figures 2g-2h), and (iii) the same as (ii), but with an undulating bedrock surface with bumps of variable wavelengths and amplitudes (Figure 3). Internal horizons are parallel to bedrock bumps at the base of the ice. Amplitudes of bedrock-related undulations in the ice horizons decrease to zero at the ice surface (Figure 3a). In these models (see detailed comparisons in Table S2 in Supporting Information SI), we varied the following parameters: (1) bed condition (i) for Models 1-2, bed condition (ii) for Model 3, and bed condition (iii) (variable amplitude bumps up to 400 m) for Models 4-7; (2) isotropic ice for Model 1, Model 5 and Model 7, and anisotropic ice for all other models; (3) softness in ice viscosities (adapted $A_0$ value) for Models 6-7.

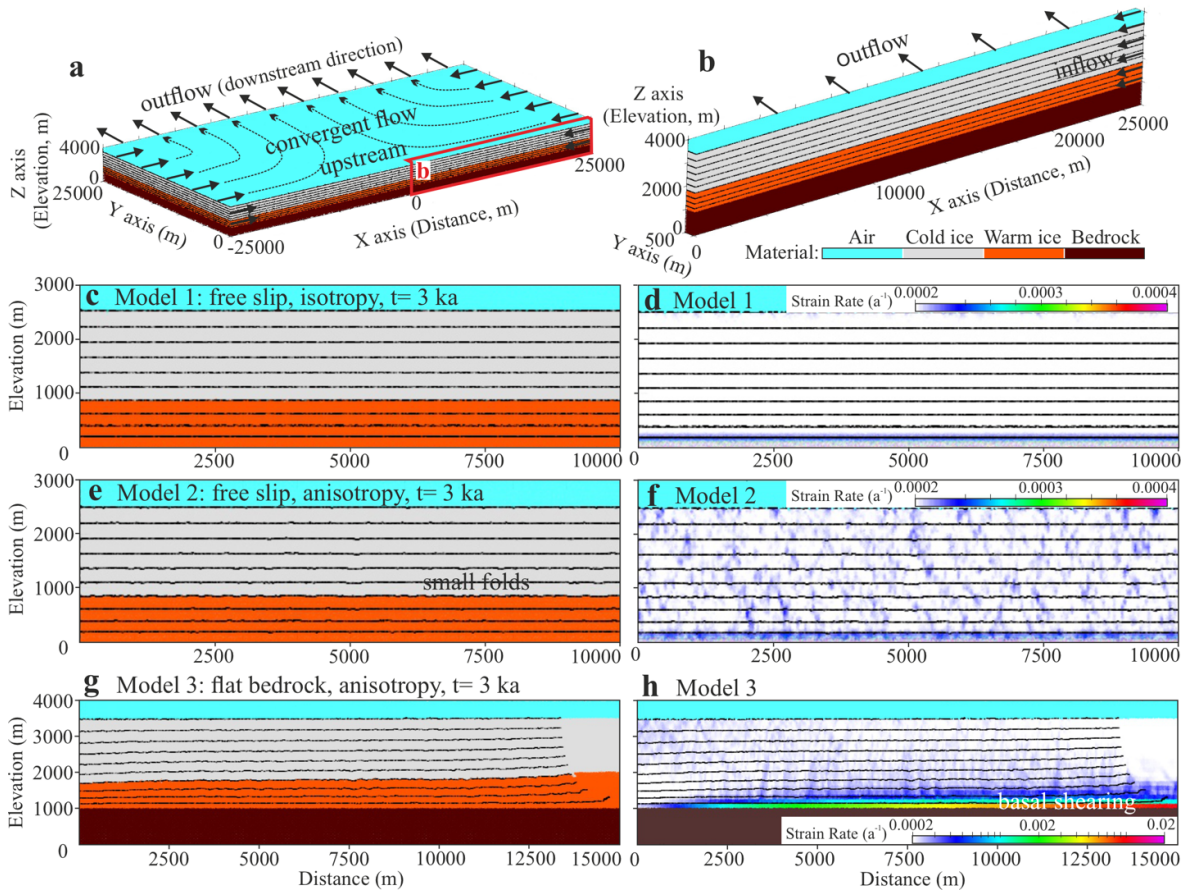


Figure 2. Model design and snapshots of results from Models 1-3 after 3000 years: (a) 3D view of initial model (example from flat bedrock model) and (b) the adapted model to enable a higher model resolution (see location in Figure 2a); (c-h) profile snapshots of the layer geometry and the second invariant of strain-rate magnitude parallel to x-z coordinate plane (at $y = 250$ m, same in Figures 3&4) for (c-d) Model 1, (e-f) Model 2 and (g-h) Model 3.

## 3. Results

### 3.1 Anisotropy vs. vertical viscosity and density gradients

In the simulations of isotropic ice on a free-slip bottom boundary (Model 1), ice layers stay nearly flat for at least 3000 years, even with vertical viscosity and density gradients (Figures 2c-2d). Nevertheless, when anisotropy is included in the models, a large number of small folds form (Model 2; Figures 2e-2f), due to the Gaussian variability of the c-axis orientation of particles. Compared to the very homogeneous strain rates resulting from the isotropic Model 1 (Figure 2d), the strain-rate map of Model 2 is much more heterogeneous with zones

of elevated strain rates (Figure 2f). In the scenario where the bedrock is added as a horizontal flat layer underneath the anisotropic ice (Model 3; Figures 2g-2h) bedrock-parallel shearing occurs in the basal ice layers as the ice is frozen to the bedrock. Due to strain-rate softening, this enhances the vertical viscosity contrasts between the ice layers (Figure S6 in Supporting Information SI). However, no large-scale folds form, but instead abundant small folds similar to Model 2.

### 3.2 Anisotropic vs. isotropic ice on the bumpy bedrock

For the scenario with a bumpy bedrock topography (anisotropic Model 4), the initial ice layers on bedrock bumps start to evolve into large-scale folds (up to 300 m amplitude in 2000-3000 years) with additional small folds in between (Figures 3a-3d). Here we compare three large-scale fold sets A, B, and C in the anisotropic Model 4 and isotropic Model 5 (Figure 3), in terms of the fold amplitudes as a function of layer height. Amplitude is here defined as the difference in elevation of a marker horizon at a fold crest and adjacent trough (Jansen et al. 2024). We consider 10 stratigraphic layers labeled 1-10 from bottom to top (Figure 3a). The amplitude-layer values of Layers 3-10 are shown in Figure S5 in Supporting Information SI (note that Layers 1-2 are too close to the bedrock and therefore strongly sheared). In Model 4, the amplitude of the initial layer depth variation is largest in the near-base layers and zero at the ice surface. The largest fold amplitudes are in middle layers (Layers 4-6) and mostly exceed the initial depth variation. In the isotropic Model 5 we observe large-scale folds that are inherited from the initial depth variation. They are smaller and without small folds in between (Figures 3e-3g). Folds with the largest amplitudes are found in the deepest layers, and amplitudes of most folds are smaller than the initial depth variation. Strain rates in Model 5 are high close to the ice base, decrease towards the ice surface in the upper layers and are distributed in a regular pattern associated with bedrock bumps (Figure 3g).

Considering ice flowing over variable bedrock bumps, folds do not always show monotonic growth over time in Model 4. The only difference in the settings between Models 4&5 is the anisotropy in the ice, thus we analyze the anisotropy contribution to fold growth by subtracting the fold amplitude (fold sets A, B and C) of the isotropy model (Model 5) from that of the anisotropy model (Model 4). After 3000 years (Figure 3h), the amplitude differences between Models 4&5 of most folded layers are larger than 0 m, indicating that

anisotropy does amplify folds after this period. The maximum amplification of over 100 m is in the middle layers (Layers 5-7).

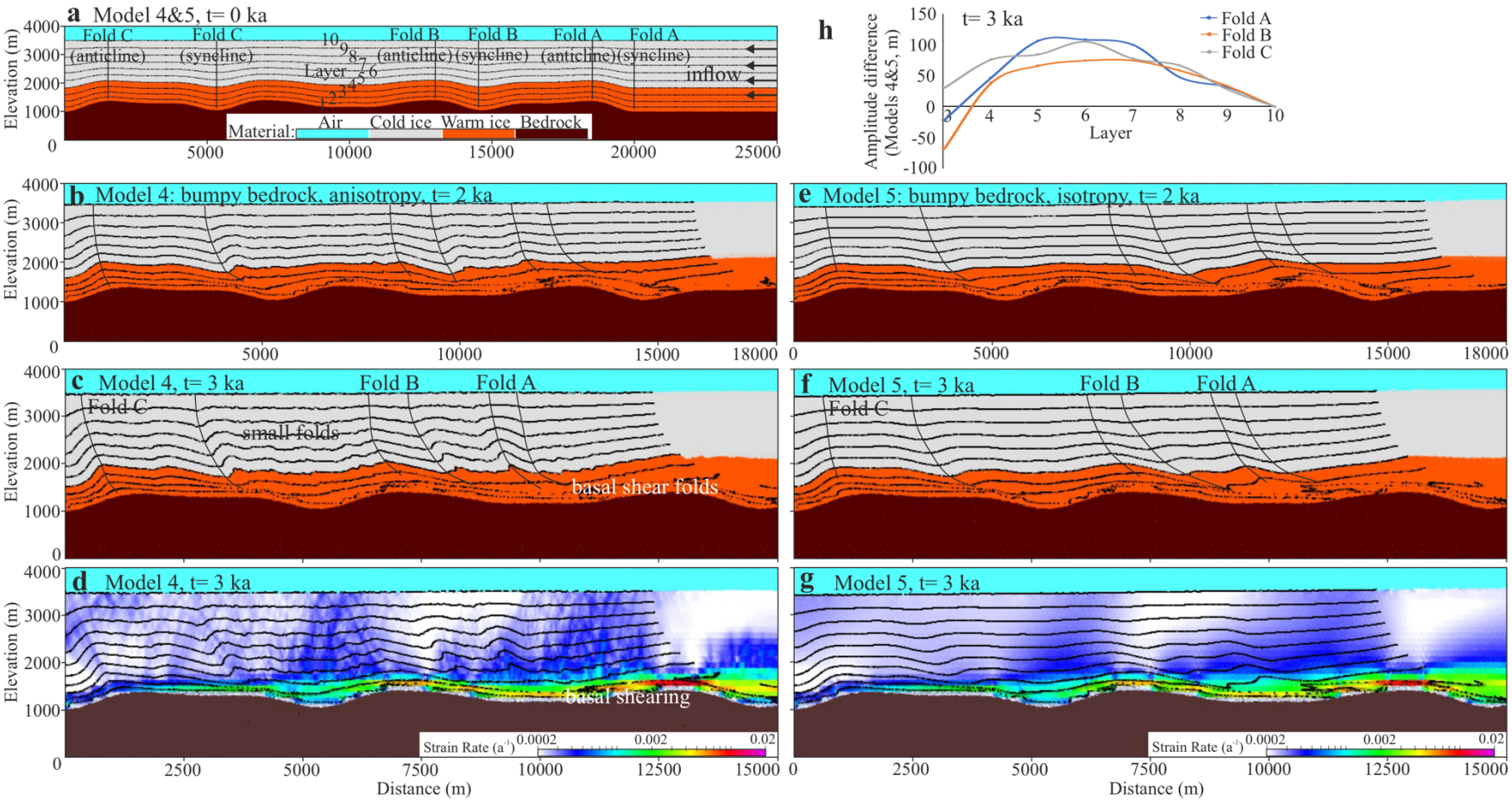


Figure 3. Snapshots of comparison of anisotropic Model 4 and isotropic Model 5 with identical bedrock topography with 400 m tall bumps in both models shown in (a): (b-c) Layer geometry snapshots of Model 4 after (b) 2000 years and (c) 3000 years. (d) The second invariant of strain-rate magnitude in Model 4 at 3000 years. (e-f) Layer geometry snapshots of Model 5 after 2000 and 3000 years. (g) The second invariant of strain-rate magnitude for Model 5 after 3000 years. Note that the x-axis and z-axis scales between the images of individual time steps. (h) Amplitude differences between Models 4&5 of Layers 3-10 on Fold A, Fold B and Fold C after 3000 years.

### 3.3 Anisotropy and buoyancy effects along the outflow direction

The outflow velocity in the stretching (y) direction in the semi-2D (Fig. 2b) models is only 0.1 m/yr, which is comparable to flow velocities near the divide of the ice sheet. Further away from the divide horizontal flow velocities are much higher and bedrock-parallel shear rates are thus also higher. This effectively softens due to the strain-rate softening of the power-law viscous material. The effect can be seen in the 3D model (Fig. 2a) in Figures S7-S8 in Supporting Information SI, where the outflow velocity is 5 m/yr. The strain-rate softening results in a decrease in effective viscosity and an increase in fold amplitudes in the outflow direction. This effect is simulated with Models 6 and 7 that has the same settings as Model 4 (Figure 3a), but we reduced the value of $A_0$ to reduce the effective viscosity by a factor of 30 to model the ice further downstream from the divide (See Table S1 Note in Supporting Information SI). Model 6 is for anisotropic ice and Model 7 for isotropic ice. Folds in the anisotropic Model 6 can reach over 500 m (to 987 m) in amplitude in only 1000 years (Fig. 4a), much larger (by up to 665 m) compared to the isotropic Model 7 (Figure 4b). Folds in both models grow faster compared to Models 4-5, and the most intensely folded layer of the fold sets is at the warm-cold ice interface (Layer 4), indicating the buoyancy effect of the lowermost warmer and strain-rate softened ice.

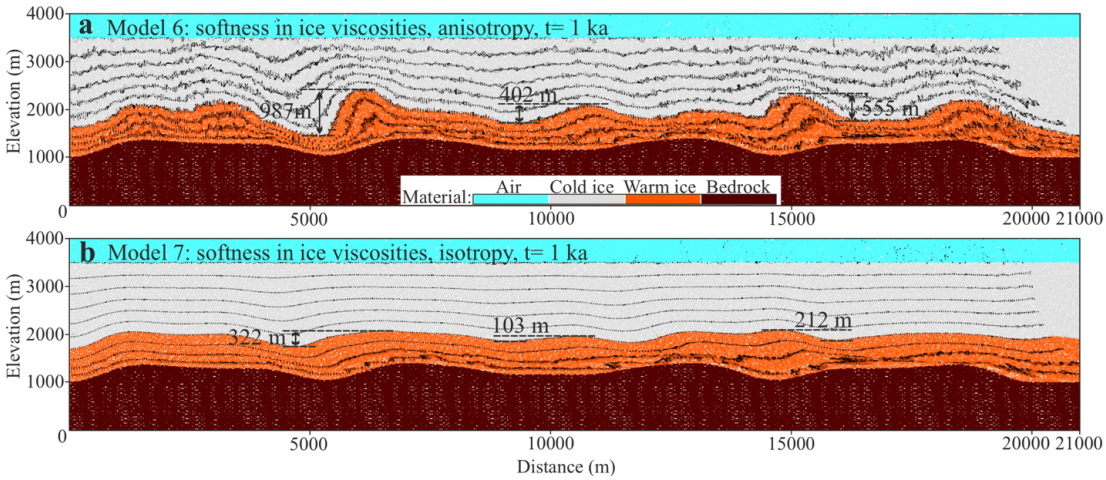


Figure 4. Layer geometry snapshots after 1000 years of (a) anisotropic Model 6 with adapted $A_0$ value for softness in ice viscosities (near-downstream) and (b) isotropic Model 7 for comparison.

## 4. Discussion

The folds observed in our modeling can be classified into three types: large-scale folds (fold amplitudes >100 m), small-scale folds (fold amplitudes <<100 m, wavelength <<km) and recumbent basal-shear folds. The large-scale folds have wavelengths in the order of one km or more. Their axial planes have a listric shape, with steep dips near the ice surface that become shallower towards the bedrock. Our simulated large-scale folds (in particular those in Models 4 and 6) show strong similarity to those observed in the GrIS by e.g., Wolovick et al. (2014), MacGregor et al. (2015), Bons et al. (2016), Franke et al. (2022a) and Jansen et al. (2024) (Figure 1).

The main controlling factors for large-scale folds in our simulations are ice anisotropy and the initial geometry dictated by the underlying bedrock topography. Folds in isotropic ice (k=1) (Figures 3e-3g) are essentially palimpsests of the underlying bedrock topography that are passively transported away from the underlying bumps. They do not amplify by themselves, but passively change their shape as they travel over bedrock bumps and valleys. In the anisotropic model with k=3 (Figures 3b-3d), we observed additional fold-shape modification and amplification with ice c-axis rotation (Figure S4 in Supporting Information SI). When k is set to 6, this effect is even stronger (Figures S10 and S12 in Supporting Information SI). This is a clear indication that the anisotropy plays a primary role in fold amplification. This anisotropy effect could be more pronounced in real ice sheets, considering the higher anisotropy values proposed by Duval et al. (1983). Buoyancy becomes a significant factor to further enhance fold amplification if overall deformation of the ice sheet is fast enough to cause a general strain rate softening of the ice.

According to classical fold theory (Biot, 1957; Schmalholz and Mancktelow, 2016) folds form by the amplification of small perturbations in the folding layer. In case of folding of a strong layer in a softer matrix, a dominant wavelength will develop as a function of layer thickness (the characteristic length scale of the system) and the viscosity ratio of the layer and matrix. The dominant wavelength is the wavelength with the highest amplification rate. In case of a single, but anisotropic medium, a characteristic length scale is absent. As a consequence there is no dominant

wavelength that amplifies the most, and folds of all wavelengths may form simultaneously, including small-scale folds (Figure 2e). Bedrock topography or variations in bed sliding and/or freezing/thawing (Leysinger-Vieli et al., 2018; Wolovick et al., 2014) at the base of the ice sheet create seed folds that may subsequently amplify. With these, the system can "skip" the initial fold nucleation stage for folds with these wavelengths. These folds amplify depending on the intensity of the anisotropy (k) and overall strain rate and concomitant strain-rate weakening to enable buoyancy effects. However, in case of anisotropy small-scale folds will also nucleate due to small-scale perturbations (here the random noise in c-axis orientations).

In our models, the lowermost ice is warmer, which creates a system with a cold and strong layer at the top and a warmer and softer layer at the bottom. Shortening of individual layers with small-scale viscosity contrasts could potentially lead to buckle folding, as has been suggested by NEEM-community (2013). Initial wavelengths for low viscosity contrasts would be at least five to ten times the layer thickness (Llorens et al., 2013; Schmalholz and Mancktelow, 2016), which in our case would be at least 5 to 10 km. However, the viscosity contrast between the warm and cold ice is relatively low and lacks a sharp boundary. Although the resulting wavelengths are in the same order as those of folds observed in the ice sheets, the amplification rate is very small (Llorens et al.,2013) and no visible folds are expected to form. These theoretical considerations, modeling by Bons et al. (2016), as well as the results of Models 1-3 (no bedrock bumps) and isotropic Model 15 (Figure S12 in Supporting Information SI), indicate that Biot-type buckle folding due to viscosity contrasts between cold and warm ice cannot lead to significant folding on the multi-km scale.

Deformation in the deepest, softest ice is approximately in simple shear. In case of bedrock bumps, the basal shear zone may localize above the bedrock-ice interface, especially across valleys or downstream of bumps in the bedrock (Figure 3g; Liu et al., 2024). This effect is more pronounced in case of anisotropy (Sachau et al., 2022). Passive shearing of layers in heterogeneous simple shear leads to tight recumbent folds (Figures 3c and 3f) that are also observed in ice sheets (Figure 1e; Bons et al., 2016). Recumbent folds may be enhanced by anisotropy, but are largely controlled by the deep bed-parallel shearing and bedrock topography, not by anisotropy.

Connection of the deep recumbent folds with a shallowly dipping axial plane with more upright folds higher up in the ice leads to the listric shape of the axial planes (Franke et al., 2022a). Variable bed conditions, e.g. enabling bed sliding, are expected to further enhance folding in the ice basal layers (Leysinger-Vieli et al., 2018; Wolovick and Creyts, 2016).

Our simulations with anisotropic ice properties appear to successfully explain large-scale folding in convergent flow especially near ice streams. The mechanism of fold amplification due to anisotropy and buoyancy is not competing with other proposed mechanisms for the formation of large, often recumbent, folds (eg., Leysinger-Vieli et al., 2018; Wolovick et al., 2014), but, instead, would act together with these to create even taller folds. Precipitation on the ice-sheet surface would, on the other hand, suppress fold amplification (Waddington et al., 2001), although our simulations show that significant fold amplitudes can still be attained within 3000 years with a moderate surface accumulation (Figure S11 in Supporting Information SI).

Fold amplification due to anisotropy or basal processes is to a large extent independent of the effective ice viscosity, but depends more on the kinematics of flow (e.g., convergent flow) or the rates of basal processes (e.g., basal freeze-on; Leysinger-Vieli et al., 2018). Effective viscosity is, however, critical for the effect of buoyancy of the deepest and warmest ice (Hughes, 2009). Our simulations (Model 6; Figure 4a) indicate that fold amplification can be significantly enhanced to form tall 'plume-like' folds, when the overall flow velocity is sufficiently high to reduce the effective viscosity enough to allow the rise of warm, buoyant ice in anticlinal cores. Our first results on the effect on buoyancy indicate that much more work is needed, as well as the need to constrain the effective viscosity of flowing ice.

## 5. Conclusions

Motivated by observations of folds in radargrams of the GrIS, our modeling results show that: (1) Large-scale folds can form in convergent ice flow, mainly controlled by its rheological anisotropy. This anisotropy is due to the CPO. Anisotropy amplifies existing undulations in the ice stratigraphy due to bedrock topography or processes at the ice-bed interface. (2) Rheological variations within the ice sheet, such as vertical

viscosity gradients that result from temperature gradients in ice layers, appear to not play a significant role. (3) Bouyancy of the deepest and warmest ice in anticlinal cores can significantly enhance fold amplifications where ice is effectively weakened by strain-rate softening due to the power-law rheology of ice. (4) As observed in ice sheets, large-scale fold amplitudes are highest in the middle of the ice column or just below. Meanwhile, near-base fold patterns are more complex and often result in recumbent folds due to the bedrock constraint. (5) Small-scale folds on initially flat internal horizons may form as well due to the anisotropy of ice. Finally, using particle tracking and strain analysis, our modeling helps to better explain ice-flow dynamics of ice sheets. In particular, an improved implementation of ice anisotropy and basal shearing can result in high-strain-rate areas where the power-law ice would be softened, even when frozen to the bed. This indicates that ice sheets could be more unstable when suddenly triggered to flow by external forcings, such as climate change, ice-sheet geometry changes or tectonic events.

## Acknowledgments

Yu Zhang was funded by the China Scholarship Council (grant no. 202006010063) recommended by Peking Univesity, and Steven Franke by the Walter Benjamin Programme of the Deutsche Forschungsgemeinschaft (DFG, German Research Foundation; project number 506043073). We acknowledge support from the Open Access Publication Fund of the University of Tübingen. We thank the editor Mathieu Morlighem as well as Michael Wolovick, Peter Hudleston, and Dave Prior for their comments that helped to improve the text.

## Open Research

Underworld is fully open-source and the version (v2.14.1b) used for this paper is available through Beucher et al. (2022). Our code files for all the models are available through Zhang (2024). The radio-echo sounding data shown in Figure 1c (profile IDs: 20180509_01_[011, 012]) and in Figure 1f (profile ID: 20180512_02_009) from

AWI's EGRIP-NOR-2018 survey are available under https://doi.org/10.1594/PANGAEA.928569 (Franke et al., 2022b), the data shown in Figure 1d (profile ID: 20110507_01_032) is available via the CReSIS Data Products (https://data.cresis.ku.edu/) and the data shown in Figure 1e (profile ID: 20180415_06_007) is available under https://doi.org/10.1594/PANGAEA.949391 (Franke et al., 2022a). Bed elevation data from Morlighem et al. (2017) and ice flow velocity data from Joughin et al. (2018) are available at the National Snow and Ice Data Center: https://nsidc.org/data/idbmg4 and https://nsidc.org/data/nsidc-0670/, respectively.

## References

Alley, R. B., Gow, A. J., Meese, D. A., Fitzpatrick, J. J., Waddington, E. T., & Bolzan, J. F. (1997). Grain-scale processes, folding, and stratigraphic disturbance in the GISP2 ice core. *Journal of Geophysical Research: Oceans*, 102(C12), 26819-26830. https://doi.org/10.1029/96JC03836

Bell, R. E., Tinto, K., Das, I., Wolovick, M., Chu, W., Creyts, T. T., et al. (2014). Deformation, warming and softening of Greenland's ice by refreezing meltwater. *Nature Geoscience*, 7(7), 497-502. https://doi.org/10.1038/ngeo2179

Beucher, R., Giordani, J., Moresi, L., Mansour, J., Kaluza, O., Velic, M., et al. (2022). Underworld2: Python Geodynamics Modelling for Desktop, HPC and Cloud (v2.14.1b) [Software]. Zenodo. https://doi.org/10.5281/zenodo.7455999

Biot, M. A. (1957). Folding instability of a layered viscoelastic medium under compression. *Proceedings of the Royal Society of London. Series A. Mathematical and Physical Sciences*, 242(1231), 444-454. https://doi.org/10.1098/rspa.1957.0187

Bons, P. D., Jansen, D., Mundel, F., Bauer, C. C., Binder, T., Eisen, O., et al. (2016). Converging flow and anisotropy cause large-scale folding in Greenland's ice sheet. *Nature communications*, 7(1), 11427. https://doi.org/10.1038/ncomms11427

Bons, P. D., Kleiner, T., Llorens, M. G., Prior, D. J., Sachau, T., Weikusat, I., & Jansen, D. (2018). Greenland Ice Sheet: Higher nonlinearity of ice flow significantly reduces estimated basal motion. *Geophysical Research Letters*, 45(13), 6542-6548. https://doi.org/10.1029/2018GL078356

Duval, P., Ashby, M. F., & Anderman, I. (1983). Rate-controlling processes in the creep of polycrystalline ice. *The Journal of Physical Chemistry*, 87(21), 4066-4074. https://doi.org/10.1021/j100244a014

Franke, S., Bons, P. D., Westhoff, J., Weikusat, I., Binder, T., Streng, K., et al. (2022a). Holocene ice-stream shutdown and drainage basin reconfiguration in northeast Greenland. *Nature Geoscience*, 15(12), 995-1001. https://doi.org/10.1038/s41561-022-01082-2

Franke, S., Jansen, D., Binder, T., Paden, J. D., Dörr, N., Gerber, T. A., et al. (2022b). Airborne ultra-wideband radar sounding over the shear margins and along flow lines

at the onset region of the Northeast Greenland Ice Stream. *Earth System Science Data*, *14*(2), 763–779. https://doi.org/10.5194/essd-14-763-2022

Franke, S., Bons, P. D., Streng, K., Mundel, F., Binder, T., Weikusat, I., et al. (2023). Three-dimensional topology dataset of folded radar stratigraphy in northern Greenland. *Scientific Data*, *10*(1), 525. https://doi.org/10.1038/s41597-023-02339-0

Gillet-Chaulet, F., Gagliardini, O., Meyssonnier, J., Zwinger, T., & Ruokolainen, J. (2006). Flow-induced anisotropy in polar ice and related ice-sheet flow modelling. *Journal of non-newtonian fluid mechanics*, 134(1-3), 33-43. https://doi.org/10.1016/j.jnnfm.2005.11.005

Goldsby, D. L., & Kohlstedt, D. L. (2001). Superplastic deformation of ice: Experimental observations. *Journal of Geophysical Research: Solid Earth*, 106(B6), 11017-11030. https://doi.org/10.1029/2000JB900336

Hudleston, P. J. (2015). Structures and fabrics in glacial ice: A review. *Journal of Structural Geology*, 81, 1-27. https://doi.org/10.1016/j.jsg.2015.09.003

Hughes, T. (2009). Thermal convection and the origin of ice streams. *Journal of Glaciology*, 55(191), 524-536. https://doi.org/10.3189/002214309788816722

Jansen, D., Llorens, M. G., Westhoff, J., Steinbach, F., Kipfstuhl, S., Bons, P. D., et al. (2016). Small-scale disturbances in the stratigraphy of the NEEM ice core: observations and numerical model simulations. *The Cryosphere*, 10(1), 359-370. https://doi.org/10.5194/tc-10-359-2016

Jansen, D., Franke, S., Bauer, C. C., Binder, T., Dahl-Jensen, D., Eichler, J., et al. (2024). Shear margins in upper half of Northeast Greenland Ice Stream were established two millennia ago. *Nature Communications*, 15(1), 1193. https://doi.org/10.1038/s41467-024-45021-8

Jennings, S. J. A., & Hambrey, M. J. (2021). Structures and deformation in glaciers and ice sheets. *Reviews of Geophysics*, 59, e2021RG000743. https://doi.org/10.1029/2021RG000743

Joughin, I. A. N., Smith, B. E., & Howat, I. M. (2018). A complete map of Greenland ice velocity derived from satellite data collected over 20 years. *Journal of Glaciology*, 64(243), 1-11. https://doi.org/10.1017/jog.2017.73

Kocher, T., Mancktelow, N. S., & Schmalholz, S. M. (2008). Numerical modelling of the effect of matrix anisotropy orientation on single layer fold development. *Journal of Structural Geology*, 30(8), 1013-1023. https://doi.org/10.1016/j.jsg.2008.04.006

Krabbendam, M. (2016). Sliding of temperate basal ice on a rough, hard bed: creep mechanisms, pressure melting, and implications for ice streaming. *The Cryosphere*, 10(5), 1915-1932. https://doi.org/10.5194/tc-10-1915-2016

Kuiper, E. J. N., De Bresser, J. H., Drury, M. R., Eichler, J., Pennock, G. M., & Weikusat, I. (2020). Using a composite flow law to model deformation in the NEEM deep ice core, Greenland–Part 2: The role of grain size and premelting on ice deformation at high homologous temperature. *The Cryosphere*, 14(7), 2449-2467. https://doi.org/10.5194/tc-14-2449-2020

Leysinger Vieli, G. M., Martin, C., Hindmarsh, R. C. A., & Lüthi, M. P. (2018). Basal freeze-on generates complex ice-sheet stratigraphy. *Nature Communications*, 9(1), 4669. https://doi.org/10.1038/s41467-018-07083-3

Liu, E. W., Räss, L., Herman, F., Podladchikov, Y., & Suckale, J. (2024). Spontaneous formation of an internal shear band in ice flowing over topographically variable bedrock. *Journal of Geophysical Research: Earth Surface*, 129(4). https://doi.org/10.1029/2022JF007040

Llorens, M. G., Bons, P. D., Griera, A., Gomez-Rivas, E., & Evans, L. A. (2013). Single layer folding in simple shear. *Journal of Structural Geology*, 50, 209-220. https://doi.org/10.1016/j.jsg.2012.04.002

MacGregor, J. A., Fahnestock, M. A., Catania, G. A., Paden, J. D., Prasad Gogineni, S., Young, S. K., et al. (2015). Radiostratigraphy and age structure of the Greenland Ice Sheet. *Journal of Geophysical Research: Earth Surface*, 120(2), 212-241. https://doi.org/10.1002/2014JF003215

Martín, C., Gudmundsson, G. H., Pritchard, H. D., & Gagliardini, O. (2009). On the effects of anisotropic rheology on ice flow, internal structure, and the age-depth relationship at ice divides. *Journal of Geophysical Research: Earth Surface*, 114(F4). https://doi.org/10.1029/2008JF001204

Morlighem, M., Williams, C. N., Rignot, E., An, L., Arndt, J. E., Bamber, J. L., et al. (2017). BedMachine v3: Complete bed topography and ocean bathymetry mapping of Greenland from multibeam echo sounding combined with mass conservation. *Geophysical research letters*, 44(21), 11-051. https://doi.org/10.1002/2017GL074954

NEEM community members. (2013). Eemian interglacial reconstructed from a Greenland folded ice core. *Nature*, 493, 489–494. https://doi.org/10.1038/nature11789

Panton, C., & Karlsson, N. B. (2015). Automated mapping of near bed radio-echo layer disruptions in the Greenland Ice Sheet. Earth and Planetary Science Letters, 432, 323-331. https://doi.org/10.1016/j.epsl.2015.10.024

Ran, H., de Riese, T., Llorens, M. G., Finch, M. A., Evans, L. A., Gomez-Rivas, E., et al. (2019). Time for anisotropy: The significance of mechanical anisotropy for the development of deformation structures. *Journal of Structural Geology*, 125, 41-47. https://doi.org/10.1016/j.jsg.2018.04.019

Robin, G. D. Q. (1955). Ice movement and temperature distribution in glaciers and ice sheets. *Journal of glaciology*, 2(18), 523-532. https://doi.org/10.3189/002214355793702028

Rogozhina, I., Martinec, Z., Hagedoorn, J. M., Thomas, M., & Fleming, K. (2011). On the long-term memory of the Greenland Ice Sheet. *Journal of Geophysical Research: Earth Surface*, 116(F1). https://doi.org/10.1029/2010JF001787

Sachau, T., Yang, H., Lang, J., Bons, P. D., & Moresi, L. (2022). ISMIP-HOM benchmark experiments using Underworld. *Geoscientific Model Development*, 15(23), 8749-8764. https://doi.org/10.5194/gmd-15-8749-2022

Schmalholz, S. M., & Mancktelow, N. S. (2016). Folding and necking across the scales: a review of theoretical and experimental results and their applications. *Solid Earth*, 7(5), 1417-1465. https://doi.org/10.5194/se-7-1417-2016

Sharples, W., Moresi, L. N., Velic, M., Jadamec, M. A., & May, D. A. (2016). Simulating faults and plate boundaries with a transversely isotropic plasticity model. *Physics of the Earth and Planetary Interiors*, 252, 77-90. https://doi.org/10.1016/j.pepi.2015.11.007

Thorsteinsson, T., & Waddington, E. D. (2002). Folding in strongly anisotropic layers near ice-sheet centers. *Annals of Glaciology*, 35, 480-486. https://doi.org/10.3189/172756402781816708

Waddington, E. D., Bolzan, J. F., & Alley, R. B. (2001). Potential for stratigraphic folding near ice-sheet centers. *Journal of Glaciology*, 47(159), 639-648. https://doi.org/10.3189/172756501781831756

Wolovick, M. J., & Creyts, T. T. (2016). Overturned folds in ice sheets: Insights from a kinematic model of traveling sticky patches and comparisons with observations. *Journal of Geophysical Research: Earth Surface*, 121(5), 1065-1083. https://doi.org/10.1002/2015JF003698

Wolovick, M. J., Creyts, T. T., Buck, W. R., & Bell, R. E. (2014). Traveling slippery patches produce thickness-scale folds in ice sheets. *Geophysical Research Letters*, 41(24), 8895-8901. https://doi.org/10.1002/2014GL062248

Zhang, Y. (2024). Underworld modeling of large-scale folds in ice sheets. Zenodo. https://doi.org/10.5281/zenodo.11396618

## Reference From the Supporting Information

Fuchs, L., Schmeling, H., & Koyi, H. (2011). Numerical models of salt diapir formation by down-building: the role of sedimentation rate, viscosity contrast, initial amplitude and wavelength. *Geophysical journal international*, 186(2), 390-400. https://doi.org/10.1111/j.1365-246X.2011.05058.x

Gillet-Chaulet, F., Gagliardini, O., Meyssonnier, J., Montagnat, M., & Castelnau, O. (2005). A user-friendly anisotropic flow law for ice-sheet modeling. *Journal of Glaciology*, 51(172), 3-14. https://doi.org/10.3189/172756505781829584

Hills, B. H., Harper, J. T., Humphrey, N. F., & Meierbachtol, T. W. (2017). Measured horizontal temperature gradients constrain heat transfer mechanisms in Greenland ice. *Geophysical Research Letters*, 44(19), 9778-9785. https://doi.org/10.1002/2017GL074917

Marion, G. M., & Jakubowski, S. D. (2004). The compressibility of ice to 2.0 kbar. *Cold Regions Science and Technology*, 38(2-3), 211-218. https://doi.org/10.1016/j.coldregions.2003.10.008

Moresi, L., & Mühlhaus, H. B. (2006). Anisotropic viscous models of large-deformation Mohr–Coulomb failure. *Philosophical Magazine*, 86(21-22), 3287-3305. https://doi.org/10.1016/S0021-9991(02)00031-1

Moresi, L., Dufour, F., & Mühlhaus, H. B. (2003). A Lagrangian integration point finite element method for large deformation modeling of viscoelastic geomaterials. *Journal of computational physics*, 184(2), 476-497. https://doi.org/10.1016/S0021-9991(02)00031-1

Pattyn, F., Perichon, L., Aschwanden, A., Breuer, B., De Smedt, B., Gagliardini, O., et al. (2008). Benchmark experiments for higher-order and full-Stokes ice sheet models (ISMIP–HOM). *The Cryosphere*, 2(2), 95-108. https://doi.org/10.5194/tc-2-95-2008

Pettit, E. C., Waddington, E. D., Harrison, W. D., Thorsteinsson, T., Elsberg, D., Morack, J., & Zumberge, M. A. (2011). The crossover stress, anisotropy and the ice flow law at Siple Dome, West Antarctica. *Journal of Glaciology*, 57(201), 39-52. https://doi.org/10.3189/002214311795306619

Vollmer, F. W. (2024). Orient: Directional data analysis software. https://vollmerf.github.io/orient/

## Supporting Information

**Including:**

Text S1

Tables S1 to S2

Figures S1 to S12

In the following, we provide additional information for the Method in Text S1, Table S1 and Figures S1-S2; we supplement the results of Model 4 in Figures S3-S4, fold amplitude analysis of Models 4-5 in Figure S5, and final viscosity maps for Models 1-7 in Figure S6. In addition, we provide the results of supplement models for some special cases and comparisons with Model 4 in Figures S7-S12. We make a summary and comparison for all the models in Table S2.

Text S1. Supplement for Method

1 Full-Stokes Code Underworld2

We used the full-Stokes software "Underworld2" (Beucher et al., 2022). The code was originally designed and developed for modeling and tracking internal deformation in geodynamic processes and is therefore specifically optimized for our case. Some of the advantages are (i) tracking of material "particles" during deformation and (ii) local fabric evolution can be coupled to the local rheological anisotropy.

Underworld2 uses the material point method (MPM), which is related to the better-known particle-in-cell method (Moresi et al., 2003). MPM uses an Eulerian finite-element mesh to calculate the incremental development of the velocity field and other field variables, such as temperature and pressure, while Lagrangian material points ("particles") carry the density, viscosity, lattice orientation, and other relevant local material parameters. This code is already well established in complex geodynamic modeling with a full-Stokes solution for isotropic and anisotropic elasto–visco–plastic

materials (Moresi & Mühlhaus, 2006; Sharples et al., 2016). The software has also passed the usual benchmark tests for full-Stokes ice sheet models of Pattyn et al. (2008) (Sachau et al., 2022).

2 Physics

In our model, the temperature ($T$, ℃) is -30 ℃ ($T_0$) for cold ice and, below a height $h_{warmice}$, in what is here termed "warm ice", the temperature increases downward to -3 ℃ ($T_{bed}$) at the base (Hills et al., 2017; Rogozhina et al., 2011; Robin, 1955) with a parabolic equation:

$$T = T_{bed} + (T_0 - \mathrm{T_{bed}})(\frac{y-h_{bed}}{h_{warmice}-h_{bed}})^{\mathrm{m}} \quad (1)$$

where $y$ is the height in warm ice, and $h_{bed}$ and $h_{warmice}$ are the heights for bedrock surface and warm ice surface. The specific form of the vertical temperature distribution would be complicated but a slight change of the exponent $m$ from 1.0 to 1.4 will not make much difference to the result as we test. We therefore use an approximated $m$ = 1.2 here. This parameter is also tested as the adaption of mesh-layer deformation in Sachau et al. (2022).

The ice density ($\rho, \mathrm{kg/m^3}$) is given as a function of temperature by:

$$\rho = \frac{1.802\times10^4}{19.30447 - 7.988471\times10^{-4}\cdot(T+273) + 7.563261\times10^{-6}\cdot(T+273)^2}. \quad (2)$$

Equation (2) is derived from the molar volume equation for pure ice at 1 atm in Marion and Jakubowski (2004), where the molar mass of $H_2O$ is assumed to be $1.802 \times 10^4$ kg/mol.

The non-linear viscous ice flow is based on Kuiper's flow law for dislocation creep (Kuiper et al., 2020), where the strain rate ($\dot{\varepsilon}_{ij}$) is proportional to the deviatoric stress ($\tau_{ij}$) to the power $n$,

$$\dot{\varepsilon}_{ij} = A_0 \mathrm{e}^{\frac{-Q}{R(T+273)}} {\tau_{II}}^{\mathrm{n-1}} \tau_{ij} \quad (3)$$

where $A_0$ is the material parameter, $Q$ the activation energy, $R$ the gas constant and $\tau_{\mathrm{II}}$ the second invariant of the deviatoric stress tensor $\tau_{ij}$, and the stress exponent $n$ is 4

for polar ice sheets (Bons et al., 2018). The power-law viscosity of ice (isotropic viscosity $\eta_1$, Pa · s) is derived from temperature ($T$, °C) and strain rate ($\dot{\varepsilon}_{ij}$, $\mathrm{yr}^{-1}$) (Sachau et al., 2022)

$$\eta_1 = \frac{1}{2}\left(A_0 \mathrm{e}^{\frac{-Q}{R(T+273)}}\right)^{\frac{-1}{n}} \cdot \dot{\varepsilon}_{II}^{\frac{1-n}{n}} \cdot 10^6 \quad (4)$$

where $\dot{\varepsilon}_{II}$ is the second invariant of the strain rate tensor. We do not apply both components of Kuiper's composite flow law (dislocation creep and GBS-limited creep) since in Underworld2 there are no individual grains in the model and a single ice particle represents an aggregate of ice grains. In addition, we test in modeling including GBS-limited regime by adding an assumed constant grain size value in the composite flow law but found that it does not make any significant difference to the large-scale deformation of whole ice sheet and would only complicate the model after considering a full range of grain sizes. Furthermore, Bons et al. (2018) found that a power law with $n = 4$ appears adequate to describe the flow in most of the Greenland ice sheet.

The c-axis orientation of the ice crystal is stored for each particle in Underworld2. Initial c-axis directions of ice particles are perpendicular to the local layer orientation with a Gaussian random distribution with a standard deviation of $\pm 5°$. As the simulation progresses, the c-axes rotate in the flow field according to the symmetric deformation-rate tensor $D$ and the skew-symmetric rotation-rate tensor $W$

$$D = \frac{1}{2}(L + L^{\mathrm{T}}) \quad (5)$$

$$W = \frac{1}{2}(L - L^{\mathrm{T}}) \quad (6)$$

where $L$ is the velocity gradient tensor (see Appendix B in Sharples et al. (2016) for detailed rotation equations).

The anisotropy of the ice crystal is modeled as transverse isotropy, which is a common practice in numerical modeling (Gillet-Chaulet et al., 2005; Martín et al., 2009; Sharples et al., 2016). Transverse isotropic viscosity is defined by two viscosity values: a general viscosity $\eta_1$ (Pa · s) and a second viscosity $\eta_2$ (Pa · s) for shearing parallel to the plane perpendicular to the c-axis direction. $\eta_1$ is set proportional to $\eta_2$:

$$\eta_1 = k\eta_2 \quad (7)$$

where $k$ represents the rheological anisotropy value. According to Duval et al. (1983), the stress required for non-basal deformation of ice monocrystals is at least 60 times higher than for basal slip; for macroscopic ice polycrystals, the ratio is about ten. For the assumed $n = 4$ in our macroscopic ice model, $k$ could thus be approximately six or even larger. However, $k = 6$ requires a high grid resolution to avoid numerical instabilities that may lead to artificial amplification of small folds. For this reason we employed a smaller $k = 3$ for the models in the main text, which thus underestimates the expected anisotropy in the ice. We also provide the $k = 6$ supplement models for comparison in Supporting Information (Figures S10- S12).

| Parameter | Value | Unit |
|---|---|---|
| Model size ($x$, $y$, $z$) | 25000, 500, 4000 | m |
| Thickness air | 500 | m |
| Thickness ice (cold ice & warm ice) | 2500 ($1667 + 833$) | m |
| Thickness bedrock | 1000 | m |
| Velocity inflow | 5.0 | $\mathrm{m/yr}$ |
| Velocity outflow | around 0.1 | $\mathrm{m/yr}$ |
| Temperature ice | $-30$ to $-3$ | ℃ |
| Density ice | 917.51 to 921.41 | $\mathrm{kg/m^3}$ |
| Viscosity air | $1.0 \times 10^9$ (or at least 100 times softer than min ice viscosity) | $\mathrm{Pa \cdot s}$ |
| Viscosity bedrock | $1.0 \times 10^{19}$ | $\mathrm{Pa \cdot s}$ |
| $A_0$ ($T < -11$℃) | $5.0 \times 10^5$ | $\mathrm{MPa^{-4.0} s^{-1}}$ |
| $A_0$ ($T > -11$℃) | $6.96 \times 10^{23}$ | $\mathrm{MPa^{-4.0} s^{-1}}$ |
| $Q$ ($T < -11$℃) | 64 | $\mathrm{kJ/mol}$ |
| $Q$ ($T > -11$℃) | 155 | $\mathrm{kJ/mol}$ |
| $R$ | 0.008314 | $\mathrm{J \cdot mol^{-1} K^{-1}}$ |
| Stress exponent $n$ | 4.0 | |

Table S1. Basic model set-up parameters and their values.

Note. (1) The velocity field applied on the model boundary for the inflow (& outflow) is where $z > h_{bed}$ but not $z \geq h_{bed}$ to keep the inflow (& outflow) velocity 0 on the ice-bedrock interface, and there is a velocity change in the basal ice unit near the boundary (Figure S2d). This setting can also keep basal ice and bedrock particles more stable near the boundary. This boundary condition is also applied to the free-slip models (bedrock always has zero velocity) since we want to keep the same inflow (& outflow) setting for all main models for a better comparison. But inside the model domain of free-slip models, the ice is slipping freely on the base.

(2) The flow law parameters $A_0$, $Q$ and the transition temperature (-11 ℃) are from the dislocation-creep regime in Table 3 of Kuiper et al. (2020) which is modified after Goldsby & Kohlstedt (2001).

(3) Pettit et al. (2011) found a crossover stress below which power-law ice flow becomes linear. Using this value in Kuiper's (2020) flow law gives a max effective viscosity of $1.0 \times 10^{17}$ $\mathrm{Pa \cdot s}$. We set this viscosity value as the max general viscosity $\eta_1$.

(4) If we consider an average shear stain rate of $10^{-7}$ $\mathrm{s^{-1}}$ from the surface velocity and ice thickness data of the NEGIS downstream (Bons et al., 2018), we will obtain a

viscosity value of $3.06 \times 10^{12}$ Pa · s (-3 ℃) or $9.2 \times 10^{12}$ Pa · s (-30 ℃) according to Equation 4, which is much lower than the general viscosity values ($\eta_1$) $2.5 \times 10^{14}$~$3.2 \times 10^{16}$ Pa · s in Model 4 (Figure S6). Therefore, we multiply $A_0$ by $30^n$ in Models 6-7, which, according to Equation 4, reduces the general viscosity $\eta_1$ by a factor 30 times. We also set a min limitation for the general viscosity $\eta_1$ $1.0 \times 10^{13}$ Pa · s (second viscosity $\eta_2$ $3.33 \times 10^{12}$ Pa · s) to avoid artificial softness from boundary effects and to control ice viscosities on a reasonable scale.

| No. | Bedrock condition | Anisotropy | Other factors | Results |
|---|---|---|---|---|
| Model 1 | Free-slip bottom boundary without bedrock | Isotropy | | No folds |
| Model 2 | Free-slip bottom boundary without bedrock | $\eta_1 = 3\eta_2$ | | Small folds |
| Model 3 | Flat bedrock surface | $\eta_1 = 3\eta_2$ | | Small folds, basal shearing |
| Model 4 | Bumpy bedrock surface | $\eta_1 = 3\eta_2$ | | Large-scale folds, small folds, basal shear folds |
| Model 5 | Bumpy bedrock surface | Isotropy | | None amplified (large-scale) folds, basal shear folds |
| Model 6 | Bumpy bedrock surface | $\eta_1 = 3\eta_2$ | softness in ice viscosities | Large-scale folds up to over 500 m to around km |
| Model 7 | Bumpy bedrock surface | Isotropy | softness in ice viscosities | Large-scale folds by buoyancy amplification but much lower compared to Model 6 |
| Model 8 | Bumpy bedrock surface | $\eta_1 = 3\eta_2$ | 3D extension in the outflow direction | Trend of larger folds and softer ice viscosities along the outflow direction |
| Model 9 | Bumpy bedrock surface, lower bumps | $\eta_1 = 3\eta_2$ | | Lower large-scale folds compared to Model 4 |
| Model 10 | Bumpy bedrock surface, higher bumps | $\eta_1 = 3\eta_2$ | | Higher large-scale folds compared to Model 4 |
| Model 11 | Bumpy bedrock surface | $\eta_1 = 6\eta_2$ | | Slightly higher large-scale folds compared to Model 4 |
| Model 12 | Bumpy bedrock surface | $\eta_1 = 6\eta_2$ | with ice precipitation (0.1 m/yr) | Large-scale folds in a reasonable scale range under slight suppression |
| Model 13 | Flat bedrock surface | $\eta_1 = 6\eta_2$ | Pre-existed folds (300 m) | Fold amplification with increasing strain |
| Model 14 | Flat bedrock surface | $\eta_1 = 3\eta_2$ | Pre-existed folds (300 m) | Slight change of anisotropy value makes a difference |

| | | | | |
|---|---|---|---|---|
| Model 15 | Flat bedrock surface | Isotropy | Pre-existed folds (300 m) | Pre-existed folds do not grow much |

Table S2. Summary and comparison of all models: main Models 1-7 in the main text and supplement Models 8-15 in the Supporting Information.

Note. The equation of the bedrock topography consists of multiple cosine functions, $z_1$, $z_2$, $z_3$ and $z_4$, each of which has an amplitude (difference between the min and max heights) and wavelength of $h_{A1}$, $h_{A2}$, $h_{A3}$, $h_{A4}$ and $x_{w1}$, $x_{w2}$, $x_{w3}$, $x_{w4}$. And $x_{max}$ represents the x-axis area with bedrock bumps, which in our model is 20 km. $h_{Amax}$ is the max bedrock bump amplitude that we define as 400 m, but 200 m in Model 9 and 600 m in Model 10. In this way, the bedrock topography can be noisy and natural, thus bedrock bumps are not with constant amplitude and wavelength values. Bedrock topography ($z$) equations are as follows:

1) $x_{w1} = x_{max}/4$
2) $x_{w2} = x_{max}/7$
3) $x_{w3} = x_{max}/8$
4) $x_{w4} = x_{max}/11$
5) $h_{A1} = h_{Amax}$
6) $h_{A2} = h_{Amax}/2$
7) $h_{A3} = h_{Amax}/4$
8) $h_{A4} = h_{Amax}/8$
9) $z_1 = (\cos(x * (2\pi/x_{w1}) + \pi) + 1) * h_{A1}/2$
10) $z_2 = (\cos(x * (2\pi/x_{w2}) + \pi) + 1) * h_{A2}/2$
11) $z_3 = (\cos(x * (2\pi/x_{w3}) + \pi) + 1) * h_{A3}/2$
12) $z_4 = (\cos(x * (2\pi/x_{w4}) + \pi) + 1) * h_{A4}/2$
13) $z_5 = \frac{z_1+z_2+z_3+z_4}{1.0 + 0.5 + 0.25 + 0.125}$
14) $z = h_{bed} + \frac{h_{Amax}}{z_{5max}} z_5$

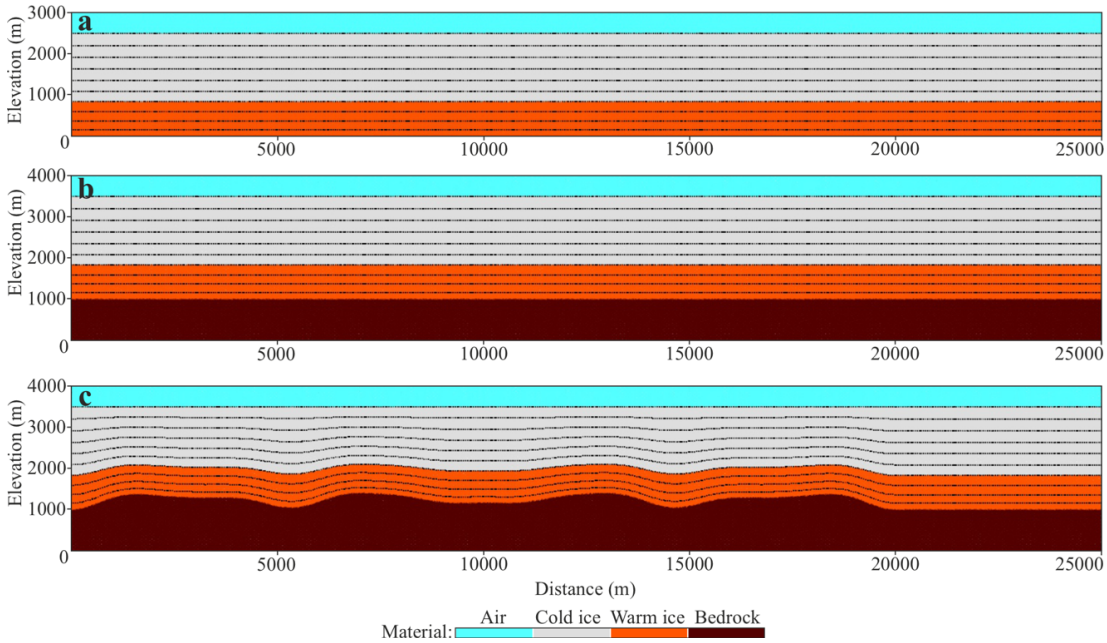


Figure S1. Comparison of three bedrock types and initial layer geometries: (a) free-slip bottom boundary (Models 1-2), (b) flat bedrock surface (Model 3) and (c) bumpy bedrock surface (Models 4-7).

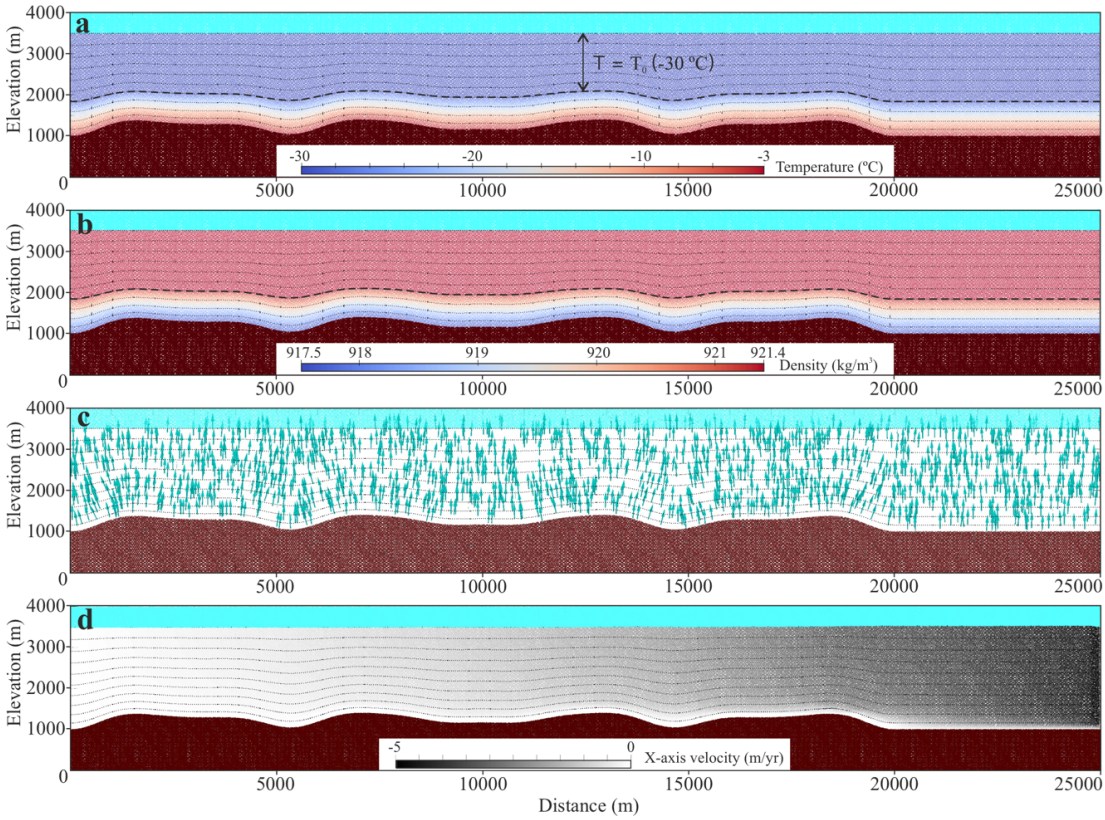


**Figure S2.** An example (Model 4) of the initial model settings: (a) temperature field in the ice sheet, showing a vertical temperature gradient from -3 °C ($T_{bed}$) to -30 °C ($T_0$); (b) ice density field with a vertical gradient from 917.51 kg/m$^3$ (-3 °C) to 921.41 kg/m$^3$ (-30 °C); (c) c-axis orientations (arrows) of ice particles. (d) Velocity field in the x-axis direction after the model starts to run.

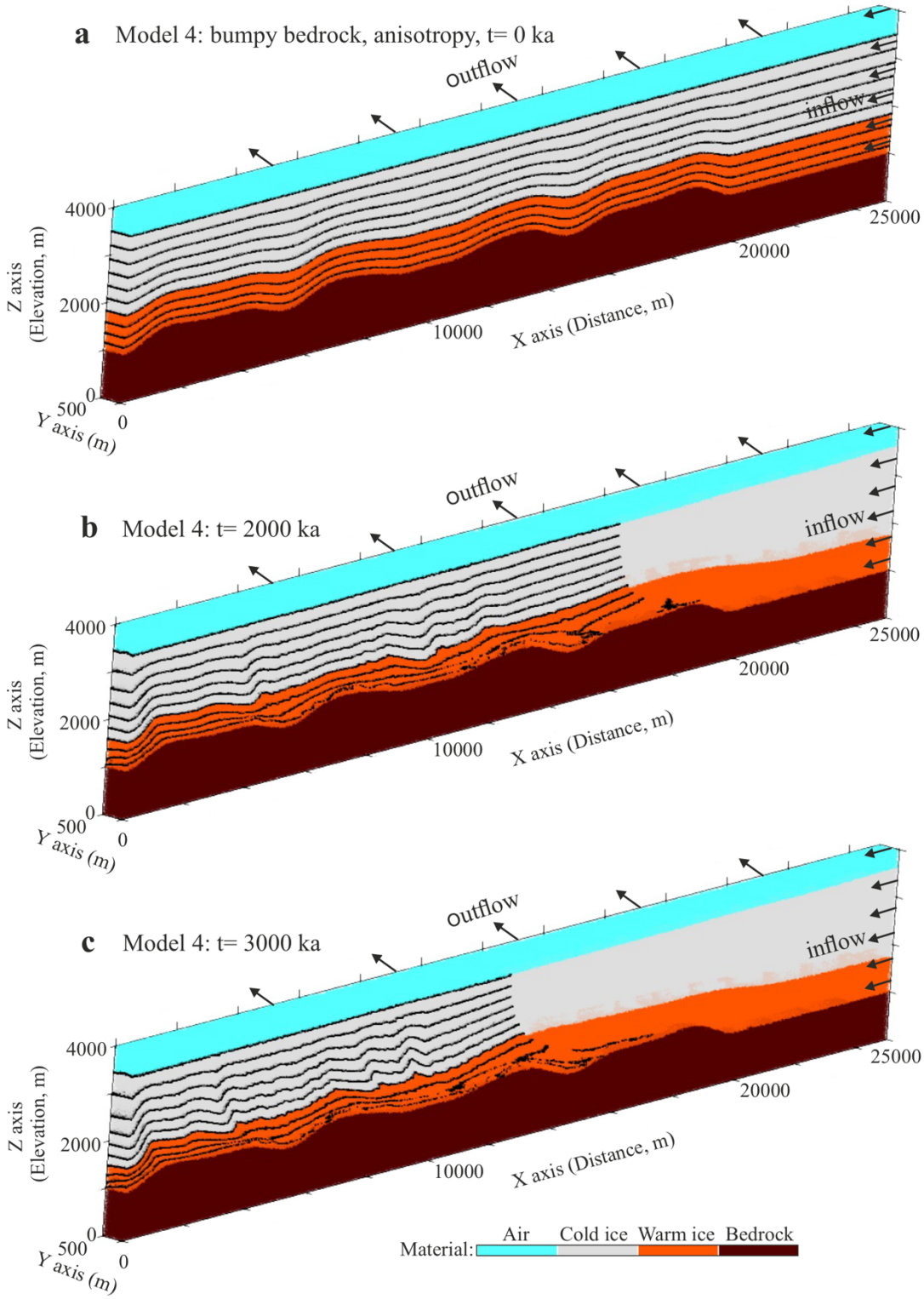


Figure S3. 3D views of Model 4 in (a) 0 year, after (b) 2000 years and (c) 3000 years.

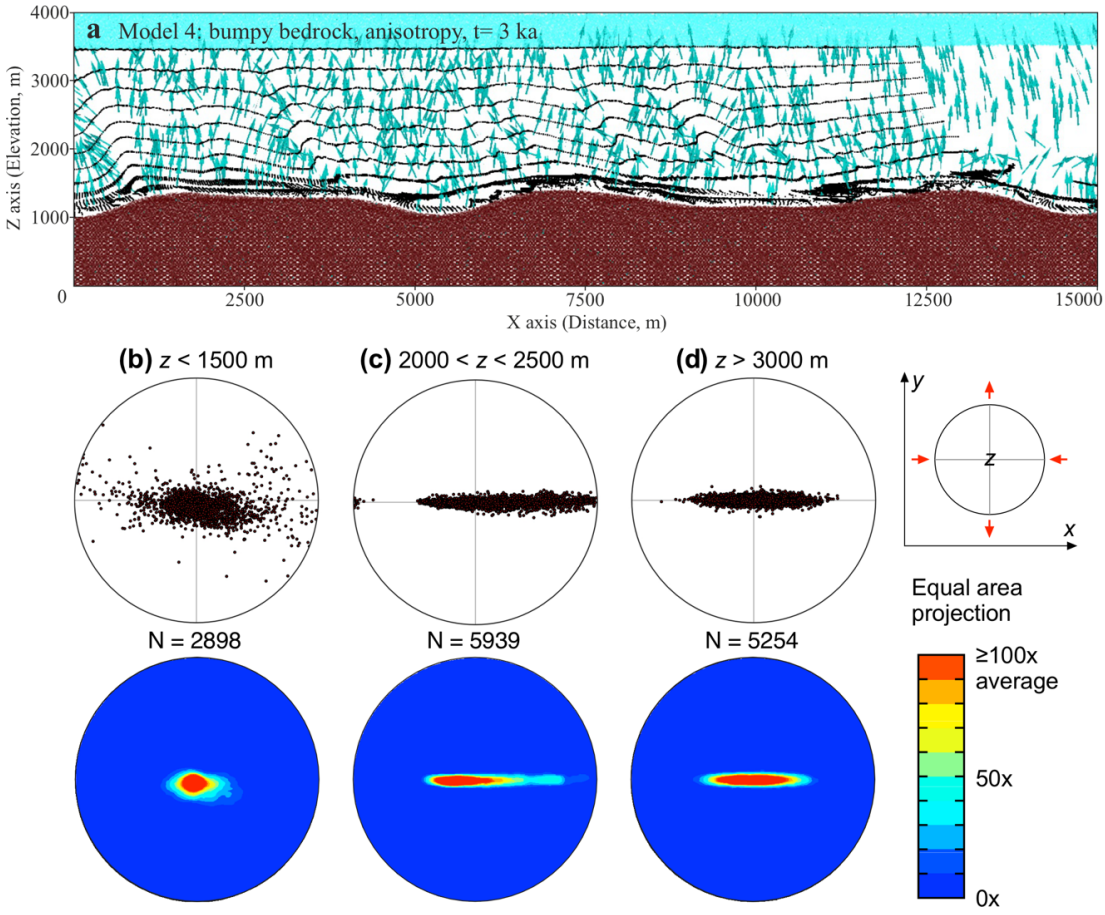


Figure S4. (a) Snapshot (at y=250 m) of c-axis orientations of ice particles in Model 4 after 3000 years. (b-d) C-axis lower-hemisphere, equal-area stereoplots of ice particles from ice elevations in (b) 1000-1500 m (basal layers), (c) 2000-2500 m (middle layers), and (d) 3000-3500 m (top layers). Horizontal coordinates of these ice particle samples are between $0 < x < 10000$ m and $125 < y < 375$ m. Projection is looking down from the top of the model. The c-axis orientations are plotted with the software Orient v3.24 (Vollmer, 2024). Except for basal ice layers sheared parallel to the bedrock, c-axes of ice particles are observed to rotate into a girdle pattern during folding.

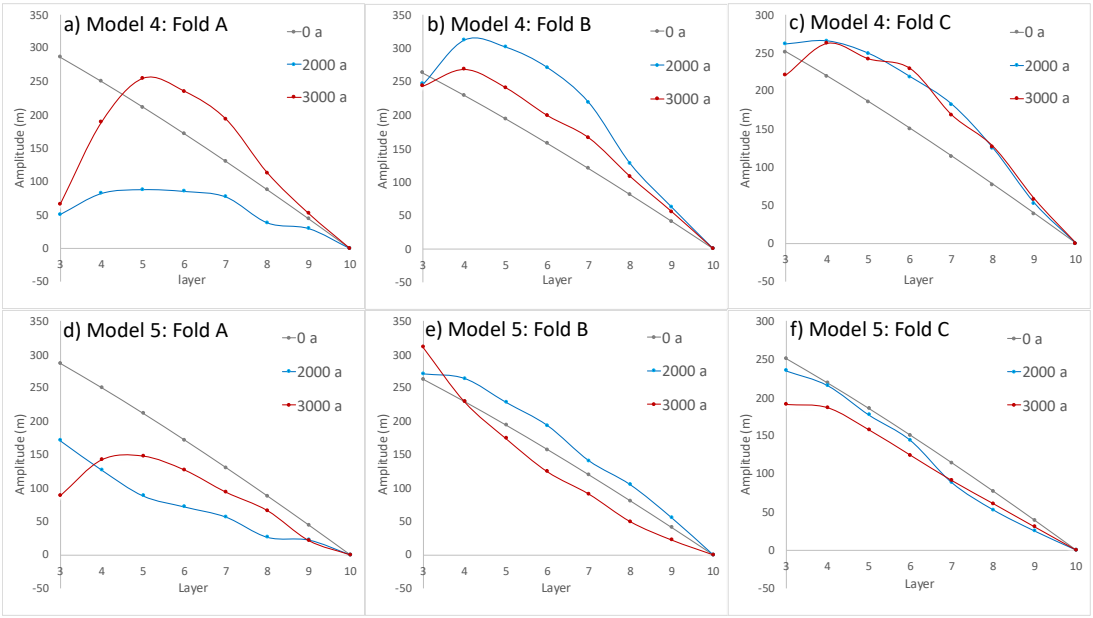


Figure S5. Fold amplitudes and amplification comparison of Model 4 (anisotropy) and Model 5 (isotropy): (a-c) The amplitude-layer diagrams of (a) Fold A, (b) Fold B and (c) Fold C in Model 4. The colored lines represent data from 0 (grey) to 2000 (blue) and 3000 years (red). (d-f) The amplitude-layer diagrams for Model 5, where the same color code applies.

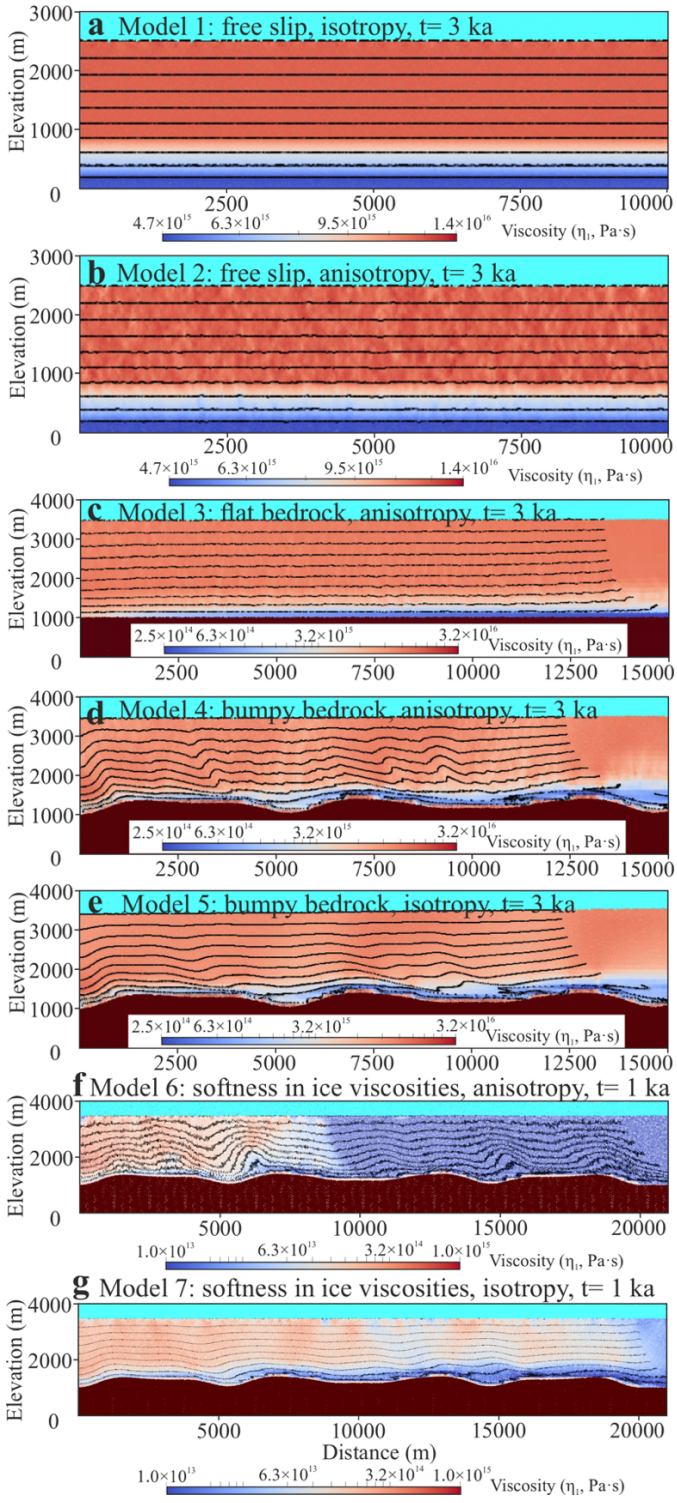


Figure S6. Snapshots (at y=250 m) of the effective general viscosity ($\eta_1$) of ice: (a-e) after 3000 years in (a) Model 1, (b) Model 2, (c) Model 3, (d) Model 4, and (e) Model 5; (f-g) after 1000 years in (f) Model 6 and (g) Model 7. In Models 6-7 there is a min limitation for the general viscosity $\eta_1$ ($1.0 \times 10^{13}$ Pa · s) to avoid artificial softness from boundary effects and control ice viscosities on a reasonable scale.

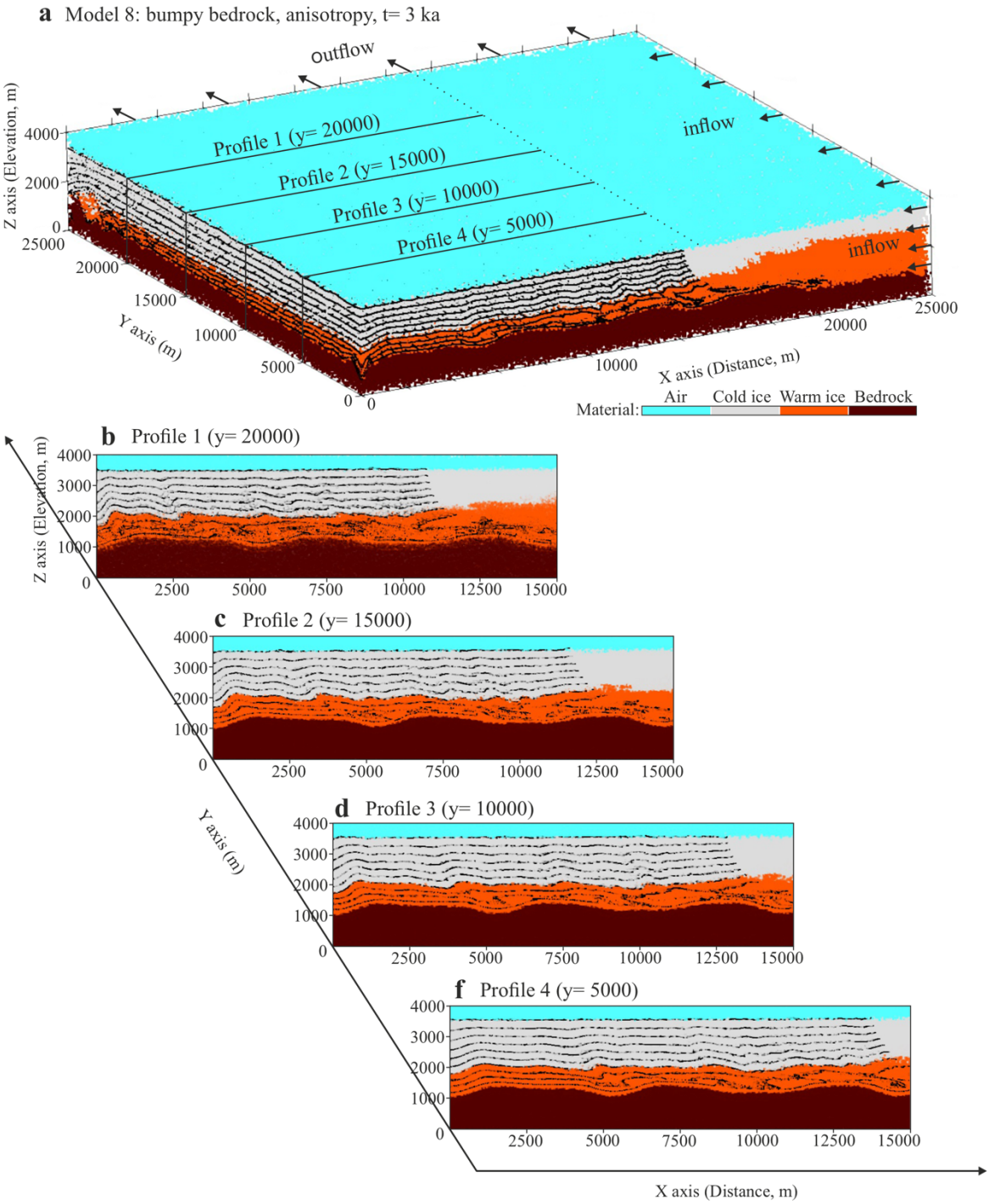


Figure S7. Supplement Model 8: 3D extension in the outflow (positive y-axis) direction based on Model 4. To compensate the inflow (5 m/yr), the outflow velocity is increased to around 5 m/yr. (a) 3D view of the model after 3000 years and (b-f) snapshots of layer geometry profiles at different y-axis positions. This model resolution is relatively low due to a larger size and the result may not be as accurate as Model 4. The result shows that fold patterns are similar between profiles but indicate a trend of increasing fold amplitudes along the outflow direction.

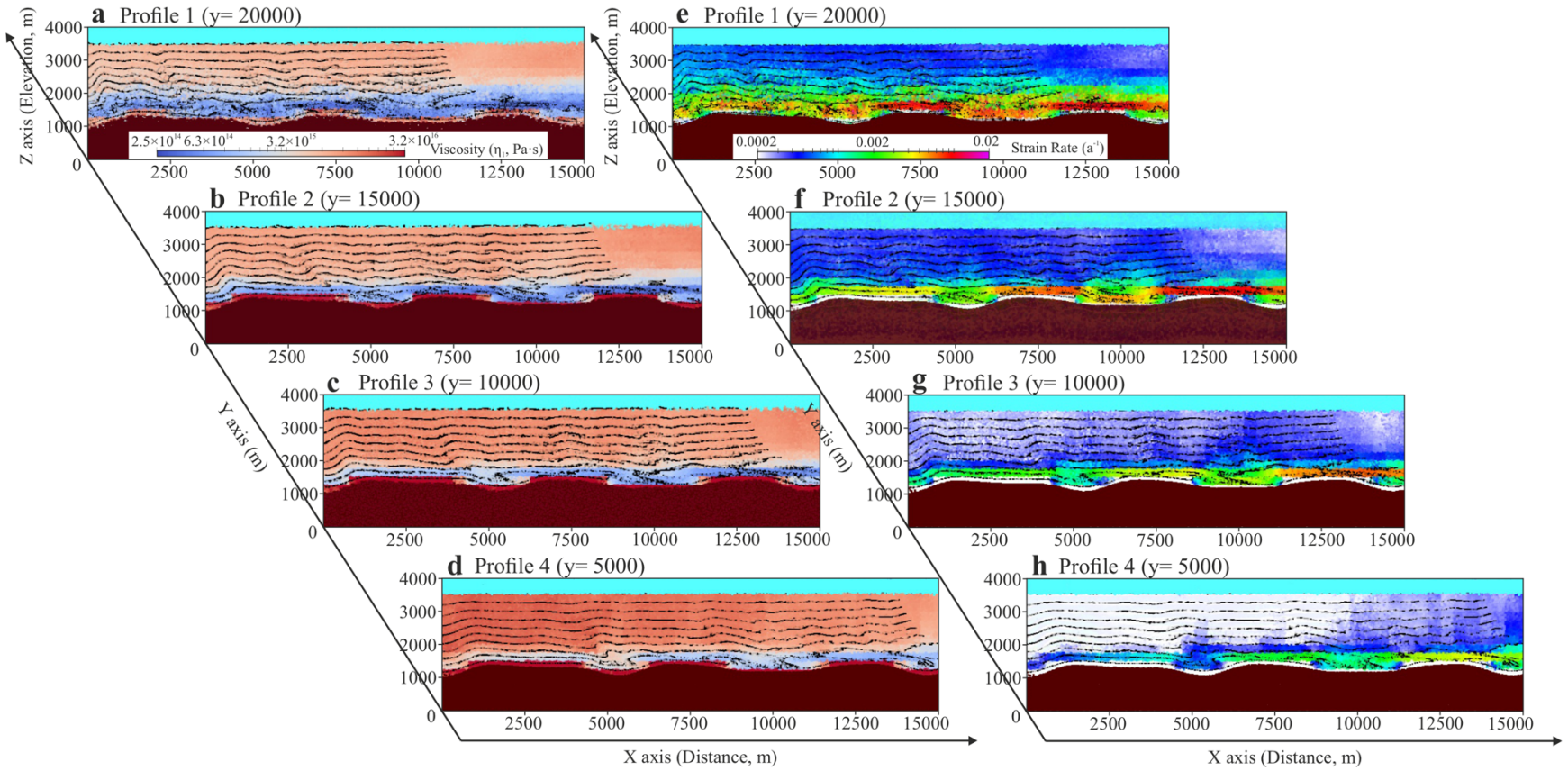


Figure S8. Supplement Model 8. Snapshots of viscosity ($\eta_1$) profiles (a-d) and strain-rate profiles (e-h; the second invariant of strain-rate magnitude) at different y-axis positions (see Figure S7a). These profiles show a trend of generally increasing strain rate and decreasing viscosity along the outflow direction, which mainly results from the increasing stretching velocity on a frozen bed. The decreasing viscosity would then speed up the fold growth.

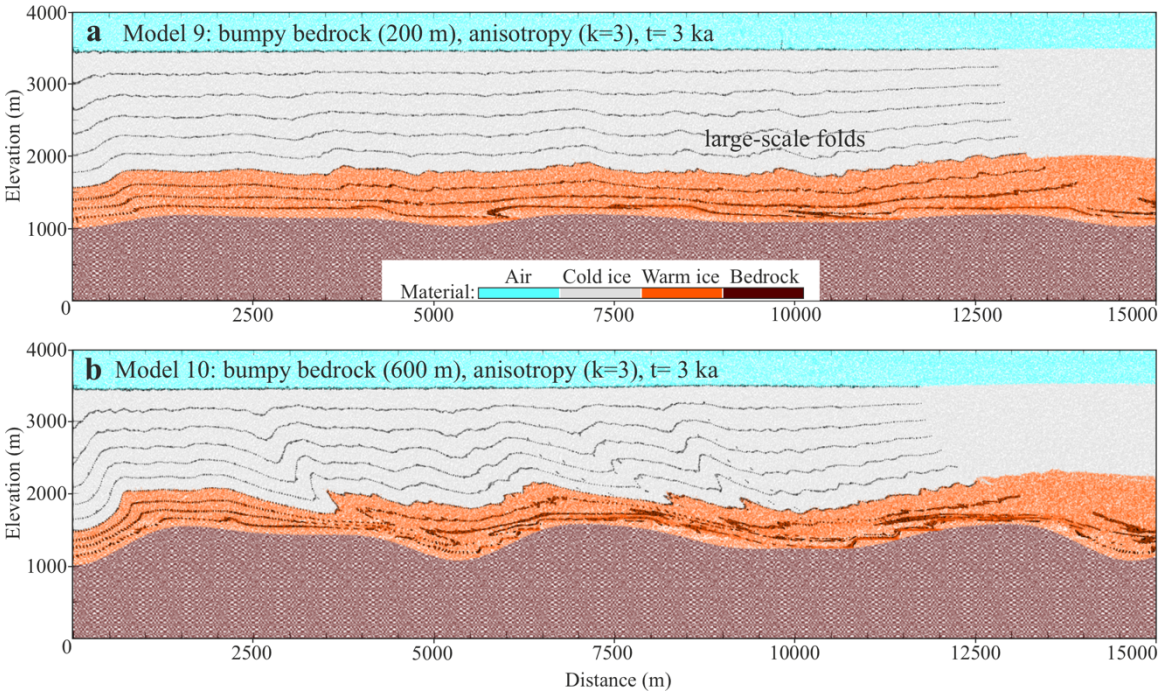


Figure S9. Supplement Models 9&10: small-amplitude bedrock bumps (maximum 200 m) and high-amplitude bedrock bumps (maximum 600 m) compared to Model 4. Results (snapshots at y=250 m) after 3000 years of (a) small-bump Model 9 and (b) high-bump Model 10, show much higher amplitudes of large-scale folds on high bedrock bumps. It should be noted that in the result some small zig-zag areas may appear in basal ice near a high bedrock bump. This is a resolution problem that the boundary between basal ice and high bedrock bump may not be perfectly defined in Underworld2 since ice and rock particles may be mixed in a square grid. This, however, does not influence the deformation in the bulk of the ice.

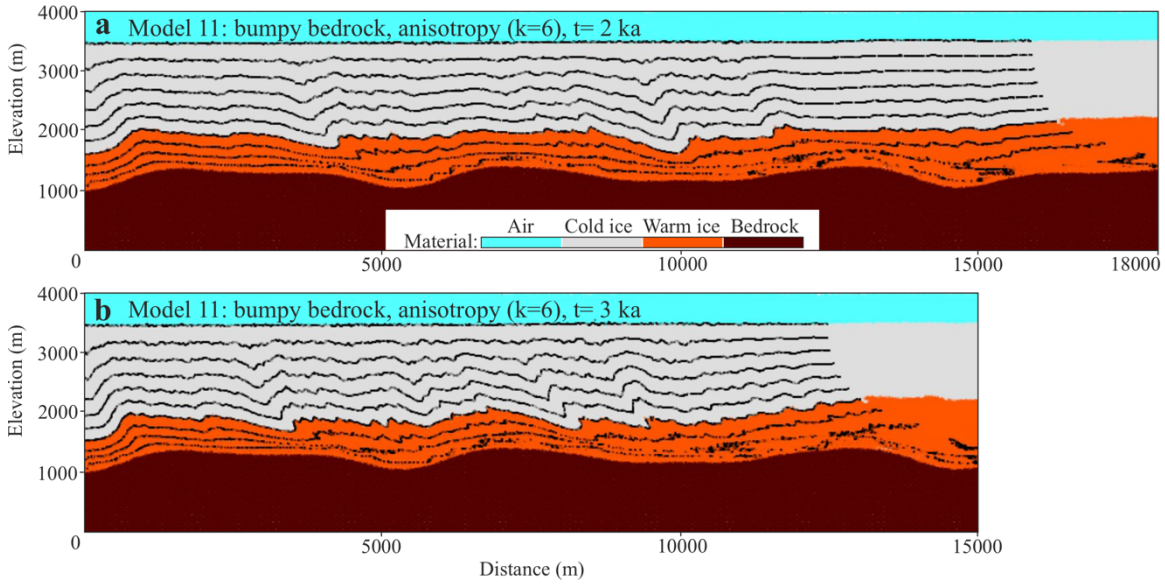


Figure S10. Supplement Model 11: larger anisotropy value (k=6) compared to Model 4. Results (snapshots at y=250 m) after (a) 2000 years and (b) 3000 years, show slightly higher amplitudes of large-scale folds than Model 4. There is a resolution problem that small folds appear to be affected by Underworld2 grids. Artificial amplification of small folds may hinder the nucleation and growth of large-scale folds.

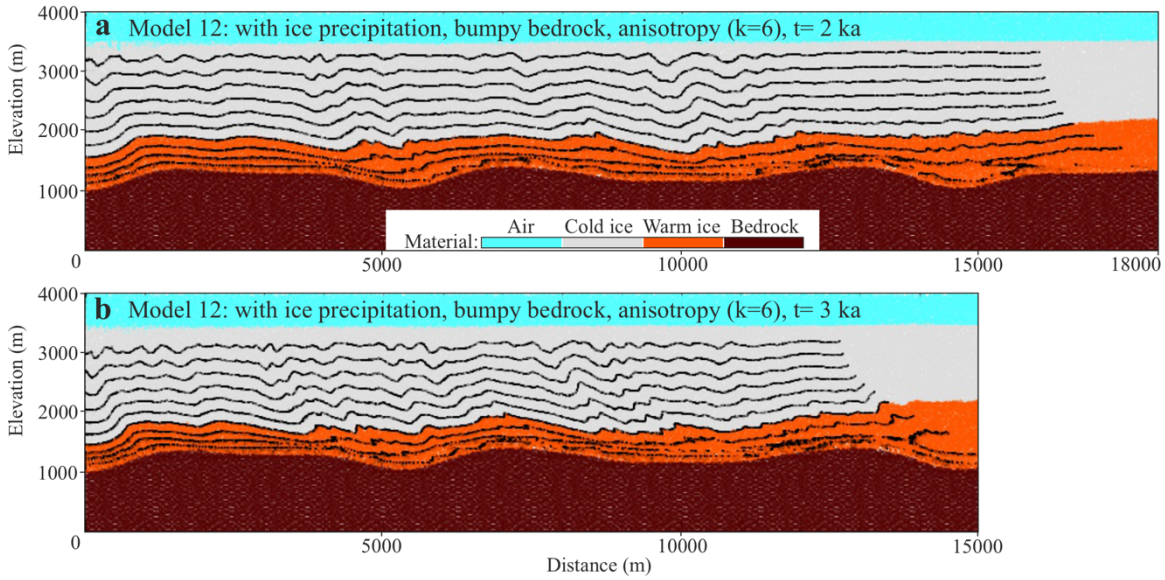


Figure S11. Supplement Model 12: with ice precipitation based on Model 11. The outflow velocity is increased to 0.13 m/yr (compared with 0.1 m/yr in Model 11) to compensate the inflow (5 m/yr) and the precipitation on the ice surface (surface accumulation rate 0.1 m/yr). Results (snapshots at y=250 m) after (a) 2000 years and (b) 3000 years, show an influence (suppression) of ice precipitation on fold growth, however, these folds can still grow to a reasonable scale range in 3000 years with a total 300 m surface accumulation. Anyway, the syn-sedimentation models for salt diapir growth are good indications (eg., Fuchs et al., 2011), where 'fold' patterns would be different from the way of 'surface accumulation' and layer thickness, etc. It deserves more work in the future to carefully constrain and find a balance between the negative vertical strain rates from surface accumulation, the increased horizontal stretching rate (outflow) and the buoyancy effect through viscosity changes, etc.

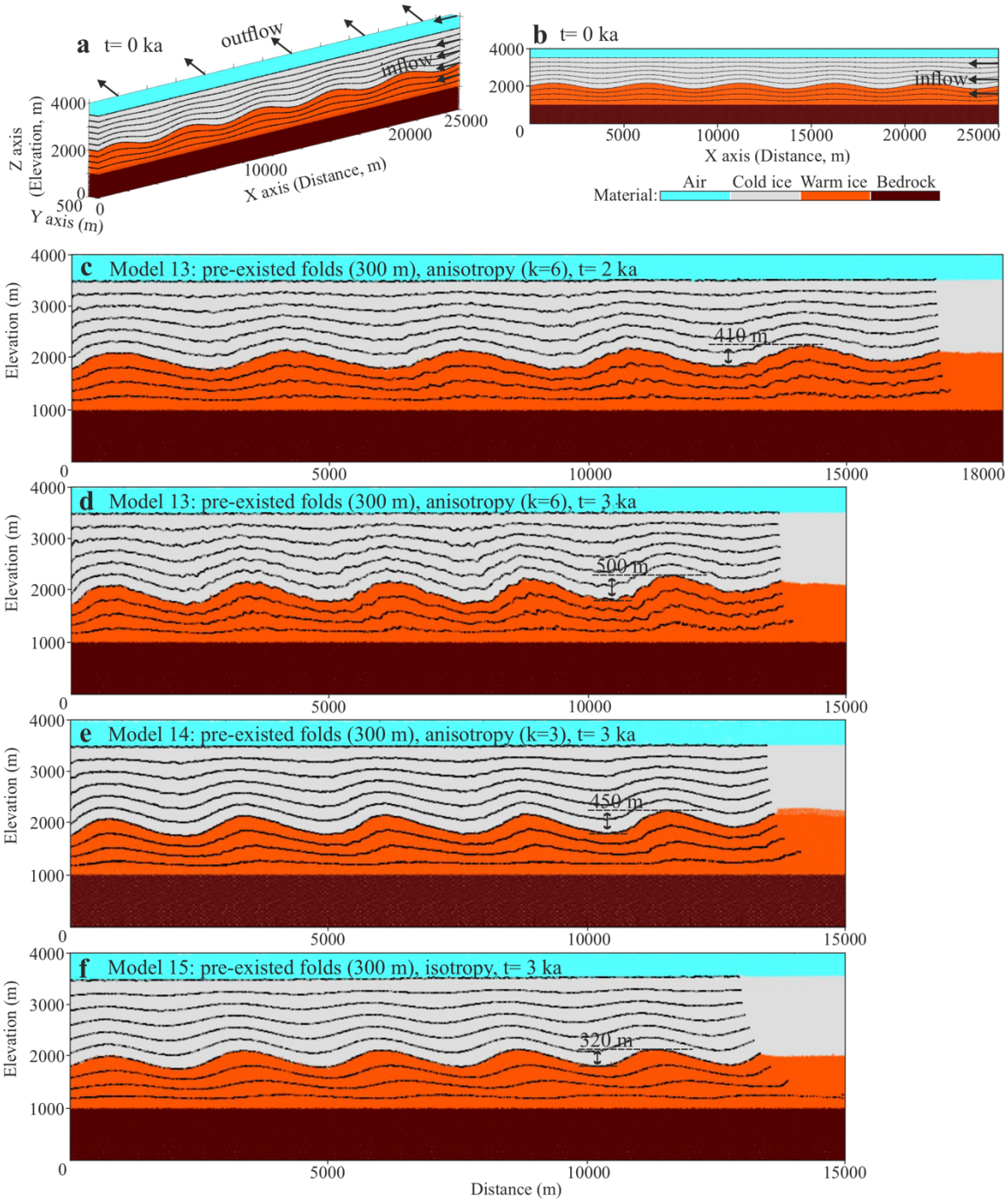


Figure S12. Supplement Models 13-15: deformation of pre-existed folds (amplitude 300 m at the cold-warm ice interface) in a convergent flow. Model 13: anisotropy value (k=6); Model 14: anisotropy value (k=3); Model 15: isotropy. (a-b) 3D view of the initial model and the profile parallel to x-z coordinate plane (at y=250 m). (c-d) Results of Model 13 after 2000 years and 3000 years. Fold amplitudes have reached up to around 410 m (2000 years) and 500 m (3000 years). (e) Result of Model 14 after 3000 years. Fold amplitudes have reached up to around 450 m. (f) Result of Model 15 after 3000 years. Fold amplitudes stay nearly the same and are slightly increased to around 320 m (buoyancy effect, etc.). Since we have already

obtained 300 m-scale folds in the results of Model 4, Models 13-15 can also be regarded as a later stage after the time scale of Model 4. The results suggest that: (1) Fold can be amplified more with an increasing strain through time and will also grow faster with increasing amplitude. (2) A slight change in the anisotropy value will make an obvious difference when the fold amplitude reaches a certain degree (due to the well-aligned c-axes of ice crystals).

# Chapter 3

## Rapid ice stream formation due to mechanical anisotropy

**Yu Zhang[1], Steven Franke[1,2], Till Sachau[1], Daniela Jansen[2], Haibin Yang[3], Dian Li[1,4], Yuanbang Hu[1], Ilka Weikusat[1,2], and Paul D. Bons[1,5]**

[1]Department of Geosciences, Tübingen University, Tübingen, Germany.

[2]Alfred Wegener Institute, Helmholtz Centre for Polar and Marine Research, Bremerhaven, Germany.

[3]School of Earth Sciences, Zhejiang University, Hangzhou, China.

[4]College of Earth and Planetary Science, Chengdu University of Technology, Chengdu, China.

[5]School of Earth Science and Resources, China University of Geosciences (Beijing), Beijing, China.

Manuscript submitted for publication in Science Advances. The reader should note that the final manuscript may deviate slightly from the version printed here.

## Abstract

Radio-echo sounding (RES) shows large-scale englacial stratigraphic folds are ubiquitous in Greenland's ice sheet. However, there is no consensus yet on how these folds form. Here, we use the full-Stokes code Underworld2 to simulate ice movements in three-dimensional convergent flow, mainly considering ice anisotropy due to a crystallographic preferred orientation, vertical viscosity and density gradients in ice layers, and bedrock topography. Our simulated folds show complex patterns and are classified into: large-scale folds (>100 m amplitude), small-scale folds (<<100 m) and basal-shear folds. The amplitudes of large-scale folds tend to be at their maximum in the middle of the ice column or just below, in accordance with observations in RES data. We conclude that ice anisotropy amplifies the perturbations in ice layers (mainly due to bedrock topography) into large-scale folds during flow. Density differences between the warm deep ice and cold ice above may enhance fold amplification.

## 1. Introduction

Projecting future global sea level as accurately as possible is crucial for human society and ecosystems on Earth. One of the most significant contributors to sea-level rise is the discharge of land ice from glaciers and ice sheets, yet this process remains the largest source of uncertainty in Earth system models (IPCC). Ice streams, which transport vast amounts of ice from the interiors of the Antarctic and Greenland ice sheets (GrIS) toward the ocean (*1–3*), play a critical role in this process. These fast-flowing corridors accelerate ice discharge and thus directly influence sea-level rise and climate change (*4–6*). The Northeast Greenland Ice Stream (NEGIS; Fig. 1) is a particularly important feature that extends for more than 500 km from the central GrIS ice divide to its outlets, with flow velocities up to ten times higher than in the surrounding ice (*2*, *8*). Despite extensive research, the mechanisms responsible for ice stream formation, particularly the establishment of their shear margins, remain poorly understood. Previous studies have proposed various external forcing mechanisms such as bedrock topography or subglacial geology (*9*), enhanced geothermal heat flux (*10–12*), or subglacial hydrology (*13*, *14*) to explain ice stream formation. However, no model has so far been able to test whether ice stream initiation can solely result from the evolving internal properties of the ice itself, without relying on external forcing.

Ice in ice sheets is a power-law viscous material that mainly deforms by dislocation creep (*15*, *16*). Ice is strongly anisotropic because it deforms more easily parallel to its crystallographic basal plane than perpendicular to it along the crystal's c-axis (*17*), which during deformation leads to a preferred alignment of the crystal lattice orientations, known as a crystallographic preferred orientation (CPO) (*16*). This anisotropy has significant implications for ice flow, particularly in regions of high shear such as the margins of ice streams, where the easy-glide crystallographic basal planes rotate toward the shear plane (*18–22*) that thus becomes effectively much softer (*23–25*).

Here, we apply the particle-in-cell full-Stokes code “Underworld2” (*26*, *27*) to simulate anisotropic ice flow in 3D large-scale ice-sheet models (*28*, *29*). By incorporating an anisotropic, non-linear viscosity and evolving c-axis orientations into our model, we are able to simulate the formation and behavior of ice streams under realistic, internally driven conditions, providing new insights into the fundamental processes governing ice stream dynamics.

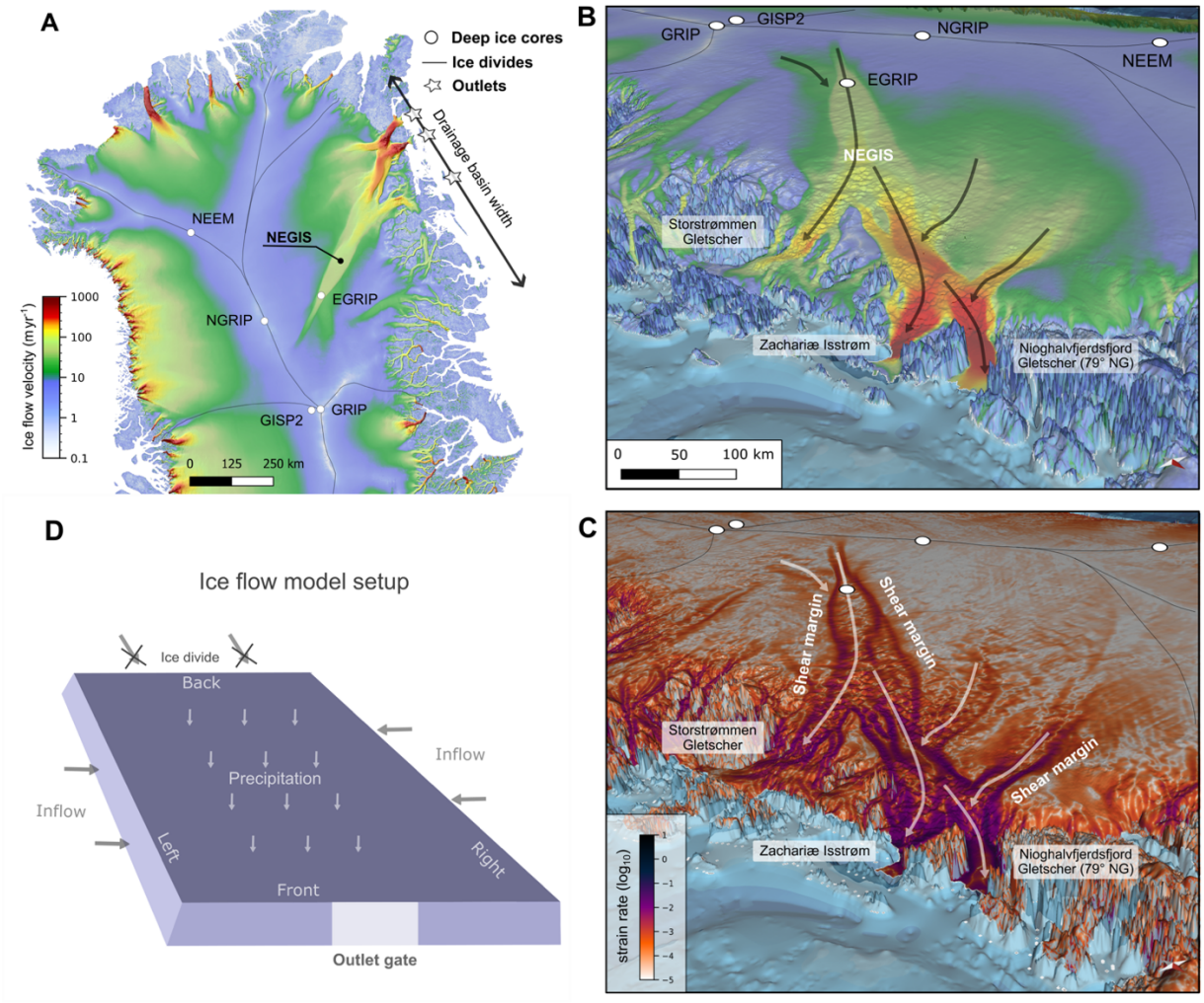


Fig. 1. Overview of the North-East Greenland's ice flow. (A) Surface velocity of the Northern Greenland ice sheet (*7*). (B, C) Close-up of NEGIS and its coastal outlets, showing surface flow velocity (B) (*7*), and strain rates (C) (*7*). The shear margins are observed as high strain rate areas bounding NEGIS. (D) Ice flow model setup characteristics.

## 2. Ice-stream organization under different boundary conditions

Our model setup consists of a rectangular box (40 × 50 km, and 3 km height) where ice can leave the system at one 10 km wide outlet gate only, mimicking the general drainage basin configuration in NE Greenland (Fig. 1). To maintain a constant ice volume, ice precipitates on the surface and flows into the modeling domain from the left and right boundaries of the model. Ice does not flow into the system from the back side of the model that thus represents the ice divide. Detailed model design and physics can be found in the supplementary materials

(materials and methods, figs. S1–S2 and tables S1–S2). We perform several model runs up to 4000–5000 years to explore the effect of varying boundary conditions, such as zero or free slip (supplementary text and figs. S18–S23) at the ice base, symmetry or asymmetry of inflow from the sides, and varying anisotropies (table S2).

Models 1–3 have a zero velocity at the base of the ice sheet, simulating ice that is frozen to the bedrock (Fig. 2). In all models, ice first shows convergent flow towards the outlet gate. The convergent ice flow is symmetric when lateral inflow is identical on the left and right side (Model 1; Fig. 2A). Two symmetrical shear margins develop after 2000 years that bound the convergent flow zone (fig. S4) and form the proto ice stream (Fig. 2B). The shear margins then extend towards the inland ice sheet and after 4000 years new shear margins are established inside the ice stream oblique to the original shear margins, dividing the ice stream into two tributaries (Fig. 2, C and D). The two tributaries are nearly symmetric, despite the initial CPO noise (fig. S2C).

Convergent flow is asymmetric when the left inflow flux is twice as large as the right one (Model 2; Fig. 2E). This effectively simulates a ca. 700 km wide drainage basin (supplementary text) where the outflow gate is not centered in the middle, as is the case in the NE Greenland drainage basin of NEGIS (Fig. 1A). The left shear margin develops faster (fig. S8) and forms the dominant tributary with stronger shearing at its margins (fig. S10) compared to the right tributary (Fig. 2F). The dominant tributary later also extends further inland (Fig. 2, G and H). When the rheological anisotropy parameter ($k$) is elevated from 10 in Model 2 to 100 (Model 3), the ice stream establishes faster in time with more distinct shear margins (figs. S14 and S15) and a larger difference in flow velocity across these margins (Fig. 2, I–L).

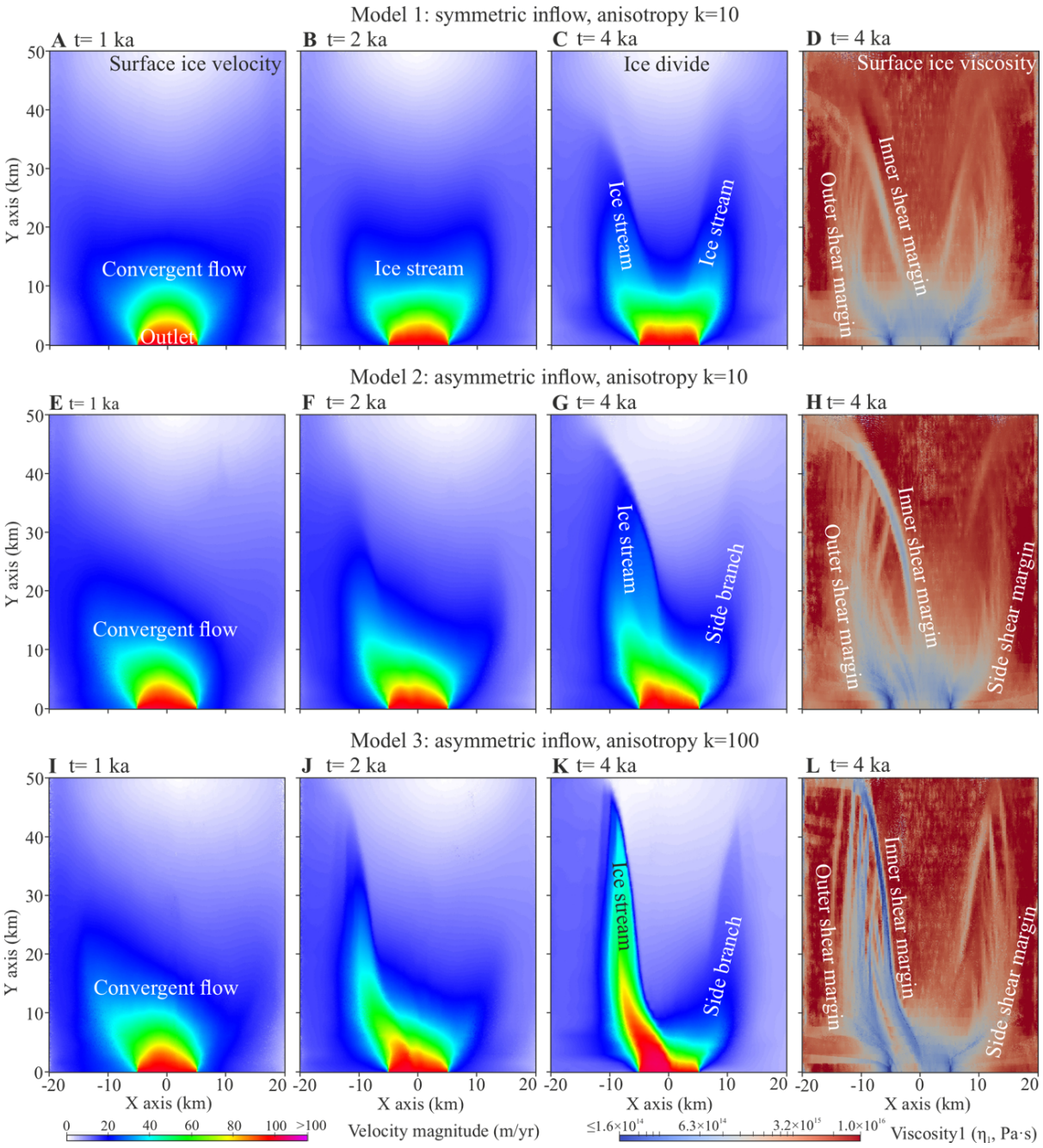


Fig. 2. Results and comparisons of ice stream formation. (A–D) The tributary-type ice stream after 1000 years (A), 2000 years (B), and 4000 years (C) in Model 1. General viscosities $\eta_1$ from the ice surface at 4000 years (D) show shear margins with localized softening. (E–H) The NEGIS-type ice stream in Model 2. (I–L) The NEGIS-type ice stream in Model 3. Detailed results can be found in the supplementary materials (see figure and movie lists in table S2).

## 3. C-axis rotation and shear-margin establishment

No ice stream forms when the ice is modeled as an isotropic material (fig. S23). This clearly shows that the formation of the ice streams is related to the mechanical anisotropy of ice, as is illustrated in 3D views of the NEGIS-type ice stream (Model 2; Fig. 3) and vertical sections across the ice stream (Fig. 4). The shear margins are zones of lowered effective viscosity that extend vertically from the surface down to the base of the ice sheet (Fig. 4, A and B). C-axes are mostly oriented horizontally inside the margins (Fig. 4, C and D). C-axes have thus rotated from the original Gaussian distribution around the vertical (±5° standard deviation (*30*); fig. S2C) to the horizontal inside the shear margins.

C-axis rotations calculated by our model (materials and methods) cause the directional alignment of the easy-glide crystallographic basal planes towards the vertical shear-margin plane, making the ice effectively softer (*20*, *22*). A shear zone is then established due to the localized shearing in the vertical plane. Shear zones usually form in pairs that bound the ice stream that can now flow much faster as the lateral resistance to flow is strongly reduced due to the new CPO in the established shear margins. It is worth noting that the c-axis orientations of the basal ice remain almost vertically upward due to the strong bedrock-parallel shearing (Fig. 4 and fig. S11). Because the shear margins are not controlled by external forcing, but by the properties (CPO) of the ice inside these margins, the shear margins advect together with the surrounding ice (figs. S8 and S9, movie S2). As the streams evolve, new shear margins establish and subdivide the flow into tributaries depending on inland ice dynamics (figs. S4 and S8). In addition, new shear margins develop in the upstream part of the ice stream as it narrows due to the enhanced flow inside the ice stream.

The rotation of c-axes, an inherent material behavior that is implemented in Underworld2, is the primary mechanism for the formation of shear margins, and, hence, ice streams in our simulations. These factors, as well as control by bedrock topography that is not included in our simulations, may explain the variety in tributary geometries in reality (*31–33*). The geometry of one main ice stream with a small tributary (Models 2 and 3) is very similar to that of NEGIS. In both cases, the influx of ice from either side of the outflow gate(s) is asymmetric, in case of NEGIS because the three gates, which are combined into one in our model domain, are in the NE corner of the drainage basin. In such a ‘NEGIS-type' ice stream,

the main ice stream is oblique to the ice-sheet margin and drains the larger part of the drainage basin. The smaller tributary, draining into 79° North Glacier (79NG; Fig. 1), drains the remainder of the basin. Our models show that shear-induced CPO change by itself is enough to establish shear margins and an ice stream like NEGIS if the drainage is constrained by a relatively narrow outflow gate. Without ice anisotropy, shear margins and an ice stream cannot be established under our model conditions (fig. S23). Bedrock topography, bedrock sliding, elevated geothermal heat flux, or shear heating (*34*) may still play a role as additional or modifying factors, or in the further development of the ice stream as shear heating affects the shear margins formed due to CPO rotation.

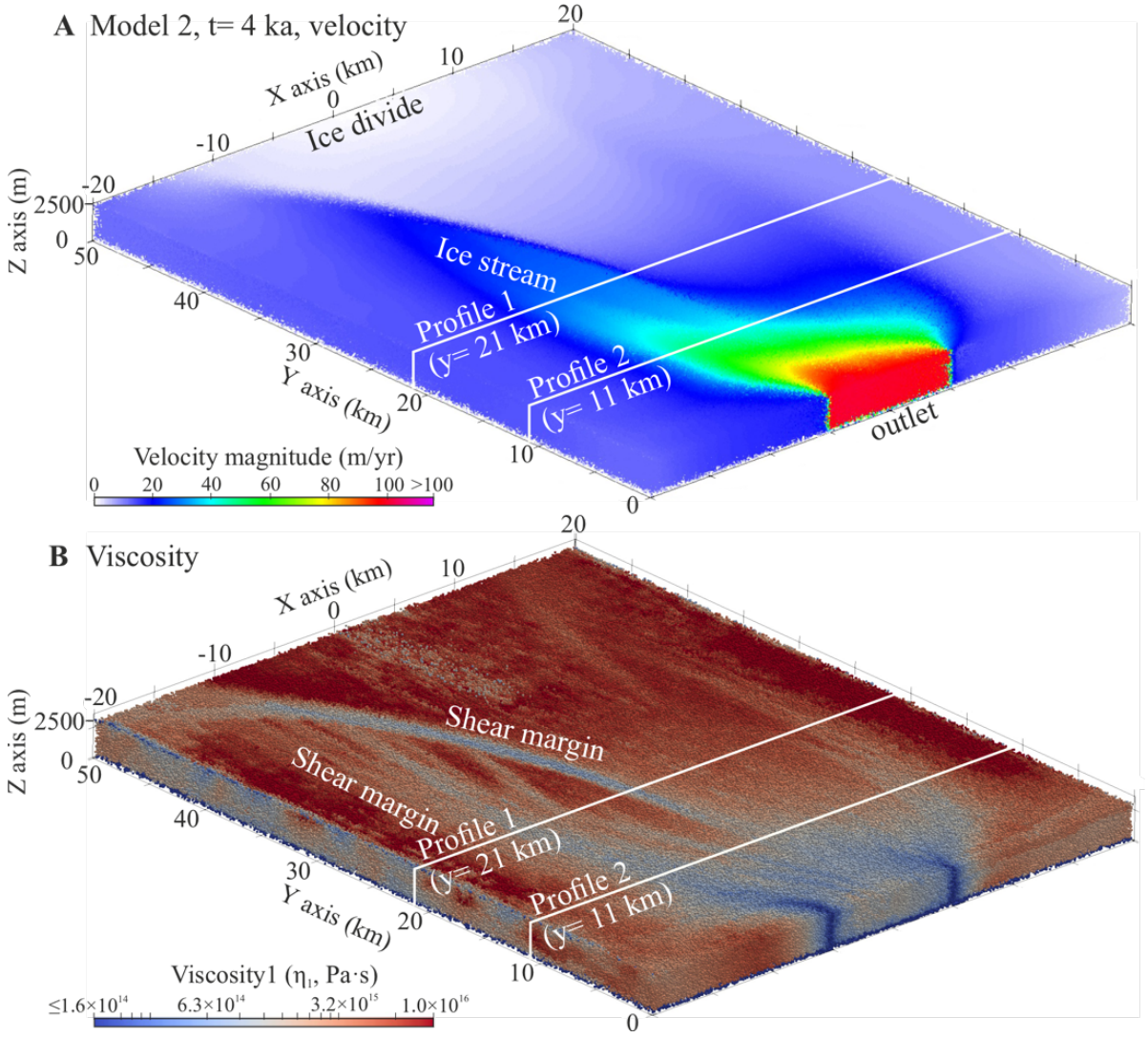


Fig. 3. 3D views of the NEGIS-type ice stream in Model 2 at 4000 years. (A) Ice velocity. (B) Effective viscosity $\eta_1$. The ice surface topography is presented in greater detail in fig. S12.

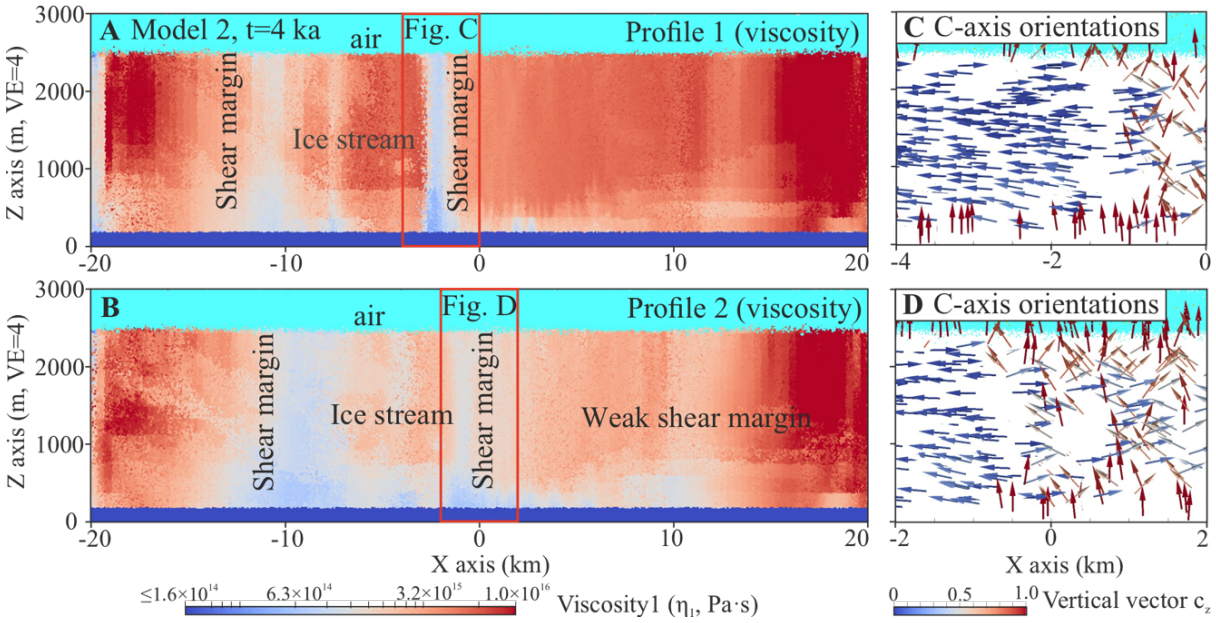


Fig. 4. Profile snapshots of the NEGIS-type ice stream in Model 2 at 4000 years. (A–B) Ice general viscosities $\eta_1$ on Profile 1 (A) and Profile 2 (B) transverse the ice stream (profile locations in Fig. 3), showing vertical shear margins from the model center to near the outlet. Note the vertical exaggeration (4×) in the profiles. (C–D) C-axis orientations (arrows) of ice particles as developed by the model at a shear margin (marked in A–B). Arrow colors represent vertical vectors, with deep blue being horizontal (0) and deep red being vertical (1.0).

## 4. Ice Stream Evolution and Future Projections

Shear margin migration has been observed in both Greenland and Antarctic ice streams through repeated surface velocity measurements and radio-echo sounding data (*35*–*37*), and is supported by various modeling efforts (*21*, *38*, *39*). Formation, shifts, and cessation of ice streams, such as in Northeast Greenland all within the Holocene (*36*, *40*), highlight the dynamic nature of these systems. Our model results reinforce this understanding, showing that ice streams initiate and evolve primarily by the formation and movement of shear margins (*41*) in relation to the location of outlet gates within the drainage basin. Such gates are determined by the bedrock topography at the ice-sheet margin and may possibly be modified by regional warming (*5*, *37*, *42*). We demonstrate that ice anisotropy can initiate a proto ice stream draining ice towards the outlet(s) in approximately 1000 to 2000 years. As the ice

stream evolves and develops its tributaries, the dominant tributaries, such as NEGIS, can extend inland, nearly reaching the ice divide. Radar observations constrain the timing of when the shear margins of NEGIS fully developed to about 2000 years before present (*37*), and our simulations suggest that the lead-up time to this state was another 1000–2000 years. This would allocate the overall initiation of NEGIS to about 3–4 ka BP at the end of the warm phase that caused the retreat of the glaciers at the outlets in NE Greenland (*37*, *43*, *44*).

Our modeling indicates that future ice stream evolution will likely involve continuous geometry and position changes due to shear margin migration, occurring on a thousand-year timescale. These systems are sensitive to shifts in ice mass, which alter inland ice flows, potentially leading to the emergence of new tributaries, or their shutdown (*36*, *37*). Additionally, abrupt changes at the ice sheet front, such as variations in basal conditions, could result in the rapid formation of new ice streams and shear margins. The dynamic nature of ice streams may accelerate when processes such as basal melting or shear heating are additionally involved.

Our most important finding is that internal ice anisotropy alone can drive ice stream formation and evolution on a time scale of only thousands of years, without external forcing by, for example, basal melting, shear heating or bedrock topography. This underscores the dynamic nature of ice streams, with their evolving margins and tributaries, and must be considered in future projections of ice sheet stability under climate change scenarios.

## References and Notes

1. T. Hughes, West Antarctic ice streams. *Rev. Geophys.* **15**, 1–46 (1977). doi:10.1029/rg015i001p00001
2. C. R. Bentley, Antarctic Ice Streams: A review. *J. Geophys. Res.* **92**, 8843–8858 (1987). doi:10.1029/jb092ib09p08843
3. M. A. Fahnestock, R. A. Bindschadler, R. Kwok, K. C. Jezek, Greenland ice sheet surface properties and ice dynamics from ERS-1 SAR imagery. *Science* **262**, 1530–1534 (1993). doi:10.1126/science.262.5139.1530
4. R. B. Alley, P. U. Clark, P. Huybrechts, I. Joughin, Ice-sheet and sea-level changes. *Science* **310**, 456-460 (2005). doi:10.1126/science.1114613
5. S. Khan, K. Kjær, M. Bevis, J. L. Bamber, J. Wahr, K. K. Kjeldsen, A. A. Bjørk, N. J. Korsgaard, L. A. Stearns, M. R. van den Broeke, L. Liu, N. K. Larsen, L. S. Muresan, Sustained mass loss of the northeast Greenland ice sheet triggered by regional warming. *Nat. Clim. Change* **4**, 292–299 (2014). doi:10.1038/nclimate2161

6. S. A. Khan, Y. Choi, M. Morlighem, E. Rignot, V. Helm, A. Humbert, J. Mouginot, R. Millan, K. H. Kjær, A. A., Bjørk, Extensive inland thinning and speed-up of Northeast Greenland Ice Stream. *Nature* **611**, 727–732 (2022). doi:10.1038/s41586-022-05301-z

7. I. A. N. Joughin, B. E. Smith, I. M. Howat, A complete map of Greenland ice velocity derived from satellite data collected over 20 years. *J. Glaciol.* **64**, 1–11 (2018). doi:10.1017/jog.2017.73

8. J. Mouginot, E. Rignot, B. Scheuchl, I. Fenty, A. Khazendar, M. Morlighem, A. Buzzi, J. Paden, Fast retreat of zachariæ isstrøm, northeast Greenland. *Science* **350**, 1357–1361 (2015). doi:10.1126/science.aac7111

9. S. Anandakrishnan, D. D. Blankenship, R. B. Alley, P. L. Stoffa, Influence of subglacial geology on the position of a West Antarctic ice stream from seismic observations. *Nature* **394**, 62–65 (1998). doi:10.1038/27889

10. M. Fahnestock, W. Abdalati, I. Joughin, J. Brozena, P. Gogineni, High Geothermal Heat Flow, Basal Melt, and the Origin of Rapid Ice Flow in Central Greenland. *Science* **294**, 2338– 2342 (2001). doi:10.1126/science.1065370

11. I. Rogozhina, A. G. Petrunin, A. P. M. Vaughan, B. Steinberger, J. V. Johnson, M. K. Kaban, R. Calov, F. Rickers, M. Thomas, I. Koulakov, Melting at the base of the Greenland ice sheet explained by Iceland hotspot history. *Nat. Geosci.* **9**, 366–369 (2016). doi:10.1038/ngeo2689

12. S. Smith-Johnsen, B. de Fleurian, N. Schlegel, H. Seroussi, K. Nisancioglu, Exceptionally high heat flux needed to sustain the Northeast Greenland Ice Stream. *Cryosphere* **14**, 841–854 (2020). doi:10.5194/tc-14-841-2020

13. K. Christianson, L. E. Peters, R. B. Alley, S. Anandakrishnan, R. W. Jacobel, K. L. Riverman, A. Muto, B. A. Keisling, Dilatant till facilitates ice-stream flow in northeast Greenland. *Earth Planet. Sci. Lett.* **401**, 57–69 (2014). doi:10.1016/j.epsl.2014.05.060

14. T. M. Kyrke-Smith, R. F. Katz, A. C. Fowler, Subglacial hydrology as a control on emergence, scale, and spacing of ice streams. *J. Geophys. Res. Earth Surf.* **120**, 1501–1514 (2015). doi:10.1002/2015JF003505

15. J. Weertman, Creep deformation of ice. *Annu. Rev. Earth Planet. Sci.* **11**, 215–240 (1983).

16. W. F. Budd, T. H. Jacka, A review of ice rheology for ice sheet modelling. *Cold Reg. Sci. Technol.* **16**, 107–144 (1989). doi:10.1016/0165-232X(89)90014-1

17. P. Duval, M. F. Ashby, I. Andermant, Rate-controlllng processes in the creep of polycrystalline ice. *J. Phys. Chem.* **87**, 4066–4074 (1983). doi:10.1021/j100244a014

18. R. B. Alley, Fabrics in polar ice sheets: development and prediction. *Science* **240**, 493–495 (1988). doi:10.1126/science.240.4851.493

19. B. Journaux, T. Chauve, M. Montagnat, A. Tommasi, F. Barou, D. Mainprice, L. Gest, Recrystallization processes, microstructure and crystallographic preferred orientation evolution in polycrystalline ice during high-temperature simple shear. *Cryosphere* **13**, 1495–1511 (2019). doi:10.5194/tc-13-1495-2019

20. C. Qi, D. J. Prior, L. Craw, S. Fan, M. G. Llorens, A. Griera, M. Negrini, P. D. Bons, D. L. Goldsby, Crystallographic preferred orientations of ice deformed in direct-shear experiments at low temperatures. *Cryosphere* **13**, 351–371 (2019). doi:10.5194/tc-13-351-2019

21. D. A. Lilien, N. M. Rathmann, C. S. Hvidberg, D. Dahl-Jensen, Modeling Ice-Crystal Fabric as a Proxy for Ice-Stream Stability, *J. Geophys. Res. Earth Surf.* **126**, e2021JF006306 (2021). doi:10.1029/2021JF006306

22. M. G. Llorens, A. Griera, P. D. Bons, I. Weikusat, D. Prior, E. Gomez-Rivas, T. de Riese, I. Jimenez-Munt, D. Garcia-Castellanos, R. A. Lebensohn, Can changes in deformation regimes be inferred from crystallographic preferred orientations? *Cryosphere* **16**, 2009–2024 (2022). doi:10.5194/tc-16-2009-2022

23. E. C. Smith, A. F. Baird, J. M. Kendall, C. Martín, R. S. White, A. M. Brisbourne, A. M. Smith, Ice fabric in an Antarctic ice stream interpreted from seismic anisotropy. *Geophys. Res. Lett.* **44**, 3710–3718 (2017). doi:10.1002/2016GL072093

24. T. J. Young, D. M. Schroeder, T. M. Jordan, P. Christoffersen, S. M. Tulaczyk, R. Culberg, N. L. Bienert, Inferring Ice Fabric From Birefringence Loss in Airborne Radargrams: Application to the Eastern Shear Margin of Thwaites Glacier, West Antarctica. *J. Geophys. Res. Earth Surf.* **126**, e2020JF006023 (2021). doi:10.1029/2020JF006023.

25. T.A. Gerber, D. A. Lilien, N. M. Rathmann, S. Franke, T. J. Young, F. Valero-Delgado, M. R. Ershadi, R. Drews, O. Zeising, A. Humbert, N. Stoll, I. Weikusat, A. Grinsted, C. S. Hvidberg, D. Jansen, H. Miller, V. Helm, D. Steinhage, C. O'Neill, J. Paden, S. P. Gogineni, D. Dahl-Jensen, O. Eisen, Crystal orientation fabric anisotropy causes directional hardening of the Northeast Greenland Ice Stream. *Nat. Commun.* **14**, 2653 (2023). doi:10.1038/s41467-023-38139-8

26. J. Mansour, J. Giordani, L. Moresi, R. Beucher, O. Kaluza, M. Velic, R. Farrington, S. Quenette, A. Beall, Underworld2: Python Geodynamics Modelling for Desktop, HPC and Cloud. *J. Open Source Softw.* **5**, 1797 (2020). doi:10.21105/joss.01797

27. R. Beucher, J. Giordani, L. Moresi, J. Mansour, O. Kaluza, M. Velic, R. Farrington, S. Quenette, A. Beall, D. Sandiford, L. Mondy, C. Mallard, P. Rey, G. Duclaux, A. Laik, S. Morón, A. Beall, B. Knight, N. Lu, Underworld2: Python Geodynamics Modelling for Desktop, HPC and Cloud (v2.15.1b), Zenodo (2024); https://doi.org/10.5281/zenodo.10976370.

28. T. Sachau, H. Yang, J. Lang, P. D. Bons, L. Moresi, ISMIP-HOM benchmark experiments using Underworld. *Geosci. Model Dev.* **15**, 8749–8764 (2022). doi:10.5194/gmd-15-8749-2022

29. Y. Zhang, T. Sachau, S. Franke, H. Yang, D. Li, I. Weikusat, P. D. Bons, Formation mechanisms of large- scale folding in Greenland's ice sheet. *Geophys. Res. Lett.* **51**, e2024GL109492 (2024). doi:10.1029/ 2024GL109492

30. I. Weikusat, D. Jansen, T. Binder, J. Eichler, S. H. Faria, F. Wilhelms, S. Kipfstuhl, S. Sheldon, H. Miller, D. Dahl-Jensen, T. Kleiner, Physical analysis of an Antarctic ice core—towards an integration of micro- and macrodynamics of polar ice. *Phil. Trans. R. Soc. A* **375,** 20150347 (2017). doi:10.1098/rsta.2015.0347

31. E. Rignot, J. Mouginot, B. Scheuchl, Ice flow of the Antarctic ice sheet. *Science* **333**, 1427–1430 (2011). doi:10.1126/science.1208336

32. E. Rignot, J. Mouginot, Ice flow in Greenland for the International Polar Year 2008–2009. *Geophys. Res. Lett.* **39**, L11501 (2012). doi:10.1029/2012gl051634

33. F. Ng, Spatial complexity of ice flow across the Antarctic Ice Sheet. *Nat. Geosci.* **8**, 847–850 (2015). doi:10.1038/ngeo2532

34. T. Perol, J. R. Rice, Shear heating and weakening of the margins of West Antarctic ice streams. *Geophys. Res. Lett.* **42**, 3406–3413 (2015). doi:10.1002/2015GL063638

35. K. A. Echelmeyer, W. D. Harrison, Ongoing margin migration of Ice Stream B, Antarctica. *J. Glaciol.* **45**, 361–369 (1999). doi:10.3189/S0022143000001866

36. S. Franke, P. D. Bons, J. Westhoff, I. Weikusat, T. Binder, K. Streng, D. Steinhage, V. Helm, O. Eisen, J. D. Paden, G. Eagles, D. Jansen, Holocene ice-stream shutdown and drainage basin reconfiguration in northeast Greenland. *Nat. Geosci.* **15**, 995–1001 (2022). doi:10.1038/s41561-022-01082-2

37. D. Jansen, S. Franke, C. C. Bauer, T. Binder, D. Dahl-Jensen, J. Eichler, O. Eisen, Y. Hu, J. Kerch, M. G. Llorens, H. Miller, N. Neckel, J. Paden. T. de Riese, T. Sachau, N. Stoll, I. Weikusat, F. Wilhelms, Y. Zhang, P. D. Bons, Shear margins in upper half of Northeast Greenland Ice Stream were established two millennia ago. *Nat. Commun.* **15**, 1193 (2024). doi:10.1038/s41467-024-45021-8

38. C. Schoof, Thermally driven migration of ice-stream shear margins. *J. Fluid Mech.* **712**, 552–578 (2012). doi:10.1017/jfm.2012.438

39. M. Haseloff, C. Schoof, O. Gagliardini, The role of subtemperate slip in thermally driven ice stream margin migration. *Cryosphere* **12**, 2545–2568 (2018). doi:10.5194/tc-12-2545-2018

40. I. Tabone, A. Robinson, M. Montoya, J. Alvarez-Solas, Holocene thinning in central Greenland controlled by the Northeast Greenland Ice Stream. *Nat. Commun.* **15**, 6434 (2024). doi:10.1038/s41467-024-50772-5

41. M. Jackson, B. Kamb, The marginal shear stress of Ice Stream B, West Antarctica. *J. Glaciol.* **43**, 415–426 (1997). doi:10.3189/S0022143000035000

42. Y. Axford, A. de Vernal, E. C. Osterberg, Past warmth and its impacts during the Holocene thermal maximum in Greenland. *Annu. Rev. Earth Planet. Sci.* **49**, 279–307 (2021). doi:10.1146/annurev-earth-081420-063858

43. O. L. E. Bennike, A. Weidick, Late Quaternary history around Nioghalvfjerdsfjorden and Jøkelbugten, North-East Greenland. *Boreas* **30**, 205–227 (2001). doi: 10.1111/j.1502-3885.2001.tb01223.x

44. G. H. Miller, J. Brigham-Grette, R. B. Alley, L. Anderson, H. A. Bauch, M. S. V. Douglas, M. E. Edwards, S. A. Elias, B. P. Finney, J. J. Fitzpatrick, S. V. Funder, T. D. Herbert, L. D. Hinzman, D. S. Kaufman, G. M. MacDonald, L. Polyak, A. Robock, M. C. Serreze, J. P. Smol, R. Spielhagen, J. W. C. White, A. P. Wolfe, E. W. Wolff, Temperature and precipitation history of the Arctic. *Quat. Sci. Rev.* **29**, 1679–1715 (2010). doi:10.1016/j.quascirev.2010.03.001

45. L. Moresi, F. Dufour, H. B. Mühlhaus, A Lagrangian integration point finite element method for large deformation modeling of viscoelastic geomaterials. *J. Comput. Phys*. **184**, 476–497 (2003). doi:10.1016/S0021-9991(02)00031-1

46. L. Moresi, H. B. Mühlhaus, Anisotropic viscous models of large-deformation Mohr–Coulomb failure. *Phil. Mag.* **86**, 3287–3305 (2006). doi:10.1016/S0021-9991(02)00031-1

47. W. Sharples, L. N. Moresi, M. Velic, M. A. Jadamec, D. A. May, Simulating faults and plate boundaries with a transversely isotropic plasticity model. *Phys. Earth Planet. Inter.* **252**, 77–90 (2016). doi:10.1016/j.pepi.2015.11.007

48. F. Pattyn, L. Perichon, A. Aschwanden, B. Breuer, B. de Smedt, O. Gagliardini, G.H. Gudmundsson, R.C. Hindmarsh, A. Hubbard, J.V. Johnson, T. Kleiner, Y. Konovalov, C. Martin, A. J. Payne, D. Pollard, S. Price, M. Rückamp, F. Saito, O. Souček, S. Sugiyama, T. Zwinger, Benchmark experiments for higher-order and full-Stokes ice sheet models (ISMIP–HOM). *Cryosphere* **2**, 95–108 (2008). doi:10.5194/tc-2-95-2008

49. I. Rogozhina, Z. Martinec, J. M. Hagedoorn, M. Thomas, K. Fleming, On the long-term memory of the Greenland Ice Sheet. *J. Geophys. Res. Earth Surf.* **116**, F01011 (2011). doi:10.1029/2010JF001787

50. G. D. Q. Robin, Ice movement and temperature distribution in glaciers and ice sheets. *J. Glaciol.* **2**, 523–532 (1955). doi:10.3189/002214355793702028

51. B. H. Hills, J. T. Harper, N. F. Humphrey, T. W. Meierbachtol, Measured horizontal temperature gradients constrain heat transfer mechanisms in Greenland ice. *Geophys. Res. Lett.* **44**, 9778–9785 (2017). doi:10.1002/2017GL074917

52. G. M. Marion, S. D. Jakubowski, The compressibility of ice to 2.0 kbar. *Cold Reg. Sci. Technol.* **38**, 211–218 (2004). doi:10.1016/j.coldregions.2003.10.008

53. J. W. Glen, The creep of polycrystalline ice. *Proc. R. Soc. Lond. A* **228**, 519–538 (1955). doi:10.1098/rspa.1955.0066

54. D. L. Goldsby, D. L. Kohlstedt, Superplastic deformation of ice: Experimental observations. *J. Geophys. Res. Solid Earth* **106**, 11017–11030 (2001). doi:10.1029/2000JB900336

55. E. J. N. Kuiper, J. H. de Bresser, M. R. Drury, J. Eichler, G. M. Pennock, I. Weikusat, Using a composite flow law to model deformation in the NEEM deep ice core, Greenland–Part 2: The role of grain size and premelting on ice deformation at high homologous temperature. *Cryosphere* **14**, 2449–2467 (2020). doi:10.5194/tc-14-2449-2020

56. P. D. Bons, T. Kleiner, M. G. Llorens, D. J. Prior, T. Sachau, I. Weikusat, D. Jansen, Greenland Ice Sheet: Higher nonlinearity of ice flow significantly reduces estimated basal motion. *Geophys. Res. Lett.* **45**, 6542–6548 (2018). doi:10.1029/2018GL078356

57. M. Ranganathan, B. Minchew, A modified viscous flow law for natural glacier ice: Scaling from laboratories to ice sheets. *Proc. Natl. Acad. Sci.* **121**, e2309788121 (2024). doi:10.1073/pnas.2309788121

58. D. H. Richards, S. S. Pegler, S. Piazolo, O. G. Harlen, The evolution of ice fabrics: A continuum modelling approach validated against laboratory experiments. *Earth Planet. Sci. Lett.* **556**, 116718 (2021). doi:10.1016/j.epsl.2020.116718

59. F. Gillet-Chaulet, O. Gagliardini, J. Meyssonnier, M. Montagnat, O. Castelnau, A user-friendly anisotropic flow law for ice-sheet modeling. *J. Glaciol.* **51**, 3–14 (2005). doi:10.3189/172756505781829584

60. C. Martín, G. H. Gudmundsson, H. D. Pritchard, O. Gagliardini, On the effects of anisotropic rheology on ice flow, internal structure, and the age-depth relationship at ice divides. *J. Geophys. Res. Earth Surf.* **114**, F04001 (2009). doi:10.1029/2008JF001204

61. P. Pimienta, P. Duval, V. Y. Lipenkov, "Mechanical behavior of anisotropic polar ice" in *The Physical Basis Of Ice Sheet Modeling (Proceedings Of The Vancouver Symposium, August 1987)* (IAHS Publication, 1987), pp. 57–66.

62. E. W. Burgess, R. R. Forster, J. E. Box, E. Mosley-Thompson, D. H. Bromwich, R. C. Bales, L. C. Smith, A spatially calibrated model of annual accumulation rate on the Greenland Ice Sheet (1958–2007). *J. Geophys. Res.* **115**, F02004 (2010). doi:10.1029/2009JF001293

63. J. A. MacGregor, M. A. Fahnestock, G. A. Catania, A. Aschwanden, G. D. Clow, W. T. Colgan, S. P. Gogineni, M. Morlighem, S. M. Nowicki, J. D. Paden, S. F. Price, H. Seroussi, A synthesis of the basal thermal state of the Greenland Ice Sheet. J. Geophys. Res. Earth Surf. 121, 1328–1350 (2016). doi:10.1002/2015JF003803

64. C. S. Hvidberg, A. Grinsted, D. Dahl-Jensen, S. A. Khan, A. Kusk, J. K. Andersen, N. Neckel, A. Solgaard, N. B. Karlsson, H. A. Kjær, P. Vallelonga, Surface velocity of the Northeast Greenland Ice Stream (NEGIS): assessment of interior velocities derived from satellite data by GPS. *Cryosphere* **14**, 3487–3502 (2020). doi:10.5194/tc-14-3487-2020

65. N. Holschuh, D. A. Lilien, K. Christianson, Thermal weakening, convergent flow, and vertical heat transport in the Northeast Greenland Ice Stream shear margins. *Geophys. Res. Lett.* **46**, 8184–8193 (2019). doi:10.1029/2019GL083436

66. P. Hunter, C. Meyer, B. Minchew, M. Haseloff, A. Rempel, Thermal controls on ice stream shear margins. *J. Glaciol.* **67**, 435–449 (2021). doi:10.1017/jog.2020.118

67. T. Perol, J. R. Rice, J. D. Platt, J. Suckale, Subglacial hydrology and ice stream margin locations. *J. Geophys. Res. Earth Surf.* **120**, 1352–1368 (2015). doi:10.1002/2015JF003542

68. B. A. Keisling, K. Christianson, R. B. Alley, L. E. Peters, J. E. Christian, S. Anandakrishnan, K. L. Riverman, A. Muto, R. W. Jacobel, Basal conditions and ice dynamics inferred from radar-derived internal stratigraphy of the northeast Greenland ice stream. *Ann. Glaciol.* **55**, 127–137 (2014). doi:10.3189/2014AoG67A090

69. M. A. Fahnestock, I. Joughin, T. A. Scambos, R. Kwok, W. B. Krabill, S. Gogineni, Ice-stream-related patterns of ice flow in the interior of northeast Greenland. *J. Geophys. Res. Atmos.* **106**, 34035–34045 (2001). doi:10.1029/2001JD900194

70. C. F. Raymond, Deformation in the vicinity of ice divides. *J. Glaciol.* **29**, 357–373 (1983). doi:10.3189/S0022143000030288

71. K. E. Alley, T. A. Scambos, R. B. Alley, N. Holschuh, Troughs developed in ice-stream shear margins precondition ice shelves for ocean-driven breakup. *Sci. Adv.* **5**, eaax2215 (2019). doi:10.1126/sciadv.aax2215

72. A. Grinsted, C. S. Hvidberg, D. A. Lilien, N. M. Rathmann, N. B. Karlsson, T. Gerber, H. A. Kjær, P. Vallelonga, D. Dahl-Jensen, Accelerating ice flow at the onset of the Northeast Greenland Ice Stream. *Nat. Commun.* **13**, 5589 (2022). doi:10.1038/s41467-022-32999-2

## Acknowledgments

This work used resources of the Deutsches Klimarechenzentrum (DKRZ)

granted by its Scientific Steering Committee (WLA) under project ID bb1405.

Funding:

China Scholarship Council grant 202006010063 (YZ)
German Research Foundation grant 506043073 (SF)

## Author contributions

Conceptualization: YZ, PDB
Methodology: YZ, TS, HY, DL
Investigation: YZ, DL, TS, YH, SF, DJ
Visualization: YZ, SF
Funding acquisition: YZ, SF
Project administration: YZ
Supervision: PDB, IW
Writing – original draft: YZ
Writing – review & editing: All authors

## Data and materials availability

Underworld is fully open-source and the version (v2.15.1b) used for this paper is available through Beucher et al. (2024) https://doi.org/10.5281/zenodo.10976370. Our code files for all the models are available through Zenodo https://doi.org/10.5281/zenodo.13925401.

## Supplementary Materials

**Including:**

Materials and Methods

Supplementary Text

Figs. S1 to S23

Tables S1 to S2

Movies S1 to S4

### Materials and Methods

Underworld2

We used the full-Stokes software "Underworld2" (*27*) for the numerical modeling in this study. Underworld2 uses the material point method (MPM), which is related to the better-known particle-in-cell method (*45*). MPM uses a Eulerian finite-element mesh to calculate the incremental development of the velocity field and other field variables, such as temperature and pressure, while Lagrangian material points ("particles") carry the density, viscosity, lattice orientation, and other relevant local material parameters. Underworld2 is already well established with a full-Stokes solution for isotropic and anisotropic elasto–visco–plastic materials in complex geodynamic modeling (*46*, *47*). The software has also passed the usual benchmark tests (*48*) for full-Stokes ice sheet models (*28*), and has been used for the three-dimensional, large-scale modeling of anisotropy-induced folding in ice sheets (*29*). Some of the specific advantages of Underworld2 for our case are that (i) detailed tracking of the internal stress and strain history is possible, (ii) it facilitates the recalculation and tracking of other important local properties such as fabric orientation, and (iii) local fabric evolution can be coupled to the local rheological anisotropy.

Model physics

Temperature

Due to the geothermal heat flux (or strain heating) (*49*), ice temperature increases with depth in ice sheets (*50*, *51*). In our model, the initial temperature ($T$, °C) is –30 °C ($T_0$) for upper "cold ice". Below a height $h_{warmice}$, in what we term “warm ice”, temperature increases with a parabolic equation to –3 °C ($T_{bed}$) at the base (fig. S2A):

$$T = T_{bed} + (T_0 - T_{bed})\left(\frac{y}{h_{warmice}}\right)^m \quad (1)$$

where $y$ is the height in warm ice, and the exponent $m$ is set at 1.2 instead (*29*).

Density

Ice density ($\rho$, $\mathrm{kg/m^3}$) is given as a function of temperature ($T$, °C) by:

$$\rho = \frac{1.802\times10^4}{19.30447 - 7.988471\times10^{-4}\cdot(T+273) + 7.563261\times10^{-6}\cdot(T+273)^2}. \quad (2)$$

Eq. 2 is derived from the molar volume equation for pure ice at 1 atm (*52*), where the molar mass of $H_2O$ is assumed to be $1.802 \times 10^4$ kg/mol. The density gradient (fig. S2B) is from 917.51 $\mathrm{kg/m^3}$ (–3 °C) to 921.41 $\mathrm{kg/m^3}$ (–30 °C).

Power-law viscosity

Ice in the interior of ice sheets is generally assumed to flow as a non-linear, power-law viscous material, due to deformation by dislocation creep (*16*, *53*). Here we used the dislocation creep component of the composite flow law of Goldsby and Kohlstedt (*54*). The flow law has two parameterizations, one for high and one for low temperature, and the parameters used are those modified by Kuiper (*55*) to ensure no discontinuity at the transition temperature (–11 °C). The strain rate ($\dot{\varepsilon}_{i,j}$) is proportional to the deviatoric stress ($\tau_{ij}$) to the power $n$:

$$\dot{\varepsilon}_{i,j} = A_0 \mathrm{e}^{\frac{-Q}{R(T+273)}} {\tau_{II}}^{\mathrm{n}-1} \tau_{ij} \quad (3)$$

where $A_0$ is the material parameter, $Q$ the activation energy, $R$ the gas constant and $\tau_{II}$ the second invariant of the deviatoric stress tensor $\tau_{ij}$. The power-law viscosity of ice (general viscosity $\eta_1$, Pa · s) is then derived from temperature ($T$, °C) and strain rate ($\dot{\varepsilon}_{i,j}$, $\mathrm{yr}^{-1}$) (*28*)

$$\eta_1 = \frac{1}{2}\left(A_0 \mathrm{e}^{\frac{-Q}{R(T+273)}}\right)^{\frac{-1}{n}} \cdot \dot{\varepsilon}_{II}^{\frac{1-n}{n}} \quad 4$$

where $\dot{\varepsilon}_{II}$ is the second invariant of the strain rate tensor. Note the unit conversion of stress and time. The stress exponent was set to $n = 4$ based on experimental results (*54*) and studies on both the Greenland and Antarctic ice sheets (*56*, *57*).

Anisotropy

The c-axis orientation of the ice crystal is stored for each particle in Underworld2. It is represented as a dimensionless unit vector ($c_x$, $c_y$, $c_z$). In our model, the initial c-axis directions of ice particles are perpendicular to the local layer orientation with a Gaussian random distribution with a standard deviation of $\pm 5°$ (fig. S2, C and D). The c-axes rotate in the flow field according to the symmetric deformation-rate tensor $D$ and the skew-symmetric rotation-rate tensor $W$

$$D = \frac{1}{2}(L + L^{\mathrm{T}}) \quad 5$$

$$W = \frac{1}{2}(L - L^{\mathrm{T}}) \quad 6$$

where $L$ is the velocity gradient tensor (see detailed c-axis rotation equations in Appendix B in *47*). Note that this routine does not include other processes, such as recrystallization, that may affect c-axis orientations (*20*, *21*, *58*).

The anisotropy of the ice crystal is modeled as transverse isotropy, which is a common practice in numerical modeling (*59*, *60*). Transverse isotropic viscosity is defined by two viscosity values: a general viscosity $\eta_1$ (Pa · s) and a second viscosity $\eta_2$ (Pa · s). $\eta_1$ is set proportional to $\eta_2$:

$$\eta_1 = k\eta_2 \quad 7$$

where $k$ represents the rheological anisotropy parameter. The general viscosity $\eta_1$ represents the maximum value for shortening or stretching parallel to the c-axis maximum, and the second viscosity $\eta_2$ is the minimum value for shearing along the plane perpendicular to the c-axis maximum (crystallographic basal plane). As shown in experiments (*17*, *61*), the stress required for non-basal-plane deformation of ice monocrystals is at least 60 times to max 100 times higher than for basal-plane slip (perpendicular to the c-axis direction), while for macroscopic ice polycrystals the ratio is about ten (*16*). The measured ice fabric in an ice stream also shows a strong directional contrast in mechanical properties that can result in shearing 9.1 times more easily along the ice flow direction than across flow (*23*). For our macroscopic ice model, we therefore use $k = 10$ as the standard anisotropy parameter and also a higher $k = 100$ for comparison.

To avoid extreme viscosity values due to boundary effects, we set a maximum limit $1.0 \times 10^{16}$ Pa · s for the general viscosity $\eta_1$ and a minimum limit $1.0 \times 10^{13}$ Pa · s (*29*). The resulting minimum second viscosity $\eta_2$ would be $1.0 \times 10^{12}$ Pa · s when $k$ is 10 (or $1.0 \times 10^{11}$ Pa · s, $k = 100$). The average bedrock-parallel shear rate (surface velocity/ice thickness) in most of the N Greenland ice sheet is $<10^{-8}$ s$^{-1}$. Allowing for a ten times higher shear-strain rate at the base of the ice sheet, our set viscosity range should apply to shear rates $<10^{-7}$ s$^{-1}$. For this strain rate, Eq. 4 gives viscosity values of $3.06 \times 10^{12}$ Pa · s at –3 °C to $9.2 \times 10^{12}$ Pa · s at –30 °C. This means our minimum viscosity bounds are not reached under normal conditions, but may be reached at model singularities, such as the edge of the outflow gate.

Model design

The basic model setup is shown in figs. S1 and S2, and detailed parameters are listed in table S1. The horizontal $x$-axis and $y$-axis represent the width and length of the model respectively ($40 \times 50$ km), while the $z$-axis is the elevation (3000 m). The model consists of an air layer (initially 500 m) and an ice layer (initially 2500 m) with 10 internal marker horizons associated with ice temperature gradient. In one $x$-wall ($y = 0$ km) there is a 'gate' with a width of 10 km ($-5 \leq x \leq 5$ km) for the outflow ($v_y = 100$ m/yr), while the opposite $x$-wall ($y = 50$ km) represents the inland ice divide with a zero ice flux across it. To compensate the outflow and maintain a constant ice volume, there is low-velocity inflow ($v_{x1}$ & $v_{x2}$) from the two $y$-

walls ($x$ = -20 km & 20 km) and precipitation on the ice surface (surface accumulation rate $v_{pr}$ = 0.15 m/yr) (*62*).

Overview of model grouping

Seven models are compared here to explore the effect of various boundary conditions and anisotropy (table S2): (1) no-slip bottom boundary for Models 1–3 and free-slip bottom boundary for Models 4–7; (2) symmetric inflow for Models 1, 4, 6 and 7, and asymmetric inflow for Models 2, 3 and 5; (3) anisotropy parameter $k$ = 10 for Models 1, 2, 4 and 5, and $k$ = 100 for Models 3 and 6. Model 7 is the isotropic model. Velocities for symmetric inflow are both 8.8 m/yr. Velocities for asymmetric inflow are 11.734 m/yr (left $y$-wall) and 5.867 m/yr (right $y$-wall). It should be noted that, in no-slip models, the velocity field applied on the model boundary for the outflow (& inflow) is where $z > 0$ but not $z \geq 0$ to keep the outflow (& inflow) velocity 0 on the ice-bed interface, and there is a velocity change in the basal ice unit near the boundary, which can keep basal ice particles more stable near the boundary.

**Supplementary Text**

Results of free-slip models

Several studies suggested that the basal ice at NEGIS and its surroundings is not frozen to the bedrock, but sliding due to the presence of meltwater and/or subglacial till (*12*, *13*, *63*). As a basal friction law is not implemented in our Underworld2-model, we tested the effect of a free-slipping ice-bedrock interface. Keeping all other settings the same as in no-slip Models 1 and 2, we observe the formation of a single ice stream that extends to the divide (Model 4, fig. S18; Model 5, fig. S19). No branching occurs and the ice stream develops a bottleneck shape. Without basal friction, lateral stresses can be transferred over long distances, allowing a single, wide ice stream to develop. This shows that the limited lateral stress transfer with basal friction or a frozen bedrock constrains the width and branching of the developing ice stream.

We compare free-slip models of variable anisotropy parameters ($k$) as well, since the anisotropy effect can be better observed when bedrock constraint is not playing a role.

Compared with Model 4 ($k$ = 10), Model 6 ($k$ = 100) shows a faster ice-stream evolution process with stronger shear margins (fig. S20–S22). However, in the isotropic Model 7, there is no ice-stream formation on the slippery bed (fig. S23).

Scale and limitation of our model results

The drainage basin of the Northeast Greenland Ice Stream (NEGIS) is about 16% of the total area of the Greenland Ice Sheet (*64*). NEGIS extends over 500 km from three main outlet glaciers: Nioghalvfjerdsfjorden Glacier (NG), Zachariae Isstrøm (ZI), and Storstrømmen Glacier (SG), and to its onset near the ice divide in the interior of northern Greenland (Fig. 1). To be approximately the same scale as the flow area of NEGIS, the horizontal model size was originally designed as 400 × 500 km with the outflow gate of a total 100 km, and the inflow flux represents ice from the model's outside area which can be regarded as an extension of our model width. If the inflow ($v_x$) is 8.8 m/yr with an ice thickness ($h_{ice}$) of 2500 m, the extra model width ($x_{ex}$) would be equal to 146.67 km where the losing ice is compensated by ice precipitation ($v_{pr}$) of 0.15 m/yr ($v_x\, h_{ice} = v_{pr}\, x_{ex}$). For the asymmetric inflow of 11.734 m/yr and 5.867 m/yr, the extra widths would be equal to 195.57 km and 97.78 km separately. The total width of our modeling area would then be approximately 700 km.

To maximize the model resolution and accuracy of the anisotropy code (*28*, *29*), we scale down the horizontal model size but also the outflow gate size by a factor of ten. Meanwhile, we define a low outflow velocity 100 m/yr. Considering the ice thickness of 2500 m in our model, the ice mass loss through per km gate can be comparable to around 250-m-height ice with a higher velocity of 1000 m/yr at the NEGIS front (*8*, *64*). However, the real velocities at the NEGIS front are variable through space and time and can reach up to more than 1000 m/yr (*6*). A higher ratio of velocity and ice thickness would cause a higher vertical stretching rate and a lower effective viscosity. This means our ice viscosities near the ice front or downstream are possibly higher than reality (*29*).

Shear heating would also cause ice softness in shear margins and the basal ice (*34*, *65*, *66*), which we do not include in our model. According to Eq. 4, ice viscosity is, for example, 3 times lower when ice temperature increases from –30 °C to –3 °C, while ice viscosity can be up to 10 times lower when the anisotropy parameter increases from $k$ = 10 (standard anisotropy model) to $k$ = 100 (exaggerated anisotropy model). In the NEGIS shear margins,

temperature anomalies are suggested to be only around 2 °C to 6 °C (*25*, *65*). Thus our exaggerated anisotropy models ($k$ = 100) can well indicate the evolution of an ice stream with possibly lower ice viscosities in shear margins. As for basal melting, we show model cases of free-slip bottom boundary, but the modeled free slip cannot yet equal meltwater channeling with variable basal frictions underneath an ice stream (*13*, *67*).

Combining the above-mentioned factors, we propose the real NEGIS may have a faster evolution process than our standard model (no slip; $k$ = 10). However, the time scale of our modeling is still in a reasonable range (figs. S7 and S8), which conforms to the previous study of fold observation in radargrams and strain analysis that shear margins in the upper NEGIS were fully developed ca. 2000 years ago (*37*). In addition, compared with exaggerated anisotropy models ($k$ = 100; figs. S13 and S20) and free-slip models (figs. S18–S20), the ice-stream formation processes do not show thousands of years of differences, which means influences from small viscosity changes and a general bedrock slip are limited on the time scale of ice stream formation.

We also need to point out a boundary effect when shear margins develop close to $y$-walls in no-slip models (figs. S4, S8 and S14). C-axes of particles that enter the model to simulate influx have, on average, the same orientation as the particles at the local boundary. When the shearing has rotated the CPO at the boundary, the c-axes of newly introduced ice particles will mimic this CPO, which can make the outer shear margin easier to migrate but not localize individually. In free-slip models, shear margins experience less boundary effect since the ice stream develops in the center of the model. The dominant shear margin can be observed on each side of the ice stream (figs. S18–S20), with a clear c-axis orientation difference compared to surrounding areas (figs. S22).

Our modeling mainly aims to investigate the effect of ice anisotropy, with the hypothesis that this is the main factor that governs the formation and evolution of ice streams in general. Modeling the evolution of a specific ice stream is complicated and may require more work in the future, considering variable ice mass loss and surface accumulation through time and space, shear heating and basal melting, as well as improving model size, resolution and boundary effects.

| Parameter | Value | Unit |
|---|---|---|
| Model size ($x$, $y$, $z$) | 40000, 50000, 3000 | m |
| Model element numbers | 128, 32, 16 | |
| Particle numbers of each element | $\geq 30$ | |
| Thickness air | 500 | m |
| Thickness ice (cold ice & warm ice) | 2500 (1667+833) | m |
| gate width | 10000 | m |
| Velocity outflow ($v_y$) | 100 | m/yr |
| Velocity symmetric inflow ($v_x$) | 8.8 | m/yr |
| Velocity asymmetric inflow ($v_x$) | 11.734; 5.867 | m/yr |
| surface accumulation rate ($v_{pr}$) | 0.15 | m/yr |
| Temperature ice ($T_{bed}$; $T_0$) | $-30$ to $-3$ | ℃ |
| Density ice ($\rho$) | 917.51 to 921.41 | $\mathrm{kg/m^3}$ |
| Viscosity air | $1.0 \times 10^{10}$ (or $1.0 \times 10^{9}$ depending on min ice viscosity) | $\mathrm{Pa \cdot s}$ |
| $A_0$ ($T < -11$℃) | $5.0 \times 10^{5}$ | $\mathrm{MPa^{-4.0}s^{-1}}$ |
| $A_0$ ($T > -11$℃) | $6.96 \times 10^{23}$ | $\mathrm{MPa^{-4.0}s^{-1}}$ |
| $Q$ ($T < -11$℃) | 64 | kJ/mol |
| $Q$ ($T > -11$℃) | 155 | kJ/mol |
| $R$ | 0.008314 | $\mathrm{J \cdot mol^{-1}K^{-1}}$ |
| Stress exponent $n$ | 4.0 | |
| Anisotropy parameter $k$ | 10; 100 | |

Table S1. Basic model set-up parameters and their values. The flow law parameters $A_0$ and $Q$ and the transition temperature (–11 ℃) refer to the dislocation-creep regime in Table 3 of Kuiper (*55*) which is modified after Goldsby and Kohlstedt (*54*).

| No. | Bed condition | Anisotropy parameter ($k$) | Inflow | Result for each model | Figure & movie lists |
|---|---|---|---|---|---|
| Model 1 | No-slip | 10 | Symmetric | Tributary ice stream | figs. S3–S6; Movie S1 |
| Model 2 | No-slip | 10 | Asymmetric | Ice stream dominant in one direction (NEGIS-type) | figs. S7–S12; Figs. 3–4; Movie S2 |
| Model 3 | No-slip | 100 | Asymmetric | Ice stream dominant in one direction (NEGIS-type); faster and stronger compared to Model 2 | figs. S13–S17; Movie S3 |
| Model 4 | Free-slip | 10 | Symmetric | Single ice stream perpendicular to the outlet | fig. S18 |
| Model 5 | Free-slip | 10 | Asymmetric | Single ice stream perpendicular to the outlet | fig. S19 |
| Model 6 | Free-slip | 100 | Symmetric | Single ice stream perpendicular to the outlet; faster and stronger compared to Model 4 | figs. S20–S22; Movie S4 |
| Model 7 | Free-slip | Isotropy | Symmetric | No ice stream formation | fig. S23 |

Table S2. Summary and comparison of all models.

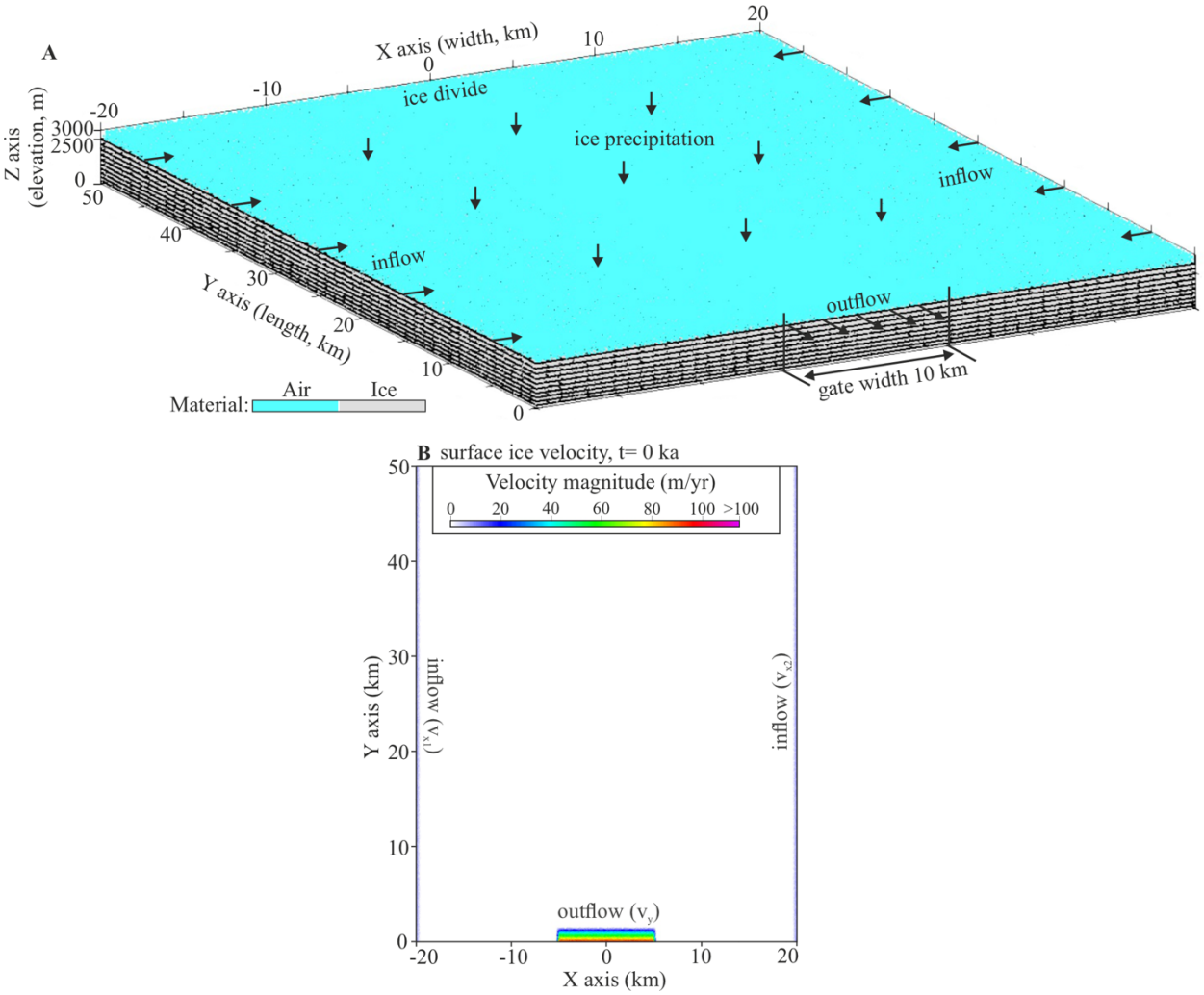


Fig. S1. Model design. (A) 3D view of an initial model at $t$ = 0 ka. An outflow in the $y$-direction through the outlet at $x$-wall ($y$ = 0 km) with a gate width of 10 km ($\mathbf{-5 \leq x \leq 5}$ km). Ice precipitation on the ice surface and lateral inflow from $y$-walls ($x$ = –20 & 20 km) to compensate for the outflow. Ice divide is the 0-velocity $x$-wall ($y$ = 50 km). (B) Surface ice velocity map at $t$ = 0 ka (example from Model 1 with symmetric inflow).

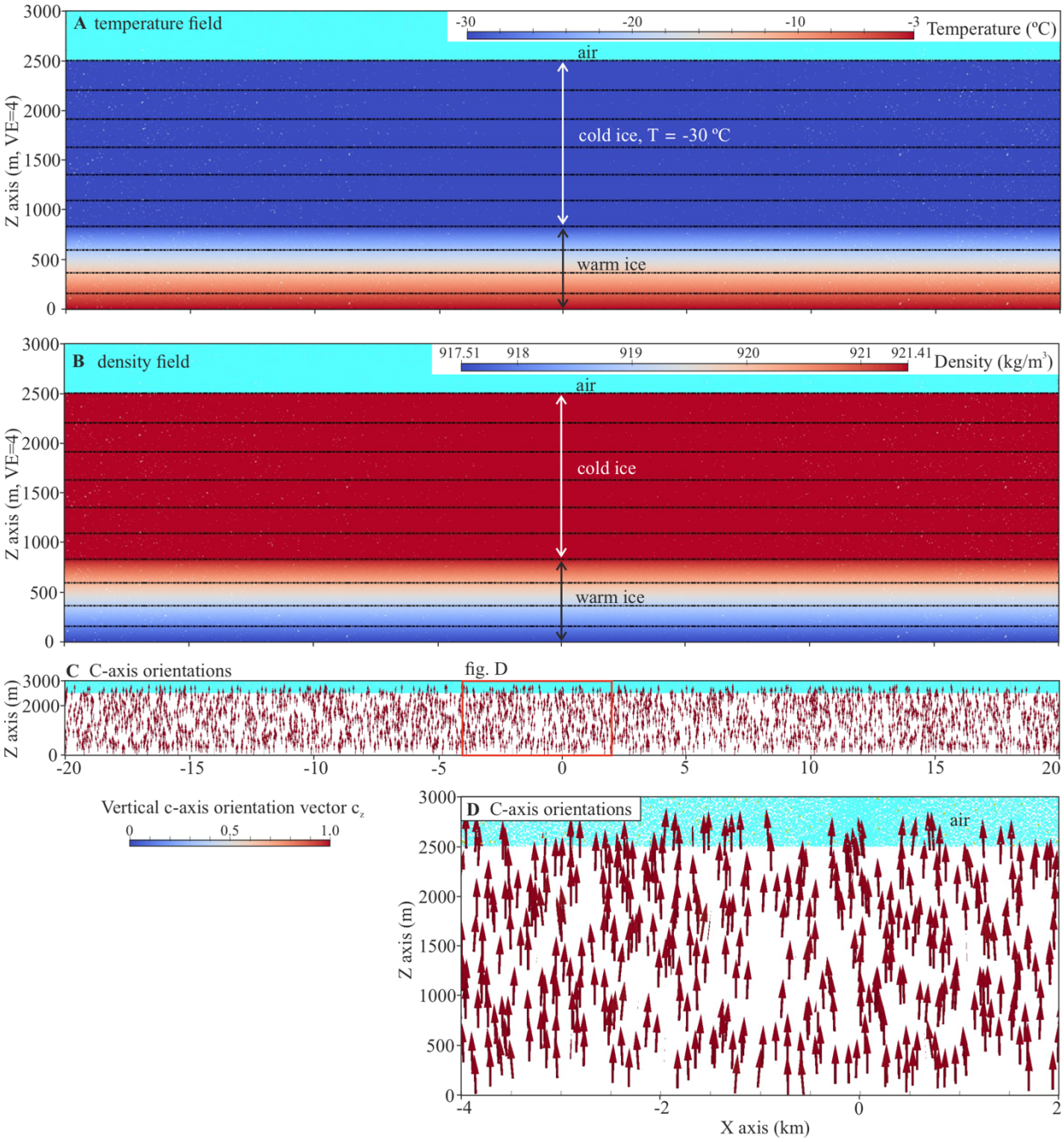


Fig. S2. Initial physical settings. (A) Vertical temperature field from –3 °C ($T_{bed}$) to –30 °C ($T_0$) at $z$ > 833 m. (B) Ice density field with a vertical gradient from 917.51 kg/m$^3$ (–3 °C) to 921.41 kg/m$^3$ (–30 °C). Note the vertical exaggeration (4×) in the temperature and density profiles. (C–D) C-axis orientations (arrows) of ice particles. Arrow colors represent vertical vectors, with deep red being vertical (1.0).

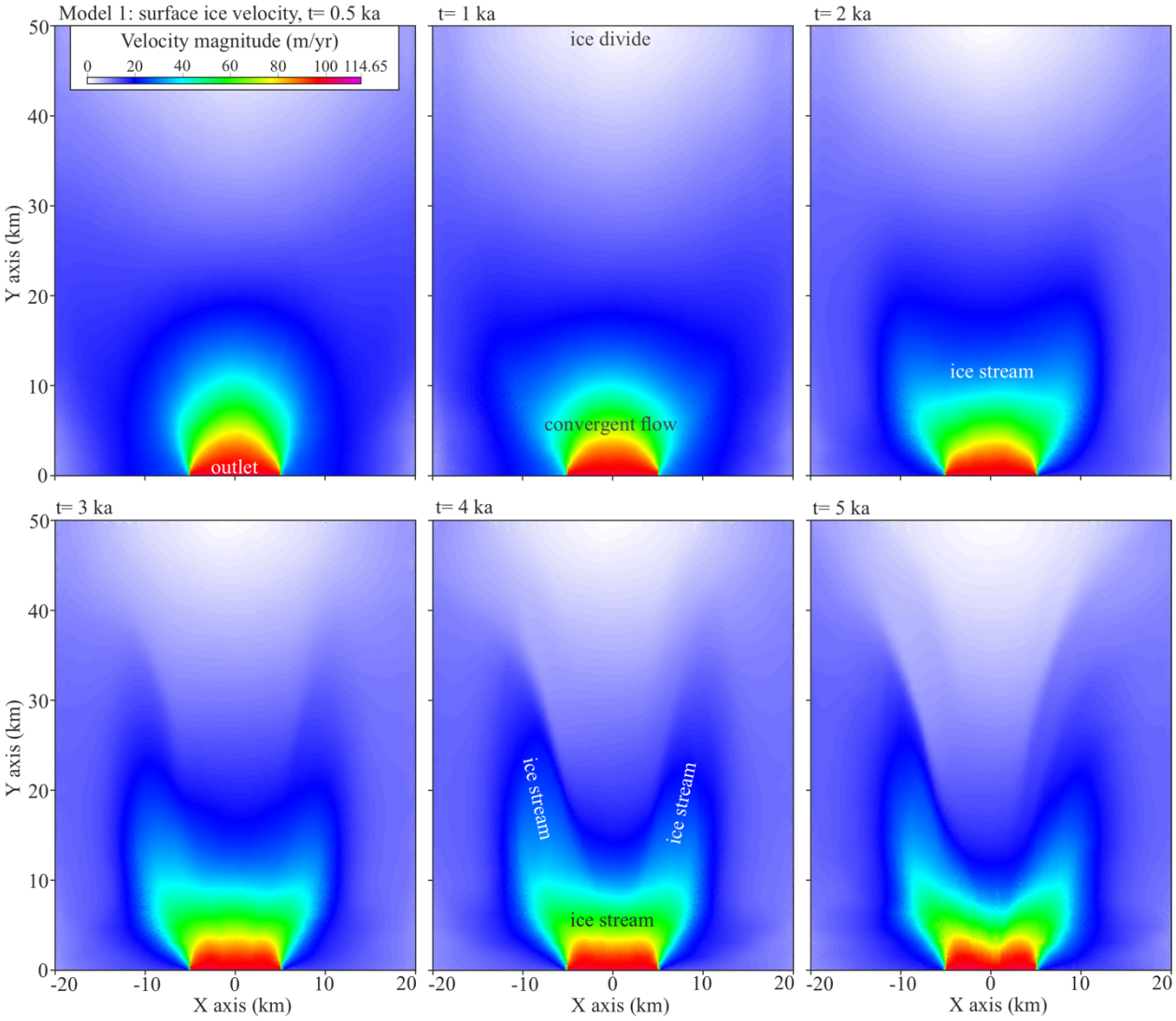


Fig. S3. Evolution of surface ice velocities in Model 1 (no slip; symmetric inflow; anisotropy k = 10) from 500 to 5000 years. At the beginning, there is a convergent flow around the narrow outlet and ice velocities gradually decrease in surrounding ice. Between 1000 and 2000 years, the area of the fast ice flow narrows and develops a larger velocity difference with surrounding ice and forms the proto ice stream. From 2000 to 4000 years, the ice stream grows inland by two tributaries and gradually shows a clear velocity difference with surrounding ice. At 5000 years, the ice stream continues to change its shape and position slightly. Both tributaries become narrower and more oblique to the outlet.

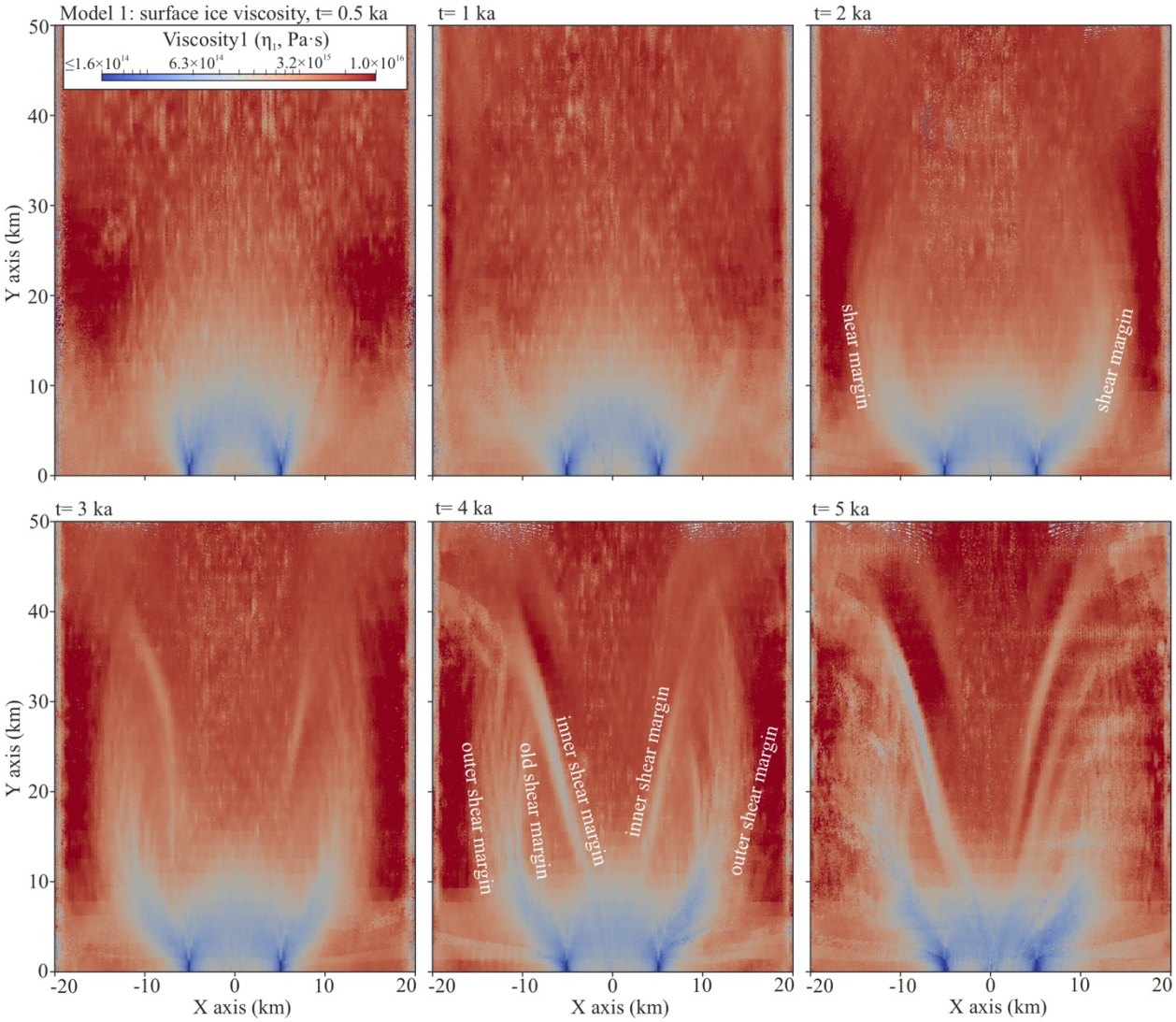


Fig. S4. Evolution of general viscosities $\eta_1$ from the ice surface in Model 1 from 500 to 5000 years. Between 1000 and 2000 years, two shear zones (low viscosity area) develop in the convergent flow and become the shear margins of the proto ice stream. At 3000 years, the original shear margins grow inland, accompanied by inner shear margins established to form the tributaries of the ice stream. At 4000 years, shear margins of ice stream's tributaries are distinct. Shear margin migrations can be observed towards y-walls (x = –20 & 20 km). Shear margins of the two tributaries are near-symmetric but not identical due to the initial noises in c-axis orientations (fig. S2C).

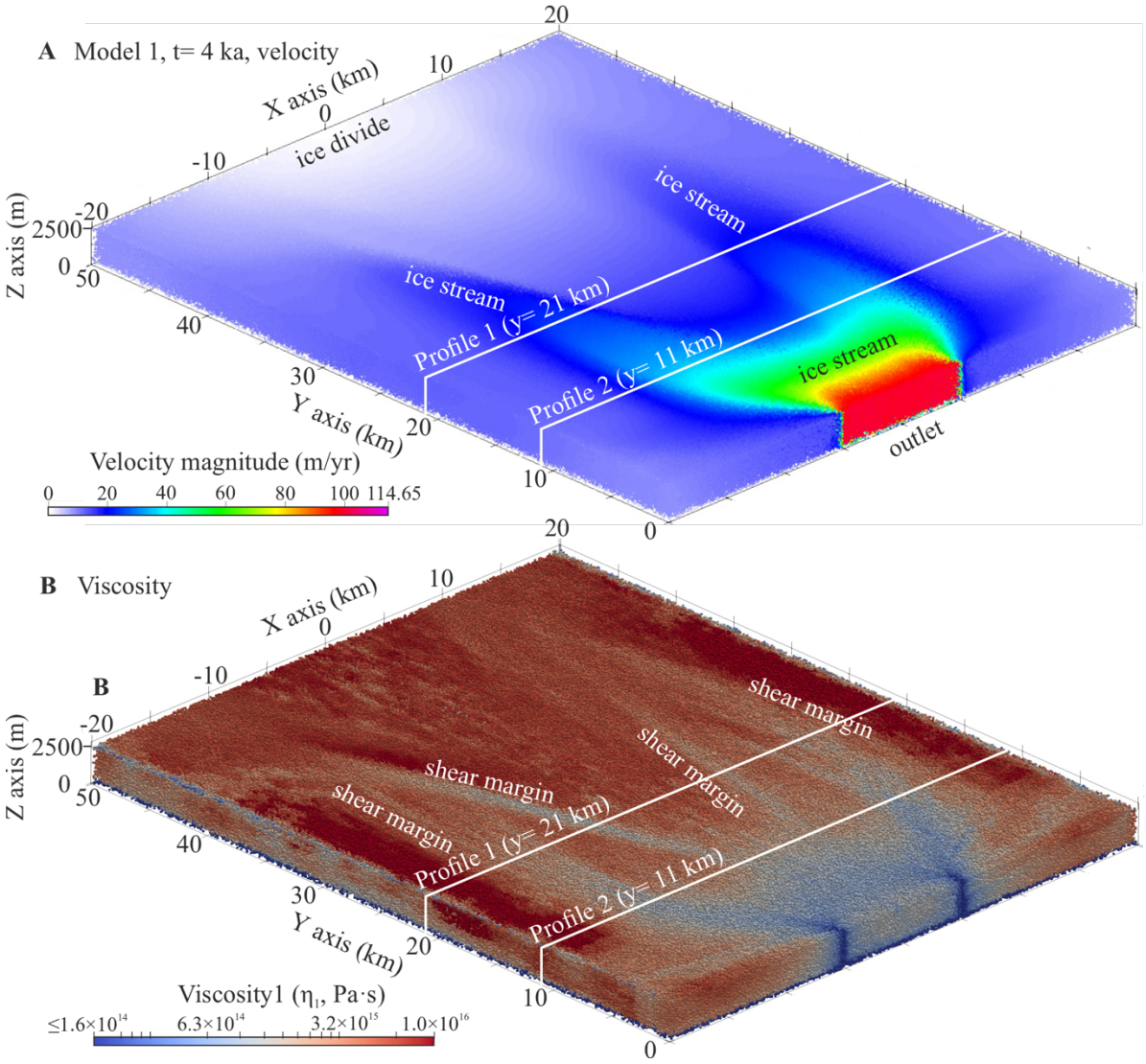


Fig. S5. 3D views of the tributary-type ice stream in Model 1 at 4000 years. (A) Ice velocities. (B) Ice general viscosities $\eta_1$.

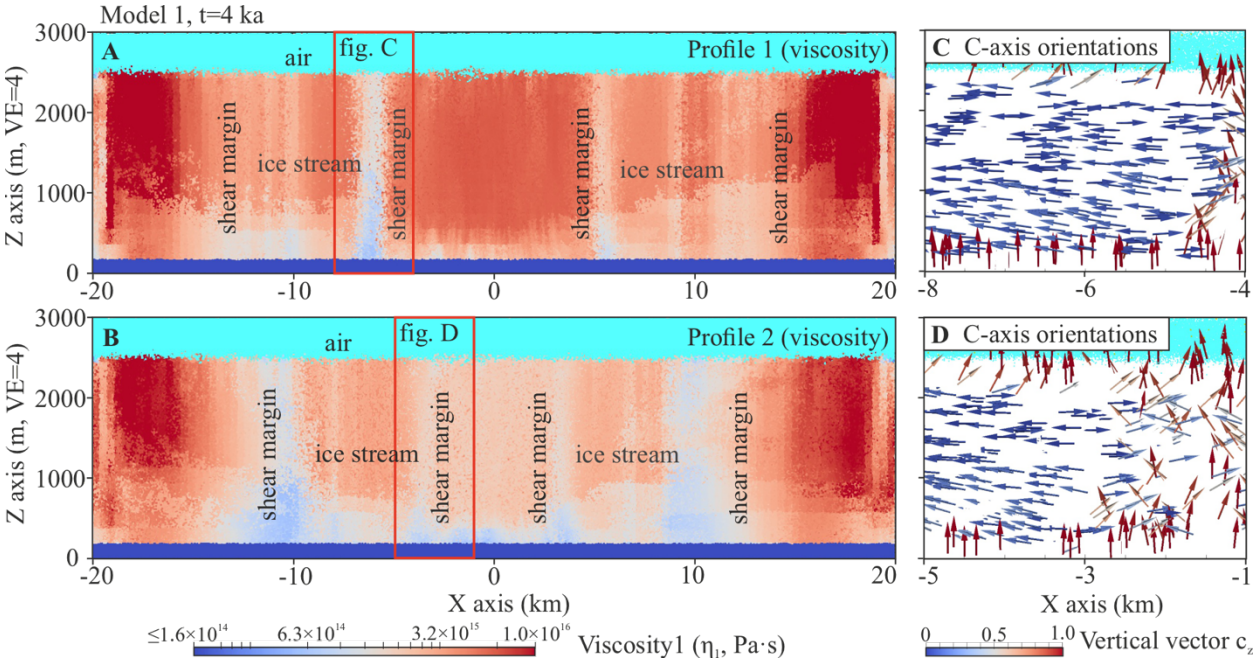


Fig. S6. Profile snapshots of the tributary-type ice stream in Model 1 at 4000 years. (A–B) Ice general viscosities $\eta_1$ on Profile 1 (A) and Profile 2 (B) transverse the ice stream (profile locations in fig. S5). Note the vertical exaggeration (4×) in the profiles. (C–D) C-axis orientations (arrows) of ice particles at the shear margin marked in profiles with red frames. Arrow colors represent vertical vectors. Viscosity profiles show two pairs of shear margins at the ice stream's tributaries. Vertical shear zones inside the tributaries are old shear margins. Taking an example from an inner shear margin, except for the basal ice, c-axis orientations of ice particles inside and around the shear margin are rotated into horizontal or small angles to the horizontal plane.

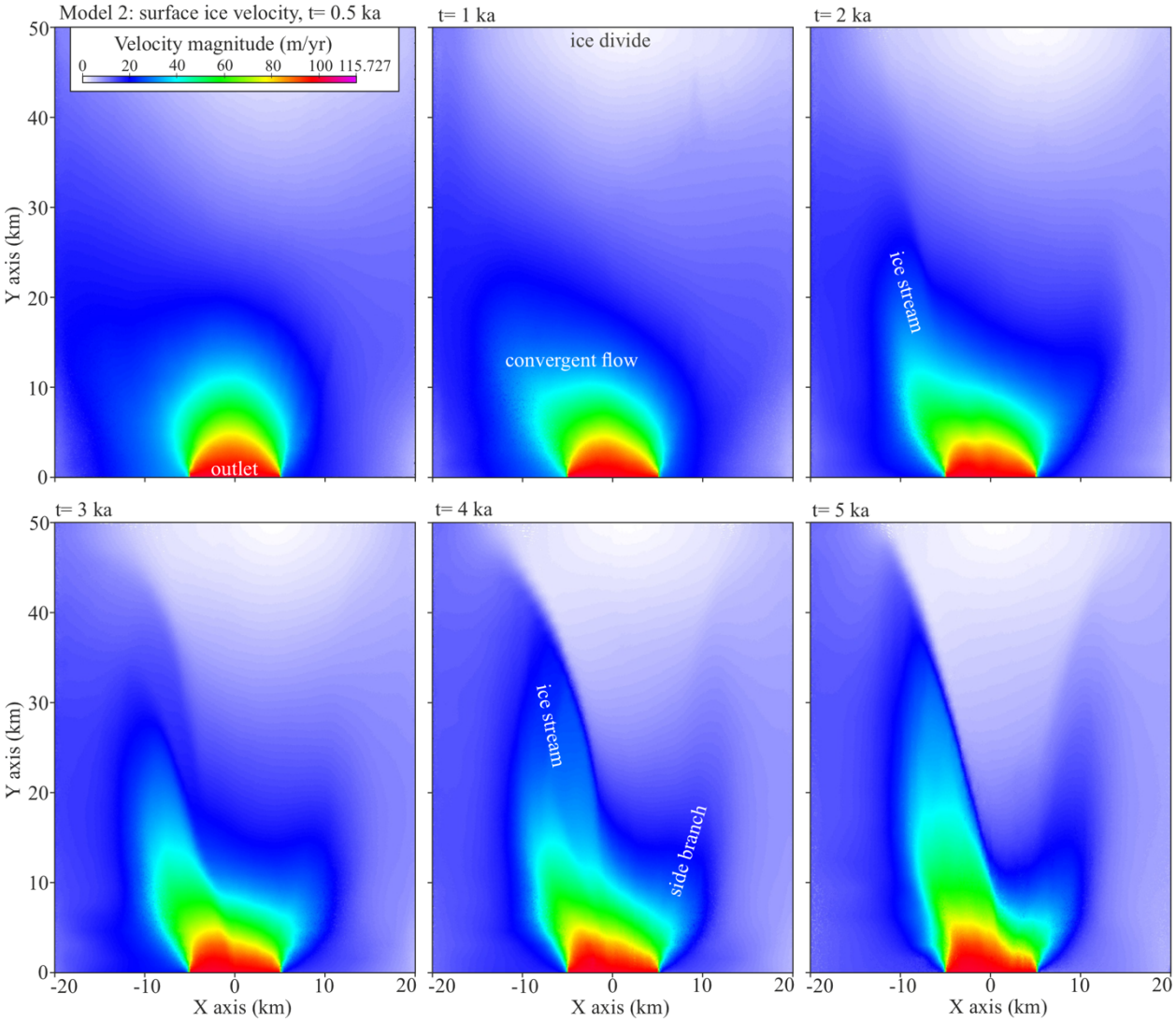


Fig. S7. Evolution of surface ice velocities in Model 2 (no slip; asymmetric inflow; anisotropy k = 10) from 500 to 5000 years. The convergent flow around the narrow outlet is asymmetric at the beginning. Between 1000 and 2000 years, the fast ice flow develops along the higher ice inflow on the left side and forms the initial ice stream (NEGIS-type) with a weak branch on the other right side. At 4000 years, the ice stream grows farther inland and closes at the ice divide. From 4000 to 5000 years, the ice stream gradually narrows and develops a larger velocity difference with surrounding ice. The ice stream's position has a slight shift towards the model center (left to right). The side branch is slowly developing as well.

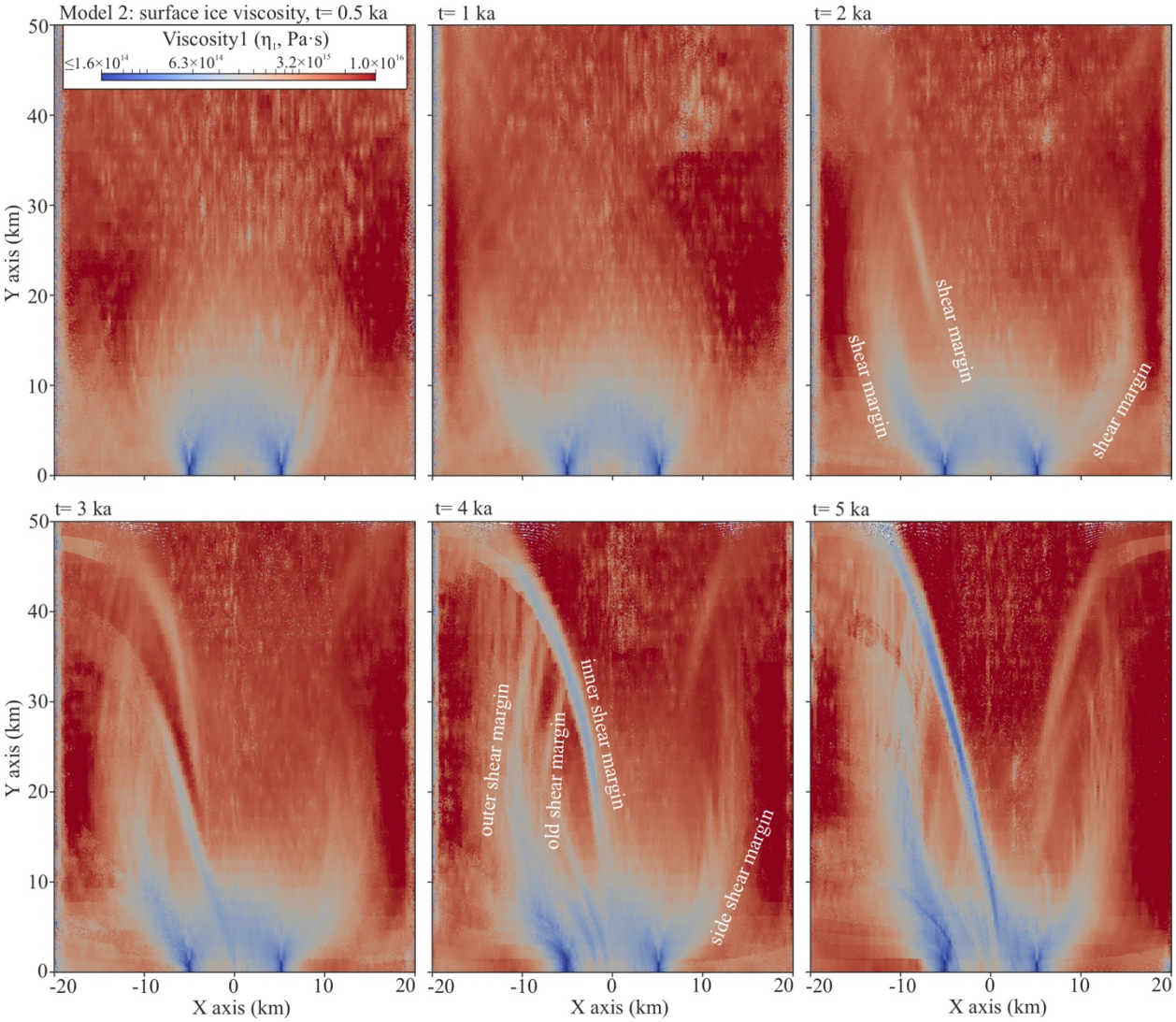


Fig. S8. Evolution of general viscosities $\eta_1$ from the ice surface in Model 2 from 500 to 5000 years. At 1000 years, a shear zone develops firstly in the left part of the convergent flow. At 2000 years, the shear margins of the ice stream are established; the outer shear margin of the ice stream's side branch develops as well while the inner shear margin is not obvious. From 2000 to 4000 years, shear margins develop farther inland. Some old shear margins flow into the ice stream and new shear margins form around. Shear margin migrations are along with ice flow directions (fig. S9), not the same as Model 1 (fig. S4). At 5000 years, shear margins become more distinct, including at the ice stream's side branch. Some old shear margins inside the ice stream can be observed to have disappeared.

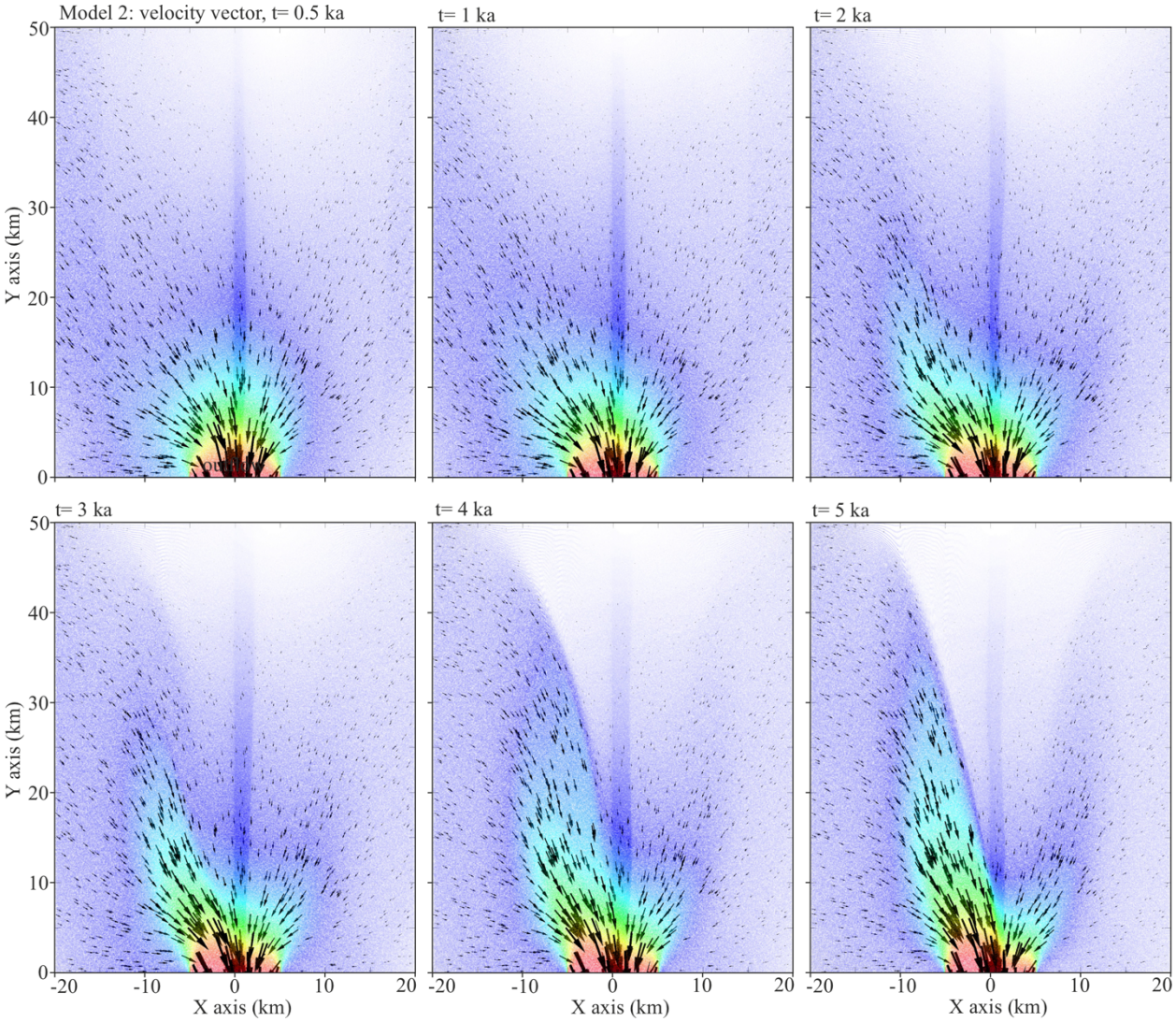


Fig. S9. Top views of ice velocity vectors (arrows) in Model 2 from 500 to 5000 years. Arrow orientations point to ice flow directions. The arrow size is scaled with ice flow speed. Ice stream position is shown with the translucent velocity magnitude map from fig. S7. Ice velocity vectors change through time along with the ice stream's evolution. The velocity vector field of the modeled NEGIS-type ice stream shows a similarity to the real NEGIS (*13, 68*).

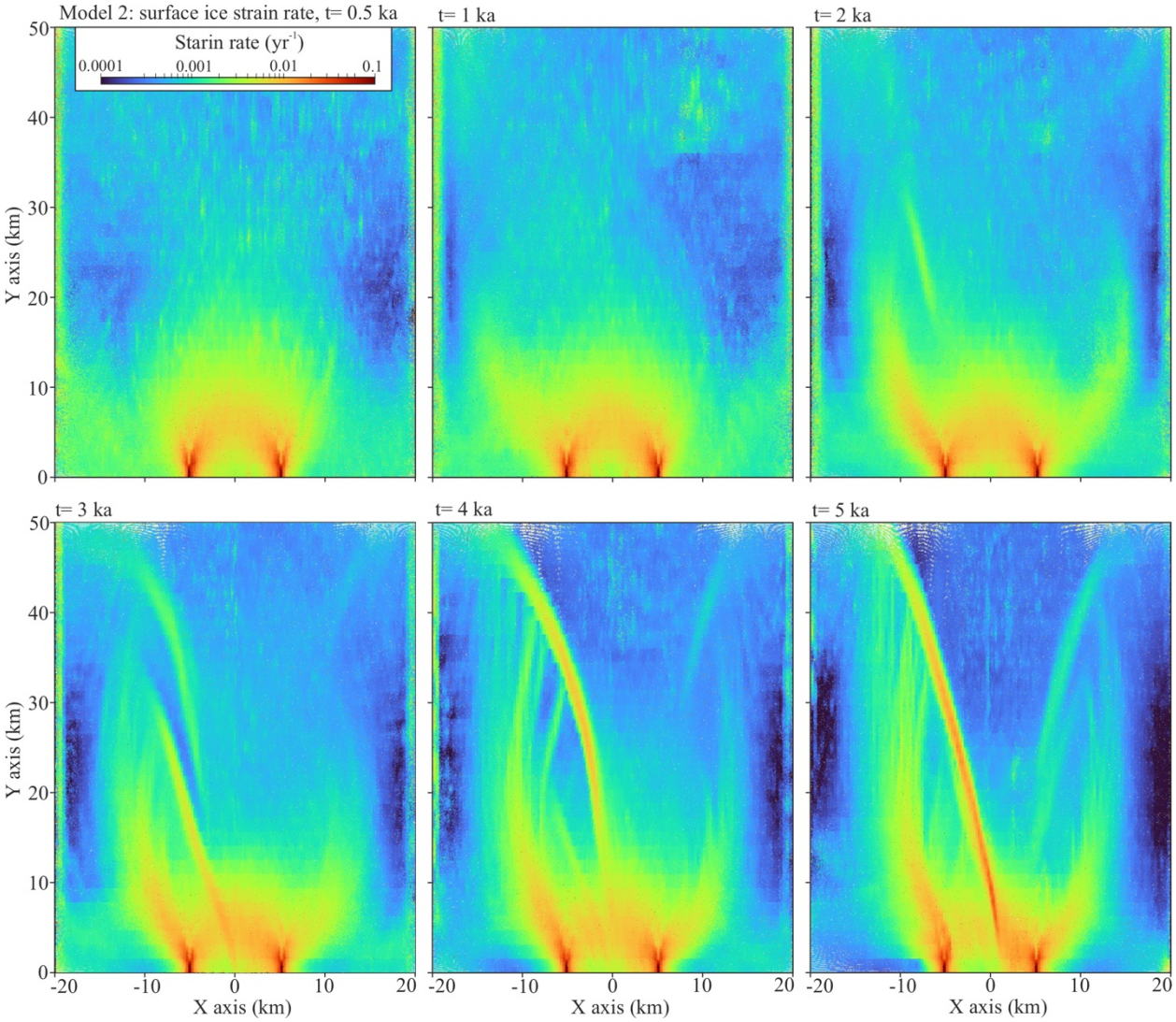


Fig. S10. Top views of ice strain rates (the second invariant of strain-rate magnitude) in Model 2 from 500 to 5000 years. Shearing in shear margins can be observed in the high strain-rate areas with strain-rate values around 0.01 yr-1. Except for a more dispersed pattern of the outer shear margin due to a boundary effect, the strain-rate map at 4000 years is comparable with the maximum shear strain rate map of real NEGIS (*69*).

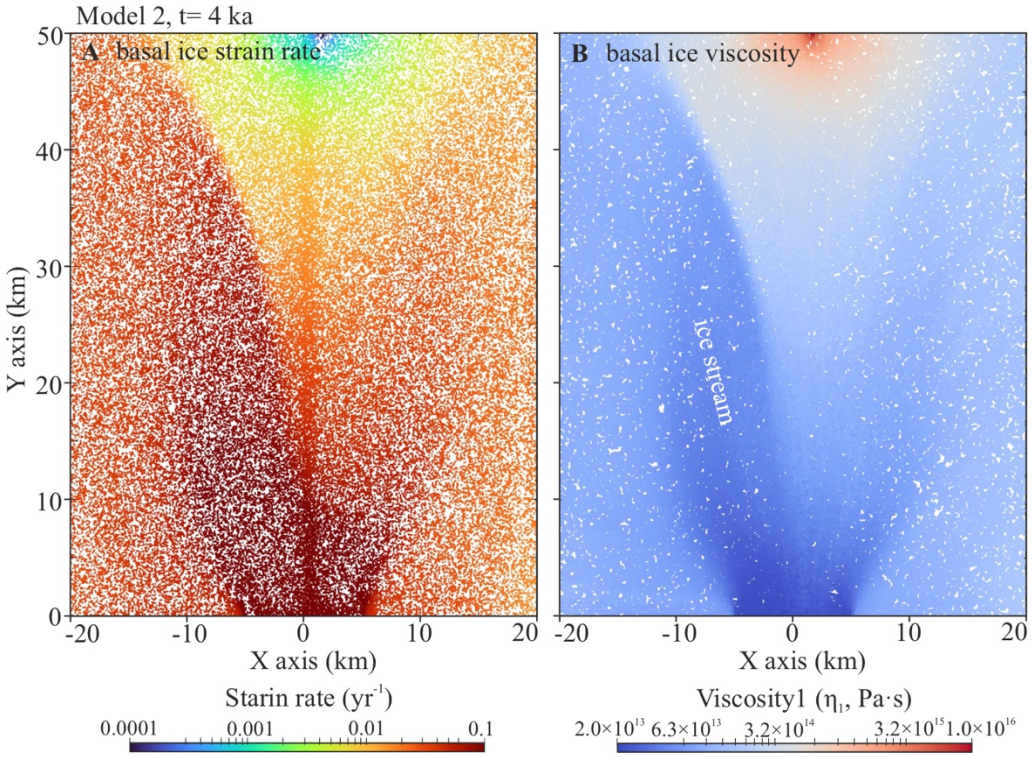


Fig. S11. Properties of a basal ice layer (z = 100 m) at 4000 years in Model 2. (A) Strain rates (the second invariant of strain-rate magnitude). (B) General viscosities $\eta_1$. The basal ice on the no-slip boundary experiences bedrock-parallel shearing and strain softening along with the ice flow. It should be noted that the real basal environment would be more complicated considering shear heating, basal melting/freeze-on, and bedrock topography.

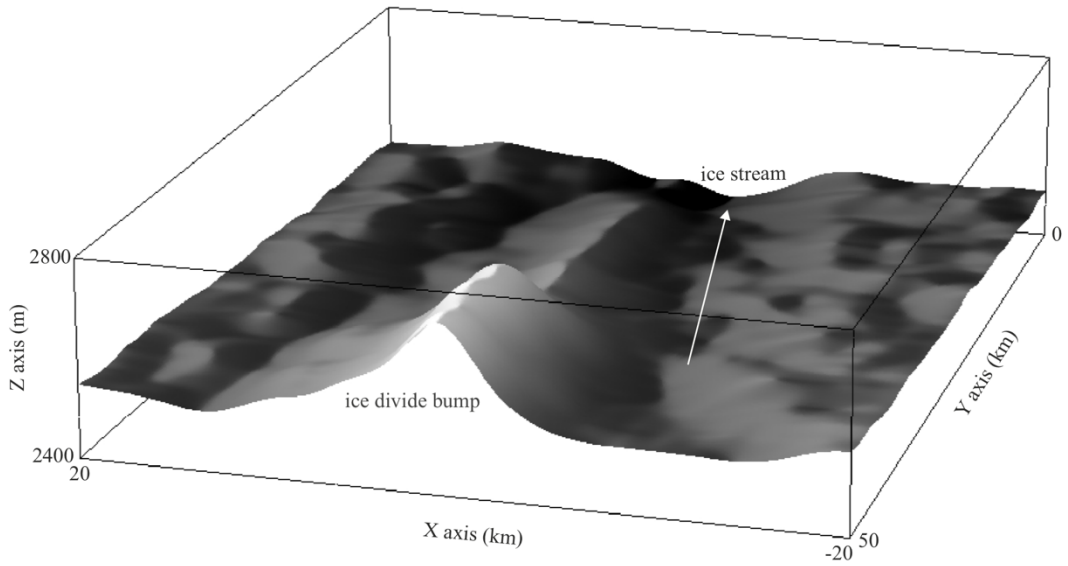


Fig. S12. 3D geometry of the ice surface in Model 2 at 4000 years. The bump at the ice divide has a similar mechanism to the Raymond bump (*60, 70*), which can also be indicated by the low strain rate and high viscosity area in fig. S11. The shear-margin trough (*71, 72*) can be observed especially at the inner shear margin of the ice stream.

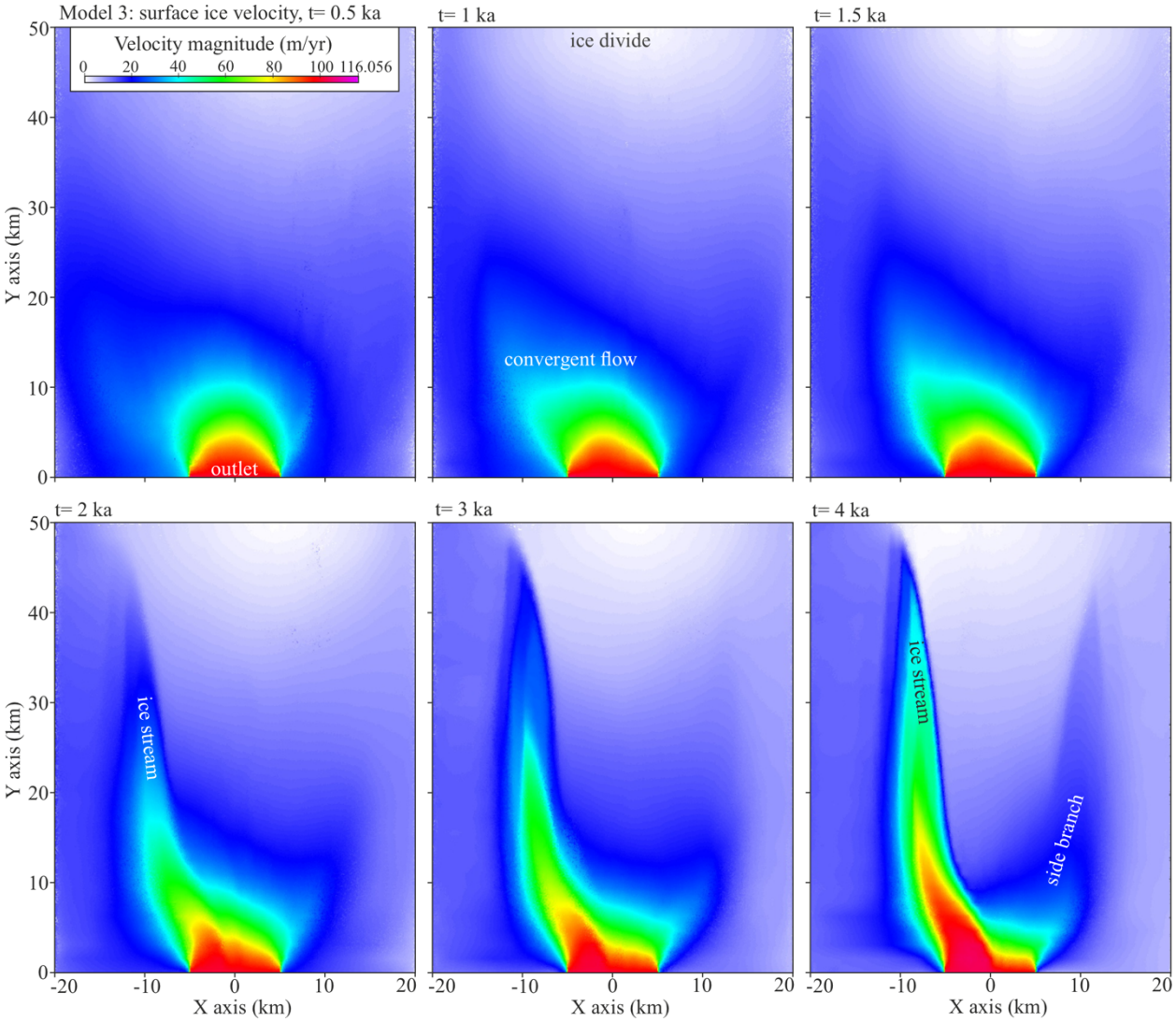


Fig. S13. Evolution of surface ice velocities in Model 3 (no slip; asymmetric inflow; anisotropy k = 100) from 500 to 4000 years. The evolution process of the NEGIS-type ice stream in Model 3 is faster than in Model 2 (k = 10; fig. S7). At 2000 years, the ice stream already exhibits a large velocity difference with surrounding ice. At 3000 years, the ice stream grows close to the ice divide. At 4000 years, the ice stream is narrower and has a much larger velocity difference with surrounding ice than in Model 2.

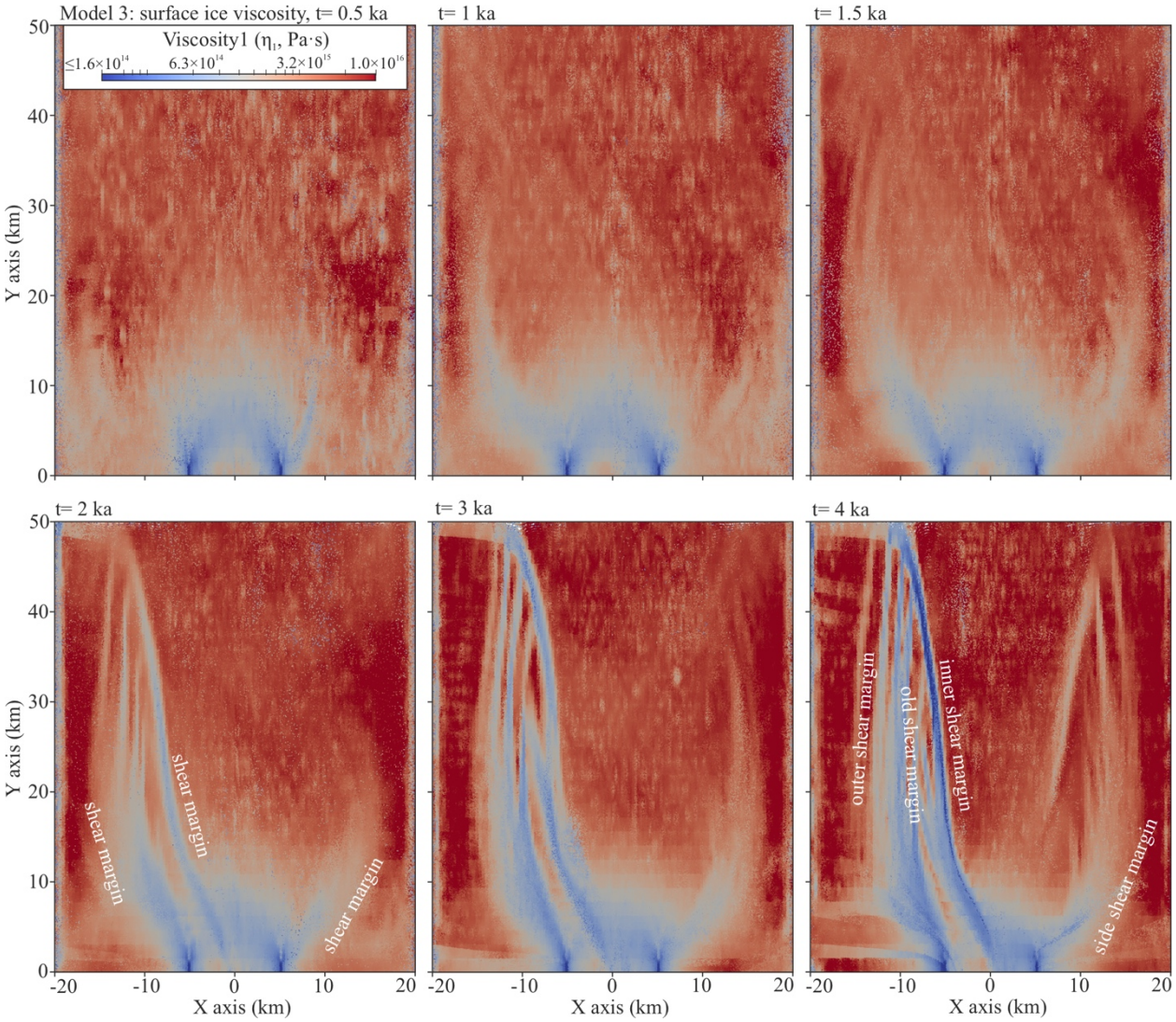


Fig. S14. Evolution of general viscosities $\eta_1$ from the ice surface in Model 3 from 500 to 4000 years. At 2000 years, the shear margins of the ice stream are already established. At 4000 years, shear margins are softened more than in Model 2 (fig. S8).

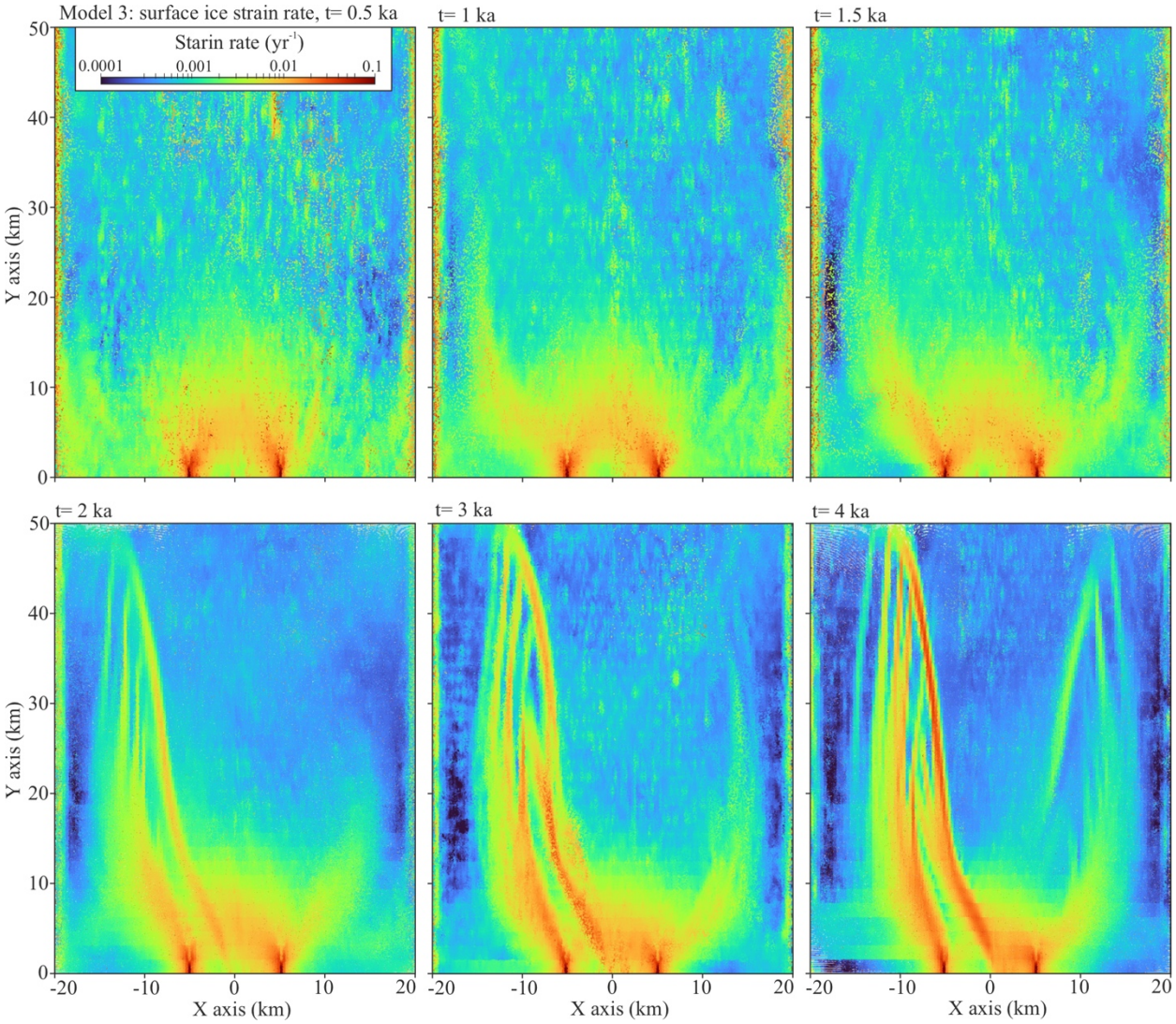


Fig. S15. Top views of ice strain rates (the second invariant of strain-rate magnitude) in Model 3 from 500 to 4000 years. Strain rates in shear margins can be observed higher than in Model 2 (fig. S10).

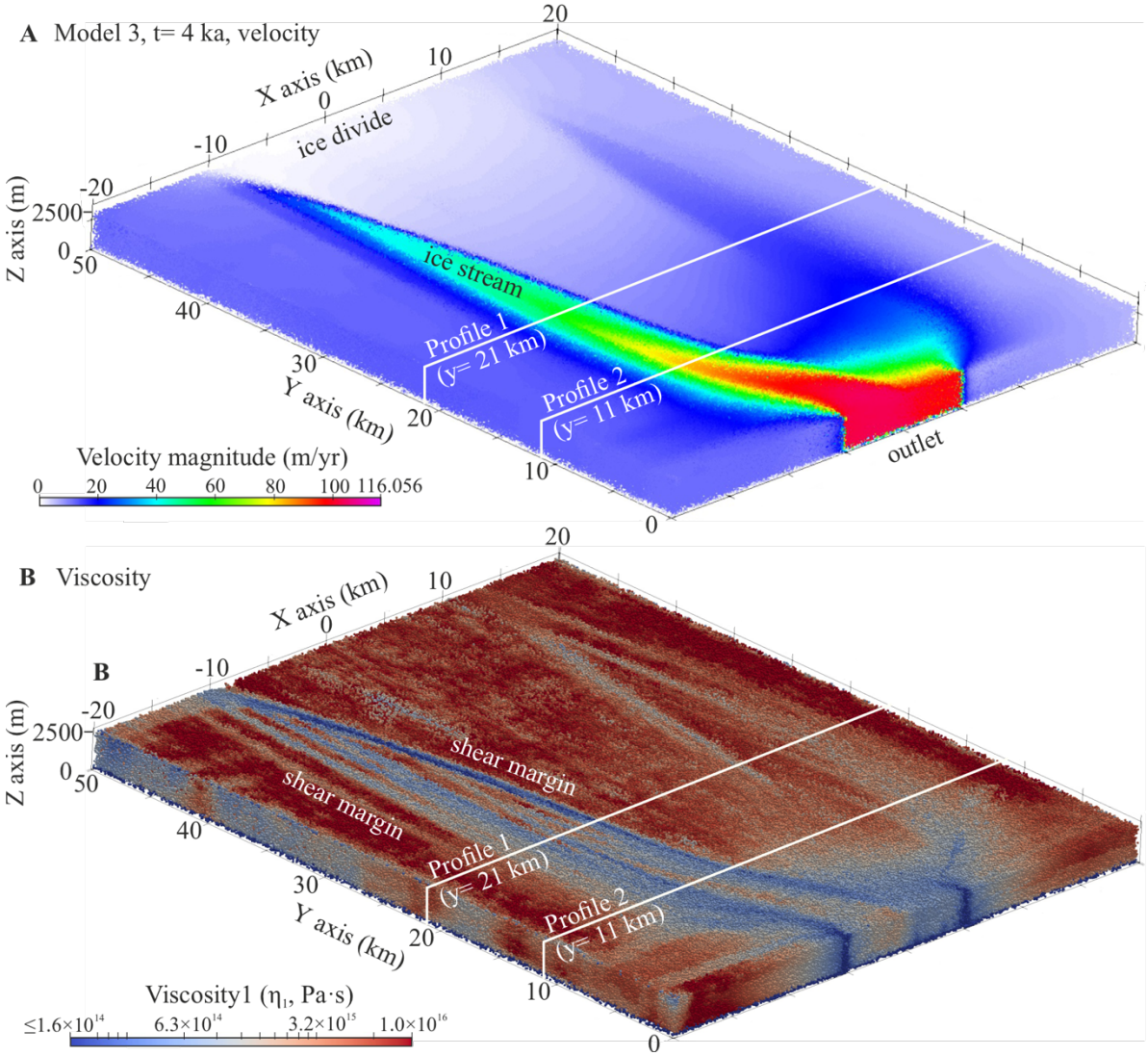


Fig. S16. 3D views of the NEGIS-type ice stream in Model 3 at 4000 years. (A) Ice velocities. (B) Ice general viscosities $\eta_1$.

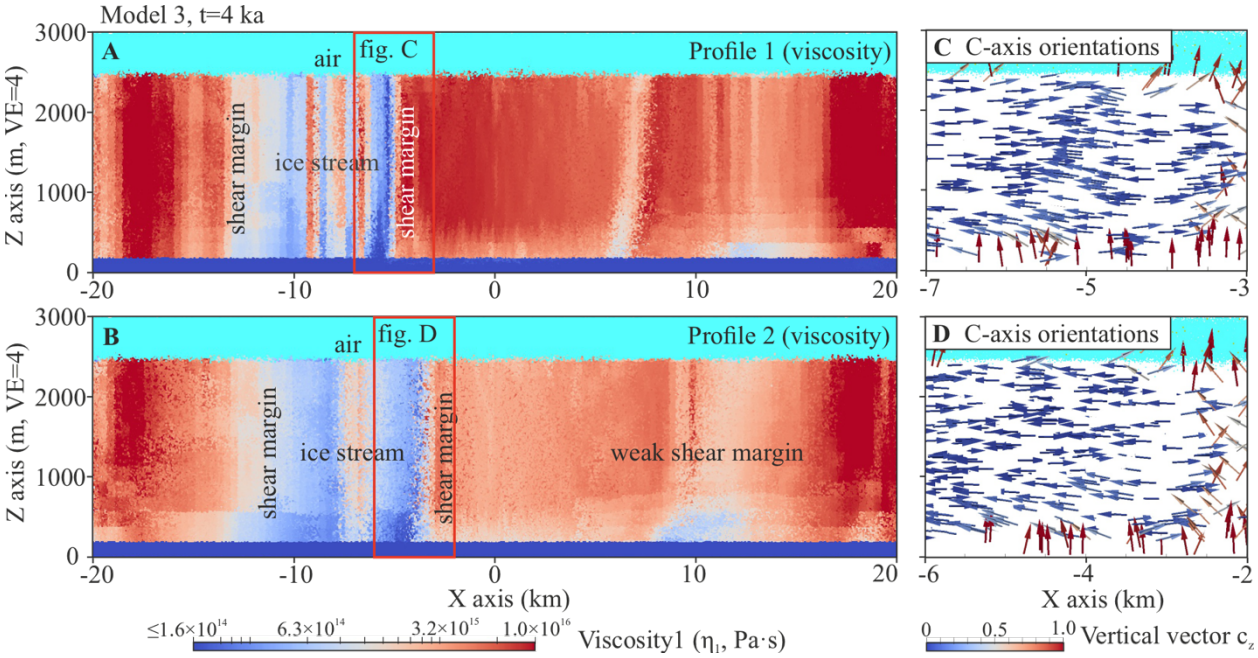


Fig. S17. Profile snapshots of the NEGIS-type ice stream in Model 3 at 4000 years. (A–B) Ice general viscosities $\eta_1$ on Profile 1 (A) and Profile 2 (B) transverse the ice stream (profile locations in fig. S16). Note the vertical exaggeration (4×) in the profiles. (C–D) C-axis orientations (arrows) of ice particles at the shear margin marked in profiles with red frames. Arrow colors represent vertical vectors. Shear margins (or old shear margins inside the ice stream) are indicated by vertical zones of strongly softened ice. Weak shear margin(s) can be observed at the ice stream's side branch as well. Except for the basal ice, the c-axis orientations of ice particles inside and around the strong shear margin are rotated into horizontal or small angles to the horizontal plane.

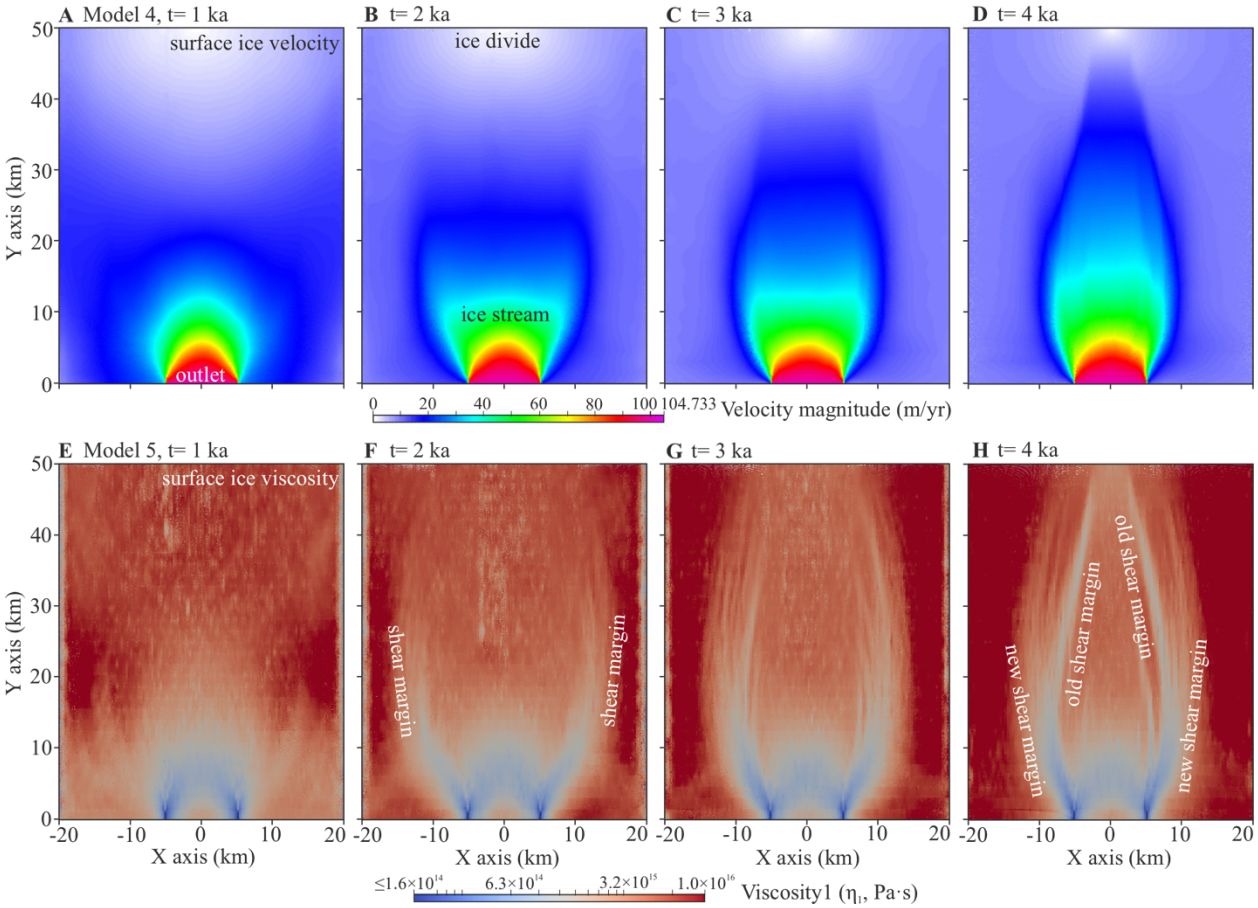


Fig. S18. Evolution of surface ice velocities (A–D) and general viscosities $\eta_1$ (E–H) in Model 4 (free slip; symmetric inflow; anisotropy k = 10) from 1000 to 4000 years. The ice stream seems to quickly form between 1000 and 2000 years with its shear margins close to the ice divide. Compared with no-slip Model 1 (figs. S3–S4), the ice stream does not later develop its tributaries but evolves along the outlet to the ice divide with a bottleneck shape. From 2000 to 4000 years, the single ice stream narrows its width; shear margins flow towards the center of the ice stream accompanied by the gradual formation of new shear margins outside.

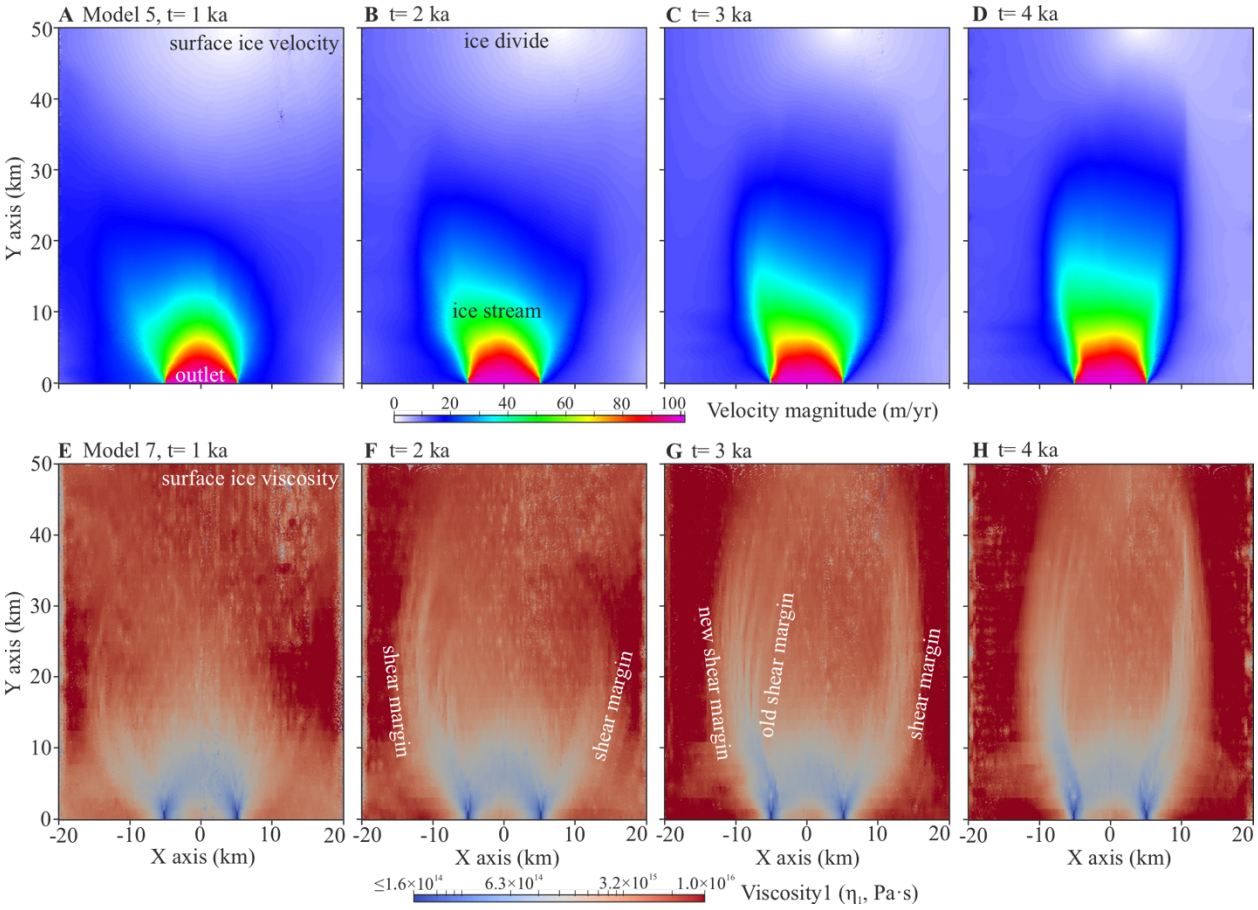


Fig. S19. Evolution of surface ice velocities (A–D) and general viscosities $\eta_1$ (E–H) in Model 5 (free slip; asymmetric inflow; anisotropy k = 10) from 1000 to 4000 years. The ice stream is slightly asymmetric and the left shear margin (at the faster inflow side) migrates faster than the right one. Compared with no-slip Model 2 (figs. S7–S8), the ice stream develops along the outlet and directly to the ice divide, without a side branch.

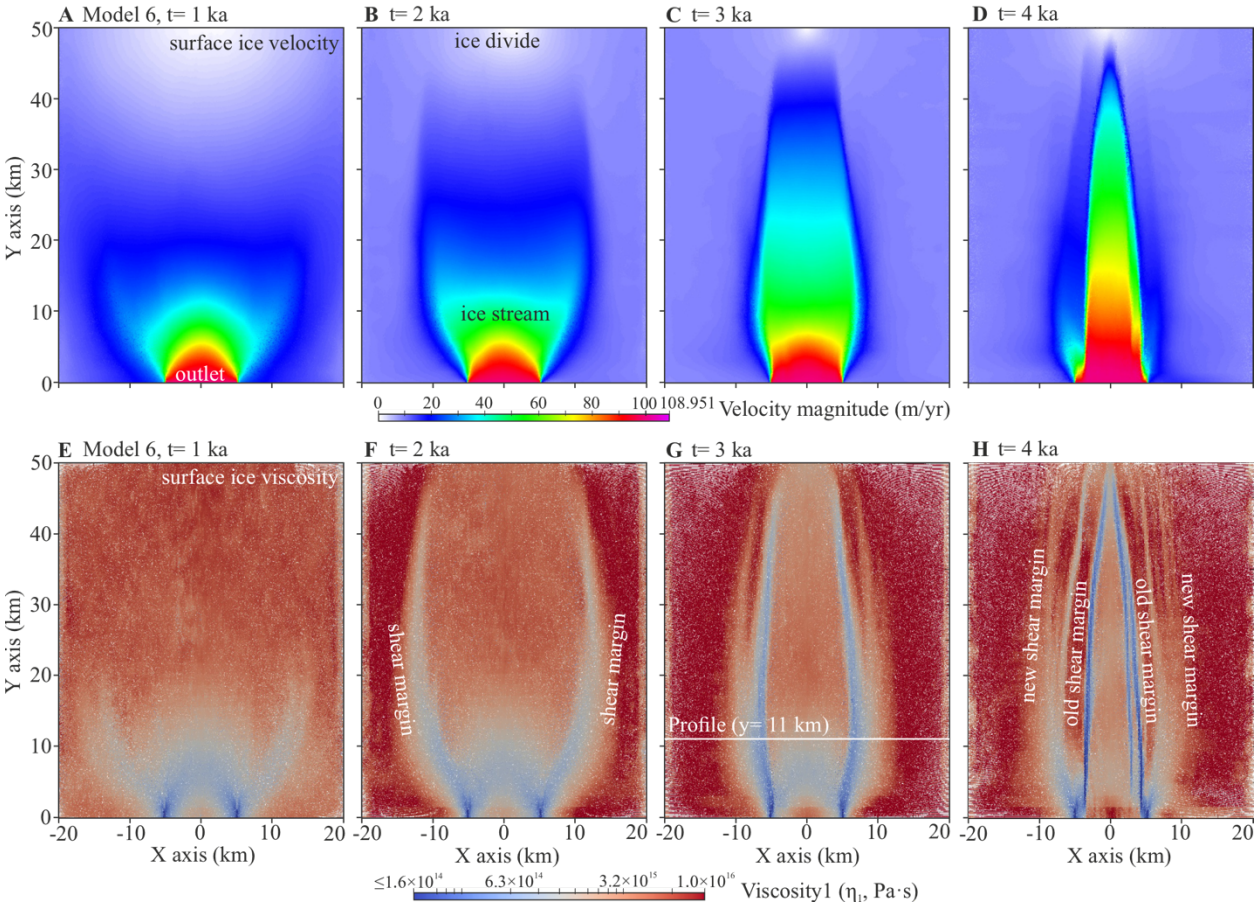


Fig. S20. Evolution of surface ice velocities (A–D) and general viscosities $\eta_1$ (E–H) in Model 6 (free slip; symmetric inflow; anisotropy k = 100) from 1000 to 4000 years. The evolution process of the ice stream in Model 6 is faster than in Model 4 (k = 10; fig. S18). The ice stream is well-developed in 2000 years with distinct shear margins close to the ice divide. At 3000 years, the ice stream is narrower and has a larger velocity difference with surrounding ice than in Model 4, separated by softer shear margins. From 2000 to 4000 years, shear margin migration can be observed as well.

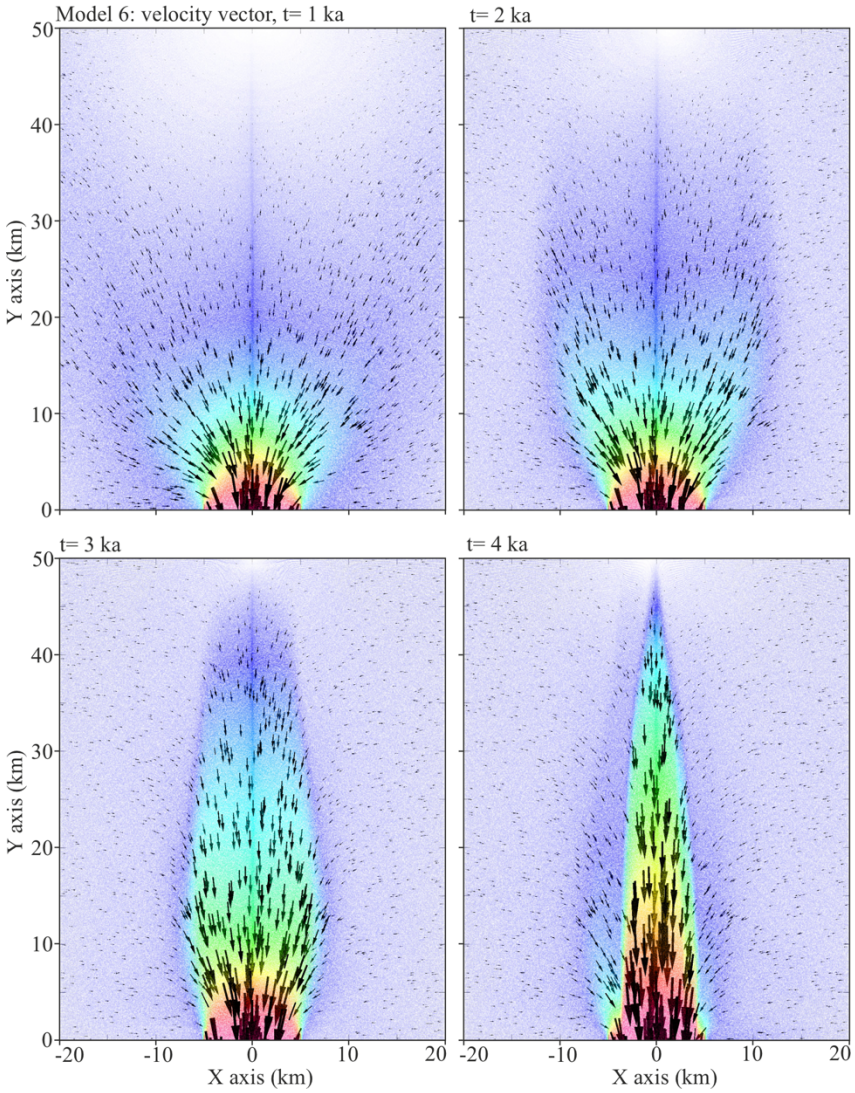


Fig. S21. Top views of ice velocity vectors (arrows) in Model 6 from 1000 to 4000 years. Arrow orientations point to ice flow directions. The arrow size is scaled with ice flow speed. Ice stream position is shown with the translucent velocity magnitude map from fig. S20. This model clearly shows the velocity vector field around a single ice stream changes through time.

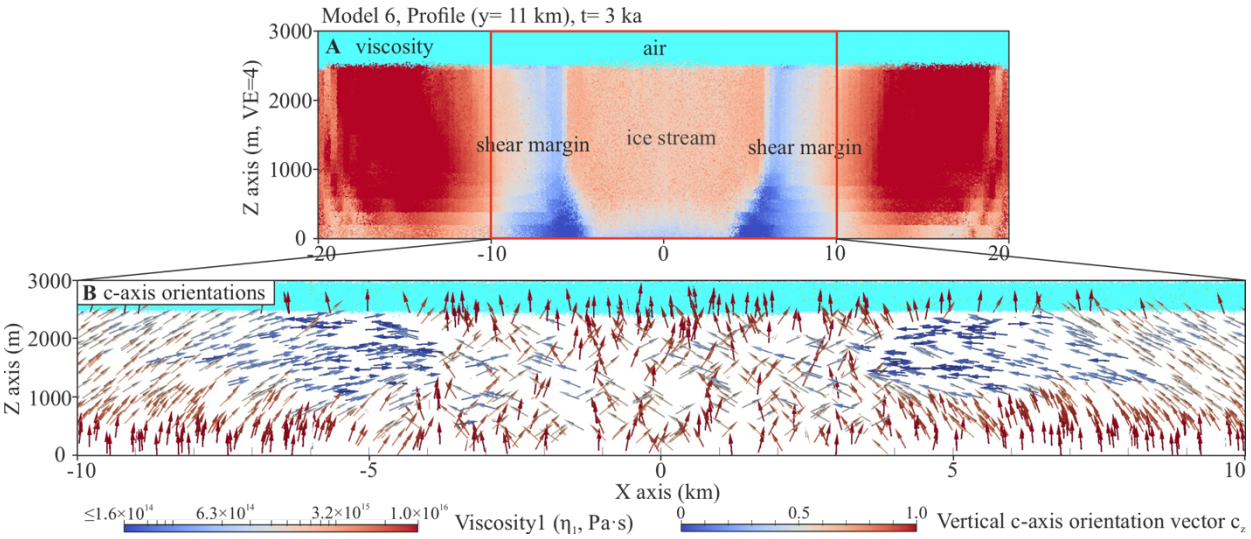


Fig. S22. Profile snapshots of the single ice stream in Model 6 at 3000 years. Profile location is in fig. S20. (A) Ice general viscosities $\eta_1$ transverse the ice stream. Note the vertical exaggeration (4×) in the profiles. (B) C-axis orientations (arrows) of ice particles around the ice stream marked in profile (A) with red frames. Arrow colors represent vertical vectors. This single ice-stream model has a larger distance between lateral model boundaries (y-walls) and its shear margins. With less boundary effect, the c-axis orientation patterns in and near both shear margins are more distinct. Except for the basal ice, c-axis orientations of ice particles inside and around shear margins are rotated towards the horizontal or small angles to the horizontal plane.

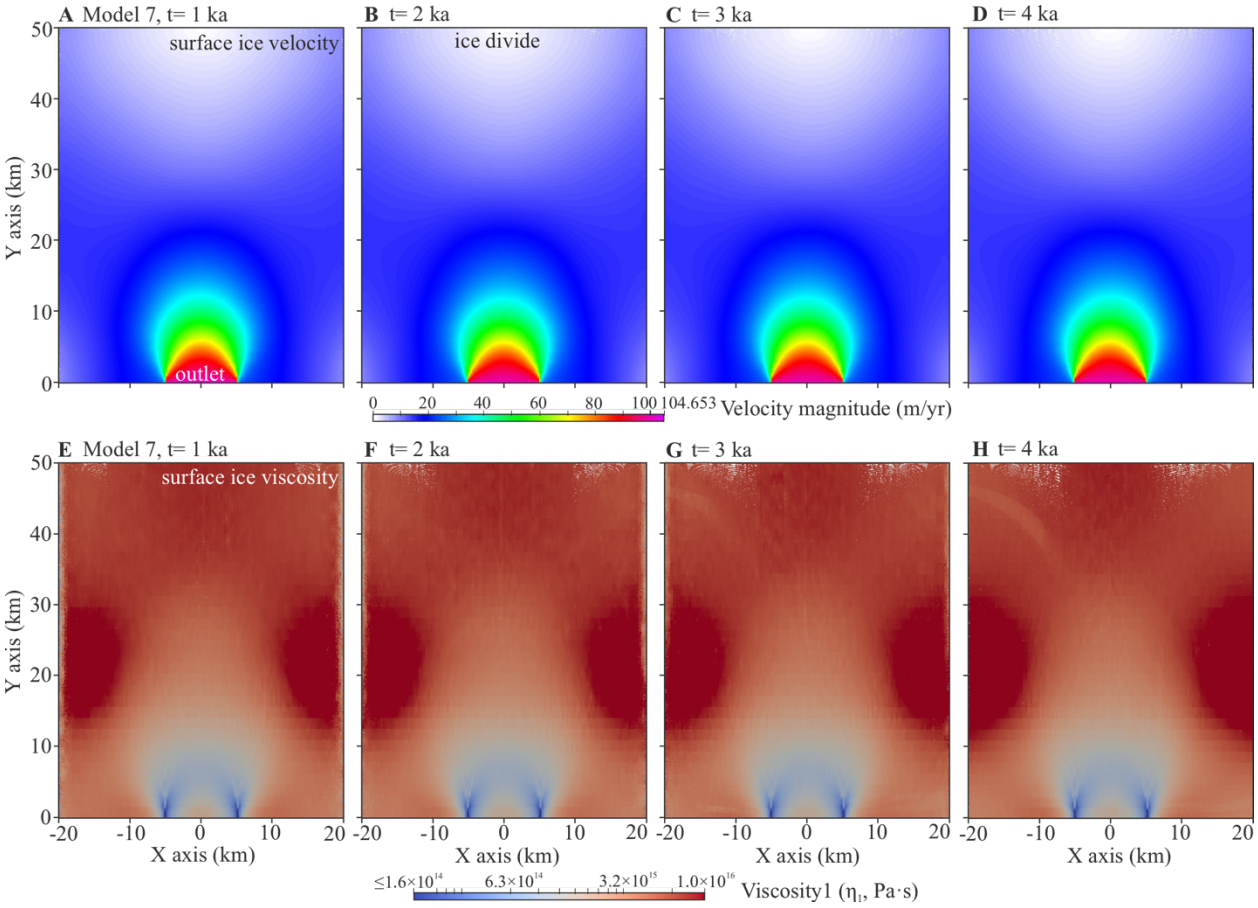


Fig. S23. Evolution of surface ice velocities (A–D) and isotropic viscosities $\eta_1$ (E–H) in Model 7 (free slip; symmetric inflow; isotropy) from 1000 to 4000 years. However, shear margins cannot be established under our model conditions (even on a slippery bed), and no ice stream forms.

Movies can be accessed through https://mega.nz/folder/GGYgjIrT#RZVT-HeanmLj7e9sX_dvRg

Movie S1. Supplement to fig. S3: A whole evolution process of surface ice velocities in Model 1 (no slip; symmetric inflow; anisotropy k = 10) from 0 to 5000 years.

Movie S2. Supplement to fig. S7: A whole evolution process of surface ice velocities in Model 2 (no slip; asymmetric inflow; anisotropy k = 10) from 0 to 5000 years.

Movie S3. Supplement to fig. S13: A whole evolution process of surface ice velocities in Model 3 (no slip; asymmetric inflow; anisotropy k = 100) from 0 to 4000 years.

Movie S4. Supplement to fig. S20: A whole evolution process of surface ice velocities in Model 6 (free slip; symmetric inflow; anisotropy k = 100) from 0 to 4000 years.

# Chapter 4

## Shear margins in upper half of Northeast Greenland Ice Stream were established two millennia ago

**Daniela Jansen[1], Steven Franke[1,2], Catherine C. Bauer[2], Tobias Binder[1,3], Dorthe Dahl-Jensen[4,5], Jan Eichler[1,6], Olaf Eisen[7,1], Yuanbang Hu[2,8], Johanna Kerch[1,9] MariaGema Llorens[10], Heinz Miller[1], Niklas Neckel[1], John Paden[11], Tamara de Riese[2], Till Sachau[2], Nicolas Stoll[1,12], Ilka Weikusat[1,2], Frank Wilhelms[1,9], Yu Zhang[2], Paul D. Bons[2,13]**

[1]Department of Geosciences, Tübingen University, Tübingen, Germany.

[1]Alfred Wegener Institute Helmholtz Centre for Polar and Marine Research, Bremerhaven Germany

[2]Department of Geosciences, Tübingen University, Tübingen, Germany

[3]Now at ATLAS ELEKTRONIK GmbH, Bremen

[4]Niels Bohr Institute, Physics of Ice, Climate and Earth, University of Copenhagen, Copenhagen, Denmark

[5]Center for Earth Observation Sciences, University of Manitoba, Winnipeg, Canada

[6]Now at Laboratoire de Géologie de Lyon: Terre, Planètes, Environnement (LGL-TPE), ENS Lyon, Université Claude Bernard Lyon 1, CNRS, Villeurbanne, France

[7]University of Bremen, Bremen, Germany

[8]College of Earth Science, Chengdu University of Technology, Chengdu, China

[9]Geoscience Centre, University of Göttingen, Germany

[10]GEO3BCN, CSIC, Lluís Solé Sabarís s/n, 08028 Barcelona

[11]Center for Remote Sensing and Integrated Systems (CReSIS), University of Kansas, Lawrence, KS, USA

[13]Now at Department of Environmental Sciences, Informatics and Statistics, Ca'Foscari University Venice, Italy

[14]School of Earth Science and Resources, China University of Geosciences (Beijing), Beijing, China

Published in Nature Communications, 15(1), 1193. doi:10.1038/s41467-024-45021-8

This is an author version of the manuscript. The fulltext (copy-edited publishers version) can be accessed at: https://doi.org/10.1038/s41467-024-45021-8

## Abstract

Only a few localised ice streams drain most of the ice from the Greenland Ice Sheet. Thus, understanding ice stream behaviour and its temporal variability is crucially important to predict future sea-level change. The interior trunk of the 700 km-long North-East Greenland Ice Stream (NEGIS) is remarkable due to the lack of any clear bedrock channel to explain its presence. Here, we present a 3-dimensional analysis of the folding and advections of its stratigraphic horizons, which shows that the localised flow and shear margins in the upper NEGIS were fully developed only ca 2000 years ago. Our results contradict the assumption that the ice stream has been stable throughout the Holocene in its current form and show that upper NEGIS-type development of ice streaming, with distinct shear margins and no bed topography relationship, can be established on time scales of hundreds of years , which is a major challenge for realistic mass-balance and sea-level rise projections.

## 1. Introduction

Most of the discharge of ice into the oceans takes place by solid ice flow via ice streams[1,2]. These are river-like zones where ice flow is significantly faster than in their surroundings, assumed to be triggered by either bedrock properties[3,4], enhanced sliding[2,5], and/or by deformation mechanisms leading to shear localization[6]. The most conspicuous one in Greenland is the North East Greenland Ice Stream (NEGIS; Fig. 1a), which extends for about 700 km inland from its outlets in northeast Greenland, and its catchment covers 17 % of the ice sheet area[7].

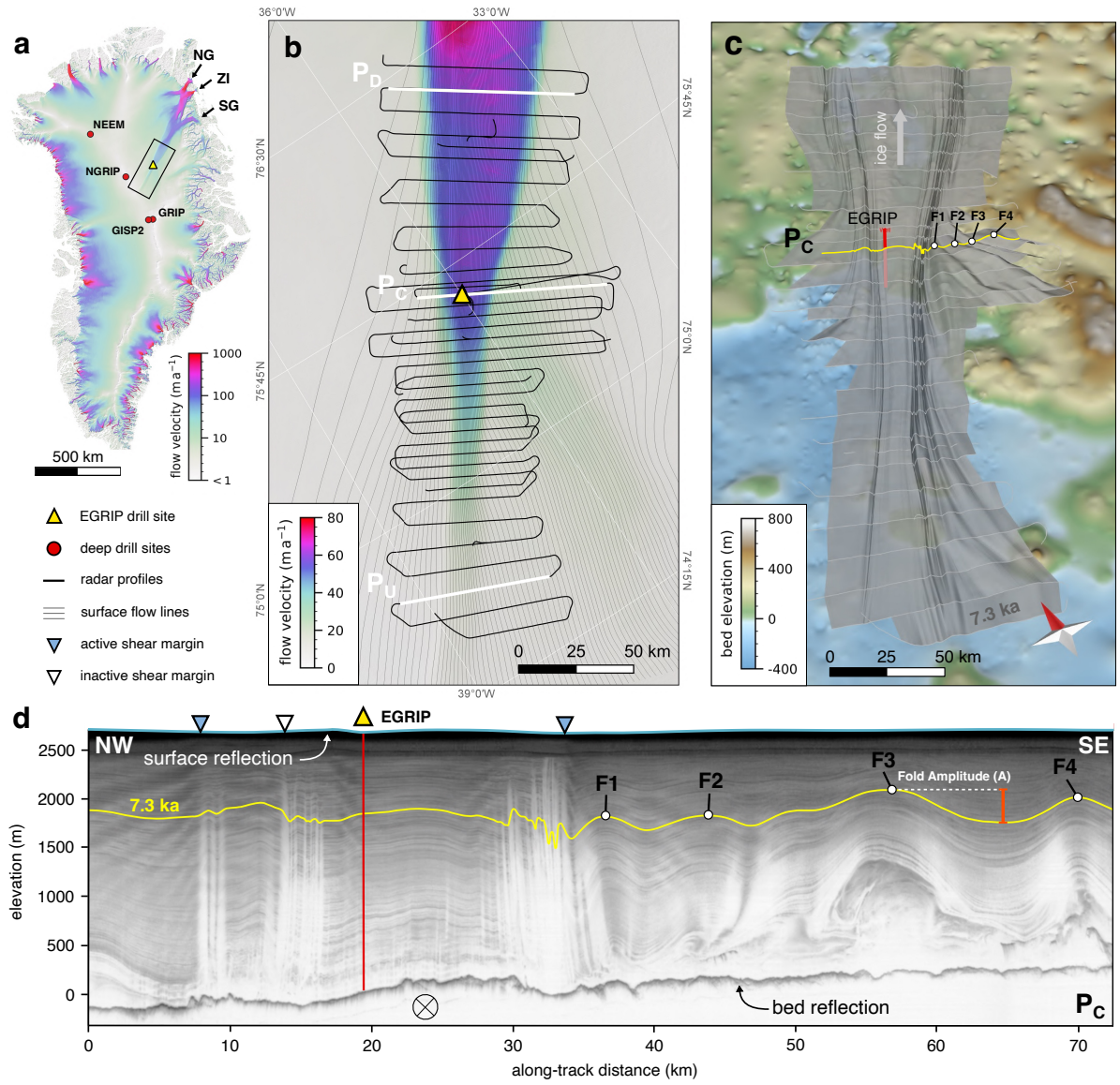


Fig. 1. Area and outline of the radar survey. (a, b) Maps of the survey area and radar lines with ice flow velocity8. NG: Nioghalvfjerdsfjorden Glacier, ZI: Zachariae Isstrøm, SG: Storstrømmen Glacier. Radar profile, $P_C$ is shown in panel (d) and in Figure 2b, $P_U$ and $P_D$ are shown in Figure 2a,c. C stands for Centre, D for Downstream and U for Upstream. (c) 7150 years BP isochrone horizon as a shaded relief above bedrock[64] (10 times vertical exaggeration). F1-F4 indicate the location of fold anticlines also highlighted in the radar profile $P_C$ in panel (d). The location of $P_C$ is indicated by a yellow line. (d) Profile $P_C$ across NEGIS in the centre of the survey area. F1-F4 indicate the anticlines highlighted in panel (c).

NEGIS reaches up to the central ice divide (Fig. 1a), but while the gates in the coastal mountain range in northeast Greenland clearly determine the location of the coastal outlet, its course in the interior of the ice sheet appears not to be constrained by bed topography[10–12]. The flow velocity increases from about 3 m $yr^{-1}$ close to the divide to 55 m $yr^{-1}$ at the EGRIP (East Greenland Ice core Project) drilling camp[8,13], ca 40 m $yr^{-1}$ faster than the ice flow directly adjacent to NEGIS. The present-day shape and surface velocity of NEGIS are well constrained by satellite observations[8], but much less is known about the spatial and temporal evolution of the stream, and the processes which trigger the exceptionally high flow velocities in its upstream region. Satellite and GPS measurements show that NEGIS is accelerating slightly, indicating that the ice-dynamic regime is possibly not in equilibrium[14]. Previously it was assumed that this ice stream existed in its current shape at least during most of the Holocene, and that its presence can be explained by an area of strongly enhanced geothermal heat flux at upper NEGIS[10] causing substantial basal melting of the ice sheet. To explain the annual layer thickness along the ice column, Fahnestock and colleagues[10] suggest a basal ice loss of ca 0.1 m per year over the last 9 kyrs. This would require an exceptionally high geothermal heat flux of 950 $mWm^2$. However, a comparison with global geothermal heat fluxes shows that the proposed values exceed natural heat fluxes by about an order of magnitude[15].

Here we use isochronous radar reflections as passive tracers of ice deformation to reveal the history of NEGIS over the past few thousand years, and show that the shear margins that define it in its present form in the upstream region have been active for only about the last 2000 yrs. This indicates that streaming can be triggered on short time scales, leading to abrupt ice-flow reconfigurations[16], which is contradictory to it being triggered and sustained by a local, long-term heat flow anomaly[10,17].

## 2. Results and Discussion

### 2.1 Radar Stratigraphy

The data presented in this study have been derived from an airborne radar survey in May 2018 using an ultra-wide-band radar system (AWI-UWB[18,19]) with an array of 8 transmitters and receivers mounted beneath the fuselage of the AWI aircraft Polar 6[20]. The layout of the survey was designed for mapping radar stratigraphy and bedrock properties in the vicinity of the

EGRIP drilling camp, with an area stretching along flow from 150 km upstream of the camp to 150 km downstream. The profiles used in this study were recorded in narrow-band mode, with the frequency range set to 180-210 MHz. Due to the focus on stratigraphy, the radar lines are mostly perpendicular to ice flow in order to best reproduce the deformation pattern in the shear margins. Here we only use data from across-flow profiles (Fig. 1b). The distance between the profiles is 5 km in the central part of the survey region, in the outer area the distance is 10 km.

The ages of distinct layers in the radargrams were derived from tracing to or correlating layers at the EGRIP drill site where ages are known as a function of depth[21]. This results in a set of layers with known depositional ages. In the central profile up to 21 layers that are < 8 kyrs BP old (according to EGRIP chronology) could be connected to the EGRIP site, while in the downstream profile this number was reduced to at least five. The error in dating of the reference layers is up to 200 years towards 8 kyrs BP layers for the absolute age, which is a conservative estimation (Franke et al., 2023). For the following analysis only the relative age difference between the layers is relevant, which corresponds to the error of the ice core dating[21]. Most layers within one fold limb cannot be traced all the way to the drill site or can be recognised in the radargram at that site. Their ages are estimated by interpolation (see methods).

## 2.2 Folds in ice: a record of deformation

Disturbances in radar isochrones have been conclusive to constrain temporal shifts in ice stream flow regimes in Greenland and Antarctica[16,23–25]. Modern radar systems now make it possible to investigate the processes that influence the shape of the isochrones in great detail[26–31], and, depending on the arrangements of profiles, also in 3D[16,32].

To analyse the overall structure of the distortion of the radar isochrones, we visualised a selected reflector as a 3D horizon[22] (see Methods) in the abovementioned dense array of radargrams (Fig. 1b). We chose one of the deepest layers in the upper half of the ice column, deposited approximately 7150 yrs BP (EGRIP-core dating[21]) that could still be traced continuously and reliably over the entire survey area (Fig. 1d). The plot of the complete 7150 yr-layer (Fig. 1c) reveals that the ice stream has left a significant imprint on the layer shape over the entire survey area, with complexity, amplitude, and number of the folds increasing downstream.

Outside of upper NEGIS, we find upright, cylindrical folds with wavelengths up to about ten kilometres. Here we define the wavelength as the distance between two adjacent crests or troughs of folds, measured perpendicular to their hinge lines. The amplitude is then defined as the difference in depth of trough and crest. Hinge lines converge on the ice stream in a fan-like pattern (Fig. 1c), with angles relative to NEGIS increasing downstream up to ca 55° southeast of EGRIP. Here the tallest folds are found with amplitudes ($A$) that reach up to ca 500 m in the 7150 yr layer (Fig. 1d). Disturbed ice without a clear stratigraphy is brought up to over a kilometre in the cores of these folds. In the adjacent synclines, the layer of deep disturbed ice is strongly reduced in thickness.

The hinge lines of the folds can be traced from outside of the ice stream into the shear margins and, in some cases, even across the shear margin into the interior of upper NEGIS (yellow dotted line in Fig. 3). Inside the shear margin, the fold hinges rotate to almost parallel to the shear margin, their wavelengths decrease strongly to < 1 km, and their amplitude is less than outside of NEGIS. It should be noticed that hinge lines are at an angle to streamlines (also called flow lines) of the current surface velocity field.

## 2.3 Timescale of fold formation

Dating of the active folding process is essential to constrain fold formation but also to determine the age of the flow perturbations that lead to fold growth, in this case, the formation of upper NEGIS. Here we address this issue by presenting the results of a method, which is based on an analysis of how the fold amplitudes change with the age of the layers, and is introduced in detail in the method section. The method is so far not used in glaciology, but based on standard principles used in geology[33].

The method to date the folding events is based on the principle that a new event leads to a steady increase in fold amplitude with depth in all existing layers. Layers deposited after the folding event are not folded. The timing of the end of the last fold event can thus be derived by determining at what age the amplitude-depth trend starts to deviate from zero. Multiple superimposed folding events result in breaks in the amplitude trend, with each break representing a folding event (Methods). Here we focus on the end of fold amplification only.

The relationship between depth and age is not exactly, but close to linear in the Holocene ice in the study area. In Figure 3, we therefore show amplitude-age, instead of amplitude-depth

graphs, for 14 individual crest-through pairs from three radargrams perpendicular to NEGIS. One (labelled C) is at the EGRIP site in the centre of the survey area, one 130 km upstream (U), and one 90 km downstream (D) (Figs. 2, 3 and Methods). Folds well outside of NEGIS ($C_{6\text{-}7}$, and $U_3$) and inside NEGIS ($D_{3\text{-}4}$) show amplitudes that already start to increase from zero at the surface, which indicates currently active fold amplification. Folds inside the shear margins ($D_{1\text{-}2}$, $C_{1\text{-}3}$, and $U_{1\text{-}2}$) and just adjacent to it southeast of EGRIP ($C_{4\text{-}5}$) show very different amplitude-age trends. Here amplitudes in layers younger than 2 kyrs BP are close to zero, signifying that all these folds stopped growing by about 2 kyrs at the latest. The difference in the fold groups is clearly visible in Figure 3b, which shows the combined-normalised amplitude-age graphs.

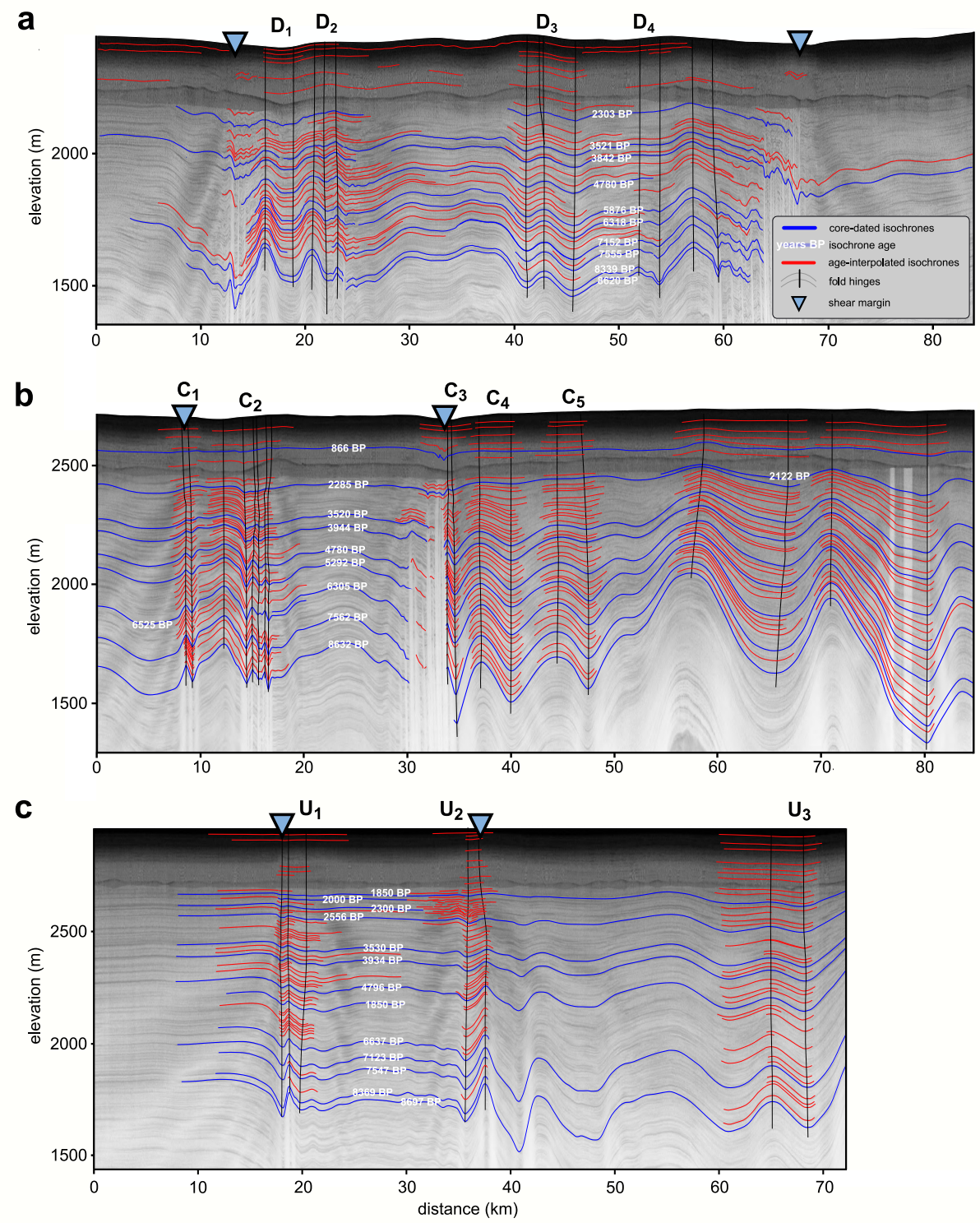


Fig. 2. Radar sections with the picked layers for fold analysis and the reference age horizons. Black lines indicate the hinge positions or axial planes of the syn- and anticlines. Letters at the top identify folds in amplitude age plots in Figure 3. (a) Downstream radar profile, $P_D$, composed of 2 frames (20180509_01_009 and 20180509_01_010). (b) Central radar profile, $P_C$, composed of 2 radar tracks (20180508_06_004 and 20180514_03_001). (c) Upstream

radar profile $P_U$, composed of one radar track frame (20180514_03_014). Triangles indicate the shear margins.

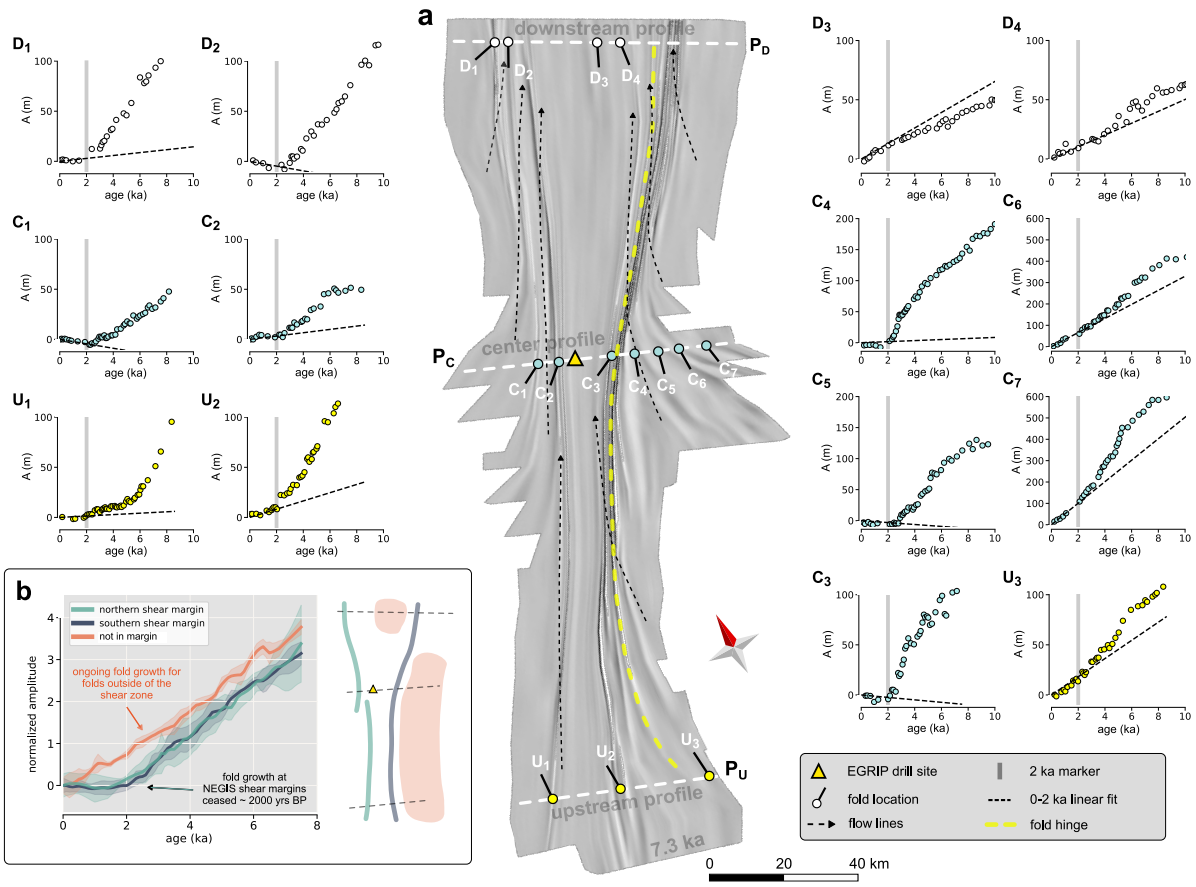


Fig. 3. Amplitude-age graphs. (a) The centre of the figure shows the 3D visualisation of the 7150 years BP isochrone horizon as a hillshade to highlight the overall structure. (b) The graph on the lower left shows the mean normalised fold amplitudes vs age for the two margins and the outside of NEGIS with shaded standard deviation. The sketch to the right shows the origin area of the mean amplitude values. Subfigures show fold amplitude vs. age at fold locations for three selected across-flow radar profiles. Black dotted lines in subfigures represent a linear fit to the data points from 2000 yrs BP until today and then extrapolated to older ages. Letters U, C, and D (Upstream, Central and Downstream) and numbers (increasing from left to right) indicate folds and their locations.

To compare all age-amplitude graphs in order to identify certain events in time it is necessary to normalise the amplitudes plotted on the y-axes of the inset plots of figure 3. For this we used the Procrustes analysis, to remove the absolute amplitude and scale. In this way common trends in the data can be made visible (details are given in the methods section).Whereas the end of folding is clearly marked, the onset of the last folding is difficult to determine. The onset of folding would be the age where the amplitudedepth trend reaches a steady slope because layers deposited towards the end of a folding event experienced less folding than those deposited at the beginning. Amplitudes in all folds start to increase steadily with depth and, hence, the age for layers older than ca 3.5-4 kyrs BP. However, some amplitude-age trends also show bends at other ages, such as ca 5-6 kyrs ($U_1$, $C_2$, $C_{3\text{-}7}$, $D_2$, $D_4$, and $U_3$) and ca 8 kyrs ($D_4$ and $C_{4\text{-}7}$). This suggests that the ice sheet here experienced multiple folding events over time, which we cannot resolve here. However, here we are concerned with the final cessation of fold amplification, which was ca 2 kyrs in and near the shear margins, while fold growth is still ongoing away from the shear margins, both outside NEGIS and in its interior.

## 2.4 Folds reveal the history of NEGIS

A conceptual model for the development of the structures in NEGIS that we see in our isochrone horizon is summarised in Figure 4. In the upstream region of NEGIS folding was initiated before 2 kyrs. The fold hinges trend towards the exit gate of the ice stream (Fig. 4a), which is consistent with folding due to convergent flow of ice with a horizontal anisotropy, similar to the fold pattern that is observed at Petermann Glacier[32].

The folds are sheared where they are transected by the shear margins, causing their rotation and tightening (Fig. 4d). This implies that the folds existed before the shear margins developed. Convergent flow implies the development of horizontal velocity gradients and, hence, strain-rate gradients, including zones of non-coaxial strain that are amenable to strain localisation in an anisotropic material such as ice[34,35]. Within the developing shear margins, simple shear along the vertical shear plane dominates over all other strain rate components, such as flattening due to precipitation. This leads to a rotation of the crystal basal planes to vertical and parallel to the shear margins, with concomitant geometric weakening (see the c-axes stereoplots in Fig.4b). This kind of fabric has been inferred from airborne radar measurements in the shear margins of Thwaites glacier[36], and NEGIS[37]. Ice fabric measurements from deep ice cores at flank or dome positions with simple shear conditions

towards the base of the ice sheet show that glacier ice develops a single maximum fabric with the c axis normal to the plane in which the shear is located[38]. The predominating fabric regimes are indicated in Figure 4a,b as schematic Schmidt-plots for c-axes orientations. Numerical simulation suggests that the weakening by this change in crystallographic preferred orientation could easily be an increase in shear strain rate of one or two orders of magnitude at a given shear stress (Methods). Figure 4c shows an example of a shear zone in which folds are rotated towards parallelism with the shear zone. Here the anisotropy in metamorphic turbidites is formed by a strong alignment of the highly anisotropic mineral biotite axial planar to folds in a composite bedding and schistosity. As with the shear margins of NEGIS, the rotating anisotropy is thought to have caused localisation of deformation in shear zones[39,40].

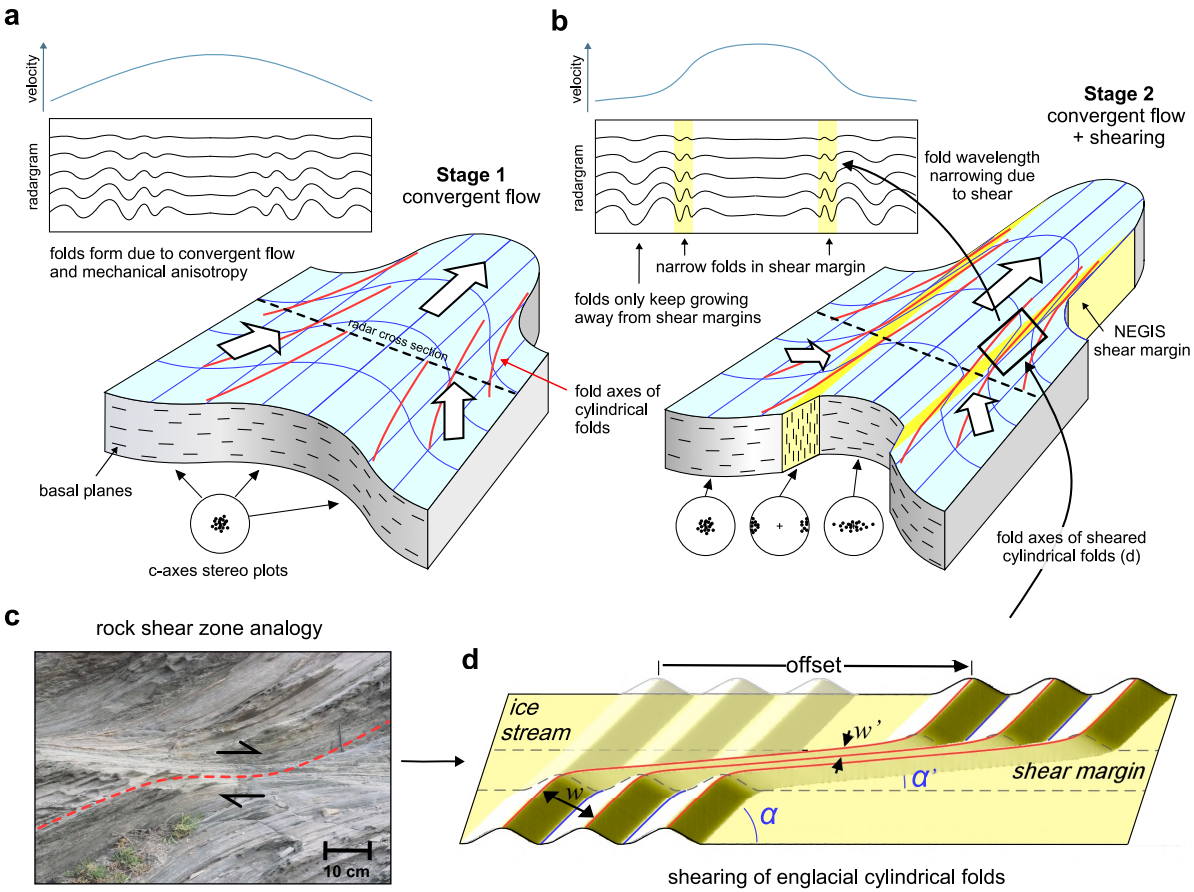


Fig. 4. Conceptual model of fold formation. (a) Situation before localisation of strain in shear margins. Red lines indicate fold hinges, and white arrows the direction of flow. Below the

block diagrams the dominating crystal fabric of the ice is illustrated as Schmidt-plots of c-axed directions. (b) After the establishment of shear zones (highlighted in yellow) and a plug-flow like regime in the central part: Inside of the shear margin the fold hinges are rotated towards paralellism with the shear margins. (c) Shear zone in schistose rock, with the foliation bending into the top-to-the-right shear zone. The picture was taken at Tudela, Cap de Creus, Spain. (d) Sketch to illustrate the three strain indicators at the shear margins: (i) reduction of wavelength, (ii) rotation and (iii) offset of fold hinges.

Numerical simulations with anisotropic ice (see methods, figs. 7 and 8), with the full-field Elle+VPFFT[41–43] code shows that folds form when basal planes are initially aligned to the shortening direction[44]. However, the shortening quickly rotates the basal planes towards parallelism with the extension direction, which causes a cessation of fold amplification. We thus explain the cessation of fold amplification in and near the shear margins by the rotation of the anisotropy that caused the shear localisation in the shear margins, as compression at a high angle to the planar anisotropy does not lead to folding or fold amplification.

Where the shear margin intersects folds, the hinges of the fold trains rotate towards parallelism with the shear margins (Fig. 4d) as the ice in the ice stream is moving faster, and the fold hinges are advected with the ice flow. This is apparent in the isochrone horizon shown in Figure 1c and the centre panel of Figure 3, but becomes even more apparent when the image is shortened along the flow direction (Figure 5). The observed offset of fold trains southeast of EGRIP is in the order of 75 km. The rotation of the hinges and the resulting shortening of the wavelengths of the folds (Figs. 4d and 5) provide additional indications of the amount of finite strain in the shear margins, resulting in an estimated shear strain of $\gamma \approx 18$ (Methods). The total offset is the product of width of the shear margin and finite shear strain. At a width of 3-4 km, this results in a total offset of ca 55-75 km. With the current velocity difference of 40 m $yr^{-1}$ across the shear margin, this offset would be achieved in 1375-1875 years. This is underestimated as the velocity difference across the shear margin decreases upstream. Thus, the current flow velocity is consistent with an age of about 2 kyrs BP, which is the time when fold amplification ceased in the shear margins (Fig. 3).

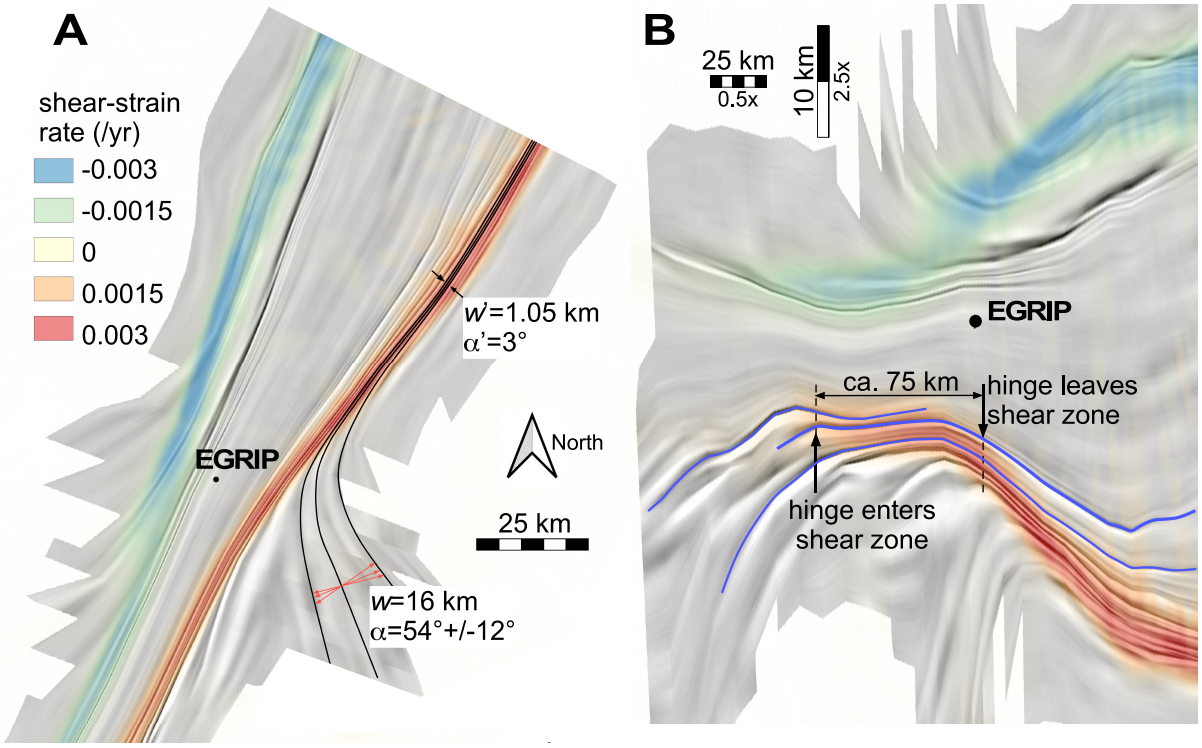


Fig. 5. (a) Folded isochrone horizon as a hillshade with overlay of shear strain rate. Black lines indicate traced fold hinges listed in Table 1. Location of the East Greenland Ice core Project (EGRIP) drill camp is shown as the black dot. (b) Same image, but now rotated 63° (long axis of North East Greenland Ice Stream, NEGIS) and then stretched 5x in the vertical direction of the rotated figure, i.e., perpendicular to the main flow direction, to highlight bends in the hinges.

From the amplitude graphs and the strain measurements, we can conclude that the upstream part of NEGIS and, thus, that the present-day NEGIS as an ice stream with distinct shear margins (Fig. 4b) was fully established by about 2 kyrs BP. Geological evidence from the northeast Greenland coast showed that the three major outlets of NEGIS (Fig.1a, the Nioghalvfjerdsfjorden Glacier (NG), the Zachariae Isstrøm (ZI), and the Storstrømmen Glacier (SG) retreated behind their current extent and advanced again at least twice during the last 45 kyrs[45]. During the Holocene Thermal Maximum (HTM) in the Early to Middle Holocene, temperatures in the Arctic were higher than today[46]. This had a large effect on Greenland ice volume and frontal positions of outlet glaciers[47]. The onset and end of this warm period were regionally different, and there is evidence from geological data that in the area of the three major outlets of the NEGIS that warming started around 8 kyrs BP and ended

approximately 4 kyrs BP[46] Accordingly, Nioghalvfjerdsfjorden Glacier was smaller than today in its extent until at least 4.6 kyrs BP[48].

The two- with established shear margins, could be interpreted as a result of increasing discharge from the NEGIS catchment area, following the readvance of the ice front after the HTM, as ice stream activity is linked to the geometry changes of an ice sheet, with increasing intensity of streaming for higher ice volume[49]. Around 4 kyrs BP, a still distributed increase of the outflow led to a drawdown of ice from the flanks and a confluent flow regime due to the geometry of the catchment and the outlet in the northeast. Localisation due to the emerging simple shearing along the vertical plane subsequently led to localised shear and the establishment of the shear margins, which was completed by about 2 kyrs BP, with an error for the absolute age of 200 years, according to our data. Enhanced flow within the ice stream induced ice-stream normal flow in the adjacent ice sheet to compensate for the stretching inside the upstream part of the ice stream, resulting in the typical bottleneck shape of NEGIS, as the shear margins are advected towards the centre of the ice stream[50].

Our observations and dating of folding require a paradigm change in our thinking on NEGIS and, therefore, other such ice streams. So far, NEGIS was considered a long-lived structure[4,10] controlled by external boundary conditions, in particular high geothermal heat flux at its upstream end[10,17]. Instead, upper NEGIS is only a few thousand years old and still changing. Our results show that an ice sheet is a delicately balanced system in which the whole flow pattern can change from shallow ice-type flank flow to effective drainage systems reaching up to the divide, facilitated by shear localization. Together with the study by Franke and colleagues[16], we are able to draw a holistic picture of the dynamics of NEGIS-style ice streams, namely that these streams can switch between branches in their catchment area, and that such a change happened in North east Greenland about 2000 years ago. This time scale is another indicator that the initiation of streaming is much more likely triggered by ice sheet geometry and processes at the boundaries than local heat flow anomalies[15]. Considering that the ice sheets are now expected to experience massive changes in their boundary conditions[51], it is imperative to include these dynamics in ice-sheet models and predictions of future sea-level rise.

# 3. Methods

## 3.1 3D Isochrone horizon

In order to assess the distortion of the radar isochrones in terms of their deformation history to determine the dynamic setting of the ice stream, the 2dimensional profiles have to be combined to produce a 3-dimensional model of the folded isochrone surfaces[16,22,32] . For this purpose, we picked selected internal reflections, which are detectable throughout most of the survey area. To ensure spatial continuity, we restrict our analysis to reflections from the upper half of the ice column. By manually assigning profile sections from two neighbouring lines to each other, a surface can be generated in a half-automated way. For this step of the analysis, we used the structural geology modelling software MOVE, a tool for analysis and 3-D visualisation in geosciences and previously employed to visualise folds in northwest Greenland's Petermann Glacier[32] and upstream of Nioghalvfjerdsfjorden Glacier in northeast Greenland. The isochrones are dated by tying them in the depth domain to the age dating of the EGRIP ice core[21] and transferring age in a particular depth to the respective isochrone at that depth. The absolute age and its uncertainty of ca 90 yrs are of minor importance in our study, as we focus on the overall deformation of the initial flat shape of the considered isochrones.

## 3.2 Dating of folding events

The method is based on the assumption that a folding event leads to a steady increase in fold amplitude with depth in all layers older than the folding event. Thus, every change in the amplitude-age trend represents a folding event. If this event happened at time $t_1$, layers younger than $t_1$ are not folded, i.e., have zero amplitudes. The amplitude trend caused by a subsequent folding event at $t_2$ will again affect all existing layers (Fig. 6). Layers between $t_1$ and $t_2$ in age only show the resulting amplitude-depth trend from the second folding event, while older layers show the cumulative effect of both folding events. Every change in the amplitudeage trend thus represents a folding event. It should be borne in mind that folding is not expected to occur at a distinct single point in time but over a certain period and that a change in the amplitude-age trend will be spread out over that period.

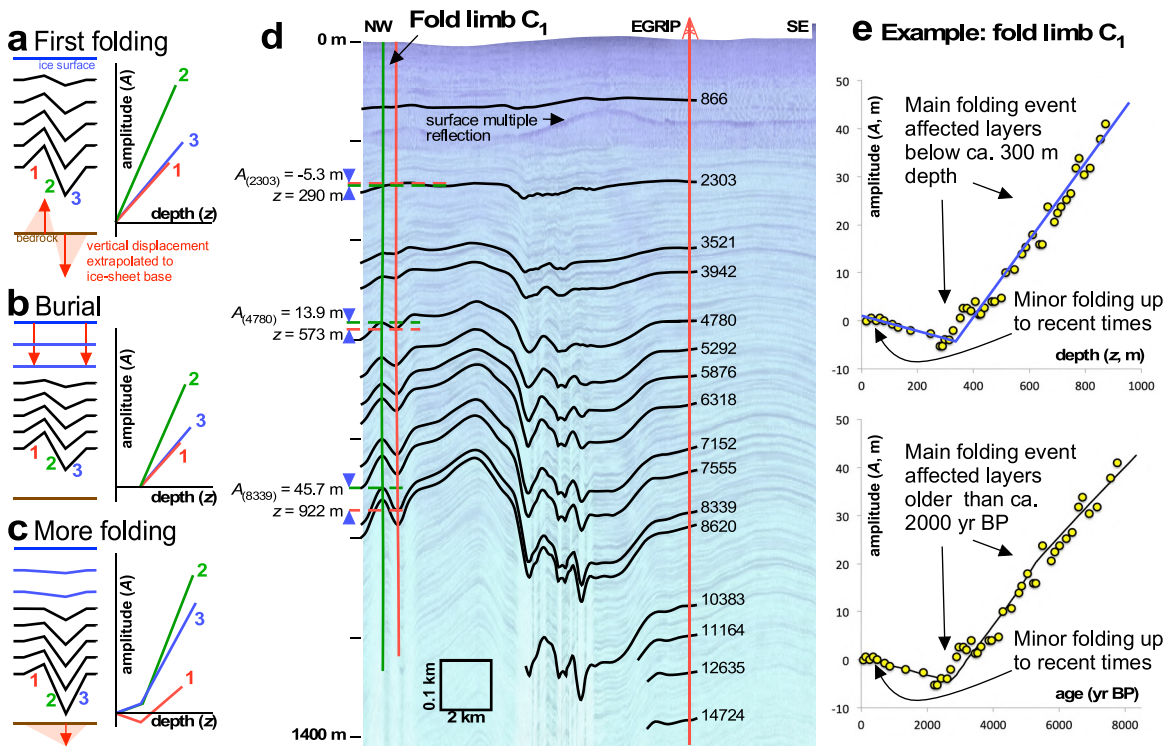


Fig. 6. Development of fold amplitudes. (a-c) Conceptual sketches for the effect of folding on layer disturbance and development of fold amplitudes (1-3) as a function of depth. (d) Part of radargram shown in Figure 2 with traced layers and respective folds. Shown are the uppermost 1400 m with y-axes ticks spaced 200 m. Numbers on the left show amplitudes and the corresponding reference depth for 3 examples (subscript indicates age of layer), green/red vertical lines on the left indicate the position of the fold hinges of the anti- and synclines. Red vertical line on right indicates the location of the East Greenland Ice core Project (EGRIP) core with each reference layer annotated with its age; in years BP. (e) Distribution of amplitudes of fold limb C1. The top panel shows amplitude as a function of depth and the bottom amplitude as a function of age The yellow dots indicate the data points derived from the radar layers. Red arrows indicate data points of example folds picked in (d). The black and blue lines indicate the trend with a clear kink around 300 m depth or 2000 yrs of age.

Folding of stratigraphy causes a change in vertical position of layers, either upwards (anticlines) or downwards (synclines) relative to the undisturbed layer level. This change in height increases downwards from approximately zero at the surface since the surface of ice sheets shows no or little expression of folding (less than a few tens of metres at the most in the study area). We may assume[52,53] that the vertical flattening or thickening strain is

approximately constant throughout most of the ice sheet, except in the bottom-most layers. This assumption is not dependent on the cause of the folding, as it essentially states that folding is caused by vertical movements that increase towards the base of the ice sheet. This could be because of basal melting or freezing[28,30], variable slip rates[31], folding due to lateral shortening[32] or even due to flow over bedrock bumps or depressions[54]. The vertical displacement can be described with the parameter:

$$z = \varepsilon z_0 \quad (1)$$

A problem is that $\varepsilon$ can only be determined if the original depth $z_0$ of a layer is known. As this is usually not the case, we can compare two adjacent vertical sections with strain $\varepsilon_1$ and $\varepsilon_2$. The difference $A$ in depth for a layer is now given by:

$$A = z_1 - z_2 \quad (2)$$

As long as positions 1 and 2 are close to each other (as in the hinges of a single fold), the pre-fold depths ($z_0$) of a layer at both locations are expected to be approximately the same. This results in a linear relationship between the amplitude $A$ and the mean depth of a layer $\langle z \rangle = (z_1+z_2)/2$:

$$\frac{z_1}{\varepsilon_1} = \frac{z_2}{\varepsilon_2} \Leftrightarrow \langle z' \rangle = \frac{z_1+z_2}{2} = \frac{(\varepsilon_1^{-1}+\varepsilon_2^{-1})}{2(\varepsilon_2^{-1}-\varepsilon_1^{-1})} A \quad (3)$$

To determine the amplitude-depth curves, as many layers in a radargram as possible were manually traced for anticline-syncline pairs. Axial planes are constructed as lines that connect the fold hinges. Near the ice surface, folds may die out upwards, in which case the axial planes are extended vertically towards the surface. Depth ($z$) of a stratigraphic layer is now defined as the vertical distance between a hinge of that layer and the ice surface at the point where it is intersected by the axial plane. Comparison of independent depth determinations by two of the authors (PDB and YZ) showed differences in $z$ up to 3 m, with a standard deviation of the differences of 0.9 m. For each anticline-syncline pair, referred to as a fold limb, this results in a set of $z_{anti}(i)$ and $z_{syn}(i)$ data for each layer $(i)$ that was deposited at time $t(i)$. The fold-limb amplitude is now defined as $A(i)=z_{syn}(i)-z_{anti}(i)$, with associated mean depth $\langle z(i) \rangle = (z_{syn}(i)+z_{anti}(i))/2$.

Ages of layers were derived from tracing to or correlating layers at the EGRIP drill site where ages are known as a function of depth[21]. This results in a set of layers with known

depositional ages. In the central profile up to 21 layers < 8 kyrs BP old could be connected to the EGRIP site, while in the downstream profile this number was reduced to at least five. The error in dating of the reference layers is in the order of a few tens of years for the youngest few thousand-year-old layers, increasing to over 100 years towards 8 kyrs BP layers. Most layers within one fold limb cannot be traced all the way to the drill site or can be recognised in the radargram at that site. Their ages are estimated by interpolation, assuming that the relation between height of the layer above the bedrock ($h$) and age ($t$) is given by:

$$\frac{\langle h \rangle}{H} = Ce^{-kt} \qquad (4)$$

with $H$ the local thickness of the ice sheet, and $C$ and $k$ two constants derived by fitting to the nearest dated layers above and below the layer of unknown age.

This corresponds to a Nye-type approach of age depth relationship, where $C$ and $k$ are dependent on initial layer thickness and initial total ice thickness, both not well constrained in a dynamically variable setting[37] As layer thickness are relatively constant down to layers ca 8 kyrs in age, this interpolation is close to linear. Note that mean depths for each fold were used for the interpolation. All ages are reported as before the year 2000 CE.

## 3.3 Procrustes analysis

To determine common trends, we use principles of shape analysis as used in biology or anthropology. These disciplines often face the problem of comparing shapes, for example to assign or distinguish fossil remains of modern humans versus Neanderthals[55]. Here the issue is to find commonalities and difference between the shapes of the various amplitude ($A$) versus depth ($z$) or age (t) graphs (*Az or At*-graphs). We therefore employ a similar normalisation procedure, known as Procrustes analysis[56,57], to remove scale and absolute amplitude of the *Az*graphs. Furthermore, to be able to group folds, we need comparable data points, known as "landmarks" in geometric morphometrics. For this we first determine the amplitude *A(t,i)* of each fold limb ($i$) for a fixed series of ages ($t$), here every 100 years, by linear interpolation of the raw amplitude-age data. This was done for the period from 7500 yr BP to the present, to ensure that data for this period are available for all fold limbs. Each *Az*-graph is thus defined by 76 such landmarks.

The first step of the Procrustes normalisation is shifting all landmarks to a common reference, here the mean amplitude (<*A(i)*>): *A′(t,i)= A(t,i)* - <*A(i)*>. The next step is the normalisation for scale, defined by the mean absolute shifted amplitude <|*A′(i)*|>: *A″(t,i)= A′(t,i)*/< |*A′(i)*|>.

Fold limbs were then divided into two groups: (i) folds in or near the shear margins, and (ii) folds inside NEGIS (only measured in the downstream section) and folds well outside of the shear margin on the southeastern side of NEGIS. Due to the very strong distortion in the southern shear margin, no folds were analysed directly inside this margin. Depths of layers are measured from the surface of the ice sheet, which means that amplitudes at the surface are zero by definition. For plotting, the normalised *A″* data are therefore shifted so that *A″*(i)=0 m. Data are plotted (Fig. 3) with 1σ error bars.

### 3.4 Strain from rotation of fold hinges and the reduction of fold wavelength

Outside NEGIS fold hinges are oriented at an angle $\alpha$ relative to the shear margin (Fig. 4d). Inside the shear margin the hinges are rotated to an angle $\alpha'$, depending on the amount of shear strain ($\gamma$). The shear strain is given, assuming perfect simple shear, by:

$$\gamma = 2\left\{\frac{(1-\cos(2\alpha))}{\tan(\alpha-\alpha')} - \sin(2\alpha)\right\}^{-1} \quad (5)$$

Shear in the margins does not only rotate the fold axes, but also reduces the wavelength. Folds in the shear margins are therefore much narrower than outside the margins. We use the ratio $w/w'$, where $w$ is the wavelength outside the shear margin and $w'$ the wavelength inside the shear margin, measured in the direction perpendicular to the shear margin (Fig. 4d). Assuming simple shear we obtain:

$$\frac{w}{w'} = \sqrt{1+\gamma^2}\cos(\tan^{-1}(\gamma) - \alpha) \quad (6)$$

Unfortunately, there is no simple analytical solution to this equation, but the iterative solution for $\gamma$ is trivial.

Three fold traces (shown in black in Fig. 5a) were traced. They enter the shear margin to the east of EGRIP. Their spacing $w$ was determined where the fold-hinge trend $\alpha$, relative to the shear margin, ranges from 54° to 75° and $w$ from 15.9 to 16.6 km. In the marginal shear zone, the fold train narrows to approximately one km, giving $w/w'$ ranging from 15.9 to 16.6,

depending on the value of $\alpha$ that varies within the fold train. Within the shear margin $\alpha$' is about 3°. Table 1 provides the shear strain estimates, resulting in an estimated shear strain of $\gamma \approx 18$.

Table 1. Shear strain estimates, assuming perfect simple shear and a final angle of α'=3° and final wavelength of w'=1.05 km for three traced fold axes, treated as passive marker lines.

| fold | $\alpha$ (°) | $w_0$ (km) | $\gamma$ (wavelength) | $\gamma$ (rotation) |
|---|---|---|---|---|
| 1 | 54.1 | 16.2 | 19.3 | 18.4 |
| 2 | 62.1 | 15.9 | 17.5 | 18.6 |
| 3 | 74.8 | 16.6 | 16.9 | 18.8 |
| mean | | | 17.9 | 18.6 |

## 3.4 Shear zone softening

The full-field ELLE+VPFFT[33,58–60] simulation code was used to estimate the amount of weakening due to simple shearing along a vertical plane in ice with a strong crystallographic preferred orientation (CPO) in which the basal planes are initially aligned along the horizontal plane. In the semi-2D model, the material is described by 256x256 elements or crystallites, each with their own crystallographic orientation. C-axes were initially randomly oriented within ±5° perpendicular to the model plane. The code uses a spectral solver[39] to determine the stress and strain-rate field compatible with the imposed boundary conditions. An average dextral simple-shear velocity field and zero strain rate in the 3rd dimension was used as boundary conditions.

The code assumes that deformation is achieved by power-law slip along the basal, prismatic and pyramidal crystallographic planes of ice 1h, using a stress exponent[62] of 4. The strong anisotropy of ice 1h is incorporated by setting the friction parameter or critical resolved shear stress 16x lower for the basal plane than for any other slip planes. Ice deforming by basal slip only is thus 16x weaker than ice deforming by slip along the other planes at a given strain rate. Von Mises stress and strain-rates are used to describe the bulk strength of the material as a function of strain (Fig. 7). Each step, the velocity field is used to calculate and update the lattice rotation in each element. The CPO is visualised (Fig. 7) by plotting the c-axes' ODF (orientation density function) which represents the volume fraction of crystallites with a

certain orientation in a lower hemisphere stereographic projection (using the texture analysis software MTEX[63]).

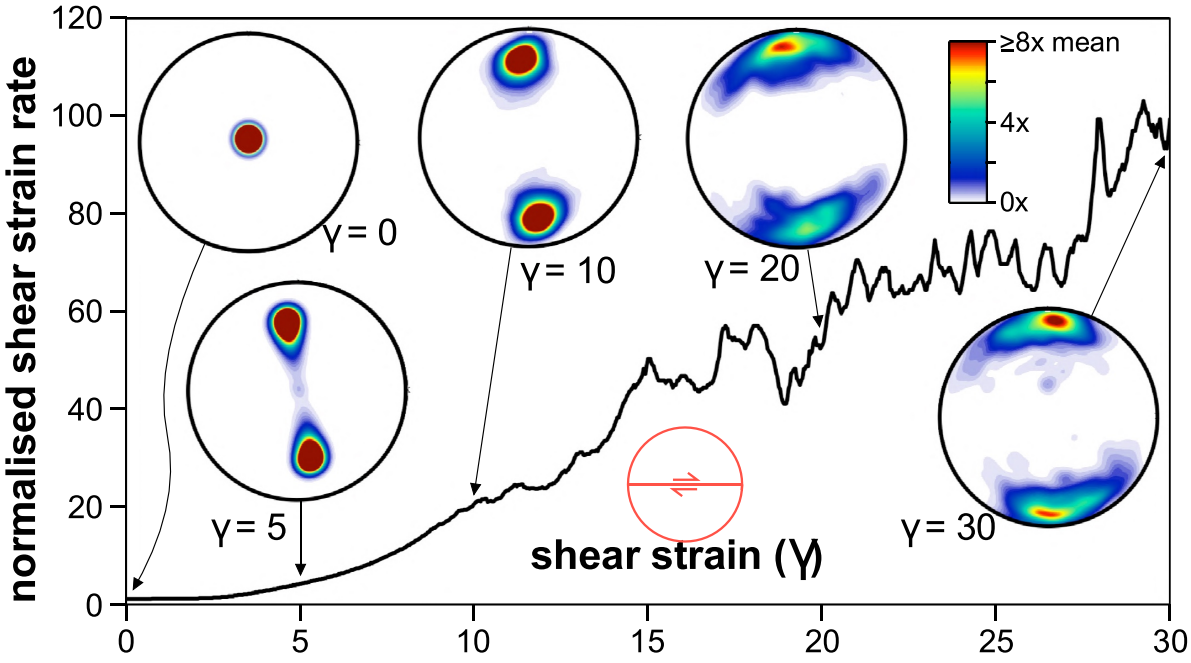


Fig. 7. Modelling shear zone softening. ELLE+VPFFT35,58 results of simple shearing of ice 1h, starting with a strong vertical point maximum of the c-axis orientations (±5°), a 16x weaker basal plane, and a stress exponent of 4 61. ELLE is a numerical simulation platform for modelling microstructure in geological processes. VPFFT indicates the viscoplastic deformation code. The simulation illustrates the evolution and reorientation of the CPO from the ice sheet into the shear margin. The modelled plane is horizontal (bedrock parallel) and is then subjected to simple shear with a vertical shear plane. The graph shows the normalized shear strain rate (at a constant stress) vs. shear strain as well as pole figures (lower hemisphere; classical glaciologic projection looking down a drill core into the ice) until a shear strain of $\gamma$=30. The single point maximum orientation of c-axes first divides into two point maxima until a shear strain of $\gamma$=10. Between $\gamma$=10 and $\gamma$=20 a transition occurs, when the two point maxima rotate towards a broad new single maximum perpendicular to the shear plane. The total softening is about a hundred at a shear strain of $\gamma$=30, and already 20 at a shear strain of $\gamma$=10.

## 3.5 Folding of anisotropic ice

In another ELLE+VPFFT simulation, similar to that to model the shear softening, we investigated the folding of passive lines parallel to the shortening direction in pure-shear shortening. Modelling code and all settings were identical to those described for modelling shear softening (see above), except for the boundary conditions. The initially square model was deformed under plane-strain, pureshear velocity boundary conditions with horizontal shortening and vertical extension in steps of 2% shortening. C-axes (normal to the easy-glide basal plane) where initially aligned parallel (±5° standard deviation) to the vertical extension direction. The deformation of initially horizontal passive marker lines was traced, using the calculated velocity field for each step, to reveal folding induced by deformation of the anisotropic material. Figure 8a shows that folds form and that the CPO evolves from an initial point maximum to a girdle with two maxima, and finally towards a point maximum parallel to the shortening direction. Fold amplitudes were determined by taking the distance between the highest and lowest point along one folded marker line. Figure 8b shows that active fold amplification ceases from about 25% shortening.

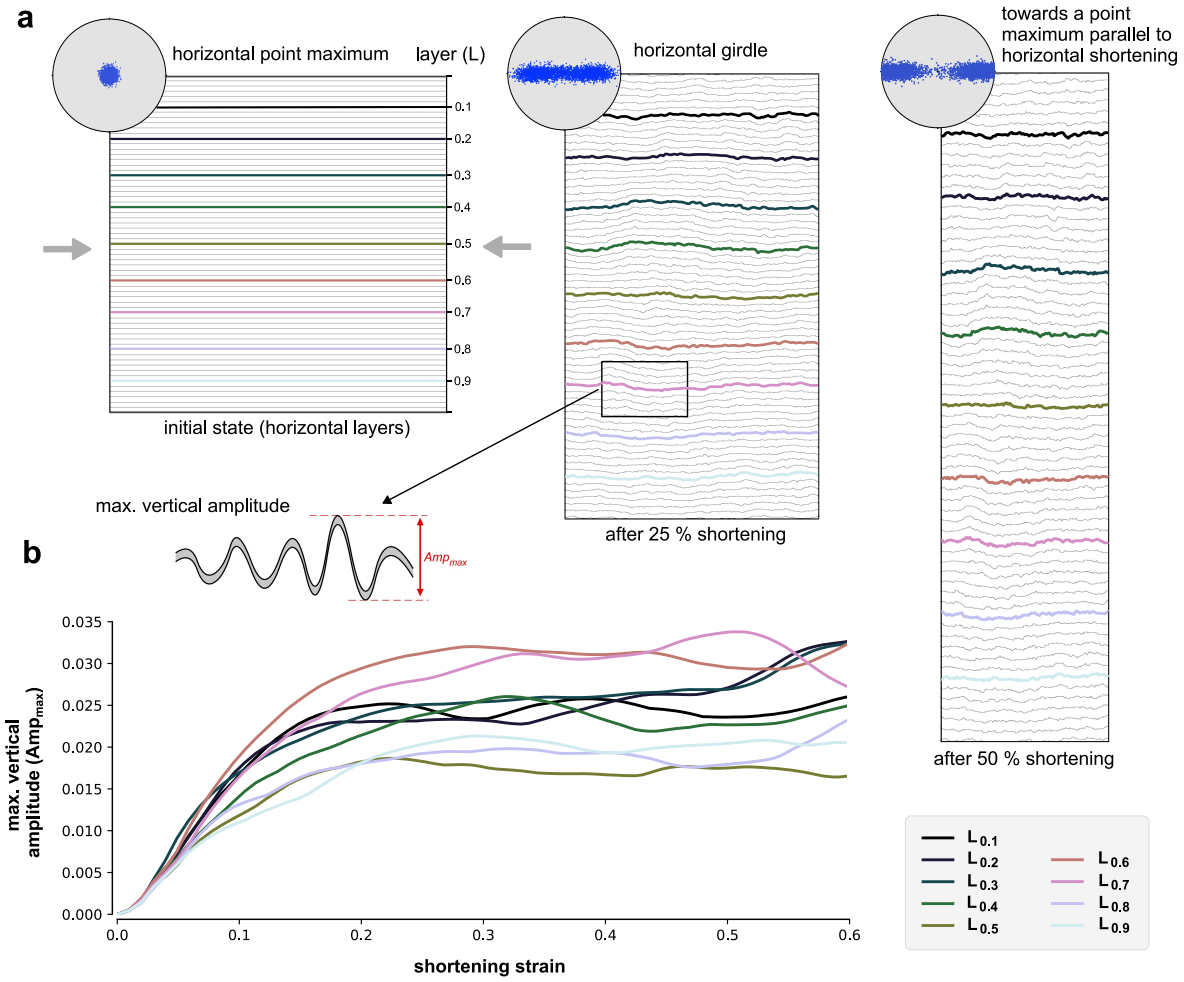


Fig. 8. Result of numerical modelling of folding in anisotropic ice (Elle+VPFFT). ELLE is a numerical simulation platform for modelling microstructure in geological processes. VPFFT indicates the viscoplastic deformation code. (a) Whole model at three stages of plane-strain horizontal shortening (0, 25 and 50%) with passive marker lines that illustrate the folding of originally horizontal, mechanically passive layers (L). Insets show the distribution of c-axes that are perpendicular to the easy glide basal planes of ice. Projection is looking down from the top of the model, parallel the vertical extension direction. C-axes are thus initially aligned parallel to the extension direction with a standard deviation of ±5°. Folding of the aligned basal planes leads to the formation of a girdle distribution with two point maxima that move to the shortening direction with increasing strain. (b) Graph of the maximum vertical amplitude of nine equally spaced, initially horizontal passive marker lines, highlighted in colour in (a). The maximum vertical amplitude is the difference between the highest and lowest point along a marker line (inset). Fold amplification ceases at about 25% shortening when the initial strong alignment of c-axes is converted to a partial girdle.

## Acknowledgements

We thank the Kenn Borek crew of the research aircraft Polar 6 andsystem engineer Lukas Kandora. Logistical support in the field was provided by the East Greenland Ice-Core Project (EGRIP). EGRIP is directed and organised by the Center of Ice and Climate at the Niels Bohr Institute. It is supported by funding agencies and institutions in Denmark (A. P. Møller Foundation, University of Copenhagen), USA (US National Science Foundation, Office of Polar Programs), Germany (Alfred Wegener Institute, Helmholtz Centre for Polar and Marine Research), Japan (National Institute of Polar Research and Arctic Challenge for Sustainability), Norway (University of Bergen and Bergen Research Foundation), Switzerland (Swiss National Science Foundation), France (French Polar Institute Paul-Emile Victor, Institute for Geosciences and Environmental research) and China (Chinese Academy of Sciences and Beijing Normal University). We acknowledge the use of the CReSIS toolbox from CReSIS generated with support from the University of Kansas, NASA Operation IceBridge grant NNX16AH54G, and NSF grants ACI-1443054, OPP-1739003, and IIS-1838230. Other funding: AWI Strategy fund (DJ, SF); Helmholtz HGF YIG VH-NG-80 (DJ); DFG Walter Benjamin Programme, project number: 563506043073 (SF); DFG grant DFG BA643/1-1 (CCB); China Scholarship Council grant no. 202006010063 (YZ) and grant no. 202008510177 (YH); Spanish Ministry of Science, Innovation and Universities, Juan de la Cierva-Incorporación fellowship, grant no. IJC2018-036826-I (MGL).

## Data Availability

The ice thickness data of the EGRIP-NOR-2018 survey and refined bed topography[11] is available at: https://doi.pangaea.de/10.1594/PANGAEA.907918 The complete radar data set will be additionally made available as part of a data collection for Northern Greenland. The GICC05-EGRIP-1 timescale for the EGRIP ice core[21] can be obtained here: https://doi.org/10.1594/PANGAEA.922139. Amplitudes, depths and age of the picked isochrones for the dating of the folds are available as Extended Data Material. The EGRIP-NOR-2018 airborne radar profiles are available from PANGAEA: https://doi.org/10.1594/PANGAEA.928569[64]. The three-dimensional 7.3 ka stratigraphic horizon of NEGIS is available from PANGAEA:

https://doi.pangaea.de/10.1594/PANGAEA.954991[65]. The data points for the age-depth graphs in figure 3 are available in the source data file.

## Author contributions

DJ, SF and PDB were the lead authors

DJ conceived the idea of folds dragged into the ice stream, while PDB conceived the method to date folding events

TB, DJ, and OE designed the grid of airborne radar flights with input from PDB

TB, DJ, and JP collected the radar data

SF, JP and DJ processed the radar data

SF and DJ constructed the 3D model and stratigraphic surface

TdR and G-ML determined the weakening as a result of CPO change

YH carried out ELLE+VPFFT folding simulations

YZ, CCB and PDB collected the amplitude-depth data

PDB carried out the strain analyses for the shear margins

IW, JE, JK, and NS measured ice fabric data and processed the results

NN provided the data for calculating the strain rate field

DJ, SF, PDB, CCB, TB, DDJ, JE, OE, YH, JK, MGL, HM, NN, JP, TR, TS, NS, IW, FW, YZ participated in writing and discussing the final results.

## References

1. Choi, Y., Morlighem, M., Rignot, E. & Wood, M. Ice dynamics will remain a primary driver of Greenland ice sheet mass loss over the next century. *Commun Earth Environ* 2, 26 (2021).

2. Khan, S. A. *et al.* Sustained mass loss of the northeast Greenland ice sheet triggered by regional warming. *Nat Clim Change* 4, 292–299 (2014).

3. Christianson, K. *et al.* Dilatant till facilitates ice-stream flow in northeast Greenland. *Earth Planet Sc Lett* 401, 57–69 (2014).

4. Keisling, B. A. *et al.* Basal conditions and ice dynamics inferred from radarderived internal stratigraphy of the northeast Greenland ice stream. *Ann Glaciol* 55, 127–137 (2014).

5. Karlsson, N. B. & Dahl-Jensen, D. Response of the large-scale subglacial drainage system of Northeast Greenland to surface elevation changes. *Cryosphere* 9, 1465–1479 (2015).

6. Schoof, C. & Mantelli, E. The role of sliding in ice stream formation. *Proc Royal Soc* 477, 20200870 (2021).

7. Krieger, L., Floricioiu, D. & Neckel, N. Drainage basin delineation for outlet glaciers of Northeast Greenland based on Sentinel-1 ice velocities and TanDEM-X elevations. *Remote Sens Environ* 237, 111483 (2020).

8. Joughin, I., Smith, B. E. & Howat, I. M. A complete map of Greenland ice velocity derived from satellite data collected over 20 years. *J Glaciol* 64, 1–11 (2018). 9. Morlighem, M. *et al.* BedMachine v3: Complete Bed Topography and Ocean Bathymetry Mapping of Greenland From Multibeam Echo Sounding Combined With Mass Conservation. *Geophys Res Lett* 44, 11,051-11,061 (2017).

10. Fahnestock, M., Abdalati, W., Joughin, I., Brozena, J. & Gogineni, P. High Geothermal Heat Flow, Basal Melt, and the Origin of Rapid Ice Flow in Central Greenland. *Science* 294, 2338–2342 (2001).

11. Franke, S. *et al.* Bed topography and subglacial landforms in the onset region of the Northeast Greenland Ice Stream. *Ann Glaciol* 61, 143–153 (2020).

12. Franke, S. *et al.* Complex Basal Conditions and Their Influence on Ice Flow at the Onset of the Northeast Greenland Ice Stream. *J Geophys Res Earth Surf* 126, (2021).

13. Hvidberg, C. S. *et al.* Surface velocity of the Northeast Greenland Ice Stream (NEGIS): assessment of interior velocities derived from satellite data by GPS.

*Cryosphere* 14, 3487–3502 (2020).

14. Grinsted, A. *et al.* Accelerating ice flow at the onset of the Northeast Greenland Ice Stream. *Nat Commun* 13, 5589 (2022).

15. Bons, P. D. *et al.* Comment on "Exceptionally high heat flux needed to sustain the Northeast Greenland Ice Stream" by Smith-Johnsen et al. (2020). *Cryosphere* 15, 2251–2254 (2021).

16. Franke, S. *et al.* Holocene ice-stream shutdown and drainage basin reconfiguration in northeast Greenland. *Nat Geosci* 15, 995–1001 (2022). 17. Smith-Johnsen, S., Fleurian, B. de, Schlegel, N., Seroussi, H. & Nisancioglu, K. Exceptionally high heat flux needed to sustain the Northeast Greenland Ice Stream. *Cryosphere* 14, 841–854 (2020).

18. Franke, S. *et al.* Airborne ultra-wideband radar sounding over the shear margins and along flow lines at the onset region of the Northeast Greenland Ice Stream. *Earth Syst Sci Data* 14, 763–779 (2022).

19. Rodriguez-Morales, F. *et al.* Advanced Multifrequency Radar Instrumentation for Polar Research. *IEEE T Geosci Remote* 52, 2824–2842 (2013).

20. Alfred Wegener Institut, Helmholtz-Zentrum für Polar und Meeresforschung. Polar aircraft Polar5 and Polar6 operated by the Alfred Wegener Institute. *J Large-scale Res Facil Jlsrf* 2, 87 (2016).

21. Mojtabavi, S. *et al.* A first chronology for the East Greenland Ice-core Project (EGRIP) over the Holocene and last glacial termination. *Clim Past* 16, 2359–2380 (2020).

22. Franke, S., *et al.* Three-dimensional topology dataset of folded radar stratigraphy in northern Greenland. Scientific Data 10, 525 (2023).

23. Winter, K. *et al.* Airborne radar evidence for tributary flow switching in Institute Ice Stream, West Antarctica: Implications for ice sheet configuration and dynamics. *J Geophys Res Earth Surf* 120, 1611–1625 (2015).

24. Siegert, M. J. *et al.* Ice Flow Direction Change in Interior West Antarctica. *Science* 305, 1948–1951 (2004).

25. Catania, G. A., Scambos, T. A., Conway, H. & Raymond, C. F. Sequential stagnation of Kamb Ice Stream, West Antarctica. *Geophys Res Lett* 33, (2006).

26. Schroeder, D. M. *et al.* Five decades of radioglaciology. *Ann Glaciol* 61, 1–13 (2020).

27. Ross, N., Corr, H. & Siegert, M. Large-scale englacial folding and deep-ice stratigraphy within the West Antarctic Ice Sheet. *Cryosphere* 14, 2103–2114 (2020).

28. Vieli, G. J.-M. C. L., Martín, C., Hindmarsh, R. C. A. & Lüthi, M. P. Basal freeze-on generates complex ice-sheet stratigraphy. *Nat Commun* 9, 4669 (2018).

29. MacGregor, J. A. *et al.* Radiostratigraphy and age structure of the Greenland Ice Sheet. *J Geophys Res Earth Surf* 120, 212–241 (2015).

30. Bell, R. E. *et al.* Deformation, warming and softening of Greenland's ice by refreezing meltwater. *Nat Geosci* 7, 497–502 (2014).

31. Wolovick, M. J., Creyts, T. T., Buck, W. R. & Bell, R. E. Traveling slippery patches produce thickness-scale folds in ice sheets. *Geophys Res Lett* 41, 8895– 8901 (2014).

32. Bons, P. D. *et al.* Converging flow and anisotropy cause large-scale folding in Greenland's ice sheet. *Nat Commun* 7, 11427 (2016).

33. Alsop, G.I., Weiberger, R. Levi, T., and Marco, S. Cycles of passive versus active diapirism recorded along an exposed salt wall. Journal of Structural Geology 84, 47-67, (2016).

34. de Riese, T. de *et al.* Shear localisation in anisotropic, non-linear viscous materials that develop a CPO: A numerical study. *J Struct Geol* 124, 81–90 (2019).

35. Llorens, M.-G. *et al.* Full-field predictions of ice dynamic recrystallisation under simple shear conditions. *Earth Planet Sc Lett* 450, 233–242 (2016).

36. Young, T. J. *et al.* Inferring Ice Fabric From Birefringence Loss in Airborne Radargrams: Application to the Eastern Shear Margin of Thwaites Glacier, West Antarctica. *J Geophys Res Earth Surf* 126, (2021).

37. Gerber, T. A., et al. Crystal orientation fabric anisotropy causes directional hardening of the Northeast Greenland Ice Stream. Nat Commun. 14, 2653. https://doi.org/10.1038/s41467-023-38139-8, (2023).

38. Budd, William F. and Tim H. Jacka, 1989, A review of ice rheology for ice sheet modelling, *Cold Regions Science and Technology* 16, 107-144 (1989).

39. Carreras, J., Cosgrove, J. W. & Druguet, E. Strain partitioning in banded and/or anisotropic rocks: Implications for inferring tectonic regimes. *J Struct Geol* 50, 7– 21 (2013)

40. Ramsay, J. G. Shear zone geometry: A review. *J Struct Geol* 2, 83–99 (1980).

41. Lebensohn, R. A. N-site modeling of a 3D viscoplastic polycrystal using Fast Fourier Transform. *Acta Mater* 49, 2723–2737 (2001).

42. Lebensohn, R. A. & Rollett, A. D. Spectral methods for full-field micromechanical modelling of polycrystalline materials. *Comp Mater Sci* 173, 109336 (2020).

43. Griera, A. *et al.* Numerical modelling of porphyroclast and porphyroblast rotation in anisotropic rocks. *Tectonophysics* 587, 4–29 (2013).

44. Ran, H. *et al.* Time for anisotropy: The significance of mechanical anisotropy for the development of deformation structures. *J Struct Geol* 125, 41–47 (2019).

45. Larsen, N. K. *et al.* Instability of the Northeast Greenland Ice Stream over the last 45,000 years. *Nat Commun* 9, 1872 (2018).

46. Miller, G. H. *et al.* Temperature and precipitation history of the Arctic. *Quaternary Sci Rev* 29, 1679–1715 (2010).

47. Axford, Y., Vernal, A. de & Osterberg, E. C. Past Warmth and Its Impacts During the Holocene Thermal Maximum in Greenland. *Annu Rev Earth Pl Sc* 49, 1–29 (2020).

48. Bennike, O. & Weidick, A. Late Quaternary history around

Nioghalvfjerdsfjorden and Jøkelbugten, North-East Greenland. *Boreas* 30, 205– 227 (2001).

49. Stokes, C. R., Margold, M., Clark, C. D. & Tarasov, L. Ice stream activity scaled to ice sheet volume during Laurentide Ice Sheet deglaciation. *Nature* 530, 322– 326 (2016).

50. Passchier, C. W. & Platt, J. P. Shear zone junctions: Of zippers and freeways. *J Struct Geol* 95, 188–202 (2017).

51. Fox-Kemper, B. *et al.* Ocean, Cryosphere and Sea Level Change. in *Climate Change 2021: The Physical Science Basis. Contribution of Working Group I to the Sixth Assessment Report of the Intergovernmental Panel on Climate Change* (eds.

["Masson-Delmotte et al.) 1211–1362 (Cambridge University Press). doi:10.1017/9781009157896.011.

52. Dansgaard, W. & Johnsen, S. J. A Flow Model and a Time Scale for the Ice Core from Camp Century, Greenland. *J Glaciol* 8, 215–223 (1969).

53. Nye, J. F. The distribution of stress and velocity in glaciers and ice-sheets. *Proc Royal Soc Lond Ser Math Phys Sci* 239, 113–133 (1957).

54. Raymond, M. J. & Gudmundsson, G. H. On the relationship between surface and basal properties on glaciers, ice sheets, and ice streams. *J Geophys Res Solid Earth* 110, (2005).

55. Benazzi, S. *et al.* Early dispersal of modern humans in Europe and implications for Neanderthal behaviour. *Nature* 479, 525–528 (2011).

56. Rohlf, F. J. & Marcus, L. F. A revolution morphometrics. *Trends Ecol Evol* 8, 129–132 (1993).

57. O'Higgins, P. The study of morphological variation in the hominid fossil record: biology, landmarks and geometry. *J Anat* 197, 103–120 (2000).

58. Steinbach, F. *et al.* Strain localization and dynamic recrystallization in the ice– air aggregate: a numerical study. *Cryosphere* 10, 3071–3089 (2016).

59. Llorens, M.-G. *et al.* Dynamic recrystallization during deformation of polycrystalline ice: insights from numerical simulations. *Philosophical Transactions Royal Soc Math Phys Eng Sci* 375, 20150346 (2017).

60. Piazolo, S. *et al.* A review of numerical modelling of the dynamics of microstructural development in rocks and ice: Past, present and future. *J Struct Geol* 125, 111–123 (2019).

61. Bons, P.D., *et al*. Greenland Ice Sheet – Higher non-linearity of ice flow significantly reduces estimated basal motion. *Geophysical Research Letters* 45, 6542-6548. Doi:10.1029/2018GL078356 (2018).

62. Bons, P. D. *et al.* Greenland Ice Sheet: Higher Nonlinearity of Ice Flow Significantly Reduces Estimated Basal Motion. *Geophys Res Lett* 45, 6542–6548 (2018).

63. Mainprice, D., Bachmann, F., Hielscher, R. & Schaeben, H. Descriptive tools for the analysis of texture projects with large datasets using MTEX: strength, symmetry and components. *Geological Soc Lond Special Publ* 409, 251–271 (2015).

64. Franke, S. et al., Ultra-wideband radar over the shear margins and along flow lines at the onset region of the Northeast Greenland Ice Stream (NEGIS), PANGAEA, https://doi.org/101594/PANGAEA.928569 (2023).

65. Franke, S. et al. Three-dimensional anatomy of folded radar stratigraphy in polar ice sheets. PANGAEA, https://doi.org/10.1594/PANGAEA.954991 (2023).

# Chapter 5

## Comment on “Exceptionally high heat flux needed to sustain the Northeast Greenland Ice Stream” by Smith-Johnsen et al.(2020)

**Paul D. Bons[1,2], Tamara de Riese[2], Steven Franke[3], Maria-Gema Llorens[4], Till Sachau[2], Nicolas Stoll[3], Ilka Weikusat[2,3], Julien Westhoff[5], Yu Zhang[2]**

[1]School of Earth Science and Resources, China University of Geosciences, Beijing, China

[2]Department of Geosciences, Eberhard Karls University Tübingen, Tübingen, Germany

[3]Alfred Wegener Institute Helmholtz Centre for Polar and Marine Research, Bremerhaven Germany

[4]Geosciences Barcelona, CSIC, Barcelona, Spain

[5]Physics of Ice, Climate and Earth, University of Copenhagen, Copenhagen, Denmark

Published in The Cryosphere, 15(5), 2251–2254. doi:10.5194/tc-15-2251-2021

This is an author version of the manuscript. The fulltext (copy-edited publishers version) can be accessed at: https://doi.org/10.5194/tc-15-2251-2021

## Abstract

Smith-Johnsen et al. (The Cryosphere, 14, 841–854, https://doi.org/10.5194/tc-14-841-2020, 2020) model the effect of a potential hotspot on the Northeast Greenland Ice Stream (NEGIS). They argue that a heat flux of at least 970 mW $m^{-2}$ is required to have initiated or to control NEGIS. Such an exceptionally high heat flux would be unique in the world and is incompatible with known geological processes that can raise the heat flux. Fast flow at NEGIS must thus be possible without the extraordinary melt rates invoked in Smith-Johnsen et al. (2020).

## 1. Introduction

The prominent Northeast Greenland Ice Stream (NEGIS) is an exceptionally large ice stream in the Greenland Ice sheet. It is over 500 km long, almost reaches the central ice divide and contributes significantly to overall ice drainage from the Greenland Ice sheet (Rignot and Mouginot, 2012; Aschwanden et al., 2016). What causes or drives this ice stream remains enigmatic. Several authors have suggested that NEGIS was initiated or is controlled by an elevated geothermal heat flux from the underlying bedrock (Fahnestock et al., 2001; Keisling et al., 2014; MacGregor et al., 2016). This hypothesis was investigated in the modelling study of Smith-Johnsen et al. (2020). They conclude that "a minimum heat flux value of 970 mW $m^{-2}$ located close to the East Greenland Ice-core Project (EGRIP) is required locally to reproduce the observed NEGIS velocities, giving basal melt rates consistent with previous estimates. The value cannot be attributed to geothermal heat flux alone and we suggest hydrothermal circulation as a potential explanation for the high local heat flux". It should be noted that this statement is preceded by the caveat "In our model experiment". The high minimum heat flux of 970 mW $m^{-2}$ mainly derives from Fahnestock et al. (2001), who inferred it from their interpreted 0.1 m $yr^{-1}$ melt rate in the upstream area of NEGIS. MacGregor et al. (2016) obtained similar high melting rates in the upstream area of NEGIS, actually in a larger area than that assumed by Smith-Johnsen et al. (2020) in their modelling. However, Buchardt and Dahl-Jensen (2007) obtained a more than 10 times lower melt rate along the ridge between GRIP and NorthGRIP, which is on the margin of the high-melting rate area of MacGregor et al. (2016).

## 2. Discussion

An elevated geothermal heat flux is usually attributed to the trail of the Iceland plume (Rogozhina et al., 2016; Martos et al., 2018; Artemieva, 2019). For example, Rogozhina et al. (2016) suggest that the Iceland hotspot left a 400 km wide, roughly NW–SE-oriented swath of elevated geothermal heat flux across Greenland as the crust there was positioned above the hotspot 35–80 Myr ago. However, the elevated geothermal heat flux in the trail only reaches values of the order of 100 mW $m^{-2}$ and is not expected to have local spikes. Viscous fingering of hot asthenosphere from the Iceland hotspot can potentially heat the overlying crust as far away as the North Sea according to Schoonman et al. (2017). However, temperatures drop off away from the central Iceland hotspot, especially underneath Greenland, as shown by, for example, the temperature at 80–150 km depth beneath Iceland and the adjacent Atlantic Ocean (Fig. 8 in Lebedev et al., 2017).

Fahnestock et al. (2001) base their inferred high heat flux on the depths of stratigraphic ice layers up to 9000 years in age, suggesting that the heat flux has at least been so high for the last few thousands of years. A steady-state 970 mW $m^{-2}$ heat flux would imply a local geothermal gradient close to a staggering ca. 400 °C $km^{-1}$, at which felsic rocks would melt at about 2 km depth. Although Fahnestock et al. (2001) suggest that the local bedrock topography is consistent with volcanism, there is no independent evidence for volcanism that is expected above such shallow melting.

Fahnestock et al. (2001) already note that 970 mW $m^{-2}$ is many times the background median value of about 60 mW $m^{-2}$ in continental crust, in which worldwide geothermal heat flux values rarely exceed 200 mW $m^{-2}$ (Hofmeister and Criss, 2005; Davies, 2013). Recently, Rezvanbehbahani et al. (2017) used a machine learning technique that includes tectonic setting, regional geology and ice core measurements to predict a geothermal heat flux in a range of 20–150 mW $m^{-2}$ across Greenland. These values are in line with geothermal heat flux values determined for Antarctica (Dziadek et al., 2017; Burton-Johnson et al., 2020a, b; Shen et al., 2020), with only local excursions above 200 mW $m^{-2}$ in the tectonically active West Antarctic Rift System (Schroeder et al., 2014).

The geothermal heat flux map of Iceland (Jóhannesson et al., 2020) shows patches, several tens of kilometres in size, with >200 mW $m^{-2}$ and one smaller spot with 300–350 mW $m^{-2}$, still far below 970 mW $m^{-2}$. Similarly, Yellowstone, which is one of the most active

continental hotspots, shows a geothermal heat flux just exceeding 150 mW $m^{-2}$ (Blackwell and Richards, 2004). These two very active hotspots with active volcanic activity thus have geothermal heat fluxes well below 970 mW $m^{-2}$. If geothermal heat flux values in the Iceland hotspot are <350 mW $m^{-2}$, it is highly unlikely that higher heat fluxes are encountered in its trail.

Active hotspots, such as Iceland and Yellowstone, are characterised by volcanic activity that implies the presence of magma chambers or shallow intrusions. Smith-Johnsen et al. (2020), recognising that 970 mW $m^{-2}$ is unrealistically high for a geothermal heat flux, suggest several potential alternative processes that may enhance the high heat flux, such as shallow intrusions. This is in line with Stevens et al. (2016), who conclude, regarding melt, that "ice-age cycling could help it migrate upward to shallow depth or erupt, contributing to the high observed geothermal heat flux", but with the caveat "if melt occurs at depth". The conclusion is based on the vug-wave magma-transport model of Morgan and Holtzman (2005), which is similar to the mobile-hydrofracture transport model of Bons (2001) and Bons et al. (2001). Magma transport in vug waves or mobile hydrofractures may be enhanced by ice-age cycling or tectonic events, but this will only have an effect if magma is present in the source region. The question remains if and why this would be the case underneath the upstream area of NEGIS. Furthermore, the same magma-transport mechanism also applies to igneous activity in hotspots such as Iceland. If the geothermal heat flux there is only raised locally to <350 mW $m^{-2}$, it is unlikely that it would be raised 3 times more in the Greenland crust, where there is no obvious evidence or reason for significant igneous activity.

Another potential cause for the high heat flux that is invoked by Smith-Johnsen et al. (2020) (and others, e.g. Artemieva, 2019) is hydrothermal fluid flow, which is the flux of hot fluids from deeper levels in the crust that typically leave mineral deposits (Oliver et al., 2006). An indication of the fluid flux required to achieve 0.1 m $yr^{-1}$ basal melting can be obtained by assuming that the melting is achieved by 100 °C aqueous fluids that melt basal ice at 0 °C while themselves cooling down to 0 °C. Using a heat capacity of 4.2 kJ $kg^{-1}$ $K^{-1}$ and a latent heat of 334 kJ $kg^{-1}$ for melting ice, we obtain a required fluid flux of  kg $m^{-2}$ $s^{-1}$ (or ~0.07 $m^3$ $m^{-2}$ $yr^{-1}$). This is more than 3 orders of magnitude more than the 2– kg $m^{-2}$ $s^{-1}$ expected for metamorphic fluid fluxes (Connolly and Thompson, 1989) that could potentially provide the hot fluids. Even the much lower estimated melting rate of 6.1 mm $yr^{-1}$ of Buchardt and Dahl-Jensen (2007) would require >10 times more mass of hot

fluid than expected. Hydrothermal fluid flow can therefore not produce all the heat required for a significantly elevated basal melting rate.

Uranium enrichments are known in southern Greenland in the Gardar Province (e.g. Bartels et al., 2016), and their radiogenic heat production can add to the geothermal heat flux directly, and indirectly through enhanced hydrothermal fluid flow, as is the case in the uranium-rich Mount Painter Inlier in South Australia (Weisheit et al., 2013), where the geothermal heat flux is raised to about 120 mW $m^{-2}$ (Sandiford et al., 1998). In the sediments above the world's largest known U deposit, Olympic Dam in South Australia, the geothermal heat flux is raised by only 43 mW $m^{-2}$ from a background value of 73 mW $m^{-2}$ (Houseman et al., 1989).

## 3. Conclusions

In summary, a heat flux of 970 mW $m^{-2}$ is geologically unfeasible. Any heat flux above about 100–150 mW $m^{-2}$ should be treated with caution in the absence of other evidence, such as volcanic or tectonic activity. Most other studies actually do propose much more moderate and realistic geothermal heat flux values below the Greenland Ice sheet (e.g. Buchardt and Dahl-Jensen, 2007; Rogozhina et al., 2016; Rezvanbehbahani et al., 2017; Artemieva, 2019). The original 970 mW $m^{-2}$ stems from Fahnestock et al. (2001), who derive this value from variations in radar stratigraphy elevation, which they assume to have been caused by basal melting (up to 0.1 m $yr^{-1}$). The improbable heat flux value they derive means that such elevation variations cannot be solely due to basal melting, and we need to consider other causes, such as flow heterogeneities in space or time (e.g. due to folding; Bons et al., 2016), as well as the underlying assumptions in determining basal melting.

Even though the extraordinary heat flux invoked in Smith-Johnsen et al. (2020) cannot exist at NEGIS, their model results are definitively useful. They indicate that some other weakness exists in the NEGIS system that enables the fast flow, most likely with a supporting role of geologically plausible heat fluxes. The studies by both Fahnestock et al. (2001) and Smith-Johnsen et al. (2020) thus highlight the exciting challenge still ahead to truly understand ice streams such as NEGIS and ice sheet dynamics in general.

## Author contributions

PDB provided the initial idea and concept of the paper, which was discussed and written jointly by all authors.

## Acknowledgements

Maria-Gema Llorens is supported by a Juan de la Cierva-Incorporación fellowship, funded by the Spanish Ministry of Science, Innovation and Universities, Nicolas Stoll and Ilka Weikusat by the Helmholtz Junior Research group "The effect of deformation mechanisms for ice sheet dynamics", Yu Zhang by the PhD programme of the China Scholarship Council (CSC), Julien Westhoff by the Villum Investigator Project IceFlow, and Steven Franke by the AWI-Strategy fund. We thank Nanna Bjørnholt Karlsson for carefully checking the original submission and Jörg Ebbing and Nicholas Holschuh for their helpful reviews.

## Financial support

This research has been supported by the Spanish Ministry of Science, Innovation and Universities (Juan de la Cierva-Incorporación fellowship grant no. IJC2018-036826-I), the China Scholarship Council, Chinese Government Scholarship (grant no. 202006010063), the Alfred Wegener Institute Helmholtz Centre for Polar and Marine Research (grant no. VH-NG-802), and the Velux Foundations (Villum Investigator Project no. 16572).

## Review statement

This paper was edited by Nanna Bjørnholt Karlsson and reviewed by Jörg Ebbing and Nicholas Holschuh.

## References

Artemieva, I. M.: Lithosphere thermal thickness and geothermal heat flux in Greenland from a new thermal isostasy method, Earth-Scie. Rev., 188, 469–481, https://doi.org/10.1016/j.earscirev.2018.10.015, 2019.

Aschwanden, A., Fahnestock, M., and Truffer, M.: Complex Greenland outlet glacier flow captured, Nat. Com., 7, 10524, https://doi.org/10.1038/ncomms10524, 2016.

Bartels, A., Nilsson, M. K. M., Klausen, M. B., and Söderlund, U.: Mesoproterozoic dykes in the Timmiarmiit area, Southeast Greenland: evidence for a continuous Gardar dyke swarm across Greenland's North Atlantic Craton, GFF, 138, 255–275, https://doi.org/10.1080/11035897.2015.1125386, 2016.

Blackwell, D. D. and Richards, M.: Geothermal Map of North America, AAPG Map, scale 1 : 6 500 000, 2004.

Bons, P. D.: The formation of large quartz veins by rapid ascent of fluids in mobile hydrofractures, Tectonophys., 336, 1–17, https://doi.org/10.1016/S0040-1951(01)00090-7, 2001.

Bons, P. D., Dougherty-Page, J., and Elburg, M. A.: Stepwise accumulation and ascent of magmas, J. Metamorphic Geol., 19, 627–633, https://doi.org/10.1046/j.0263-4929.2001.00334.x, 2001.

Bons, P. D., Jansen, D., Mundel, F., Bauer, C. C., Binder, T., Eisen, O., Jessell, M. W., Llorens, M.-G., Steinbach, F., Steinhage, D., and Weikusat, I.: Converging flow and anisotropy cause large-scale folding in Greenland ice sheet, Nat. Com., 7, 11427, https://doi.org/10.1038/ncomms11427, 2016.

Buchardt, S. L. and Dahl-Jensen, D.: Estimating the basal melt rate at NorthGRIP using a Monte Carlo technique, Ann. Glaciol., 45, 137–142, https://doi.org/10.3189/172756407782282435, 2017.

Burton-Johnson, A., Dziadek, R., Martin, C., Halpin, J. A., Whitehouse, P. L., Ebbing, J., Martos, Y., Martin, A., Schroeder, D., Shen, W., Ritz, C., Goodge, J., Van Liefferinge, B., Pattyn, F., Reading, A., Ferraccioli, F., and The SERCE Geothermal Heat Flow Sub-Group: SARC-SERCE White Paper on Antarctic Geothermal Heat Flow: Future research directions, available at: https://scar.org/scar-library/search/science-4/research-programmes/serce/5454-scar-serce-white-paper-on-antarctic-geothermal-heat-flow/ (last access: 10 March 2021), 2020a.

Burton-Johnson, A., Dziadek, R., and Martin, C.: Review article: Geothermal heat flow in Antarctica: current and future directions, The Cryosphere, 14, 3843–3873, https://doi.org/10.5194/tc-14-3843-2020, 2020b.

Connolly, J. A. D. and Thompson, A. B.: Fluid and enthalpy production during regional metamorphism, Contrib. Mineral. Petrol., 102, 347–366, 1989.

Davies, J. H.: Global map of solid Earth surface heat flow, Geochem. Geophy. Geosy., 14, 4608–4622, https://doi.org/10.1002/ggge.20271, 2013.

Dziadek, R., Gohl, K., Diehl, A., and Kaul, N.: Geothermal heat flux in the Amundsen Sea sector of West Antarctica: New insights from temperature measurements, depth to the bottom of the magnetic source estimation, and thermal modeling, Geochem. Geophy. Geosy., 18, 2657–2672, https://doi.org/10.1002/2016GC006755, 2017.

Fahnestock, M., Abdalati, W., Joughin, I., Brozena, J., and Gogineni, P.: High Geothermal Heat Flow, Basal Melt, and the Origin of Rapid Ice Flow in Central Greenland, Science, 294, 2338–2342, https://doi.org/10.1126/science.1065370, 2001.

Hofmeister, A. M. and Criss, R. E.: Earth's heat flux revised and linked to chemistry, Tectonophys., 395, 159–177, https://doi.org/10.1016/j.tecto.2004.09.006, 2005.

Houseman, G. A., Cull, J. P., Muir, P. M., and Paterson, H. L.: Geothermal signatures and uranium ore deposits on the Stuart Shelf of South Australia, Geophysics, 54, 158–170, https://doi.org/10.1190/1.1442640, 1989.

Jóhannesson, T., Pálmason, B., Hjartarson, Á., Jarosch, A. H., Magnússon, E., Belart, J. M. C., and Gudmundsson, M. T.: Non-surface mass balance of glaciers in Iceland, J. Glaciol., 66, 1–13, https://doi.org/10.1017/jog.2020.37, 2020.

Keisling, B., Christianson, K., Alley, R. B., Peters, L. E., Christian, J. E. M., Anandakrishnan, S., Riverman, K. L., Muto, A., and Jacobel, R. W.: Basal conditions and ice dynamics inferred from radar-derived internal stratigraphy of the northeast Greenland ice stream, Ann. Glaciol., 55, 127–137, https://doi.org/10.3189/2014AoG67A090, 2014.

Lebedev, S., Schaeffer, A. J., Fullea, J., and Pease, V.: Seismic tomography of the Arctic region: inferences for the thermal structure and evolution of the lithosphere, Geol. Soc., London, Spec. Pubs., 460, 419–440, https://doi.org/10.1144/SP460.10, 2017.

Macgregor, J., Fahnestock, M., Catania, G., Aschwanden, A., Clow, G., Colgan, W., Gogineni, S., Morlighem, M., Nowicki, S., Paden, J., Price, S., and Seroussi, H.: A synthesis of the basal thermal state of the Greenland Ice Sheet, J. Geophys. Res.-Earth Surf., 121, 1328–1350, https://doi.org/10.1002/2015JF003803, 2016.

Martos, Y. M., Jordan, T. A., Catalán, M., Jordan, T. M., Bamber, J. L., and Vaughan, D. G.: Geothermal heat flux reveals the Iceland hotspot track underneath Greenland, Geophys. Res. Lett., 45, 8214–8222, https://doi.org/10.1029/2018GL078289, 2018.

Morgan, P. J. and Holtzman, B. K.: Vug waves: A mechanism for coupled rock deformation and fluid migration, Geochem. Geophy. Geosy., 6, Q08002, https://doi.org/10.1029/2004GC000818, 2005.

Oliver, N. H. S., McLellan, J. G., Hobbs, B. E., Cleverley, J. S., Ord, A., and Feltrin, L.: Numerical models of extensional deformation, heat transfer, and fluid flow across basement cover interfaces during basin-related mineralization, Econ. Geol., 101, 1–31, https://doi.org/10.2113/gsecongeo.101.1.1, 2006.

Rezvanbehbahani, S., Stearns, L. A., Kadivar, A., Walker, J. D., and van der Veen, C. J.: Predicting the geothermal heat flux in Greenland: A machine learning approach, Geophys. Res. Lett., 44, 12271–12279, https://doi.org/10.1002/2017GL075661, 2017.

Rignot, E. and Mouginot, J.: Ice flow in Greenland for the International Polar Year 2008–2009, Geophys. Res. Lett., 39, 1–7, https://doi.org/10.1029/2012GL051634, 2012.

Rogozhina, I., Petrunin, A. G., Vaughan, A. P. M., Steinberger, B., Johnson, J. V., Kaban, M. K., Calov, R., Rickers, F., Thomas, M., and Koulakov, I.: Melting at the base of the Greenland ice sheet explained by Iceland hotspot history, Nat. Geosci., 9, 366–369, https://doi.org/10.1038/ngeo2689, 2016.

Sandiford, M., Hand, M., and McLaren, S.: High geothermal gradient metamorphism during thermal subsidence, Earth Planet. Sci. Lett., 163, 149–165, https://doi.org/10.1016/S0012-821X(98)00183-6, 1998.

Schoonman, C. M., White, N. J., and Pritchard, D.: Radial viscous fingering of hot asthenosphere within the Icelandic plume beneath the North Atlantic Ocean, Earth Planet. Sci. Lett., 468, 51–61, https://doi.org/10.1016/j.epsl.2017.03.036, 2017

Schroeder, D. M., Blankenship, D. D., Young, D. A., and Quartini, E.: Evidence for elevated and spatially variable geothermal flux beneath the West Antarctic Ice Sheet, P. Natl. Acad. Sci. USA, 111, 9070–9072, https://doi.org/10.1073/pnas.1405184111, 2014.

Shen, W., Wiens, D., Lloyd, A., and Nyblade, A.: A geothermal heat flux map of Antarctica empirically constrained by seismic structure, Geophys. Res. Lett., 47, e2020GL086955, https://doi.org/10.1029/2020GL086955, 2020.

Smith-Johnsen, S., de Fleurian, B., Schlegel, N., Seroussi, H., and Nisancioglu, K.: Exceptionally high heat flux needed to sustain the Northeast Greenland Ice Stream, The Cryosphere, 14, 841–854, https://doi.org/10.5194/tc-14-841-2020, 2020.

Stevens, N. T., Parizek, B. R., and Alley, R. B.: Enhancement of volcanism and geothermal heat flux by ice-age cycling: A stress modeling study of Greenland, J. Geophys. Res.-Earth Surf., 121, 1456–1471, https://doi.org/10.1002/2016JF003855, 2016.

Weisheit, A., Bons, P. D., Danisik, M., and Elburg, M. A.: Crustal-scale folding: Palaeozoic deformation of the Mt. Painter Inlier, South Australia, Geol. Soc., London, Spec. Pubs., 394, 53–77, https://doi.org/10.1144/SP394.9, 2013.

# Chapter 6

## Folding due to anisotropy in ice, from drill core-scale cloudy bands to km-scale internal reflection horizons

**Paul D. Bons[1,2], Yuanbang Hu[1,3], Gema M. Llorens[4], Steven Franke[1], Nicolas Stoll[5], Ilka Weikusat,[1,5], Julien Westhoff[6], Yu Zhang[1]**

[1]Department of Geosciences, Tübingen University, Tübingen, Germany

[2]China University of Geosciences (Beijing), Beijing, China

[3]Center for High Pressure Science and Technology Advanced Research, Beijing, China

[4]Geosciences Barcelona GEO3BCN-CSIC, Spain

[5]Alfred Wegener Institute, Helmholtz Centre for Polar and Marine Research, Bremerhaven, Germany

[6]Niels Bohr Institute, University of Copenhagen, Copenhagen, Denmark

Manuscript submitted for publication in The Cryosphere. The reader should note that the final manuscript may deviate slightly from the version printed here.

## Abstract

Upright folds in ice sheets are observed on the cm-scale in cloudy bands in drill cores and on the km-scale in radargrams. We address the question of the folding mechanism for these folds, by analysing the power spectra of fold trains to obtain the amplitude as a function of wavelength signal. Classical Biot-type buckle folds due to a rheological contrast between layers develop a characteristic wavelength, visible as a peak in the power spectrum. Power spectra of ice folds, however, follow a power law with a steady increase in amplitude with wavelength. Such a power spectrum is also observed in a folded, highly anisotropic biotite schist and in a numerical simulation of the deformation of ice Ih with a strong alignment of the basal planes parallel to the shortening direction. This suggests that the folds observed in ice are primarily due to the strong mechanical anisotropy of ice that tends to have a strong lattice preferred orientation due to ice-sheet flow.

## 1. Introduction

Folds are observed on all scales in glaciers and ice sheets. Large-scale folds (100-1000 m scale) are observed via internal reflection horizons (IRHs) in radargrams (Wolovick et al., 2014; Bell et al., 2014; Panton and Karlsson, 2015; Leysinger-Vieli et al., 2018; NEEM community members, 2013; Bons et al., 2016; Franke et al., 2023; Jansen et al., 2024) and in satellite images of the ice surface in West Greenland. Folds on the intermediate scale (~m scale) are common in glaciers (Hudleston, 2015), but more difficult to observe in ice sheets because of the snow cover. Small-scale folds (≤1 cm) in ice cores are visible as undulated cloudy bands, thin layers of elevated impurity concentration mainly occurring in glacial periods (Thorsteinsson, 1996; Alley et al., 1997; Svensson et al., 2005; Faria et al., 2010; Fitzpatrick et al., 2014; Jansen et al., 2016; Weikusat et al. 2017; Stoll et al., 2023). These folds are the main topic of this paper, using examples from the EGRIP drill core (Westhoff et al., 2021 (Fig. 1), that provided novel insights into the crystal orientation inside an ice stream (Stoll et al., 2024), i.e. the Northeast Greenland Ice Stream (NEGIS). “Cloudy bands” made visible in dark-field macroscopy in EGRIP ice are observed already in ice originating from the Younger Dryas at 1257 m of depth (Bohleber et al., 2022),but are a recurring stratigraphic feature from a depth of 1375 m (Westhoff et al., 2021, Stoll et al., 2023). Chemical data from these bands show elevated impurity concentration and more insoluble particles than in the surrounding layers (Bohleber et al., 2022, Stoll et al., 2023). Stoll et al. (2023) define different

cloudy band types and discuss their formation, but little is known about the folding mechanism of these bands that are observed below 1375 m at EGRIP. Folds are not always observed below this depth, which can be explained by the orientation of the drill-core section relative to the fold axis. Only sections at a large angle to the fold axis will reveal folds in the cloudy bands (Figure 4 in Westhoff et al., 2021).

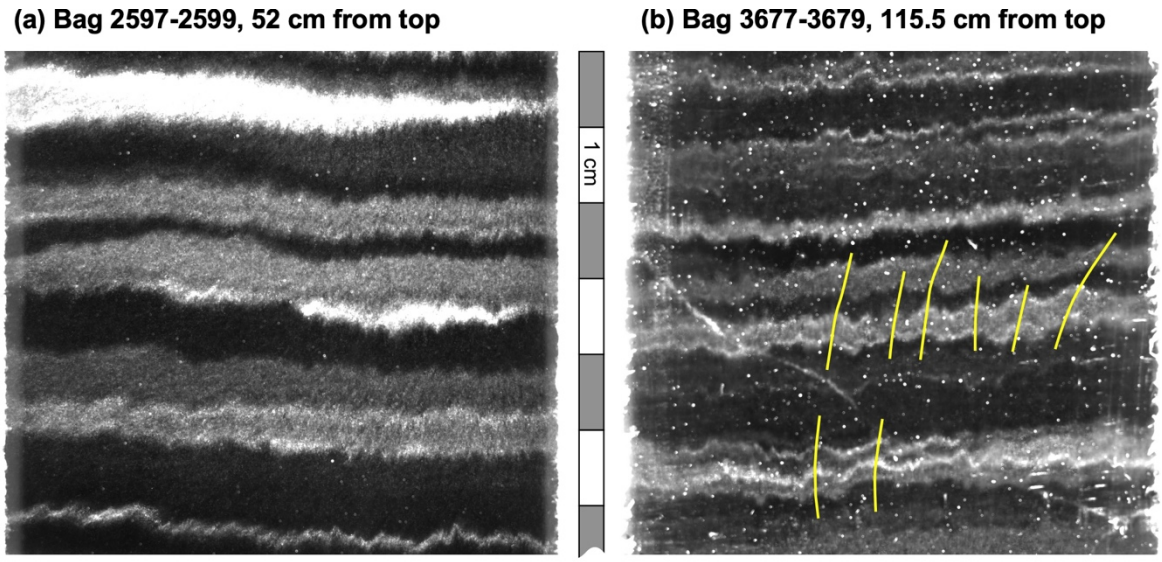


Figure 1. Two visual stratigraphy line scan examples of folded cloudy bands in the EGRIP drill core from a depth of (a) 1427.8 m and (b) 2017.45 m. Cloudy bands vary in thickness from about one to more than 10 mm. Eight axial planes are drawn as yellow lines in (b). These show that the folds are upright or moderately inclined. The folds are disharmonic, as axial planes cannot be traced for over more than a few times the fold wavelength at the most.

Nabavi and Fossen (2021) define folds as "curviplanar structures that form by transformation of any tectonic or primary foliation into curved geometries through a non-linear transformation". In geology, 'foliation' is used to denote any pervasive planar structure in a rock (which includes ice). The primary foliation in glaciers and ice sheets is the original layering formed by the deposition of snow layers on the surface. Other foliations can, for example, be healed fractures or fractures filled with frozen water (Hudleston, 2015). Numerous causes for folding in ice sheets have been proposed. Variations in bedrock elevation (Krabbendam, 2016), variable bedrock sliding (Wolovick et al., 2014), basal

melting or freeze-on (Leysinger-Vieli et al., 2018) have been proposed to explain large-scale folds of the original stratigraphy. Such external causes for folding cannot apply to small to medium-scale folds that are observed throughout the column of the ice sheet well above the ice-bedrock interface. These folds must, therefore, be the result of an internal response to layer-parallel shortening (NEEM community members, 2013; Hudleston, 2015; Bons et al., 2016; Jansen et al. 2016; Zhang et al., 2024).

A volume of a mechanically homogeneous and isotropic material will not produce folds when subject to deformation, as the material would only thicken without experiencing localized strain. Folds can form when the material has a mechanical layering that forms a 'composite anisotropy' and/or when it is 'intrinsically anisotropic', for example due to a crystallographic preferred orientation (CPO) (Griera et al., 2013; Nabavi and Fossen, 2021; Hansen et al., 2021). The latter is often the case in ice because ice normally deforms by dislocation creep (Glen, 1955; Weertman, 1983) that results in a CPO that aligns the easy-glide basal planes in certain preferred orientations (Duval et al., 1983; Budd and Jacka, 1989; Faria et al. 2014; Llorens et al., 2017). In both cases the application of a differential stress will normally lead to a heterogenous deformation field, which implies that originally straight planar surfaces get distorted: folds develop. Here we will show, based on fold theory and numerical simulations, that folds observed in cloudy bands in the EGRIP drill core primarily result from an intrinsic anisotropy due to the CPO and not from rheological differences between the individual cloudy bands.

## 2. Basic fold terminology and theory

For detailed reviews of fold geometry and terminology the reader is referred to the textbooks of Ramsay and Huber (1987) and Twiss and Moores (2007), or to the extensive review by Nabavi and Fossen (2021) that also provides an overview of fold theory. Here, we only provide a summary of the relevant terminology and theory based on the above publications, unless otherwise referenced.

Most fold trains roughly resemble a sinusoidal wavefunction (Fig. 2a). One individual fold consists of two limbs that meet at the fold hinge, the line of maximum curvature. When the fold hinges diverge downwards, the fold is termed an 'antiform', otherwise it is a 'synform'. Antiforms and synforms join at the inflection points in the fold limbs where the direction of

curvature changes sign. The terms 'anticline' and 'syncline' are reserved for folds in a stratigraphic sequence and, therefore, apply to folds observed in radargrams or cloudy bands, as these are assumed to represent sedimentary snow layers. Folds can have shapes that range from rectangular boxes, semi-ellipses, parabolas, sine waves, through to chevron or kink folds (Nabavi and Fossen, 2021). Box folds have two-fold hinges per fold, but the authors are unaware of any box folds reported in ice. Ideal chevron or kink folds have straight limbs and highly concentrated curvature in the hinges. Such folds were described in a drilled ice core by Jansen et al. (2016). As most folds resemble a sine wave, the term 'wavelength' ($l$) is one metric used to describe the length scale of folds. It is defined as double the distance between inflection points in the directions of the fold train (Fig. 2a). Accordingly, the 'amplitude' ($A$) is defined as half the distance between the average antiformal and synformal hinge lines, measured in the direction perpendicular to the fold train. Folds can, however, have multiple wavelengths (Fig. 2b), in which case defining the amplitude becomes difficult. The 'arc length' is the length of a line along the fold trace. The relative arc length ratio is the ratio of the arc length and the length of a straight line along the fold trace. The arc length is the same as the initial length if a layer only folds and does not become thicker or thinner during folding.

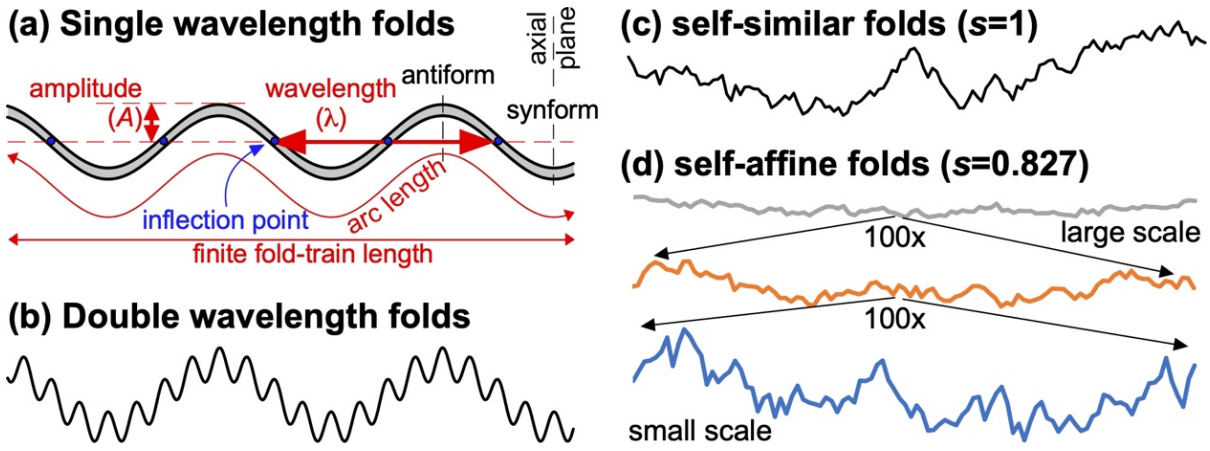


Figure 2. Fold shape and terminology. (a) Basic fold with a single wavelength. The arc length is the length of the fold train measured along the fold, while the finite length is the distance between the two ends of the fold train. (b) Fold composed of the superposition of two sine waves with different wavelengths and amplitudes. (c) Self similar fold train in which the amplitude of folds is a linear function of the wavelength ($s$=1 in Eq. 2). The artificial fold

train is sampled every 0.5 mm if the whole fold train is 65 mm, comparable to the length of fold trains analysed in the EGRIP drill core. (d) Example of a self-affine folds where the amplitude/wavelength ratio systematically decreases with increasing scale (the exponent *s* is defined in Eq. 2).

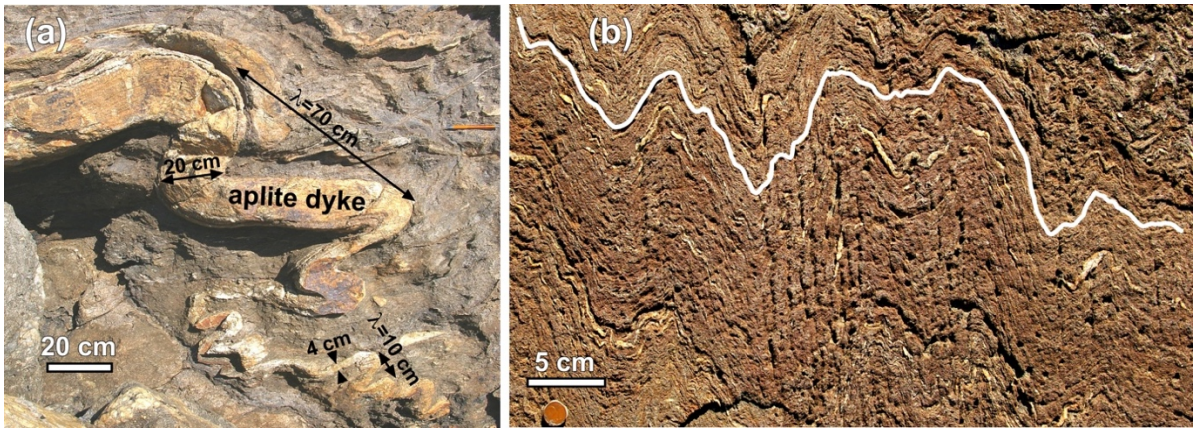


Figure 3. Examples of folds in rocks from Cap de Creus, northeast Catalonia, Spain. (a) Biot-type folding of a strong aplite dyke in a weaker granodiorite matrix. The example clearly shows the positive correlation between thickness of the dyke and wavelength that both decrease from the top left to the bottom right (Punta Fallarons; N42°20'25", E3°,15'48"). (b) Folded highly anisotropic biotite schist with thin quartz veins showing harmonic multi-wavelength folds. The hand-drawn white line was used for the analysis shown in Fig. 7b (Puig Culip; N42°19'19", E3°18'12").

Folds may form when a composite material consisting of layers with different rheology is shortened parallel to the layers. The reason for this 'buckle folding' is that it is energetically more favourable to accommodate part of the shortening by bending the stronger layers at intervals (the fold hinges) and rotating the sections in between (the fold limbs). The weaker layers in between need to accommodate this deformation by deforming at a higher rate. Biot (1957) first developed the theory that the final fold wavelength is a function of the amplification rate of an infinite range of wavelengths of initial perturbations in the original layer. The basic idea is that the final wavelength is the one with the highest amplification rate. For a single layer with thickness $H$ and linear viscosity $h_l$ embedded in an infinite matrix with viscosity $h_m$ he derived for the dominant wavelength $l_d$:

$$\lambda_d = 2\pi H \left(\frac{\eta_l}{6\eta_m}\right)^{1/3} \quad (1)$$

Since Biot's pioneering work, many authors extended and refined his theory for multilayers, elasticity, slip or no slip between layers, and for non-linear (power-law) rheologies (see Table 2 in Schmalholz and Mancktelow, 2016). All these theories have in common that when the rheological difference between layers approaches zero, the dominant wavelength reduces to approximately the layer thickness. Wavelengths smaller than the layer thickness cannot be explained by Biot-type buckle-fold theory for layers with different rheological properties. It should also be noted that the fold amplification rate decreases with decreasing rheological contrasts (Llorens, 2019) in isotropic materials. This means that while relatively short wavelengths are possible at low rheological contrast between layers, one would not see the folds as their amplitude would be too small.

Relatively little work has been done on folding due to an intrinsic anisotropy, for example the alignment of easy-glide basal planes in ice or aligned micas in a schist (Cobbold et al., 1971). Biot-type buckle-fold theory cannot be simply applied to predict a dominant wavelength, as there is no layer thickness to provide a length scale. Without a length scale in the system, folds of all wavelengths should amplify at the same rate. Instead of folds with a dominant wavelength, one would expect folds where the amplitude of each wavelength is proportional to that wavelength (Fig. 2c). In that case we get:

$$A_{(\lambda)} = \lambda_0 \cdot \lambda^s, \quad (2)$$

with $l_0$ a proportionality constant and $s$ the scaling exponent. When $s$=1 the folds are self-similar, meaning that folds at all scales look similar because the scaling of amplitude and wavelength is identical (Fig. 2c). When $s$<1, large folds have relatively smaller amplitudes than small folds (Fig. 2d). When the scaling of amplitudes and wavelengths is not identical, the folds are self-affine.

# 3. Materials and methods

## 3.1 Materials

Metamorphic schists are mechanically highly anisotropic due to the alignment of platy mica grains into a foliation. Micas are comparable to ice Ih as they deform most easily along their basal planes (Duval et al., 1983; Finch et al., 2021). Metamorphic schists at Cap de Creus, NE Catalonia, Spain, show folding of the foliation that happened during the Palaeozoic Variscan Orogeny (Druguet et al., 1997, Bons et al., 2004). The mechanical anisotropy of the foliated rock is thought to play a dominant role in the deformation of these rocks (Carreras et al., 2013; de Riese et al., 2019). We therefore use one outcrop as an example of folding of a strongly anisotropic rock in which layering is absent (Fig. 3b).

The East Greenland Ice-core Project (EGRIP) is a deep drilling project located in the middle of NEGIS at 75°37.820 N and 35°59.556 W. Visual stratigraphy line scans of the drill core reveal “cloudy bands” by imaging a polished slab of the core in dark-field macroscopy4. When the section of the core is suitably oriented relative to the flow direction, these cloudy bands show folds (Westhoff et al., 2021) (Fig. 2). We used (Fig. 4) line-scan images 2597_1_32mm.bmp, 3128_1_32mm.bmp, and 3677_1_32mm.bmp (Weikusat et al., 2020), each representing three 55 cm-bags to make a core-length of 165 cm in each image. The depth of the top of the three images is 1427.8, 1719.85, and 2021.8 m, respectively. We refer to these images by the number of their top bag and depths of individual cloudy bands are given in cm from the top of the image.

We use high-resolution radar data from the EGRIP-NOR-2018 survey (Franke et al., 2022b) from the onset region of NEGIS. The radar data were acquired in May 2018 with the AWI's (Alfred Wegener Institute Helmholtz Centre for Polar and Marine Research) airborne multichannel ultra-wideband (UWB) radar and have a horizontal resolution of ~15 m and vertical resolution of 4.31 m. The radargrams used here are centred at the EGRIP drill site and run perpendicular to ice flow (Fig. 5).

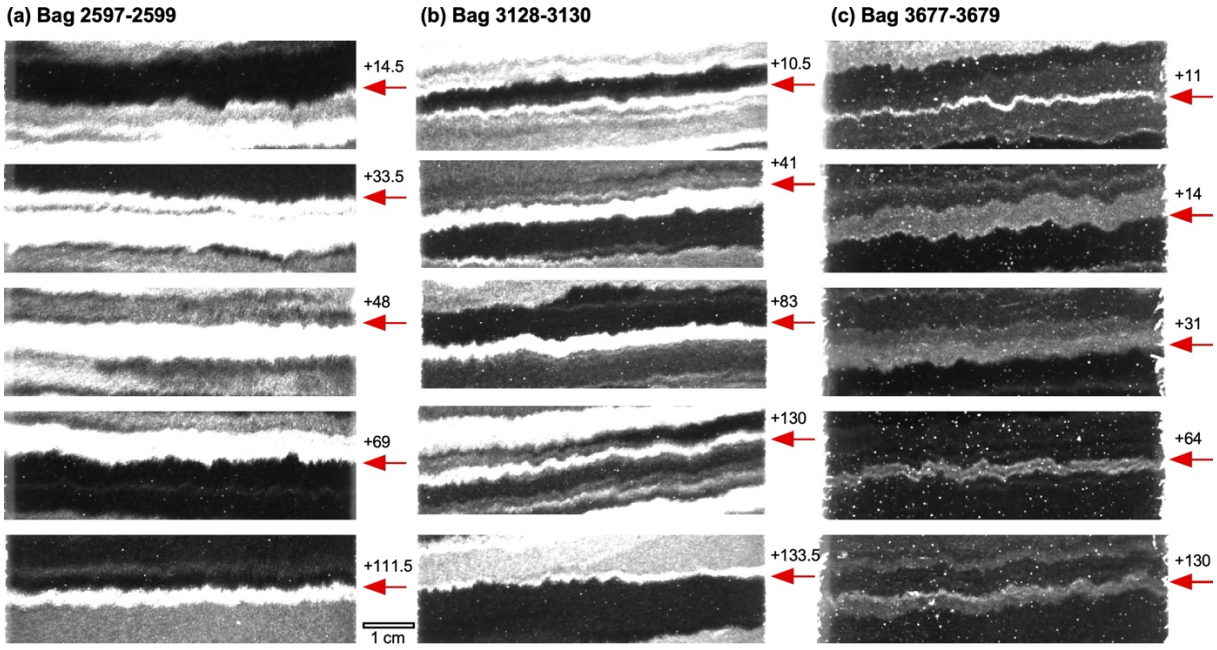


Figure 4. Images of ten of the 15 cloudy-band interfaces (red arrows) that were analysed in this study. Red arrows indicate the analysed cloudy band interface with distance from top of the line-scan image given in cm.

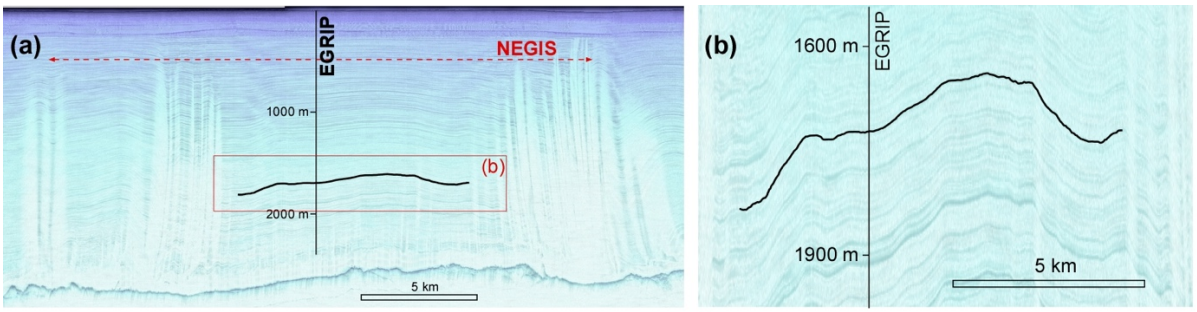


Figure 5. Traced internal reflection horizon (IRH) in a radargram going through NEGIS perpendicular to ice flow (ice flow into the page) at the location where the EGRIP ice core is drilled. The radargram shown in (a) with a 4.3x vertical exaggeration is composed of profiles 20180508_06_004 and 20180514_03_001 (Franke et al., 2021, 2022b). (b) The same profile showing only the centre of NEGIS at an 18.2x vertical exaggeration at which the layer intersecting EGRIP at 1720 m depth was manually traced.

## 3.2 Methods

### 3.2.1 Numerical modelling

We use the full-field Viscoplastic Fast Fourier Transform (VPFFT) crystal plasticity code (Lebensohn, 2001; Lebensohn et al., 2008; Lebensohn and Rollett, 2020), coupled with the modelling platform Elle (Bons et al., 2008; Piazolo et al., 2019) to illustrate the fold geometries that form when ice Ih with a mechanically anisotropy is shortened. The code has been used to simulate microstructural developments in deforming ice (Llorens et al., 2016a, 2017; Steinbach et al., 2016) and the formation of folds and other structures in intrinsically anisotropic rocks (Ran et al., 2019; de Riese et al., 2019; Hu et al., 2024). The VPFFT-code simulates deformation of a crystalline material by glide along crystallographic planes. We use the crystallography of hexagonal ice Ih, which is mechanically highly anisotropic due to much easier glide along its basal planes, compared to glide along the prismatic and pyramidal slip systems (Duval et al. 1983). This crystal symmetry approximates a transversely isotropic material (Griera et al., 2013). We use a stress exponent of four (Goldsby and Kohlstedt, 2001; Bons et al., 2018) for the power-law relation between strain rate and stress and assigned a 16-times higher slip resistance to the non-basal slip systems. At a given strain rate, the stress difference between the basal and non-basal slip systems is thus a factor 16. Details of this modelling approach can be found in Griera et al. (2013) and Llorens et al. (2017).

The 2D models consists of an initially square 256x256 grid of so-called unodes (Bons et al., 2008) that store the local lattice orientation. The unodes effectively represent crystallites or single grains with a constant internal crystal orientation, defined by three Euler angles. Using a Potts model, we created 1995 clusters of identical orientation or grains. On average, each grain is almost 6x6 unodes in size. The basal planes of the initial model were aligned, so that the c-axes normal to the basal planes form a point maximum (with a standard deviation of 10°) parallel to the vertical extension direction. Using velocity boundary conditions, the square model was deformed by horizontal shortening of 2% per calculation step up to 40% shortening, accommodated by vertical stretching.

### 3.2.2 Fold analysis

Between the two end-member fold shapes of box and chevron folds, folds resemble a wave or the addition of multiple waves. Not surprising, Fourier analyses have been applied to folds for

about 50 years (Hudleston, 1973; Ramsay and Huber, 1987; Schmalholz and Mancktelow, 2016). This can be used to determine whether the fold train has a single dominant wavelength or is composed of folds of different wavelengths (Fig. 2). We therefore applied a Fast Fourier transform to fold contours of both natural and numerical folds.

We used 2044x31550 8-bit images of the line scans with a resolution of 18.6 pixel/mm from three images. Image 'bag 2597' (Fig. 4a) and 'bag 3128' (Fig. 4b) had a suitable contrast, but a ca. 2x contrast stretch was applied to 'bag 3677' (Fig. 4c) to achieve a sufficient contrast between dark and bright cloudy bands. In each bag five boundaries between dark and bright cloudy bands were selected that were both sharp and where the adjacent cloudy bands showed no significant lateral variation in thickness. A selection of the image was then subjected to a median filter with a 4-pixel radius to reduce small-scale noise and then thresholded to a binary image. The folded trace was subsequently selected by edge detection between the now black and white bands, resulting in the lines shown in Fig. 6a. Only the middle 65 mm of the ca. 70 mm wide drill core image was used to avoid artifacts at the edges of the image. The selection was scaled to 1024 pixels, or 65 mm, width. All this was done with the freeware ImageJ (Schneider et al., 2012). A script selected the $y$-coordinates of the line for each $x$-coordinate along the trace. The equidistant $x,y$-data were then detrended by subtracting a linear least-squares best fit through the $\underline{x,y}$-data. The detrended series of 1024 $y$-data was then subjected to a discrete Fourier transform using the routine four1() of Press et al. (1992). The power spectrum was obtained by taking the square root of the sum of the squares of the real and imaginary parts of the transform for each wavelength.

For the power spectrum of the numerical folds of Llorens et al. (2013), we applied the above method to a black-and-white image of one of the modelled folds (Fig 6c) in that paper to convert to upper boundary of the folded layer in a set of 1024 equidistant $x,y$-coordinates. For the large-scale folds in NEGIS, we used a radargram that spans NEGIS (Franke et al., 2022b) and is located closely (a few meters) to the EGRIP ice core (Fig. 5) and chose a conspicuous layer at the depth of ‘bag 3128' (1719.85 m). The layer was traced for 10 km, only within NEGIS to avoid effects of the higher strain in the shear margins (Jansen et al., 2024). The image on which the layer was traced had a 18.2x vertical exaggeration. For the folded schist we used a 3008x2000 pixel field photograph (Fig. 3b). In each case the selected folded surface was hand-traced in a drawing program (Canvas12) to create a line that was further processed the same way as the cloudy band interfaces.

In case of folds in an anisotropic material, simulated with Elle-VPFFT, a straight horizontal line, consisting of 102400 nodes, at a chosen level in the model, was subjected to deformation according to the velocity field that Elle-VPFFT records for each deformation step, up to the strain for which the power spectrum was to be calculated (Fig. 6b). The resulting line was then divided in 256 *x,y*-coordinates that are equidistant in the *x*-direction by interpolating between the original nodes, after which the procedure is the same as for digitised folds in the cloudy bands.

Linear least-squares best-fits were applied to the log(*A*) versus log(*l*) data of the power spectra to obtain the scaling exponent *s* (Eq. 2), using the freeware Past4, except for the single-layer buckle fold where Eq. (2) does not apply.

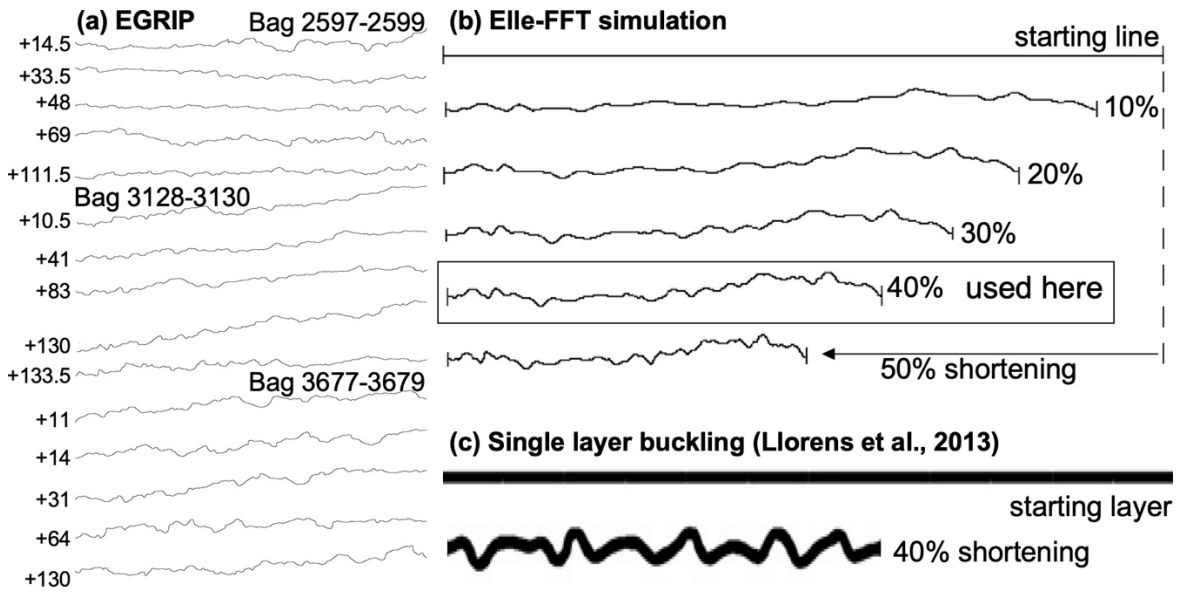


Figure 6. Fold traces. (a) Traces of folded cloudy-band interfaces in the EGRIP drill core bags 2597, 3128 and 3677. Numbers on the left indicate the distance in cm from the top of the 165 cm-long line-scan image. (b) Traces of an originally horizontal line at different amounts of horizontal shortening in a simulation with Elle-FFT with pure ice Ih (n=4) and initially a horizontal alignment of basal planes. (c) Example from fig 7c in Llorens et al. (2013) of single-layer buckling in a power-law material (n=3).

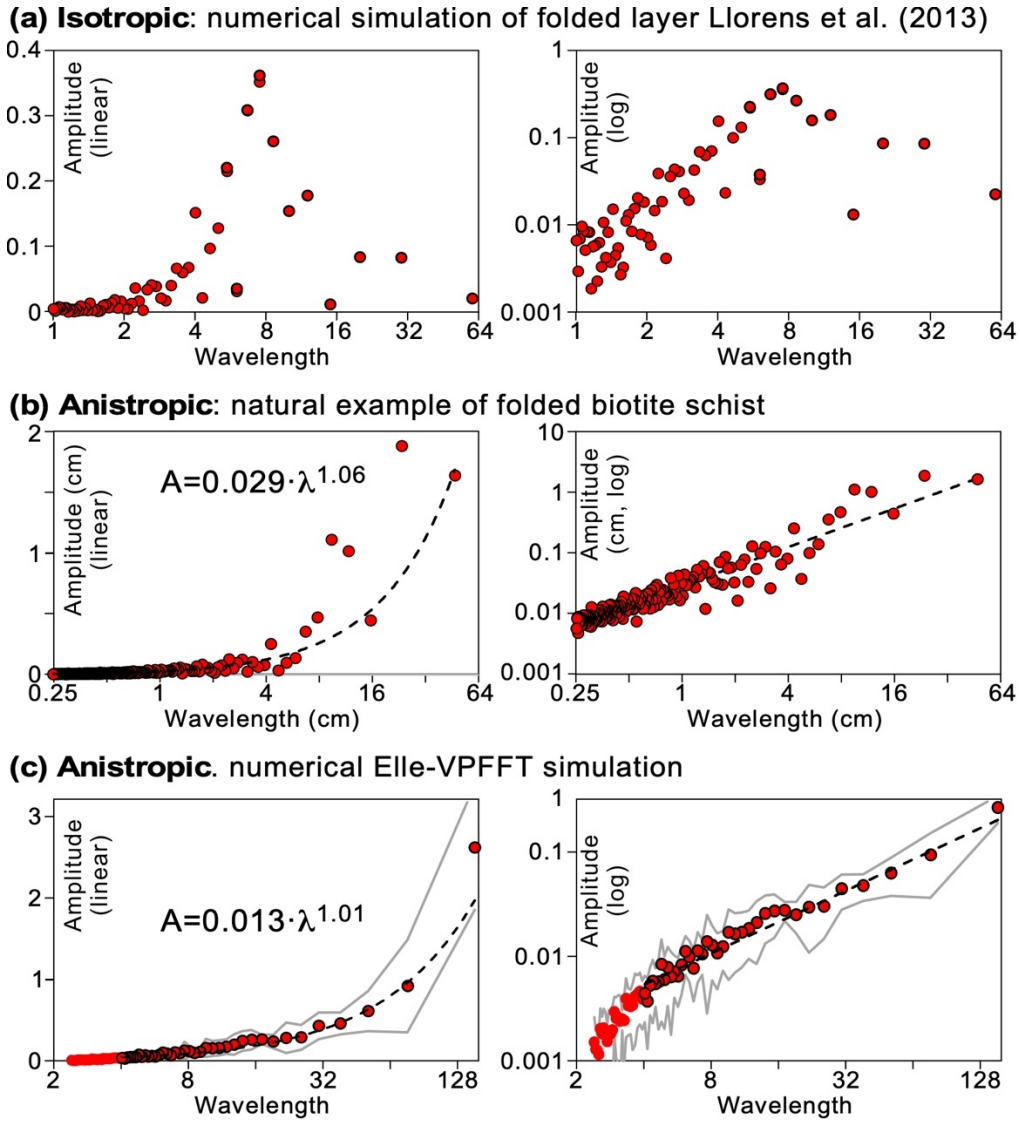


Figure 7. Power spectra of analysed folds. The vertical axis showing the amplitude is linear in the left column and logarithmic in the right column. (a) Numerical simulation of a single layer in a homogeneous and isotropic softer matrix (Llorens et al. 2013). The power spectrum shows a distinct peak at a wavelength of 8 length units with a total length of the fold train of 60 units. The layer had an initial length of 100 units. (b) Folded foliation in the biotite schist from Puig Culip shows an approximately self-similar power-law power-spectrum. (c) Numerical simulation with Elle-VPFFT of the folding of intrinsically anisotropic, pure ice that has an initial strong alignment of basal planes parallel to the shortening direction. Dots are the average of data sets in the model, while grey lines show the one standard deviation variation. The power spectrum follows an approximately self-similar power law from a wavelength of about five elements-widths of the initial 256x256 model.

Table 1. Results of power-law fits to the different fold sets.

| Fold set | *l* range | Best fit *s* | *s* range | $r^2$ |
|---|---|---|---|---|
| Biotite schist | 0.25 - 47, relative to original length of 100 | 1.057 | 0.976 - 1.152 | 0.90 |
| Elle+VPFFT | 5 - 153 elements | 1.010 | 0.935 - 1.087 | 0.68 |
| Cloudy bands | 1 - 65 mm | 0.965 | 0.884 - 1.047 | 0.58 |
| NEGIS | 100 m - 10 km | 1.487 | 1.39 - 1.62 | 0.86 |
| NEGIS + cloudy bands | 3 mm - 10 km | 0.827 | 0.80 - 0.86 | 0.99 |

# 4. Results

## 4.1 Single-layer buckle folds simulation

Llorens et al. (2013) used finite-element modelling for folding of a competent single layer in a homogeneous softer matrix. They used an isotropic power law rheology relating strain rate ($\dot{\varepsilon}$) to differential stress (s):

$$\dot{\varepsilon} = B \cdot \sigma^n \tag{3}$$

Here $B$ is the pre-exponential factor and $n$ the stress exponent that was set at $n$=3. We show (Fig. 7a) the power spectrum for 40% layer-parallel shortening of a layer of original length 100 and unit thickness. The layer was made 25 times stronger than the matrix by setting $B_{matrix} = 25 \cdot B_{layer}$. The resulting fold (Fig. 6c) shows 8-9 distinct antiforms in the fold train, but no clear folds with other wavelengths. The power spectrum (Fig. 7a) shows a distinct peak at 7.5 times the original layer thickness for a fold-train length of 60 after 40% shortening. The initial wavelength was thus about 11-12 times the layer thickness.

## 4.2 Folded biotite schist

The folded foliation in the biotite schist from Puig Culip (Fig 3b) shows a power spectrum with a steady increase of the amplitude with the wavelength (Fig. 7b). A power-law best fit results in an exponent of approximately $s$=1, implying that the amplitude is linearly proportional with the wavelength (Eq. 2) and the folds are approximately self-similar.

## 4.3 Elle-FFT simulation

We analysed ten equally spaced originally horizontal lines in the model of folding in ice with aligned basal planes (Fig. 8). We chose a finite strain of 40% shortening, as the lines folded to achieve relative arc lengths of 1.14±0.2, comparable to those obtained from the cloudy bands (see below). Initially horizontal lines are folded with various wavelengths. Medium to large folds can be traced along their axial planes over many lines, suggesting that the folds are more harmonic than those in the cloudy bands if the model is assumed to have a comparative width as the EGRIP drill core.

The power spectrum shows a steady increase in power with wavelength from $l \approx 5$ initial element widths (Fig. 7c), which is in the order of the mean grain width after 40% horizontal shortening and $A_{(l)}$ increases approximately linear with $l$, i.e., $s \approx 1$. This means that the folds are self-similar: their shape is independent of their wavelength.

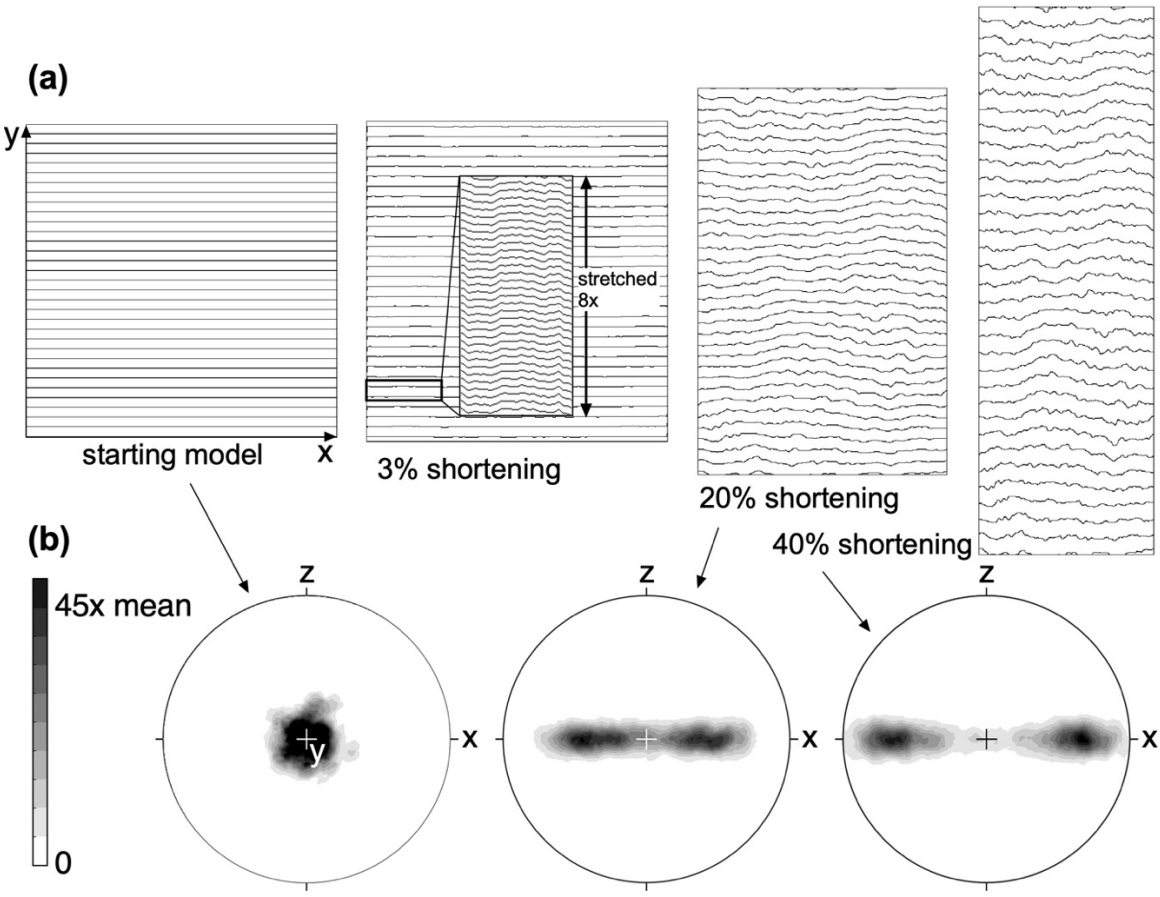

Figure 8. Result of the Elle-VPFFT simulation showing the model at 0, 3, 20, and 40% horizontal (x-axis) shortening that is compensated by vertical (y-axis) stretching in plane strain. (a) Passive markers originally aligned to the horizontally aligned basal planes. At 3% shortening, folds can barely be discerned. At 8x vertical stretch initial folds become visible. These have relatively straight limbs and sharp hinges compared to folds at higher strains. (b) Stereographs of the c-axis orientations looking down along the vertical y-axis. Plots were created with Stereonet by F.W. Vollmer, using orientations of 2500 randomly selected elements out of a total of 65536 elements.

## 4.4 Cloudy bands

Cloudy bands have a variety of thicknesses, ranging from about a mm to a few cm (Fig. 1 and 4). However, it is difficult to define the thickness of one band, as what appears like one dark or bright band may itself be composed of several thinner bands of different brightness (Stoll et al., 2023). All interfaces are folded on the mm to cm scale (Figs. 1 and 4). Folding is most conspicuous in the interfaces of very bright and very dark bands. The folds are upright with mostly vertical axial planes (Fig. 1b), although some zones with tilted axial planes were observed (Westhoff et al., 2021). Folds are disharmonic, meaning that individual axial planes can rarely be traced from one interface to another, i.e., for more than about 5 mm (Fig. 1). This means that the folds in individual interfaces appear independent of those in the next. Relative arc length ratios of the 15 folded interfaces are on average 1.15 (± 0.03 standard deviation).

The individual and average power or amplitude spectra of the 15 folded interfaces at the three selected depths show no significant differences. We therefore averaged the powers for each wavelength, as shown (Fig. 9a). We see that the amplitudes first increase up to a wavelength of about 2 mm, followed by a shallower, linear ($s \approx 1$) increase up to about $l$=20 mm. The amplitudes of the largest two wavelengths are below the trend, but it cannot be ascertained whether this is significant, or merely due to the large variation in amplitudes. No dominant wavelength well below 65 mm was observed.

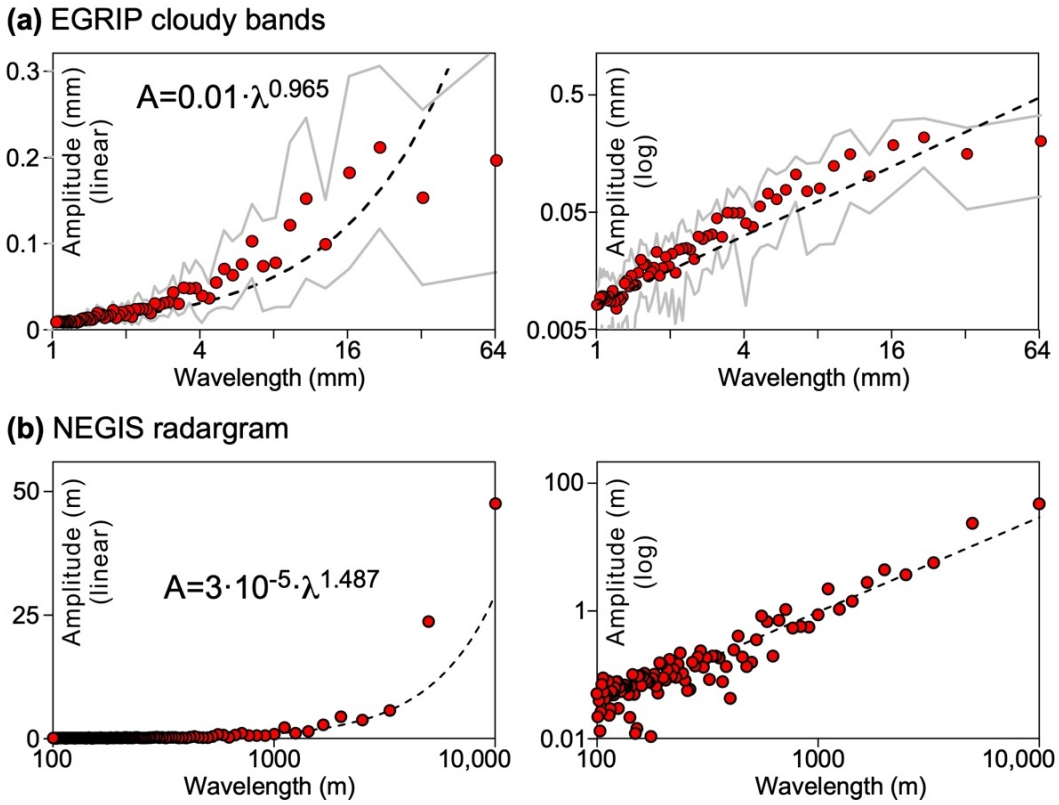


Figure 9. Power spectra for folds in ice. (a) Average power spectrum of all 15 cloudy band interfaces (red dots), shown together with plus/minus one standard deviation (grey lines) of the variation in powers. The data roughly follow a self-similar power law up to $l \approx 20$ mm. (b) Power spectrum for the internal reflection horizon (IRH) in the radargram that intersects the EGRIP drill core at ca. 1720 m depth (Figure 5) traced over a distance of 10 km perpendicular to NEGIS' flow direction. A power-law best fit for $l \geq 100$ m results in a scaling exponent of $s \approx 1.5$. The vertical amplitude axis is linear in the left column and logarithmic in the right column.

## 4.5 Large-scale folds inside NEGIS

The 1720 m depth layer in NEGIS shows a power-law amplitude-wavelength trend with $s \approx 1.5$ upwards from $l = 100$ m (Fig. 9b). This indicates that there is no characteristic wavelength and that small folds are flatter in shape than large folds. However, the fold trace may be too smooth on the small scale to correct for small vertical shifts and steps in reflector depths that are artifacts related to surface elevation variations. Underestimating amplitudes at low wavelengths would artificially increase the exponent $s$.

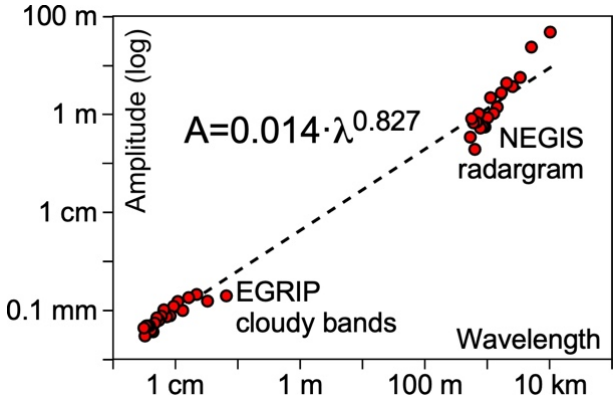


Figure 10. Combined power spectra of cloudy band interfaces and the internal reflection horizon (IRH), showing the 40 largest wavelengths of each spectrum. A power-law best fit through these data gives an exponent $s$ = 0.827, suggesting that folding is self-affine (Fig. 2d), with large folds relatively flat compared to small folds.

## 5. Discussion

Folds in the cloudy bands do not show a dominant wavelength in the wavelength range shorter than the width of the drill core section (Fig. 9a). The power spectra of the 15 sampled fold traces all overlap and show no significant variation between them, although the cloudy bands immediately adjacent vary in thickness from 1 to >10 mm. Both observations suggest that the folding has no characteristic length scale. In case of Biot-type buckle folding, this would be the thickness of the layers, here the cloudy bands. For Biot-type buckle folding one would expect shorter wavelength of the folds in the ca. 1 mm thick cloudy band 3677 + 11 than in the ten times thicker one at 3677 + 14, which are only 3 cm apart. Multiple-wavelength folds can develop in multi-layers (e.g., Fig. 11 in Frehner and Schmalholz, 2006). These form by the addition of different characteristic wavelengths of layers with different thickness and/or rheology. However, harmonic folds are then expected with axial planes extending across several layers that contributed to the multi-wavelength folds. In case of the analysed cloudy bands this is not the case, as the axial planes rarely extend for more than 5-10 mm. These observations suggest that the folds in the cloudy bands are not the result of Biot-

type buckling due to rheological differences between individual cloudy bands, where a high viscosity contrast between layers (≥ 25) is required for folding (Llorens et al., 2013).

The cloudy band folds resemble folds in the biotite schist (Figs. 3b, 7b) and the numerical ELLE-FFT folds in ice with a strong CPO (Figs. 7c, 8) much more than Biot-type buckle folds (Fig. 3a, 6c, 7a). This holds for both a visual assessment and for the power spectra. Shortening parallel to an intrinsic initial (before onset of folding) mechanical anisotropy due to a CPO is therefore the preferred mechanism to explain the observed folding in the cloudy bands, as was already suggested by Jansen et al. (2016). We observe a similar lack of a characteristic wavelength in the large-scale folds inside NEGIS (Fig. 9). This supports the suggestion by Bons et al. (2016) and the numerical simulations by Zhang et al. (2024) that such large-scale folding is also due to shortening parallel to the CPO-induced anisotropy.

The cloudy bands and internal reflection horizons are thus passive material planes whose folds reveal the heterogeneity of deformation due to CPO-induced anisotropy. This CPO was probably a vertical single maximum of the c-axis orientations. However, folding of course changes this CPO, resulting in a girdle with (Fig. 8b) or without (Stoll et al. 2023) two maxima. The passive marker planes do not reflect the current CPO, but the cumulative heterogeneous strain resulting from the evolving CPO.

Folding of an intrinsic anisotropy has no typical length scale, which explains the close to self-similar ($s \approx 1$) power spectra of the cloudy band interfaces. If the folds were perfectly self-similar and the self-similar range would extend to the 10 km scale that we observe in the traced IRH in the radargram, we would expect folds about seven times taller than the folds we observe (Fig. 5).

A power-law best fit through the combined cloudy-band and radargram folds results in a scaling exponent of $s \approx 0.8$ (Fig. 10). This would mean that the folds gradually get flatter with increasing scale. Unfortunately, we do not have sufficiently detailed observations in the length-scale range from 10 cm to about 100 m. It is therefore possible that the power spectra between the small and large scale show a break. Another possibility is that the scales are related and that the folds are self-affine (Fig 2d). Reasons for this could be the effect of the ice-sheet surface, where gravity and ice precipitation counteract the development of surface topography due to folding (Waddington et al., 2001; Zhang et al., 2024). An additional effect could be the bedrock topography or bedrock processes (Bell et al., 2014; Wolovick et al.,

2014; Leysinger Vielli et al., 2018) that impose additional folding or fold-amplitude modifications of the anisotropy-induced folds. Unfortunately, the radargrams are of poor quality for the detailed fold analyses that are applied here. A more systematic analysis of the large-scale folds is needed but is outside the scope of this study.

Having argued that folding in cloudy bands in ice sheets is the result of shortening of an intrinsic anisotropy, we now briefly address the degree of anisotropy. Materials with a very strong transverse isotropy tend to form kink or chevron type folds (Cobbold et al., 1971; Ramsay, 1974; Nabavi and Fossen, 2021). Such chevron folds, or "fabric stripes", have been described in ice with a strong CPO (Alley et al., 1997; Jansen et al., 2016). With decreasing degree of anisotropy folds become more rounded and axial planes are oriented perpendicular to the direction of maximum shortening (Cobbold et al., 1971), as is the case in the folds in cloudy bands shown here (Fig. 4). The ELLE-VPFFT simulation started with a strong single-maximum CPO (Fig. 8b). Initial (3% shortening) folds are relatively chevron-like. Such a low strain is comparable with the model proposed by Jansen et al. (2016) where chevron-type fabric stripes that develop in simple shear with a c-axes single maximum almost perpendicular to the shear plane. The situation is different in pure shear shortening that leads to much higher of cloudy bands initially perpendicular to the preferred c-axis orientation. Here the CPO evolves (Fig. 8b) together with the folding of the cloudy bands, leading to more rounded folds at all scales.

In the absence of any other factors that control folding, the proportionality factor ($l_0$) in Eq. (2) should only depend on the type of anisotropy, its intensity, and the amount of shortening. This implies that it should be possible to determine the actual anisotropy of ice with folds (e.g. the EGRIP drill core) if the initial CPO can be constrained and the amount of shortening parallel to the folded planes (e.g. the cloudy bands) is known. This could be a helpful independent estimate of the anisotropy of flowing ice, and, hence, its effective hardening or softening due to the flow field, in addition to other studies (Gerber et al., 2023). This is, however, well beyond the scope of this study.

## 6. Conclusions

We used power spectra of fold traces to determine the mechanism for folding in ice sheets. Biot-type buckle folds due to rheological contrasts between layers have a characteristic length

scale, related to the layer thickness and the rheological contrast between the layers that are internally isotropic. Numerical simulation of ice with a strong alignment of basal planes parallel to the shortening direction resulted in the development of self-similar folds with a power-law power spectrum. This is to be expected as anisotropy has no length scale. Self-similar folds were also observed in folded biotite schist and in cloudy bands in the EGRIP drill core. We therefore conclude that small-scale folds in cloudy bands are due to shortening parallel to a strong anisotropy as a result of the lattice preferred orientation with initially horizontally aligned basal planes. Combining the small cloudy band folds and large NEGIS-scale folds resulted in a self-affine trend, where largest folds are relatively flat. This may be caused by additional boundary conditions, such as vertical flattening and bedrock irregularities, that modify the anisotropy-induced folds on the large scale.

## Code availability

The updated version of Elle+FFT software package from Hao et al., (2023) can be downloaded from https://doi.org/10.5281/zenodo.10259841. We recommend using the Elle+FFT software package by Singularity container under Linux (e.g. for Ubuntu 20.04). Additional information on the software can be found in the Appendix section of PhD-thesis of Dr. Florian Steinbach, which can be downloaded from the library of Tübingen University (https://publikationen.uni-tuebingen.de/xmlui/handle/10900/76435). The Elle+VPFFT input files (ASCII text files) to rerun the simulations used in this paper and can be downloaded as supplementary data.

## Data availability

Visual stratigraphy data from the EastGRIP ice core are available at https://doi.org/10.1594/PANGAEA.925014 (Weikusat et al., 2020). The radio-echo sounding data shown in Figure 5 (profile IDs: 20180508_06_004 and 20180514_03_001 from AWI's EGRIP-NOR-2018 survey are available under https://doi.org/10.1594/PANGAEA.928569 (Franke et al., 2021, 2022b). Input files for the Elle+VPFFT numerical simulation shown here (folder supplement_Elle_VPFFT_files) are provided as Supplementary Data to this article. The data contains x-y coordinates of all analysed fold trains as tab-delimited ASCII text files.

## Author contributions

PDB conceived the study, performed most analyses, and wrote the manuscript. JW, NS and IW acquired and processed visual stratigraphy data. GML, YH, and YZ carried out numerical simulations and contributed to modelling efforts. SF processed and contributed radar data. All authors jointly contributed to the discussion of results and reviewed the manuscript.

## Acknowledgements

We acknowledge the use of software from Open Polar Radar generated with support from the University of Kansas, NASA grants 80NSSC20K1242 and 80NSSC21K0753, and NSF grants OPP-2027615, OPP-2019719, OPP-1739003, IIS-1838230, RISE-2126503, RISE-2127606, and RISE-2126468. EastGRIP is directed and organised by the Centre for Ice and Climate at the Niels Bohr Institute, University of Copenhagen. It is supported by funding agencies and institutions in Denmark (A. P. Møller Foundation, University of Copenhagen), USA (US National Science Foundation, Office of Polar Programs), Germany (Alfred Wegener Institute, Helmholtz Centre 475 for Polar and Marine Research), Japan (National Institute of Polar Research and Arctic Challenge for Sustainability), Norway (University of Bergen and Trond Mohn Foundation), Switzerland (Swiss National Science Foundation), France (French Polar Institute Paul-Emile Victor, Institute for Geosciences and Environmental research), Canada (University of Manitoba) and China (Chinese Academy of Sciences and Beijing Normal University).

Julien Westhoff acknowledges funding from Villum Investigator project IceFlow (grant no. 16572). Yu Zhang was funded by the China Scholarship Council (Grant number202006010063). Yuanbang Hu was funded by the China Scholarship Council (Grant number202008510177). Steven Franke was funded by the Walter Benjamin Programme of the Deutsche Forschungsgemeinschaft (DFG;,German Research Foundation; project number 506043073). Nicolas Stoll acknowledges funding from the Programma di Ricerche in Artico (PRA).

## References

Alley, R. B., Gow, A. J., Meese, D. A., Fitzpatrick, J. J., Waddington, E. D. and Bolzan, J. F.: Grain-scale processes, folding, and stratigraphic disturbance in the GISP2 ice core, J. Geophys. Res.,102, 26819–26830, https://doi.org/10.1029/96JC03836, 1997.

Bell, R.E., Tinto, K., Das, I., Wolovick, M., Chu, W., Creyts, T.T., Frearson, N., Abdi, A. and Paden, J.D.: Deformation, warming and softening of Greenland's ice by refreezing meltwater. Nature Geoscience, 7(7), 497-502, https://doi.org/10.1038/ngeo2179, 2014.

Biot, M. A.: Folding Instability of a Layered Viscoelastic Medium under Compression. Proceedings of the Royal Society A: Mathematical, Physical and Engineering Sciences, 242(1231), 444–454, https://doi.org/10.1098/rspa.1957.0187, 1957.

Bohleber, P., Stoll, N., Rittner, M., Roman, M., Weikusat, I., & Barbante, C.: Geochemical characterization of insoluble particle clusters in ice cores using two-dimensional impurity imaging. Geochemistry, Geophysics, Geosystems, 24, e2022GC010595. https://doi.org/10.1029/2022GC010595, 2023.

Bons, P.D., Druguet, E., Hamann, I., Carreras, J., Passchier, C.W.: Apparent boudinage in dykes. Journal of Structural Geology, 26, 625-636, http://dx.doi.org/10.1016/j.jsg.2003.11.009, 2004.

Bons, P.D., Koehn, D. and Jessell, M.W. (Eds): Microdynamic Simulation. Lecture Notes in Earth Sciences 106, Springer, Berlin. 405 pp. ISBN 978-3-540-44793-1, 2008.

Bons, P.D., Jansen, D., Mundel, F., Bauer, C.C., Binder, T., Eisen, O., Jessell, M.W., Llorens, M.G., Steinbach, F., Steinhage, D. and Weikusat, I.: Converging flow and anisotropy cause large-scale folding in Greenland's ice sheet. Nature communications, 7(1), 11427, https://doi.org/10.1038/ncomms11427, 2016.

Budd, W. F., & Jacka, T. H.: A review of ice rheology for ice sheet modeling. Cold Regions Science and Technology, 16, 107–144, https://doi.org/10.1016/0165-232X(89)90014-1, 1989.

Carreras, J., Cosgrove, J.W., Druguet, E.: Strain partitioning in banded and/or anisotropic rocks: Implications for inferring tectonic regimes. J. Struct. Geol. 50, 7-21. https://doi.org/10.1016/j.jsg.2012.12.003, 2013.

Cobbold, P.R., Cosgrove, J.W., Summers, J.M.: Development of internal structures in deformed anisotropic rocks. Tectonophysics 12, 23-53. https://doi.org/10.1016/0040-1951(71)90065-5, 1971.

Druguet, E., Passchier, C.W., Carreras, J., Victor, P., den Brok, S.W.J.: Analysis of a complex high-strain zone at Cap de Creus, Spain. Tectonophysics 280, 31-45, https://doi.org/10.1016/S0040-1951(97)00137-6, 1997.

Duval P, Ashby M, Anderman I.: Rate controlling processes in the creep of polycrystalline ice. J. Phys. Chem. 87, 4066–4074, https://doi.org/10.1021/ j100244a014, 1983.

Faria, S. H., Freitag, J., and Kipfstuhl, S.: Polar ice structure and the integrity of ice-core paleoclimate records, Quaternary Sci. Rev., 29, 338–351, https://doi.org/10.1016/j.quascirev.2009.10.016, 2010.

Faria, S. H., Weikusat, I., & Azuma, N.: The microstructure of polar ice. Part II: State of the art. Journal of Structural Geology, 61, 21–49. https://doi.org/10.1016/j.jsg.2013.11.003, 2014.

Finch, M.A., P.D.Bons, P.D., Steinbacha, F., Griera, A., Llorens, M.-G, Gomez-Rivase, E. Ran, H., de Riese, T.: The ephemeral development of C' shear bands: A numerical modelling approach. J. Struct. Geol. 139. https://doi.org/10.1016/j.jsg.2020.104091, 2020.

Fitzpatrick, J. J., Voigt, D. E., Fegyveresi, J. M., Stevens, N. T., Spencer, M. K., Cole-Dai, J., Alley, R. B., Jardine, G. E., Cravens, E. D., Wilen, L. A., Fudge, T. J., and McConnell, J. R.: Physical Properties of the WAIS Divide ice core, J. Glaciol., 60, 1181–1198, https://doi.org/10.3189/2014JoG14J100, 2014.

Franke, S., Jansen, D., Binder, T., Paden, J. D., Dörr, N., Gerber, T. A., Miller, H., Dahl-Jensen, D., Helm, V., Steinhage, D., Weikusat, I., Wilhelms, F., Eisen, O.: Ultra-wideband radar data over the shear margins and along flow lines at the onset region of the Northeast Greenland Ice Stream (NEGIS) [dataset]. PANGAEA, https://doi.org/10.1594/PANGAEA.928569, 2021.

Franke, S., Bons, P. D., Westhoff, J., Weikusat, I., Binder T., Streng, K., Steinhage, D., Helm, V., Eisen, O., Paden, J. D., Eagles, G. and Jansen, D.: Holocene ice-stream shutdown and drainage basin reorganization in northeast Greenland. Nature Geoscience, 15, 995–1001, https://doi.org/10.1038/s41561-022-01082-2, 2022a.

Franke, S., Jansen, D., Binder, T., Paden, J. D., Dörr, N., Gerber, T. A., Miller, H., Dahl-Jensen,D., Helm, V., Steinhage, D., Weikusat, I., Wilhelms, F., and Eisen, O.: Airborne ultra-wideband radar sounding over the shear margins and along flow lines at the onset region of the Northeast Greenland Ice Stream, Earth Syst. Sci. Data, 14, 763–779, https://doi.org/10.5194/essd-14-763-2022, 2022b.

Franke, S., Bons, P. D., Streng, K., Mundel, F., Binder, T., Weikusat, I., Bauer, C. C., Paden, J. D., Dörr, N., Helm, V., Steinhage, D., Eisen, O., and Jansen, D.: Three-dimensional topology dataset of folded radar stratigraphy in northern Greenland, Sci. Data, 10, 525, https://doi.org/10.1038/s41597-023-02339-0, 2023.

Frehner, M., Schmalholz, S.M.: Numerical simulations of parasitic folding in multilayers. Journal of Structural Geology 28, 1647-1657, https://doi.org/10.1016/j.jsg.2006.05.008, 2006.

Gerber, T. A., Lilien, D. A., Rathmann, N. M., Franke, S., Young, T. J., Valero-Delgado, F., Ershadi, M. R., Drews, R., Zeising, O., Humbert, A., Stoll, N., Weikusat, I., Grinsted, A., Hvidberg, C. S., Jansen, D., Miller, H., Helm, V., Steinhage, D., O'Neill, C., Paden, J., Gogineni, S. P., Dahl-Jensen, D., and Eisen, O.: Crystal orientation fabric anisotropy causes directional hardening of the Northeast Greenland Ice Stream, Nat Commun, 14, 2653, https://doi.org/10.1038/s41467-023-38139-8, 2023.

Glen, J. W.: The creep of polycrystalline ice. Proceedings of the Royal Society of London A: Mathematical, Physical and Engineering Sciences, 228(1175), 519–538, https://doi.org/10.1098/rspa.1955.0066, 1955.

Goldsby, D. L., & Kohlstedt, D. L.: Superplastic deformation of ice: Experimental observations. Journal of Geophysical Research, 106, 11017–11030, https://doi.org/10.1029/2000JB900336, 2001.

Griera, A., Llorens, M.-G., Gomez-Rivas, E., Bons, P. D., Jessell, M. W., Evans, L. A., Lebensohn, R.: Numerical modelling of porphyroclast and porphyroblast rotation in anisotropic rocks. Tectonophysics, 587, 4–29. https://doi.org/10.1016/j.tecto.2012.10.008, 2013.

Hansen, Lars N., Faccenda, M., Warren, J. M.: A review of mechanisms generating seismic anisotropy in the upper mantle, Physics of the Earth and Planetary Interiors, 313, 106662, https://doi.org/10.1016/j.pepi.2021.106662, 2021.

Hao, B., Llorens, M.-G., Griera, A., Bons, P. D., Lebensohn, R. A., Yu, Y., & Gomez-Rivas, E.: Full-Field Numerical Simulation of Halite Dynamic Recrystallization From Subgrain Rotation to Grain Boundary Migration, Journal of Geophysical Research: Solid Earth, 128, https://doi.org/10.1029/2023JB027590, 2023.

Hu, Y, Bons, P.D., de Riese, T., Liu, S, Llorens, M.-G., González-Esvertit, E., Gómez-Rivas, E., Li, D., Fu, Y., Cai, X.: Folding of a single layer in an anisotropic viscous matrix under layer-parallel shortening. J. Struct. Geol. 188, 105246. https://doi.org/10.1016/j.jsg.2024.105246, 2024.

Hudleston, P.J.: An analysis of "single-layer" folds developed experimentally in viscous media. Tectonophysics 16 (3–4), 189–214. https://doi.org/10.1016/0040-1951(73)90012-7, 1973.

Hudleston, P.J.: Structures and Fabrics in Glacial Ice: A Review, Journal of Structural Geology, 81, 1-27, https://doi.org/10.1016/j.jsg.2015.09.003, 2015.

Jansen, D., Llorens, M.-G, Westhoff, J., Steinbach, F., Kipfstuhl, S., Bons, P.D., Griera, A., Weikusat, I.: Small-scale disturbances in the stratigraphy of the NEEM ice core: observations and numerical model simulations. The Cryosphere 10, 359-370. doi:10.5194/tc-10-359-2016, 2016.

Jansen, D., Franke, S., Bauer, C. C., Binder, T., Dahl-Jensen, D., Eichler, J., Eisen, O., Hu, Y., Kerch, J., Llorens, M.-G., Miller, H., Neckel, N., Paden, J., Riese, T. de, Sachau, T., Stoll, N., Weikusat, I., Wilhelms, F., Zhang, Y., and Bons, P. D.: Shear margins in upper half of Northeast Greenland Ice Stream were established two millennia ago, Nat. Commun., 15, 1193, https://doi.org/10.1038/s41467-024-45021-8, 2024.

Krabbendam, M.: Sliding of temperate basal ice on a rough, hard bed: creep mechanisms, pressure melting, and implications for ice streaming, The Cryosphere, 10, 1915–1932, https://doi.org/10.5194/tc-10-1915-2016, 2016.

Lebensohn, R.A.: N-site modeling of a 3D viscoplastic polycrystal using Fast Fourier Transform. Acta Materialia, 49, 2723-2737. https://doi.org/10.1016/S1359-6454(01)00172-0, 2001.

Lebensohn, R.A., Brenner, R., Castelnau, O. and Rollett, A. D.: Orientation image-based micromechanical modelling of subgrain texture evolution in polycrystalline copper. Acta Materialia, 56, 3914-3926. https://doi.org/10.1016/j.actamat.2008.04.016, 2008.

Lebensohn, R.A. and Rollett, A.D.: Spectral methods for full-field micromechanical modelling of polycrystalline materials. Computational Materials Science, 173, 109336. https://doi.org/10.1016/j.commatsci.2019.109336, 2020.

Leysinger Vieli, G. J.-M. C., Martín, C., Hindmarsh, R. C. A., and Lüthi, M. P.: Basal freeze-on generates complex ice-sheet stratigraphy, Nat Commun, 9, 4669, https://doi.org/10.1038/s41467-018-07083-3, 2018.

Llorens, M. G., Bons, P. D., Griera, A., Gomez-Rivas, E. and Evans, L. A.: Single layer folding in simple shear, J. Struct. Geol., 50, 209-220, https://doi.org/10.1016/j.jsg.2012.04.002, 2013.

Llorens, M.G.: Stress and strain evolution during single-layer folding under pure and simple shear. Journal of Structural Geology, 126, 245-257m https://doi.org/10.1016/j.jsg.2019.06.009, 2019.

Llorens, M.-G., Griera, A., Steinbach, F., Bons, P.D., Gomez-Rivas, E., Jansen, D., Roessiger, J., Levensohn, R.A., Weikusat, I.: Dynamic recrystallisation during deformation of polycrystalline ice: insights from numerical simulations. Philosophical Transactions of the Royal Society A, Special Issue on Microdynamics of Ice, 375, 20150346, https://doi.org/10.1098/rsta.2015.0346, 2017.

Nabavi, S. T. and Fossen, H.: Fold geometry and folding – a review, Earth-sci Rev, 222, 103812, https://doi.org/10.1016/j.earscirev.2021.103812, 2021.

NEEM community members: Eemian interglacial reconstructed from a Greenland folded ice core. Nature, 493, 489–494, https://doi.org/10.1038/nature11789, 2013.

Panton, C., and Karlsson, N. B.: Automated mapping of near bed radio-echo layer disruptions in the Greenland Ice Sheet, Earth Planet. Sci. Lett., 432, 323–331, https://doi.org/10.1016/j.epsl.2015.10.024, 2015.

Press, W.H., Teukolsky, S.A., Vetterling, W.T., Flannery, B.P.: Numerical recipes in C, 2nd Ed. Cambridge University Press, Cambridge. 994, 1992.

Ramsay, J.G.: Development of chevron folds. GSA Bulletin 85, 1741–1754. https://doi.org/10.1130/0016-7606(1974)85<1741:DOCF>2.0.CO;2, 1974.

Ramsay, J.G., Huber, M.I.: The Techniques of Modern Structural Geology: Folds and Fractures, Vol. 2. Academic Press, London, 1987.

Schmalholz, S.M., Mancktelow, N.S.: Folding and necking across the scales: a review of theoretical and experimental results and their applications. Solid Earth, 7, 1417-1465. doi:10.5194/se-7-1417-2016, 2016.

Schneider, C., Rasband, W. & Eliceiri, K. NIH Image to ImageJ: 25 years of image analysis. Nat Methods 9, 671–675, https://doi.org/10.1038/nmeth.2089, 2012.

Stoll, N., Westhoff, J., Bohleber, P., Svensson, A., Dahl-Jensen, D., Barbante, C., and Weikusat, I.: Chemical and visual characterisation of EGRIP glacial ice and cloudy bands within, The Cryosphere, 17, 2021–2043, https://doi.org/10.5194/tc-17-2021-2023, 2023.

Stoll, N., Weikusat, I., Jansen, D., Bons, P., Darányi, K., Westhoff, J., Llorens, M.-G., Wallis, D., Eichler, J., Saruya, T., Homma, T., Drury, M., Wilhelms, F., Kipfstuhl, S., Dahl-Jensen, D., and Kerch, J.: EastGRIP ice core reveals the exceptional evolution of crystallographic preferred orientation throughout the Northeast Greenland Ice Stream, EGUsphere [preprint], https://doi.org/10.5194/egusphere-2024-2653, 2024.

Svensson, A., Wedel Nielsen, S., Kipfstuhl, S., Johnsen, J., Steffensen, J. P., Bigler, M., Ruth, U., and Röthlisberger, R.: Visual Stratigraphy of the North Greenland Ice Core Project (NorthGRIP) ice core during the last glacial period, J. Geophys. Res., 110, D02108, https://doi.org/10.1029/2004JD005134, 2005.

Thorsteinsson, T.: Textures and fabrics in the GRIP ice core, in relation to climate history and ice deformation (Thesis), Berichte zur Polarforschung, AWI Bremerhaven, Bremerhaven, 120–133, https://doi.org/10.2312/BzP_0205_1996, 1996

Waddington, E. D., Bolzan, J. F., & Alley, R. B.: Potential for stratigraphic folding near ice-sheet centers, J. Glaciol., 47, 639–648, https://doi.org/10.3189/172756501781831756, 2001.

Weertman, J.: Creep deformation of ice. Annual Review of Earth and Planetary Sciences, 11(1), 215–240, https://doi.org/10.1146/annurev.ea.11.050183.001243, 1983.

Weikusat, I., Jansen, D., Binder, T., Eichler, J., Faria, S. H., Wilhelms, F., Kipfstuhl, S., Sheldon, S., Miller, H., Dahl-Jensen, D., and Kleiner, T.: Physical analysis of an Antarctic ice coretowards an integration of micro- and macrodynamics of polar ice, Philos. Trans. R. Soc. A: Math., Phys. Eng. Sci., 375, 20150347, https://doi.org/10.1098/rsta.2015.0347, 2017.

Weikusat, I., Westhoff, J., Kipfstuhl, S., Jansen, D.: Visual stratigraphy of the EastGRIP ice core (14 m - 2021 m depth, drilling period 2017-2019) [dataset]. PANGAEA, https://doi.org/10.1594/PANGAEA.925014, 2020.

Westhoff, J., Stoll, N., Franke, S., Weikusat, I., Bons, P., Kerch, J., Jansen, D., Kipfstuhl, S. & Dahl-Jensen, D.: A Stratigraphy Based Method for Reconstructing Ice Core Orientation. Annals of Glaciology, 62 (85-86), 191-202, https://doi.org/10.1017/aog.2020.76, 2021.

Wolovick, M. J., Creyts, T. T., Buck, W. R. and Bell, R. E.: Traveling slippery patches produce thickness-scale folds in ice sheets. Geophys. Res. Letts., 41(24), 8895-8901, https://doi.org/10.1002/2014GL062248, 2014.

Zhang, Y., Sachau, T., Franke, S., Yang, H., Li, D., Weikusat, I., Bons, P. D.: Formation Mechanisms of Large-Scale Folding in Greenland's Ice Sheet. Geophys. Res. Letts., 51, e2024GL109492, https://doi.org/10.1029/2024GL109492, 2024.

# Appendix

## Code 1

This is an example code script of the large-scale fold modelling (Chapter 2, Model 4). Full-scripts of all fold models can be accessed through Zenodo (https://doi.org/10.5281/zenodo.11396618).

```
# import modules, create output directory
import numpy as np
import math
import os

from mpi4py import MPI

comm = MPI.COMM_WORLD
rank = comm.Get_rank()

import underworld as uw

from underworld import function as fn
import underworld.visualisation as vis

import pickle

if not os.getcwd().rsplit("/")[-1] == "output":
    outputPath = os.path.join(os.path.abspath("."),"output/")
    if not os.path.exists ( outputPath ):
        os.makedirs ( outputPath )

    os.chdir(outputPath)

# +
## basic parameters

g = 9.81
#ice_density = 910.

#A = 1e-16
n = 4.

MODEL_DATA = {}
coord = fn.input()
bed = 1000.0
iceHeight = 2500.0+bed
WarmiceHeight = (iceHeight-bed) * 40./100.+bed
airHeight = 500.0
zmin = 0.
zmax = 20000.
MODEL_DATA['MIN_Y'] = 0.0
MODEL_DATA['MAX_Y'] = 3000.0+bed
MODEL_DATA['MAX_X'] = 500.
MODEL_DATA['MIN_X'] = 0.0
MODEL_DATA['MIN_Z'] = 0.0
MODEL_DATA['MAX_Z'] = 25000.
MODEL_DATA['RES_X'] = 4
MODEL_DATA['RES_Y'] = 32
MODEL_DATA['RES_Z'] = 512

mi = 0.2

#elementType = "Q1/dQ0"
#elementType = "Q2/dQ1"
#elementType = "Q1/dPc1"
#elementType = "Q2/dPc1"
MODEL_DATA['ELEMENT_TYPE'] = "Q1/dQ0"
MODEL_DATA['PERIODIC_X'] = False
MODEL_DATA['PERIODIC_Y'] = False
MODEL_DATA['PERIODIC_Z'] = False
MODEL_DATA['PARTICLES_PER_CELL'] = 30

mesh = uw.mesh.FeMesh_Cartesian( elementType = ( MODEL_DATA['ELEMENT_TYPE'] ) ,
                                 elementRes  = ( MODEL_DATA['RES_X'], MODEL_DATA['RES_Y'], MODEL_DATA['RES_Z']),
                                 minCoord    = ( MODEL_DATA['MIN_X'], MODEL_DATA['MIN_Y'], MODEL_DATA['MIN_Z'] ),
                                 maxCoord    = ( MODEL_DATA['MAX_X'], MODEL_DATA['MAX_Y'], MODEL_DATA['MAX_Z'] ),
                                 periodic    = ( MODEL_DATA['PERIODIC_X'], MODEL_DATA['PERIODIC_Y'], MODEL_DATA['PERIODIC_Z'] )
                               )

velocityField    = mesh.add_variable(         dataType="double",  nodeDofCount=3 )
pressureField    = mesh.subMesh.add_variable( dataType="double",  nodeDofCount=1 )
directorField    = mesh.add_variable( dataType="double",  nodeDofCount=3 )

velocityField.data[:] = [0.,0.,0.]
directorField.data[:] = [0.,1.,0.]
pressureField.data[:] = 0.
```

```
## visualisation parameters
MODEL_DATA_FILE = outputPath + "model_data.p"
pickle.dump( MODEL_DATA, open(MODEL_DATA_FILE , "wb" ) )
# -

BW1 = (zmax-zmin)/4. #4500/100, 14000/200
BumpAmplitude = 400.
#TotalBumpWidth = BumpWidth*2.5
#min = BumpWidth*1.5
#zmax = BumpWidth*2.5
k1 = 2. * np.pi / BW1
BW2 = (zmax-zmin)/7.
BW3 = (zmax-zmin)/8.
BW4 = (zmax-zmin)/11.
k2 = 2. * np.pi / BW2
k3 = 2. * np.pi / BW3
k4 = 2. * np.pi / BW4
BA1 = BumpAmplitude
BA2 = BumpAmplitude/2.
BA3 = BumpAmplitude/4.
BA4 = BumpAmplitude/8.

# +
# Create a swarm which will define our material geometries, and will also
# track deformation and history dependence of particles.
swarm  = uw.swarm.Swarm( mesh=mesh, particleEscape=True)
#parts_per_cell = 50

swarmLayout = uw.swarm.layouts.PerCellSpaceFillerLayout( swarm=swarm, particlesPerCell=MODEL_DATA['PARTICLES_PER_CELL'] )
swarm.populate_using_layout( layout=swarmLayout )

# create pop control object
pop_control1 = uw.swarm.PopulationControl(swarm, aggressive=True, particlesPerCell=MODEL_DATA['PARTICLES_PER_CELL'])

# create advector
advector1 = uw.systems.SwarmAdvector(swarm=swarm,velocityField=velocityField, order=2)

# +
# Initialise particle properties
materialVariable = swarm.add_variable( dataType="int", count=1 )
particleDensity = swarm.add_variable ( dataType="double", count=1 )
particleInitialYPos = swarm.add_variable ( dataType="double", count=1 )

particleStrainrate = swarm.add_variable ( dataType="double", count=1 )
particleViscosity = swarm.add_variable ( dataType="double", count=1 )
particleViscosity2 = swarm.add_variable ( dataType="double", count=1 )
particleShearstress = swarm.add_variable ( dataType="double", count=1 )

particleDirector = swarm.add_variable ( dataType="double", count=3 )
# particleMeshDirector below only used to save the director if calculated as a mesh variable
#particleMeshDirector = swarm.add_variable ( dataType="double", count=3 )

#particleWeakzone = swarm.add_variable ( dataType="int", count=1 )

particleTemperature = swarm.add_variable ( dataType="double", count=1 ) ###
particleTemperature.data[:] = 0.

#particleSnowHeight = swarm.add_variable ( dataType="double", count=1 )
#particleSnowHeight.data[:] = 0.

particleVelocity = swarm.add_variable( dataType="double", count=3 )
particleVelocity.data[:] = (0.,0.,0.)

#iceSurf = swarm.add_variable ( dataType="int", count=1 )
#iceSurf.data[:] = 0

particleCreationTime = swarm.add_variable ( dataType="float", count=1 )
particleCreationTime.data[:] = 0.

bumpHeight = swarm.add_variable( dataType="double", count=1 )
WarmiceHeight = swarm.add_variable( dataType="double", count=1 )
#showPlane = swarm.add_variable ( dataType="int", count=1 )
# -
```

```
# ### Definition of materials

# +
materialV = 1  # viscoplastic ice
materialVC = 2 # viscoplastic ice in the channel
materialA = 0 # Air
materialR = 3   # rock

coord = fn.input()
z=swarm.data[:, 2]
x=swarm.data[:, 0]
y=swarm.data[:, 1]

particleInitialYPos.data[:] = np.expand_dims(coord.evaluate(swarm)[:,1], axis=1)

bumpfunc=((np.cos((z-zmin)*k1+np.pi)+1.)*BA1/2.+(np.cos((z-zmin)*k2+np.pi)+1.)*BA2/2.
         +(np.cos((z-zmin)*k3+np.pi)+1.)*BA3/2.+(np.cos((z-zmin)*k4+np.pi)+1.)*BA4/2.)/(1.0 + 0.5 + 0.25 + 0.125)
Amax = 321.4
#Amax = np.max(bumpfunc) #321.378117416
#print(Amax)
#bumpfunc=bumpfunc/Amax*BumpAmplitude+bed

bumpfunc = lambda z: bed if z<zmin or z>zmax  else
          bed+BumpAmplitude/Amax*((np.cos((z-zmin)*k1+np.pi)+1.)*BA1/2.+(np.cos((z-zmin)*k2+np.pi)+1.)*BA2/2.
        +(np.cos((z-zmin)*k3+np.pi)+1.)*BA3/2.+(np.cos((z-zmin)*k4+np.pi)+1.)*BA4/2.)/(1.0 + 0.5 + 0.25 + 0.125)
bumpfunc = np.vectorize(bumpfunc)
bumpHeight.data[:] = np.expand_dims(bumpfunc(z), 1)

WarmiceHeight = bumpHeight + 4/10*(iceHeight-bumpHeight)
zz_pow = (WarmiceHeight - bumpHeight)**mi
zz_pow_max = (iceHeight - bumpHeight)**mi
WarmiceHeight =bumpHeight + (WarmiceHeight-bumpHeight) * zz_pow / zz_pow_max
#bumpfunc = np.vectorize(bumpfunc)
#WarmiceHeight.data[:] = np.expand_dims(Warmicefunc, 1)

conditions = [
               (       coord[1] > iceHeight,    materialA    ),
               (       coord[1] > WarmiceHeight,    materialV    ),
               (       coord[1] > bumpHeight,    materialVC    ),
               (       True ,           materialR                 ),
             ]

materialVariable.data[:] = fn.branching.conditional( conditions ).evaluate(swarm)

# +
for index in np.ndindex(directorField.data.shape[0]):
    maxAngle = 5./90.*np.pi/2.
    gaus = np.random.normal(0., maxAngle) #Gaussian distribution
    bumpfunc = bed+BumpAmplitude/Amax*((np.cos((mesh.data[index][2]-zmin)*k1+np.pi)+1.)*BA1/2.
              +(np.cos((mesh.data[index][2]-zmin)*k2+np.pi)+1.)*BA2/2.+(np.cos((mesh.data[index][2]-zmin)*k3+np.pi)+1.)*BA3/2.
             +(np.cos((mesh.data[index][2]-zmin)*k4+np.pi)+1.)*BA4/2.)/(1.0 + 0.5 + 0.25 + 0.125)
    derivative_bumpfunc = BumpAmplitude/(2*Amax*(1.0+0.5+0.25+0.125)) * (-BA1*k1*np.sin(k1*(mesh.data[index][2]-zmin)+np.pi)
                    -BA2*k2*np.sin(k2*(mesh.data[index][2]-zmin)+np.pi)-BA3*k3*np.sin(k3*(mesh.data[index][2]-zmin)+np.pi)
                -BA4*k4*np.sin(k4*(mesh.data[index][2]-zmin)+np.pi)) # derivative of bumpfunc
    tangent_angle = np.arctan(derivative_bumpfunc) #angle of the tangent line
    #print(tangent_angle)
    TopAmplitude = 0.
    tangent_angle_top = 0.

    if iceHeight>=mesh.data[index][1]>bumpfunc and zmin<=mesh.data[index][2]<=zmax and 0.<tangent_angle<np.pi/2.:
        tangent_angle_func = tangent_angle + (mesh.data[index][1]-bumpfunc)/(iceHeight-bumpfunc) * (tangent_angle_top-tangent_angle)
        tangent_angle_func = tangent_angle + (tangent_angle_func-tangent_angle)
                          *((tangent_angle_func-tangent_angle)/(tangent_angle_top-tangent_angle))**mi
        directorField.data[index][1] = np.cos(gaus-tangent_angle_func)
        directorField.data[index][2] = np.sin(gaus-tangent_angle_func)
    elif iceHeight>=mesh.data[index][1]>bumpfunc and zmin<=mesh.data[index][2]<=zmax and -np.pi/2<tangent_angle<0.:
        tangent_angle_func= tangent_angle + (mesh.data[index][1]-bumpfunc)/(iceHeight-bumpfunc) * (tangent_angle_top-tangent_angle)
        tangent_angle_func = tangent_angle + (tangent_angle_func-tangent_angle)
                          *((tangent_angle_func-tangent_angle)/(tangent_angle_top-tangent_angle))**mi
        directorField.data[index][1] = np.cos(gaus-tangent_angle_func)
        directorField.data[index][2] = np.sin(gaus-tangent_angle_func)
    else:
        directorField.data[index][1] =np.cos(gaus)
        directorField.data[index][2] =np.sin(gaus)

particleDirector.data[:]  = directorField.evaluate(swarm)
```

```
## swarms to track the deformation
surfaceSwarm1 = uw.swarm.Swarm(mesh=mesh, particleEscape=True)
surfaceSwarm2 = uw.swarm.Swarm(mesh=mesh, particleEscape=True)
surfaceSwarm3 = uw.swarm.Swarm(mesh=mesh, particleEscape=True)
surfaceSwarm4 = uw.swarm.Swarm(mesh=mesh, particleEscape=True)
surfaceSwarm5 = uw.swarm.Swarm(mesh=mesh, particleEscape=True)
surfaceSwarm6 = uw.swarm.Swarm(mesh=mesh, particleEscape=True)
surfaceSwarm7 = uw.swarm.Swarm(mesh=mesh, particleEscape=True)
surfaceSwarm8 = uw.swarm.Swarm(mesh=mesh, particleEscape=True)
surfaceSwarm9 = uw.swarm.Swarm(mesh=mesh, particleEscape=True)
surfaceSwarm10 = uw.swarm.Swarm(mesh=mesh, particleEscape=True)

# create advector
advector2 = uw.systems.SwarmAdvector(swarm=surfaceSwarm1,velocityField=velocityField, order=2)
advector3 = uw.systems.SwarmAdvector(swarm=surfaceSwarm2,velocityField=velocityField, order=2)
advector4 = uw.systems.SwarmAdvector(swarm=surfaceSwarm3,velocityField=velocityField, order=2)
advector5 = uw.systems.SwarmAdvector(swarm=surfaceSwarm4,velocityField=velocityField, order=2)
advector6 = uw.systems.SwarmAdvector(swarm=surfaceSwarm5,velocityField=velocityField, order=2)
advector7 = uw.systems.SwarmAdvector(swarm=surfaceSwarm6,velocityField=velocityField, order=2)
advector8 = uw.systems.SwarmAdvector(swarm=surfaceSwarm7,velocityField=velocityField, order=2)
advector9 = uw.systems.SwarmAdvector(swarm=surfaceSwarm8,velocityField=velocityField, order=2)
advector10 = uw.systems.SwarmAdvector(swarm=surfaceSwarm9,velocityField=velocityField, order=2)
advector11 = uw.systems.SwarmAdvector(swarm=surfaceSwarm10,velocityField=velocityField, order=2)

#surfacePoints1
surfacePoints = np.array(np.meshgrid(np.linspace(0, MODEL_DATA['MAX_X'], 50),
                                     MODEL_DATA['MAX_Y'], np.linspace(0., MODEL_DATA['MAX_Z'], 500))).T.reshape(-1, 3)

x = surfacePoints[:, 0]
z = surfacePoints[:, 2]
s20 = bed+ 9/10*(iceHeight-bed) * (9/10)**mi
s30 = bed+ 8/10*(iceHeight-bed) * (8/10)**mi
s40 = bed+ 7/10*(iceHeight-bed) * (7/10)**mi
s50 = bed+ 6/10*(iceHeight-bed) * (6/10)**mi
s60 = bed+ 5/10*(iceHeight-bed) * (5/10)**mi
s70 = bed+ 4/10*(iceHeight-bed) * (4/10)**mi
s80 = bed+ 3/10*(iceHeight-bed) * (3/10)**mi
s90 = bed+ 2/10*(iceHeight-bed) * (2/10)**mi
s100 = bed+ 1/10*(iceHeight-bed) * (1/10)**mi
#print(s20,s30,s40,s50,s60,s70,s80,s90,s100)
#3203.0838153121977 2912.704999580074 2629.512351415966 2354.320677171151 2088.188204120155 1832.5532074018731 1589.502314197467 1362.3898318

surfacePoints[:, 1] = iceHeight
surfaceSwarm1.add_particles_with_coordinates(surfacePoints)
s2 = lambda z: s20 if z<zmin or z>zmax else bed+BumpAmplitude/Amax*((np.cos((z-zmin)*k1+np.pi)+1.)*BA1/2.
    +(np.cos((z-zmin)*k2+np.pi)+1.)*BA2/2.+(np.cos((z-zmin)*k3+np.pi)+1.)*BA3/2.+(np.cos((z-zmin)*k4+np.pi)+1.)*BA4/2.)/(1.0+0.5+0.25+0.125)
    + (9/10*(iceHeight-(BumpAmplitude/Amax*((np.cos((z-zmin)*k1+np.pi)+1.)*BA1/2.+(np.cos((z-zmin)*k2+np.pi)+1.)*BA2/2.
    +(np.cos((z-zmin)*k3+np.pi)+1.)*BA3/2.+(np.cos((z-zmin)*k4+np.pi)+1.)*BA4/2.)/(1.0+0.5+0.25+0.125)+bed))) * (9/10)**mi
s2 = np.vectorize(s2)
surfacePoints[:, 1] = s2(z)
surfaceSwarm2.add_particles_with_coordinates(surfacePoints)
s3 = lambda z: s30 if z<zmin or z>zmax else bed+BumpAmplitude/Amax*((np.cos((z-zmin)*k1+np.pi)+1.)*BA1/2.
    +(np.cos((z-zmin)*k2+np.pi)+1.)*BA2/2.+(np.cos((z-zmin)*k3+np.pi)+1.)*BA3/2.+(np.cos((z-zmin)*k4+np.pi)+1.)*BA4/2.)/(1.0+0.5+0.25+0.125)
     + (8/10*(iceHeight-(BumpAmplitude/Amax*((np.cos((z-zmin)*k1+np.pi)+1.)*BA1/2.+(np.cos((z-zmin)*k2+np.pi)+1.)*BA2/2.
    +(np.cos((z-zmin)*k3+np.pi)+1.)*BA3/2.+(np.cos((z-zmin)*k4+np.pi)+1.)*BA4/2.)/(1.0+0.5+0.25+0.125)+bed))) * (8/10)**mi
s3 = np.vectorize(s3)
surfacePoints[:, 1] = s3(z)
surfaceSwarm3.add_particles_with_coordinates(surfacePoints)
s4 = lambda z: s40 if z<zmin or z>zmax else bed+BumpAmplitude/Amax*((np.cos((z-zmin)*k1+np.pi)+1.)*BA1/2.
    +(np.cos((z-zmin)*k2+np.pi)+1.)*BA2/2.+(np.cos((z-zmin)*k3+np.pi)+1.)*BA3/2.+(np.cos((z-zmin)*k4+np.pi)+1.)*BA4/2.)/(1.0+0.5+0.25+0.125)
    + (7/10*(iceHeight-(BumpAmplitude/Amax*((np.cos((z-zmin)*k1+np.pi)+1.)*BA1/2.+(np.cos((z-zmin)*k2+np.pi)+1.)*BA2/2.
    +(np.cos((z-zmin)*k3+np.pi)+1.)*BA3/2.+(np.cos((z-zmin)*k4+np.pi)+1.)*BA4/2.)/(1.0+0.5+0.25+0.125)+bed))) * (7/10)**mi
s4 = np.vectorize(s4)
surfacePoints[:, 1] = s4(z)
surfaceSwarm4.add_particles_with_coordinates(surfacePoints)
s5 = lambda z: s50 if z<zmin or z>zmax else bed+BumpAmplitude/Amax*((np.cos((z-zmin)*k1+np.pi)+1.)*BA1/2.
    +(np.cos((z-zmin)*k2+np.pi)+1.)*BA2/2.+(np.cos((z-zmin)*k3+np.pi)+1.)*BA3/2.+(np.cos((z-zmin)*k4+np.pi)+1.)*BA4/2.)/(1.0+0.5+0.25+0.125)
    + (6/10*(iceHeight-(BumpAmplitude/Amax*((np.cos((z-zmin)*k1+np.pi)+1.)*BA1/2.+(np.cos((z-zmin)*k2+np.pi)+1.)*BA2/2.
    +(np.cos((z-zmin)*k3+np.pi)+1.)*BA3/2.+(np.cos((z-zmin)*k4+np.pi)+1.)*BA4/2.)/(1.0+0.5+0.25+0.125)+bed))) * (6/10)**mi
s5 = np.vectorize(s5)
surfacePoints[:, 1] = s5(z)
surfaceSwarm5.add_particles_with_coordinates(surfacePoints)
s6 = lambda z: s60 if z<zmin or z>zmax else bed+BumpAmplitude/Amax*((np.cos((z-zmin)*k1+np.pi)+1.)*BA1/2.
    +(np.cos((z-zmin)*k2+np.pi)+1.)*BA2/2.+(np.cos((z-zmin)*k3+np.pi)+1.)*BA3/2.+(np.cos((z-zmin)*k4+np.pi)+1.)*BA4/2.)/(1.0+0.5+0.25+0.125)
    + (5/10*(iceHeight-(BumpAmplitude/Amax*((np.cos((z-zmin)*k1+np.pi)+1.)*BA1/2.+(np.cos((z-zmin)*k2+np.pi)+1.)*BA2/2.
    +(np.cos((z-zmin)*k3+np.pi)+1.)*BA3/2.+(np.cos((z-zmin)*k4+np.pi)+1.)*BA4/2.)/(1.0+0.5+0.25+0.125)+bed))) * (5/10)**mi
s6 = np.vectorize(s6)
surfacePoints[:, 1] = s6(z)
surfaceSwarm6.add_particles_with_coordinates(surfacePoints)
s7 = lambda z: s70 if z<zmin or z>zmax else bed+BumpAmplitude/Amax*((np.cos((z-zmin)*k1+np.pi)+1.)*BA1/2.
    +(np.cos((z-zmin)*k2+np.pi)+1.)*BA2/2.+(np.cos((z-zmin)*k3+np.pi)+1.)*BA3/2.+(np.cos((z-zmin)*k4+np.pi)+1.)*BA4/2.)/(1.0+0.5+0.25+0.125)
    + (4/10*(iceHeight-(BumpAmplitude/Amax*((np.cos((z-zmin)*k1+np.pi)+1.)*BA1/2.+(np.cos((z-zmin)*k2+np.pi)+1.)*BA2/2.
    +(np.cos((z-zmin)*k3+np.pi)+1.)*BA3/2.+(np.cos((z-zmin)*k4+np.pi)+1.)*BA4/2.)/(1.0+0.5+0.25+0.125)+bed))) * (4/10)**mi
s7 = np.vectorize(s7)
surfacePoints[:, 1] = s7(z)
surfaceSwarm7.add_particles_with_coordinates(surfacePoints)
s8 = lambda z: s80 if z<zmin or z>zmax else bed+BumpAmplitude/Amax*((np.cos((z-zmin)*k1+np.pi)+1.)*BA1/2.
    +(np.cos((z-zmin)*k2+np.pi)+1.)*BA2/2.+(np.cos((z-zmin)*k3+np.pi)+1.)*BA3/2.+(np.cos((z-zmin)*k4+np.pi)+1.)*BA4/2.)/(1.0+0.5+0.25+0.125)
    + (3/10*(iceHeight-(BumpAmplitude/Amax*((np.cos((z-zmin)*k1+np.pi)+1.)*BA1/2.+(np.cos((z-zmin)*k2+np.pi)+1.)*BA2/2.
    +(np.cos((z-zmin)*k3+np.pi)+1.)*BA3/2.+(np.cos((z-zmin)*k4+np.pi)+1.)*BA4/2.)/(1.0+0.5+0.25+0.125)+bed))) * (3/10)**mi
s8 = np.vectorize(s8)
surfacePoints[:, 1] = s8(z)
surfaceSwarm8.add_particles_with_coordinates(surfacePoints)
s9 = lambda z: s90 if z<zmin or z>zmax else bed+BumpAmplitude/Amax*((np.cos((z-zmin)*k1+np.pi)+1.)*BA1/2.
    +(np.cos((z-zmin)*k2+np.pi)+1.)*BA2/2.+(np.cos((z-zmin)*k3+np.pi)+1.)*BA3/2.+(np.cos((z-zmin)*k4+np.pi)+1.)*BA4/2.)/(1.0+0.5+0.25+0.125)
    + (2/10*(iceHeight-(BumpAmplitude/Amax*((np.cos((z-zmin)*k1+np.pi)+1.)*BA1/2.+(np.cos((z-zmin)*k2+np.pi)+1.)*BA2/2.
    +(np.cos((z-zmin)*k3+np.pi)+1.)*BA3/2.+(np.cos((z-zmin)*k4+np.pi)+1.)*BA4/2.)/(1.0+0.5+0.25+0.125)+bed))) * (2/10)**mi
s9 = np.vectorize(s9)
surfacePoints[:, 1] = s9(z)
surfaceSwarm9.add_particles_with_coordinates(surfacePoints)
s10 = lambda z: s100 if z<zmin or z>zmax else bed+BumpAmplitude/Amax*((np.cos((z-zmin)*k1+np.pi)+1.)*BA1/2.
    +(np.cos((z-zmin)*k2+np.pi)+1.)*BA2/2.+(np.cos((z-zmin)*k3+np.pi)+1.)*BA3/2.+(np.cos((z-zmin)*k4+np.pi)+1.)*BA4/2.)/(1.0+0.5+0.25+0.125)
    + (1/10*(iceHeight-(BumpAmplitude/Amax*((np.cos((z-zmin)*k1+np.pi)+1.)*BA1/2.+(np.cos((z-zmin)*k2+np.pi)+1.)*BA2/2.
    +(np.cos((z-zmin)*k3+np.pi)+1.)*BA3/2.+(np.cos((z-zmin)*k4+np.pi)+1.)*BA4/2.)/(1.0+0.5+0.25+0.125)+bed)))*(1/10)**mi
s10 = np.vectorize(s10)
surfacePoints[:, 1] = s10(z)
surfaceSwarm10.add_particles_with_coordinates(surfacePoints)
```

```
#surfacePoints2
surfacePoints[:, 1] = iceHeight
surfaceSwarm1.add_particles_with_coordinates(surfacePoints)
s2 = lambda z: s20 if z<zmin or z>zmax else bed+BumpAmplitude/Amax*((np.cos((z-zmin)*k1+np.pi)+1.)*BA1/2.
    +(np.cos((z-zmin)*k2+np.pi)+1.)*BA2/2.+(np.cos((z-zmin)*k3+np.pi)+1.)*BA3/2.+(np.cos((z-zmin)*k4+np.pi)+1.)*BA4/2.)/(1.0+0.5+0.25+0.125)
    + (9/10*(iceHeight-(BumpAmplitude/Amax*((np.cos((z-zmin)*k1+np.pi)+1.)*BA1/2.+(np.cos((z-zmin)*k2+np.pi)+1.)*BA2/2.
    +(np.cos((z-zmin)*k3+np.pi)+1.)*BA3/2.+(np.cos((z-zmin)*k4+np.pi)+1.)*BA4/2.)/(1.0+0.5+0.25+0.125)+bed))) * (9/10)**mi
s2 = np.vectorize(s2)
surfacePoints[:, 1] = s2(z)
surfaceSwarm2.add_particles_with_coordinates(surfacePoints)
s3 = lambda z: s30 if z<zmin or z>zmax else bed+BumpAmplitude/Amax*((np.cos((z-zmin)*k1+np.pi)+1.)*BA1/2.
    +(np.cos((z-zmin)*k2+np.pi)+1.)*BA2/2.+(np.cos((z-zmin)*k3+np.pi)+1.)*BA3/2.+(np.cos((z-zmin)*k4+np.pi)+1.)*BA4/2.)/(1.0+0.5+0.25+0.125)
     + (8/10*(iceHeight-(BumpAmplitude/Amax*((np.cos((z-zmin)*k1+np.pi)+1.)*BA1/2.+(np.cos((z-zmin)*k2+np.pi)+1.)*BA2/2.
    +(np.cos((z-zmin)*k3+np.pi)+1.)*BA3/2.+(np.cos((z-zmin)*k4+np.pi)+1.)*BA4/2.)/(1.0+0.5+0.25+0.125)+bed))) * (8/10)**mi
s3 = np.vectorize(s3)
surfacePoints[:, 1] = s3(z)
surfaceSwarm3.add_particles_with_coordinates(surfacePoints)
s4 = lambda z: s40 if z<zmin or z>zmax else bed+BumpAmplitude/Amax*((np.cos((z-zmin)*k1+np.pi)+1.)*BA1/2.
    +(np.cos((z-zmin)*k2+np.pi)+1.)*BA2/2.+(np.cos((z-zmin)*k3+np.pi)+1.)*BA3/2.+(np.cos((z-zmin)*k4+np.pi)+1.)*BA4/2.)/(1.0+0.5+0.25+0.125)
    + (7/10*(iceHeight-(BumpAmplitude/Amax*((np.cos((z-zmin)*k1+np.pi)+1.)*BA1/2.+(np.cos((z-zmin)*k2+np.pi)+1.)*BA2/2.
    +(np.cos((z-zmin)*k3+np.pi)+1.)*BA3/2.+(np.cos((z-zmin)*k4+np.pi)+1.)*BA4/2.)/(1.0+0.5+0.25+0.125)+bed))) * (7/10)**mi
s4 = np.vectorize(s4)
surfacePoints[:, 1] = s4(z)
surfaceSwarm4.add_particles_with_coordinates(surfacePoints)
s5 = lambda z: s50 if z<zmin or z>zmax else bed+BumpAmplitude/Amax*((np.cos((z-zmin)*k1+np.pi)+1.)*BA1/2.
    +(np.cos((z-zmin)*k2+np.pi)+1.)*BA2/2.+(np.cos((z-zmin)*k3+np.pi)+1.)*BA3/2.+(np.cos((z-zmin)*k4+np.pi)+1.)*BA4/2.)/(1.0+0.5+0.25+0.125)
    + (6/10*(iceHeight-(BumpAmplitude/Amax*((np.cos((z-zmin)*k1+np.pi)+1.)*BA1/2.+(np.cos((z-zmin)*k2+np.pi)+1.)*BA2/2.
    +(np.cos((z-zmin)*k3+np.pi)+1.)*BA3/2.+(np.cos((z-zmin)*k4+np.pi)+1.)*BA4/2.)/(1.0+0.5+0.25+0.125)+bed))) * (6/10)**mi
s5 = np.vectorize(s5)
surfacePoints[:, 1] = s5(z)
surfaceSwarm5.add_particles_with_coordinates(surfacePoints)
s6 = lambda z: s60 if z<zmin or z>zmax else bed+BumpAmplitude/Amax*((np.cos((z-zmin)*k1+np.pi)+1.)*BA1/2.
    +(np.cos((z-zmin)*k2+np.pi)+1.)*BA2/2.+(np.cos((z-zmin)*k3+np.pi)+1.)*BA3/2.+(np.cos((z-zmin)*k4+np.pi)+1.)*BA4/2.)/(1.0+0.5+0.25+0.125)
    + (5/10*(iceHeight-(BumpAmplitude/Amax*((np.cos((z-zmin)*k1+np.pi)+1.)*BA1/2.+(np.cos((z-zmin)*k2+np.pi)+1.)*BA2/2.
    +(np.cos((z-zmin)*k3+np.pi)+1.)*BA3/2.+(np.cos((z-zmin)*k4+np.pi)+1.)*BA4/2.)/(1.0+0.5+0.25+0.125)+bed))) * (5/10)**mi
s6 = np.vectorize(s6)
surfacePoints[:, 1] = s6(z)
surfaceSwarm6.add_particles_with_coordinates(surfacePoints)
s7 = lambda z: s70 if z<zmin or z>zmax else bed+BumpAmplitude/Amax*((np.cos((z-zmin)*k1+np.pi)+1.)*BA1/2.
    +(np.cos((z-zmin)*k2+np.pi)+1.)*BA2/2.+(np.cos((z-zmin)*k3+np.pi)+1.)*BA3/2.+(np.cos((z-zmin)*k4+np.pi)+1.)*BA4/2.)/(1.0+0.5+0.25+0.125)
    + (4/10*(iceHeight-(BumpAmplitude/Amax*((np.cos((z-zmin)*k1+np.pi)+1.)*BA1/2.+(np.cos((z-zmin)*k2+np.pi)+1.)*BA2/2.
    +(np.cos((z-zmin)*k3+np.pi)+1.)*BA3/2.+(np.cos((z-zmin)*k4+np.pi)+1.)*BA4/2.)/(1.0+0.5+0.25+0.125)+bed))) * (4/10)**mi
s7 = np.vectorize(s7)
surfacePoints[:, 1] = s7(z)
surfaceSwarm7.add_particles_with_coordinates(surfacePoints)
s8 = lambda z: s80 if z<zmin or z>zmax else bed+BumpAmplitude/Amax*((np.cos((z-zmin)*k1+np.pi)+1.)*BA1/2.
    +(np.cos((z-zmin)*k2+np.pi)+1.)*BA2/2.+(np.cos((z-zmin)*k3+np.pi)+1.)*BA3/2.+(np.cos((z-zmin)*k4+np.pi)+1.)*BA4/2.)/(1.0+0.5+0.25+0.125)
    + (3/10*(iceHeight-(BumpAmplitude/Amax*((np.cos((z-zmin)*k1+np.pi)+1.)*BA1/2.+(np.cos((z-zmin)*k2+np.pi)+1.)*BA2/2.
    +(np.cos((z-zmin)*k3+np.pi)+1.)*BA3/2.+(np.cos((z-zmin)*k4+np.pi)+1.)*BA4/2.)/(1.0+0.5+0.25+0.125)+bed))) * (3/10)**mi
s8 = np.vectorize(s8)
surfacePoints[:, 1] = s8(z)
surfaceSwarm8.add_particles_with_coordinates(surfacePoints)
s9 = lambda z: s90 if z<zmin or z>zmax else bed+BumpAmplitude/Amax*((np.cos((z-zmin)*k1+np.pi)+1.)*BA1/2.
    +(np.cos((z-zmin)*k2+np.pi)+1.)*BA2/2.+(np.cos((z-zmin)*k3+np.pi)+1.)*BA3/2.+(np.cos((z-zmin)*k4+np.pi)+1.)*BA4/2.)/(1.0+0.5+0.25+0.125)
    + (2/10*(iceHeight-(BumpAmplitude/Amax*((np.cos((z-zmin)*k1+np.pi)+1.)*BA1/2.+(np.cos((z-zmin)*k2+np.pi)+1.)*BA2/2.
    +(np.cos((z-zmin)*k3+np.pi)+1.)*BA3/2.+(np.cos((z-zmin)*k4+np.pi)+1.)*BA4/2.)/(1.0+0.5+0.25+0.125)+bed))) * (2/10)**mi
s9 = np.vectorize(s9)
surfacePoints[:, 1] = s9(z)
surfaceSwarm9.add_particles_with_coordinates(surfacePoints)
s10 = lambda z: s100 if z<zmin or z>zmax else bed+BumpAmplitude/Amax*((np.cos((z-zmin)*k1+np.pi)+1.)*BA1/2.
    +(np.cos((z-zmin)*k2+np.pi)+1.)*BA2/2.+(np.cos((z-zmin)*k3+np.pi)+1.)*BA3/2.+(np.cos((z-zmin)*k4+np.pi)+1.)*BA4/2.)/(1.0+0.5+0.25+0.125)
    + (1/10*(iceHeight-(BumpAmplitude/Amax*((np.cos((z-zmin)*k1+np.pi)+1.)*BA1/2.+(np.cos((z-zmin)*k2+np.pi)+1.)*BA2/2.
    +(np.cos((z-zmin)*k3+np.pi)+1.)*BA3/2.+(np.cos((z-zmin)*k4+np.pi)+1.)*BA4/2.)/(1.0+0.5+0.25+0.125)+bed)))*(1/10)**mi
s10 = np.vectorize(s10)
surfacePoints[:, 1] = s10(z)
surfaceSwarm10.add_particles_with_coordinates(surfacePoints)

# to visualize the surface swarm in paraview we need a pseudo variable
surfaceParticle1 = surfaceSwarm1.add_variable ( dataType="int", count=1 )
surfaceParticle1.data[:] = 1
surfaceParticle2 = surfaceSwarm2.add_variable ( dataType="int", count=1 )
surfaceParticle2.data[:] = 2
surfaceParticle3 = surfaceSwarm3.add_variable ( dataType="int", count=1 )
surfaceParticle3.data[:] = 3
surfaceParticle4 = surfaceSwarm4.add_variable ( dataType="int", count=1 )
surfaceParticle4.data[:] = 4
surfaceParticle5 = surfaceSwarm5.add_variable ( dataType="int", count=1 )
surfaceParticle5.data[:] = 5
surfaceParticle6 = surfaceSwarm6.add_variable ( dataType="int", count=1 )
surfaceParticle6.data[:] = 6
surfaceParticle7 = surfaceSwarm7.add_variable ( dataType="int", count=1 )
surfaceParticle7.data[:] = 7
surfaceParticle8 = surfaceSwarm8.add_variable ( dataType="int", count=1 )
surfaceParticle8.data[:] = 8
surfaceParticle9 = surfaceSwarm9.add_variable ( dataType="int", count=1 )
surfaceParticle9.data[:] = 9
surfaceParticle10 = surfaceSwarm10.add_variable ( dataType="int", count=1 )
surfaceParticle10.data[:] = 10
# -
```

```
# +
T0 = -30. # °C
#Tbed = -5. # °C
Tbed = -3. # °C
T_Basis = bumpHeight
#DeltaT = Tbed - T0

T_func = Tbed + (coord[1]-bumpHeight)/(WarmiceHeight-bumpHeight)*(T0-Tbed)
#zz_pow = (T_func-Tbed)**mi
#zz_pow_max = (T0-Tbed)**mi
T_func = Tbed + (T_func-Tbed)*((T_func-Tbed)/(T0-Tbed))**mi

#T_func = T0 + DeltaT * ((1.-((Basis - (foldHeight - coord[1])) / Basis))**2)
#T_func = T0 + DeltaT * ((T_Basis - coord[1]) / (T_Basis)) **2

Tconditions = [
                (       coord[1] > WarmiceHeight,  T0      ),
                (       coord[1] > T_Basis,  T_func      ),
                (       True,            Tbed  ),
              ]

particleTemperature.data[:] = fn.branching.conditional( Tconditions ).evaluate(swarm)

# +
## functions, incl flow law
R = 0.008314 # kJ / (T*mol)
QhighT = 155. # kJ/mol, activation energy, Kuiper dislocation creep
QsmallT = 64.
A0smallT = 5e5 * 3.1536e7 #Mpa-4s-1 to Pa-4a-1
A0highT = 6.96e23 * 3.1536e7
#if rank == 0:
#    print(A0smallT, A0highT)

strainRateTensor = fn.tensor.symmetric(velocityField.fn_gradient)
strainRate_2ndInvariantFn = fn.tensor.second_invariant(strainRateTensor)

viscosityFnAir    = fn.misc.constant(1e9 / 3.1536e7)
minViscosityIceFn  = fn.misc.constant(1e+11 / 3.1536e7)
maxViscosityIceFn  = fn.misc.constant(1e+17 / 3.1536e7)
viscosityFnRock = fn.misc.constant(1e19 / 3.1536e7)

V1 = 0.5 * (A0smallT * fn.math.exp(-QsmallT / (R*(particleTemperature + 273.)))) ** (-1./n) * (strainRate_2ndInvariantFn**((1.-n) / float(n)))
V2 = 0.5 * (A0highT * fn.math.exp(-QhighT / (R*(particleTemperature + 273.)))) ** (-1./n) * (strainRate_2ndInvariantFn**((1.-n) / float(n)))
V1 = V1 * 1e6 #pa*a
V2 = V2 * 1e6 #pa*a
#V1 = V1 * 1e6 / 3.1536e7  #pa*a
#V2 = V2 * 1e6 / 3.1536e7

VisBaseconditions = [
                (       particleTemperature <= -11., V1 ),
                (       True,                        V2),
                ]

#viscosityMap1 = {
#                materialV:  viscosityFnIce ,
#                materialVC: viscosityFnIce,
#               }

#viscosityMap2 = {
#                 materialV:  viscosityFnColdIce,
#                materialVC: viscosityFnWarmIce,
#               }

viscosityIceFn = fn.branching.conditional( VisBaseconditions )
viscosityFnIce = fn.misc.max(fn.misc.min(viscosityIceFn, maxViscosityIceFn), minViscosityIceFn)

viscosityMap = {
                materialA:  viscosityFnAir,
                materialV:  viscosityFnIce,
                materialVC: viscosityFnIce,
                materialR: viscosityFnRock,
               }
viscosityFn = fn.branching.map( fn_key=materialVariable, mapping=viscosityMap )
#viscosityFnAir2    = 0.0
viscosityFnIce2    = (1-1/3) * viscosityFnIce
viscosityMap2 = {
                 materialA:  0.,
                 materialV:  viscosityFnIce2,
                 materialVC: viscosityFnIce2,
                 materialR: 0.,
                }
viscosityFn2 = fn.branching.map( fn_key=materialVariable, mapping=viscosityMap2 )
viscosityFn3=viscosityFn-viscosityFn2
particleViscosity.data[:] = viscosityFn.evaluate(swarm)

# +
#devStressFn = 2.0 * viscosityFn * strainRateTensor
shearStressFn = strainRate_2ndInvariantFn * viscosityFn * 2.0

densityFnIce = (18.02 / (19.30447 - 7.988471e-4 * (particleTemperature+273.) + 7.563261e-6 * ((particleTemperature+273.)**2) )) * 1000.
#917.5085940523277,921.4114212256626
densityFnAir = fn.misc.constant( 0. )
densityFnRock = fn.misc.constant( 2700. )

densityMap = {
                materialA:  densityFnAir,
                materialV:  densityFnIce,
                materialVC:  densityFnIce,
                materialR: densityFnRock
              }

densityFn = fn.branching.map(fn_key=materialVariable, mapping=densityMap)

particleDensity.data[:] = densityFn.evaluate(swarm)

#surf_inclination = 0.5 * np.pi / 180. # 0.1 = Experiment D, 0.5 = Experiment B
#z_hat = (math.sin(surf_inclination), - math.cos(surf_inclination), 0.)

z_hat = (0., -1., 0.)
buoyancyFn = densityFn * z_hat * g
# -
```

```
## set boundary conditions
iWalls = mesh.specialSets["MinI_VertexSet"] + mesh.specialSets["MaxI_VertexSet"]
jWalls = mesh.specialSets["MinJ_VertexSet"] + mesh.specialSets["MaxJ_VertexSet"]
kWalls = mesh.specialSets["MinK_VertexSet"] + mesh.specialSets["MaxK_VertexSet"]
#outerkWall = mesh.specialSets["MinK_VertexSet"]
front = mesh.specialSets["MinI_VertexSet"]
back = mesh.specialSets["MaxI_VertexSet"]
base   = mesh.specialSets["MinJ_VertexSet"]
top    = mesh.specialSets["MaxJ_VertexSet"]
leftWall = mesh.specialSets["MinK_VertexSet"]
rightWall = mesh.specialSets["MaxK_VertexSet"]

allWalls = iWalls + jWalls + kWalls

meshVz = 5.
#meshVx = 2*meshVz*maxX*maxY/(2*maxY*maxZ-BumpAmplitude*(1/k*np.sin(k*TotalBumpWidth)+TotalBumpWidth))
Sbump = BumpAmplitude*(zmax-zmin)*(BA1+BA2+BA3+BA4)/(2*Amax*(1.0 + 0.5 + 0.25 + 0.125))
meshVx = meshVz*MODEL_DATA['MAX_X']*(MODEL_DATA['MAX_Y']-bed)/((MODEL_DATA['MAX_Y']-bed)*MODEL_DATA['MAX_Z']-Sbump)
#print(Sbump,meshVx) #4978220.286247666 0.10710953121528549
#meshVx = 0.25
velocityField.data[:] = 0.
#velocityField.data[leftWall, 2] = meshVz
#velocityField.data[rightWall, 2] = -meshVz

loadA = mesh.specialSets['Empty']
for index in mesh.specialSets["MinI_VertexSet"]:
    z = mesh.data[index,2]
    if zmin<=z<=zmax:
        if mesh.data[index][1]<=bed+BumpAmplitude/Amax*((np.cos((z-zmin)*k1+np.pi)+1.)*BA1/2.+(np.cos((z-zmin)*k2+np.pi)+1.)*BA2/2.
                                +(np.cos((z-zmin)*k3+np.pi)+1.)*BA3/2.+(np.cos((z-zmin)*k4+np.pi)+1.)*BA4/2.)/(1.0 + 0.5 + 0.25 + 0.125):
            loadA+=index
    elif z>zmax:
        if mesh.data[index][1]<=bed:
            loadA+=index

loadB = mesh.specialSets['Empty']
for index in mesh.specialSets["MaxI_VertexSet"]:
    z = mesh.data[index,2]
    if zmin<=z<=zmax:
        if mesh.data[index][1]<=bed+BumpAmplitude/Amax*((np.cos((z-zmin)*k1+np.pi)+1.)*BA1/2.+(np.cos((z-zmin)*k2+np.pi)+1.)*BA2/2.
                                +(np.cos((z-zmin)*k3+np.pi)+1.)*BA3/2.+(np.cos((z-zmin)*k4+np.pi)+1.)*BA4/2.)/(1.0 + 0.5 + 0.25 + 0.125):
            loadB+=index
    elif z>zmax:
        if mesh.data[index][1]<=bed:
            loadB+=index

loadC = mesh.specialSets['Empty']
for index in mesh.specialSets["MinK_VertexSet"]:
    if mesh.data[index][1]<=bed:
        loadC+=index

loadD = mesh.specialSets['Empty']
for index in mesh.specialSets["MaxK_VertexSet"]:
    if mesh.data[index][1]<=bed:
        loadD+=index

for i in mesh.specialSets["MaxK_VertexSet"]:
    loc = mesh.data[i,1]
    if loc > bed:
        velocityField.data[i][2] = -meshVz

for i in mesh.specialSets["MaxI_VertexSet"]:
    loc = mesh.data[i,1]
    z = mesh.data[i,2]
    if zmin<=z<=zmax:
        if loc>bed+BumpAmplitude/Amax*((np.cos((z-zmin)*k1+np.pi)+1.)*BA1/2.+(np.cos((z-zmin)*k2+np.pi)+1.)*BA2/2.
                          +(np.cos((z-zmin)*k3+np.pi)+1.)*BA3/2.+(np.cos((z-zmin)*k4+np.pi)+1.)*BA4/2.)/(1.0 + 0.5 + 0.25 + 0.125):
            velocityField.data[i][0] = meshVx
        else:
            velocityField.data[i][0] = 0.
    elif z<zmin or z>zmax:
        if loc>bed:
            velocityField.data[i][0] = meshVx
        else:
            velocityField.data[i][0] = 0.

velocityBCs = uw.conditions.DirichletCondition(
                                            variable        = velocityField,
                                            indexSetsPerDof = (iWalls+base+loadC+loadD, base, kWalls+base+loadA+loadB),
                                           )
```

```
# -

def c_axis_rotation(dt, steps = 1.):

    dt /= steps

    for i in range(0, int(steps)):

        #iceIndices = np.array(np.where(materialVariable.data == materialV + materialVC)[0])
        iceIndices = np.array(np.where(np.logical_or(materialVariable.data == materialV,
                                                     materialVariable.data == materialVC))[0])
        #iceIndices = np.array(np.where(materialVariable.data == materialVC)[0])

        velGrad = velocityField.fn_gradient.evaluate(swarm).reshape(swarm.particleLocalCount, mesh.dim, mesh.dim)
        velGrad = velGrad[iceIndices]
        velGradT = velGrad.swapaxes(-1,1)

        # rate of deformation and rate of rotation
        D = 0.5 * (velGrad + velGradT)
        W = 0.5 * (velGrad - velGradT)

        particleDirector.data[iceIndices] = particleDirector.data[iceIndices] + dt * ( np.einsum("ijk,ik->ij", W, particleDirector.data[iceIndices])
                                        - np.einsum("ijk,ik->ij", D, particleDirector.data[iceIndices]) + np.einsum("ij,ij->i",particleDirector.data[iceIndices],
                                        np.einsum("ijk,ik->ij",D,particleDirector.data[iceIndices]))[:,None] * particleDirector.data[iceIndices])

        #finally normalize the c-axes
        particleDirector.data[iceIndices] = particleDirector.data[iceIndices] /
                                            np.absolute(np.linalg.norm(particleDirector.data[iceIndices], axis=1).reshape(len(iceIndices),1))

        # we want to rotate all directors, if they point towards the negative y-direction
        # this should make it easier to display them
        b = np.where(particleDirector.data[:,1] < 0.)
        particleDirector.data[b] *= -1.

# +
## setup solver and solve

stokes = uw.systems.Stokes(
    velocityField=velocityField,
    pressureField=pressureField,
    voronoi_swarm=swarm,
    conditions=[
            velocityBCs,
            ],
    fn_viscosity=viscosityFn,
    _fn_viscosity2=viscosityFn2,
    #_fn_director=directorField,
    _fn_director=particleDirector,
    fn_bodyforce=buoyancyFn,
)

solver = uw.systems.Solver(stokes)

solver.set_inner_method("mg")
solver.options.scr.ksp_type="cg"
solver.set_penalty(1.0e6) # higher penalty = larger stability + (often) faster calculation
# solver.options.scr.ksp_rtol = 1.0e-3

surfaceArea = uw.utils.Integral( fn=1.0, mesh=mesh, integrationType='surface', surfaceIndexSet=top)
surfacePressureIntegral = uw.utils.Integral( fn=pressureField, mesh=mesh, integrationType='surface', surfaceIndexSet=top)

def calibrate_pressure():

    global pressureField
    global surfaceArea
    global surfacePressureIntegral

    (area,) = surfaceArea.evaluate()
    (p0,) = surfacePressureIntegral.evaluate()
    pressureField.data[:] -= p0 / area

    # print (f'Calibration pressure {p0 / area}')
# -
```

```
# +
maxSteps = 3001
stepsize = 20.

step = 0
t = 0.

xdmf_mesh    = mesh.save('mesh.h5')

while step < maxSteps:

    if not step%stepsize: # if multiple of ..

        #print ("in step " + str(step))

        ignore = swarm.save('swarm_' + str(step) + '.h5')

        # eval swarm variables
        particleStrainrate.data[:] = strainRate_2ndInvariantFn.evaluate(swarm)
        particleViscosity.data[:] = viscosityFn.evaluate(swarm)
        particleViscosity2.data[:] = viscosityFn3.evaluate(swarm)
        particleShearstress.data[:] = shearStressFn.evaluate(swarm)
        particleVelocity.data[:]  = velocityField.evaluate(swarm)

        # save swarm variables as xdmf files
        xdmf_swarm = swarm.save('swarm_' + str(step) + '.h5')
        xdmf_surfswarm1 = surfaceSwarm1.save('surf_swarm1_' + str(step) + '.h5')
        xdmf_surfswarm2 = surfaceSwarm2.save('surf_swarm2_' + str(step) + '.h5')
        xdmf_surfswarm3 = surfaceSwarm3.save('surf_swarm3_' + str(step) + '.h5')
        xdmf_surfswarm4 = surfaceSwarm4.save('surf_swarm4_' + str(step) + '.h5')
        xdmf_surfswarm5 = surfaceSwarm5.save('surf_swarm5_' + str(step) + '.h5')
        xdmf_surfswarm6 = surfaceSwarm6.save('surf_swarm6_' + str(step) + '.h5')
        xdmf_surfswarm7 = surfaceSwarm7.save('surf_swarm7_' + str(step) + '.h5')
        xdmf_surfswarm8 = surfaceSwarm8.save('surf_swarm8_' + str(step) + '.h5')
        xdmf_surfswarm9 = surfaceSwarm9.save('surf_swarm9_' + str(step) + '.h5')
        xdmf_surfswarm10 = surfaceSwarm10.save('surf_swarm10_' + str(step) + '.h5')

        xdmf_surfaceParticle1 = surfaceParticle1.save('surfaceSwarm1_' + str(step) + '.h5')
        xdmf_surfaceParticle2 = surfaceParticle2.save('surfaceSwarm2_' + str(step) + '.h5')
        xdmf_surfaceParticle3 = surfaceParticle3.save('surfaceSwarm3_' + str(step) + '.h5')
        xdmf_surfaceParticle4 = surfaceParticle4.save('surfaceSwarm4_' + str(step) + '.h5')
        xdmf_surfaceParticle5 = surfaceParticle5.save('surfaceSwarm5_' + str(step) + '.h5')
        xdmf_surfaceParticle6 = surfaceParticle6.save('surfaceSwarm6_' + str(step) + '.h5')
        xdmf_surfaceParticle7 = surfaceParticle7.save('surfaceSwarm7_' + str(step) + '.h5')
        xdmf_surfaceParticle8 = surfaceParticle8.save('surfaceSwarm8_' + str(step) + '.h5')
        xdmf_surfaceParticle9 = surfaceParticle9.save('surfaceSwarm9_' + str(step) + '.h5')
        xdmf_surfaceParticle10 = surfaceParticle10.save('surfaceSwarm10_' + str(step) + '.h5')

        surfaceParticle1.xdmf('surfaceSwarm1_' + str(step) + '.xdmf', xdmf_surfaceParticle1,
                              "surfaceParticle1", xdmf_surfswarm1, "SurfSwarm1", modeltime=step)
        surfaceParticle2.xdmf('surfaceSwarm2_' + str(step) + '.xdmf', xdmf_surfaceParticle2,
                              "surfaceParticle2", xdmf_surfswarm2, "SurfSwarm2", modeltime=step)
        surfaceParticle3.xdmf('surfaceSwarm3_' + str(step) + '.xdmf', xdmf_surfaceParticle3,
                              "surfaceParticle3", xdmf_surfswarm3, "SurfSwarm3", modeltime=step)
        surfaceParticle4.xdmf('surfaceSwarm4_' + str(step) + '.xdmf', xdmf_surfaceParticle4,
                              "surfaceParticle4", xdmf_surfswarm4, "SurfSwarm4", modeltime=step)
        surfaceParticle5.xdmf('surfaceSwarm5_' + str(step) + '.xdmf', xdmf_surfaceParticle5,
                              "surfaceParticle5", xdmf_surfswarm5, "SurfSwarm5", modeltime=step)
        surfaceParticle6.xdmf('surfaceSwarm6_' + str(step) + '.xdmf', xdmf_surfaceParticle6,
                              "surfaceParticle6", xdmf_surfswarm6, "SurfSwarm6", modeltime=step)
        surfaceParticle7.xdmf('surfaceSwarm7_' + str(step) + '.xdmf', xdmf_surfaceParticle7,
                              "surfaceParticle7", xdmf_surfswarm7, "SurfSwarm7", modeltime=step)
        surfaceParticle8.xdmf('surfaceSwarm8_' + str(step) + '.xdmf', xdmf_surfaceParticle8,
                              "surfaceParticle8", xdmf_surfswarm8, "SurfSwarm8", modeltime=step)
        surfaceParticle9.xdmf('surfaceSwarm9_' + str(step) + '.xdmf', xdmf_surfaceParticle9,
                              "surfaceParticle9", xdmf_surfswarm9, "SurfSwarm9", modeltime=step)
        surfaceParticle10.xdmf('surfaceSwarm10_' + str(step) + '.xdmf', xdmf_surfaceParticle10,
                              "surfaceParticle10", xdmf_surfswarm10, "SurfSwarm10", modeltime=step)

        #xdmf_meshvar = velocityField.save('velocityField_' + str(step) + '.h5')
        #velocityField.xdmf('velocityField_' + str(step) + '.xdmf', xdmf_meshvar, "Velocity",
        #                   xdmf_mesh, "Mesh", modeltime=step)

        xdmf_particleStrainrate = particleStrainrate.save('particleStrainrate_' + str(step) + '.h5')
        particleStrainrate.xdmf('particleStrainrate_' + str(step) + '.xdmf', xdmf_particleStrainrate,
                                "particleStrainrate", xdmf_swarm, "Swarm", modeltime=step)

        xdmf_particleDirector = particleDirector.save('particleDirector_' + str(step) + '.h5')
        particleDirector.xdmf('particleDirector_' + str(step) + '.xdmf', xdmf_particleDirector,
                              "particleDirector", xdmf_swarm, "Swarm", modeltime=step)

        #xdmf_particleMeshDirector = particleMeshDirector.save('particleMeshDirector_' + str(step) + '.h5')
        #particleMeshDirector.xdmf('particleMeshDirector_' + str(step) + '.xdmf', xdmf_particleMeshDirector,
        #                          "particleMeshDirector", xdmf_swarm, "Swarm", modeltime=step)

        xdmf_particleViscosity = particleViscosity.save('particleViscosity_' + str(step) + '.h5')
        particleViscosity.xdmf('particleViscosity_' + str(step) + '.xdmf', xdmf_particleViscosity,
                               "particleViscosity", xdmf_swarm, "Swarm", modeltime=step)

        xdmf_particleViscosity2 = particleViscosity2.save('particleViscosity2_' + str(step) + '.h5')
        particleViscosity2.xdmf('particleViscosity2_' + str(step) + '.xdmf', xdmf_particleViscosity2,
                               "particleViscosity2", xdmf_swarm, "Swarm", modeltime=step)

        #xdmf_particleCreationTime = particleCreationTime.save('particleCreationTime_' + str(step) + '.h5')
        #particleCreationTime.xdmf('particleCreationTime_' + str(step) + '.xdmf', xdmf_particleCreationTime,
        #                          "particleCreationTime", xdmf_swarm, "Swarm", modeltime=step)

        xdmf_materialVariable = materialVariable.save('particleMaterial_' + str(step) + '.h5')
        materialVariable.xdmf('particleMaterial_' + str(step) + '.xdmf', xdmf_materialVariable,
                              "materialVariable", xdmf_swarm, "Swarm", modeltime=step)

        #xdmf_particleTemperature = particleTemperature.save('particleTemperature_' + str(step) + '.h5')
        #particleTemperature.xdmf('particleTemperature_' + str(step) + '.xdmf', xdmf_particleTemperature,
        #                         "particleTemperature", xdmf_swarm, "Swarm", modeltime=step)

        xdmf_particleDensity = particleDensity.save('particleDensity_' + str(step) + '.h5')
        particleDensity.xdmf('particleDensity_' + str(step) + '.xdmf', xdmf_particleDensity,
                               "particleDensity", xdmf_swarm, "Swarm", modeltime=step)

        xdmf_particleShearstress = particleShearstress.save('particleShearstress_' + str(step) + '_'+ str(t) + '.h5')
        particleShearstress.xdmf('particleShearstress_' + str(step) + '.xdmf', xdmf_particleShearstress,
                               "particleShearstress", xdmf_swarm, "Swarm", modeltime=step)

        # visualizing the velocityField in paraviewe doesn't work for whatever reason (Paraview just crashes)
        # so we save it as a particle property
        #particleVelocity.data[:]  = velocityField.evaluate(swarm)
        xdmf_particleVelocity = particleVelocity.save('particleVelocity_' + str(step) + '.h5')
        particleVelocity.xdmf('particleVelocity_' + str(step) + '.xdmf', xdmf_particleVelocity,
                    "particleVelocity", xdmf_swarm, "Swarm", modeltime=step)

        print (str(t) + ' years, step: ' + str(step))

    if step < maxSteps-1:
        t += flow(rotate_caxes = True)

    step += 1
```

## Code 2

This is an example code script of the ice-stream modelling (Chapter 3, Model 2). Full-scripts of all ice-stream models can be accessed through Zenodo (https://doi.org/10.5281/zenodo.11396618).

```
# import modules, create output directory
import numpy as np
import math
import os

from mpi4py import MPI

comm = MPI.COMM_WORLD
rank = comm.Get_rank()

import underworld as uw

from underworld import function as fn
import underworld.visualisation as vis

import pickle

if not os.getcwd().rsplit("/")[-1] == "output":
    outputPath = os.path.join(os.path.abspath("."),"output/")
    if not os.path.exists ( outputPath ):
        os.makedirs ( outputPath )

    os.chdir(outputPath)

# +
## basic parameters

g = 9.81
#ice_density = 910.

#A = 1e-16
n = 4.

MODEL_DATA = {}
coord = fn.input()
bed = 0.0
iceHeight = 2500.0+bed
WarmiceHeight = (iceHeight-bed) * 40./100.+bed
airHeight = 500.0
#zmin = 0.
#zmax = 20000.
MODEL_DATA['MIN_Y'] = 0.0
MODEL_DATA['MAX_Y'] = 3000.0+bed
MODEL_DATA['MAX_X'] = 50000.
MODEL_DATA['MIN_X'] = 0.0
MODEL_DATA['MIN_Z'] = -20000.
MODEL_DATA['MAX_Z'] = 20000.
MODEL_DATA['RES_X'] = 32
MODEL_DATA['RES_Y'] = 16
MODEL_DATA['RES_Z'] = 128

mi = 0.2

#elementType = "Q1/dQ0"
#elementType = "Q2/dQ1"
#elementType = "Q1/dPc1"
#elementType = "Q2/dPc1"
MODEL_DATA['ELEMENT_TYPE'] = "Q1/dQ0"
MODEL_DATA['PERIODIC_X'] = False
MODEL_DATA['PERIODIC_Y'] = False
MODEL_DATA['PERIODIC_Z'] = False
MODEL_DATA['PARTICLES_PER_CELL'] = 30

mesh = uw.mesh.FeMesh_Cartesian( elementType = ( MODEL_DATA['ELEMENT_TYPE'] ) ,
                                 elementRes  = ( MODEL_DATA['RES_X'], MODEL_DATA['RES_Y'], MODEL_DATA['RES_Z']),
                                 minCoord    = ( MODEL_DATA['MIN_X'], MODEL_DATA['MIN_Y'], MODEL_DATA['MIN_Z'] ),
                                 maxCoord    = ( MODEL_DATA['MAX_X'], MODEL_DATA['MAX_Y'], MODEL_DATA['MAX_Z'] ),
                                 periodic    = ( MODEL_DATA['PERIODIC_X'], MODEL_DATA['PERIODIC_Y'], MODEL_DATA['PERIODIC_Z'] )
                               )

with mesh.deform_mesh():

    mesh.data[:, 2] = mesh.data[:,2]*np.abs(mesh.data[:,2]/MODEL_DATA['MAX_Z'])**0.2
```

```
velocityField    = mesh.add_variable(         dataType="double",  nodeDofCount=3 )
pressureField    = mesh.subMesh.add_variable( dataType="double",  nodeDofCount=1 )
directorField    = mesh.add_variable( dataType="double",  nodeDofCount=3 )

velocityField.data[:] = [0.,0.,0.]
directorField.data[:] = [0.,1.,0.]
pressureField.data[:] = 0.

## visualisation parameters
MODEL_DATA_FILE = outputPath + "model_data.p"
pickle.dump( MODEL_DATA, open(MODEL_DATA_FILE , "wb" ) )

# +
# Create a swarm which will define our material geometries, and will also
# track deformation and history dependence of particles.
swarm  = uw.swarm.Swarm( mesh=mesh, particleEscape=True)
#parts_per_cell = 50

#if rank == 0:
#    print ('created swarm')

swarmLayout = uw.swarm.layouts.PerCellSpaceFillerLayout( swarm=swarm, particlesPerCell=MODEL_DATA['PARTICLES_PER_CELL'] )
swarm.populate_using_layout( layout=swarmLayout )

# create pop control object
pop_control1 = uw.swarm.PopulationControl(swarm, aggressive=True, particlesPerCell=MODEL_DATA['PARTICLES_PER_CELL'])

# create advector
advector1 = uw.systems.SwarmAdvector(swarm=swarm,velocityField=velocityField, order=2)

# +
# Initialise particle properties
materialVariable = swarm.add_variable( dataType="int", count=1 )
particleDensity = swarm.add_variable ( dataType="double", count=1 )
particleInitialYPos = swarm.add_variable ( dataType="double", count=1 )

particleStrainrate = swarm.add_variable ( dataType="double", count=1 )
particleViscosity = swarm.add_variable ( dataType="double", count=1 )
particleViscosity2 = swarm.add_variable ( dataType="double", count=1 )
particleViscosity1s = swarm.add_variable ( dataType="double", count=1 )
particleViscosity2s = swarm.add_variable ( dataType="double", count=1 )
particleShearstress = swarm.add_variable ( dataType="double", count=1 )

particleDirector = swarm.add_variable ( dataType="double", count=3 )
# particleMeshDirector below only used to save the director if calculated as a mesh variable
#particleMeshDirector = swarm.add_variable ( dataType="double", count=3 )

#particleWeakzone = swarm.add_variable ( dataType="int", count=1 )

particleTemperature = swarm.add_variable ( dataType="double", count=1 ) ###
particleTemperature.data[:] = 0.

#particleSnowHeight = swarm.add_variable ( dataType="double", count=1 )
#particleSnowHeight.data[:] = 0.

particleVelocity = swarm.add_variable( dataType="double", count=3 )
particleVelocity.data[:] = (0.,0.,0.)
particleVgradient = swarm.add_variable( dataType="double", count=9 )

particleStress = swarm.add_variable( dataType="double", count=6 )
previousStress = swarm.add_variable( dataType="double", count=6 )
#iceSurf = swarm.add_variable ( dataType="int", count=1 )
#iceSurf.data[:] = 0

#particleCreationTime = swarm.add_variable ( dataType="float", count=1 )
#particleCreationTime.data[:] = 0.

bumpHeight = swarm.add_variable( dataType="double", count=1 )
WarmiceHeight = swarm.add_variable( dataType="double", count=1 )
snowPlane = swarm.add_variable ( dataType="double", count=1 )
snowPlane.data[:]=iceHeight
```

```
# +
materialV = 1  # viscoplastic ice
materialVC = 2 # viscoplastic ice in the channel
materialA = 0 # Air
materialR = 3   # rock

#if rank == 0:
#    print ('created particles')

coord = fn.input()
z=swarm.data[:, 2]
x=swarm.data[:, 0]
y=swarm.data[:, 1]

particleInitialYPos.data[:] = np.expand_dims(coord.evaluate(swarm)[:,1], axis=1)

bumpHeight = bed
WarmiceHeight = bumpHeight + 4/10*(iceHeight-bumpHeight)
zz_pow = (WarmiceHeight - bumpHeight)**mi
zz_pow_max = (iceHeight - bumpHeight)**mi
WarmiceHeight =bumpHeight + (WarmiceHeight-bumpHeight) * zz_pow / zz_pow_max
#bumpfunc = np.vectorize(bumpfunc)
#WarmiceHeight.data[:] = np.expand_dims(Warmicefunc, 1)
'''
conditions = [
               (       coord[1] > iceHeight,    materialA    ),
               (       coord[1] > WarmiceHeight,    materialV    ),
               (       True,    materialVC    ),
               #(       True ,           materialR                    ),
             ]
'''
conditions = [
               (       coord[1] > iceHeight,    materialA    ),
               #(       coord[1] > WarmiceHeight,    materialV    ),
               (       True,    materialV    ),
               #(       True ,           materialR                    ),
             ]

materialVariable.data[:] = fn.branching.conditional( conditions ).evaluate(swarm)

# +
for index in np.ndindex(directorField.data.shape[0]):
    maxAngle = 5./90.*np.pi/2.
    gaus = np.random.normal(0., maxAngle) #Gaussian distribution
    directorField.data[index][1] =np.cos(gaus)
    directorField.data[index][2] =np.sin(gaus)

particleDirector.data[:]  = directorField.evaluate(swarm)
```

```
## swarms to track the deformation
surfaceSwarm1 = uw.swarm.Swarm(mesh=mesh, particleEscape=True)
surfaceSwarm2 = uw.swarm.Swarm(mesh=mesh, particleEscape=True)
surfaceSwarm3 = uw.swarm.Swarm(mesh=mesh, particleEscape=True)
surfaceSwarm4 = uw.swarm.Swarm(mesh=mesh, particleEscape=True)
surfaceSwarm5 = uw.swarm.Swarm(mesh=mesh, particleEscape=True)
surfaceSwarm6 = uw.swarm.Swarm(mesh=mesh, particleEscape=True)
surfaceSwarm7 = uw.swarm.Swarm(mesh=mesh, particleEscape=True)
surfaceSwarm8 = uw.swarm.Swarm(mesh=mesh, particleEscape=True)
surfaceSwarm9 = uw.swarm.Swarm(mesh=mesh, particleEscape=True)
surfaceSwarm10 = uw.swarm.Swarm(mesh=mesh, particleEscape=True)
airiceSwarm = uw.swarm.Swarm(mesh=mesh, particleEscape=True)
#airiceSwarm.data.setflags(write=1)

# create advector
advector2 = uw.systems.SwarmAdvector(swarm=surfaceSwarm1,velocityField=velocityField, order=2)
advector3 = uw.systems.SwarmAdvector(swarm=surfaceSwarm2,velocityField=velocityField, order=2)
advector4 = uw.systems.SwarmAdvector(swarm=surfaceSwarm3,velocityField=velocityField, order=2)
advector5 = uw.systems.SwarmAdvector(swarm=surfaceSwarm4,velocityField=velocityField, order=2)
advector6 = uw.systems.SwarmAdvector(swarm=surfaceSwarm5,velocityField=velocityField, order=2)
advector7 = uw.systems.SwarmAdvector(swarm=surfaceSwarm6,velocityField=velocityField, order=2)
advector8 = uw.systems.SwarmAdvector(swarm=surfaceSwarm7,velocityField=velocityField, order=2)
advector9 = uw.systems.SwarmAdvector(swarm=surfaceSwarm8,velocityField=velocityField, order=2)
advector10 = uw.systems.SwarmAdvector(swarm=surfaceSwarm9,velocityField=velocityField, order=2)
advector11 = uw.systems.SwarmAdvector(swarm=surfaceSwarm10,velocityField=velocityField, order=2)
airiceadvector = uw.systems.SwarmAdvector(swarm=airiceSwarm,velocityField=velocityField, order=2)

#surfacePoints1
surfacePoints = np.array(np.meshgrid(np.linspace(0, MODEL_DATA['MAX_X'], 50), MODEL_DATA['MAX_Y'],
                                     np.linspace(MODEL_DATA['MIN_Z'], MODEL_DATA['MAX_Z'], 500))).T.reshape(-1, 3)

x = surfacePoints[:, 0]
z = surfacePoints[:, 2]
s20 = bed+ 9/10*(iceHeight-bed) * (9/10)**mi
s30 = bed+ 8/10*(iceHeight-bed) * (8/10)**mi
s40 = bed+ 7/10*(iceHeight-bed) * (7/10)**mi
s50 = bed+ 6/10*(iceHeight-bed) * (6/10)**mi
s60 = bed+ 5/10*(iceHeight-bed) * (5/10)**mi
s70 = bed+ 4/10*(iceHeight-bed) * (4/10)**mi
s80 = bed+ 3/10*(iceHeight-bed) * (3/10)**mi
s90 = bed+ 2/10*(iceHeight-bed) * (2/10)**mi
s100 = bed+ 1/10*(iceHeight-bed) * (1/10)**mi
#print(s20,s30,s40,s50,s60,s70,s80,s90,s100)
#3203.0838153121977 2912.704999580074 2629.512351415966 2354.320677171151 2088.188204120155 1832.5532074018731 1589.502314197467

surfacePoints[:, 1] = iceHeight
surfaceSwarm1.add_particles_with_coordinates(surfacePoints)
airiceSwarm.add_particles_with_coordinates(surfacePoints)
surfacePoints[:, 1] = s20
surfaceSwarm2.add_particles_with_coordinates(surfacePoints)
surfacePoints[:, 1] = s30
surfaceSwarm3.add_particles_with_coordinates(surfacePoints)
surfacePoints[:, 1] = s40
surfaceSwarm4.add_particles_with_coordinates(surfacePoints)
surfacePoints[:, 1] = s50
surfaceSwarm5.add_particles_with_coordinates(surfacePoints)
surfacePoints[:, 1] = s60
surfaceSwarm6.add_particles_with_coordinates(surfacePoints)
surfacePoints[:, 1] = s70
surfaceSwarm7.add_particles_with_coordinates(surfacePoints)
surfacePoints[:, 1] = s80
surfaceSwarm8.add_particles_with_coordinates(surfacePoints)
surfacePoints[:, 1] = s90
surfaceSwarm9.add_particles_with_coordinates(surfacePoints)
surfacePoints[:, 1] = s100
surfaceSwarm10.add_particles_with_coordinates(surfacePoints)
```

```
#surfacePoints2
surfacePoints = np.array(np.meshgrid(np.linspace(0, MODEL_DATA['MAX_X'], 500), MODEL_DATA['MAX_Y'],
                                     np.linspace(MODEL_DATA['MIN_Z'], MODEL_DATA['MAX_Z'], 50))).T.reshape(-1, 3)
x = surfacePoints[:, 0]
z = surfacePoints[:, 2]
surfacePoints[:, 1] = iceHeight
surfaceSwarm1.add_particles_with_coordinates(surfacePoints)
airiceSwarm.add_particles_with_coordinates(surfacePoints)
surfacePoints[:, 1] = s20
surfaceSwarm2.add_particles_with_coordinates(surfacePoints)
surfacePoints[:, 1] = s30
surfaceSwarm3.add_particles_with_coordinates(surfacePoints)
surfacePoints[:, 1] = s40
surfaceSwarm4.add_particles_with_coordinates(surfacePoints)
surfacePoints[:, 1] = s50
surfaceSwarm5.add_particles_with_coordinates(surfacePoints)
surfacePoints[:, 1] = s60
surfaceSwarm6.add_particles_with_coordinates(surfacePoints)
surfacePoints[:, 1] = s70
surfaceSwarm7.add_particles_with_coordinates(surfacePoints)
surfacePoints[:, 1] = s80
surfaceSwarm8.add_particles_with_coordinates(surfacePoints)
surfacePoints[:, 1] = s90
surfaceSwarm9.add_particles_with_coordinates(surfacePoints)
surfacePoints[:, 1] = s100
surfaceSwarm10.add_particles_with_coordinates(surfacePoints)

# to visualize the surface swarm in paraview we need a pseudo variable
surfaceParticle1 = surfaceSwarm1.add_variable ( dataType="int", count=1 )
surfaceParticle1.data[:] = 1
surfaceParticle2 = surfaceSwarm2.add_variable ( dataType="int", count=1 )
surfaceParticle2.data[:] = 2
surfaceParticle3 = surfaceSwarm3.add_variable ( dataType="int", count=1 )
surfaceParticle3.data[:] = 3
surfaceParticle4 = surfaceSwarm4.add_variable ( dataType="int", count=1 )
surfaceParticle4.data[:] = 4
surfaceParticle5 = surfaceSwarm5.add_variable ( dataType="int", count=1 )
surfaceParticle5.data[:] = 5
surfaceParticle6 = surfaceSwarm6.add_variable ( dataType="int", count=1 )
surfaceParticle6.data[:] = 6
surfaceParticle7 = surfaceSwarm7.add_variable ( dataType="int", count=1 )
surfaceParticle7.data[:] = 7
surfaceParticle8 = surfaceSwarm8.add_variable ( dataType="int", count=1 )
surfaceParticle8.data[:] = 8
surfaceParticle9 = surfaceSwarm9.add_variable ( dataType="int", count=1 )
surfaceParticle9.data[:] = 9
surfaceParticle10 = surfaceSwarm10.add_variable ( dataType="int", count=1 )
surfaceParticle10.data[:] = 10
airiceParticle = airiceSwarm.add_variable ( dataType="int", count=1 )
airiceParticle.data[:] = 11
```

```
# +
T0 = -30. # °C
#Tbed = -5. # °C
Tbed = -3. # °C
T_Basis = bumpHeight
#DeltaT = Tbed - T0

T_func = Tbed + (coord[1]-bumpHeight)/(WarmiceHeight-bumpHeight)*(T0-Tbed)
#zz_pow = (T_func-Tbed)**mi
#zz_pow_max = (T0-Tbed)**mi
T_func = Tbed + (T_func-Tbed)*((T_func-Tbed)/(T0-Tbed))**mi

#T_func = T0 + DeltaT * ((1.-((Basis - (foldHeight - coord[1])) / Basis))**2)
#T_func = T0 + DeltaT * ((T_Basis - coord[1]) / (T_Basis)) **2

Tconditions = [
                (       coord[1] > WarmiceHeight,  T0      ),
                (       True,  T_func      ),
                #(       True,            Tbed  ),
              ]

particleTemperature.data[:] = fn.branching.conditional( Tconditions ).evaluate(swarm)

# +
## functions, incl flow law
R = 0.008314 # kJ / (T*mol)
QhighT = 155. # kJ/mol, activation energy, Kuiper dislocation creep
QsmallT = 64.
A0smallT = 5e5 * 3.1536e7 #Mpa-4s-1 to Pa-4a-1
A0highT = 6.96e23 * 3.1536e7
#if rank == 0:
#    print(A0smallT, A0highT)

strainRateTensor = fn.tensor.symmetric(velocityField.fn_gradient)
strainRate_2ndInvariantFn = fn.tensor.second_invariant(strainRateTensor)

viscosityFnAir    = fn.misc.constant(1e10 / 3.1536e7)
minViscosityIceFn  = fn.misc.constant(1e+13 / 3.1536e7)
maxViscosityIceFn  = fn.misc.constant(1e+16 / 3.1536e7)
#viscosityFnRock = fn.misc.constant(1e18 / 3.1536e7)

V1 = 0.5 * (A0smallT * fn.math.exp(-QsmallT / (R*(particleTemperature + 273.)))) ** (-1./n) * (strainRate_2ndInvariantFn**((1.-n) / float(n)))
V2 = 0.5 * (A0highT * fn.math.exp(-QhighT / (R*(particleTemperature + 273.)))) ** (-1./n) * (strainRate_2ndInvariantFn**((1.-n) / float(n)))
V1 = V1 * 1e6 #pa*a
V2 = V2 * 1e6 #pa*a
#V1 = V1 * 1e6 / 3.1536e7  #pa*a
#V2 = V2 * 1e6 / 3.1536e7

VisBaseconditions = [
                (       particleTemperature <= -11., V1 ),
                (       True,                        V2),
                ]

#viscosityMap1 = {
#                 materialV:  viscosityFnIce ,
#                 materialVC: viscosityFnIce,
#                }

#viscosityMap2 = {
#                  materialV:  viscosityFnColdIce,
#                 materialVC: viscosityFnWarmIce,
#                }

viscosityIceFn = fn.branching.conditional( VisBaseconditions )
viscosityFnIce = fn.misc.max(fn.misc.min(viscosityIceFn, maxViscosityIceFn), minViscosityIceFn)

viscosityMap = {
                 materialA:  viscosityFnAir,
                 materialV:  viscosityFnIce,
                 #materialVC: viscosityFnIce,
                 #materialR: viscosityFnRock,
                }
viscosityFn = fn.branching.map( fn_key=materialVariable, mapping=viscosityMap )
#viscosityFnAir2    = 0.0
viscosityFnIce2    = (1-1/10) * viscosityFnIce
viscosityMap2 = {
                materialA:  0.,
                materialV:  viscosityFnIce2,
                #materialVC: viscosityFnIce2,
                #materialR: 0.,
               }
viscosityFn2 = fn.branching.map( fn_key=materialVariable, mapping=viscosityMap2 )
viscosityFn3=viscosityFn-viscosityFn2
particleViscosity.data[:] = viscosityFn.evaluate(swarm)

# +
devStressFn = 2.0 * viscosityFn * strainRateTensor
shearStressFn = strainRate_2ndInvariantFn * viscosityFn * 2.0

densityFnIce = (18.02 / (19.30447 - 7.988471e-4 * (particleTemperature+273.) + 7.563261e-6 * ((particleTemperature+273.)**2) )) * 1000.

densityFnAir = fn.misc.constant( 0. )
densityFnRock = fn.misc.constant( 2700. )

densityMap = {
                materialA:  densityFnAir,
                materialV:  densityFnIce,
                #materialVC:  densityFnIce,
                #materialR: densityFnRock
              }

densityFn = fn.branching.map(fn_key=materialVariable, mapping=densityMap)

particleDensity.data[:] = densityFn.evaluate(swarm)

#surf_inclination = 0.5 * np.pi / 180. # 0.1 = Experiment D, 0.5 = Experiment B
#z_hat = (math.sin(surf_inclination), - math.cos(surf_inclination), 0.)

z_hat = (0., -1., 0.)
buoyancyFn = densityFn * z_hat * g
```

```
## set boundary conditions
iWalls = mesh.specialSets["MinI_VertexSet"] + mesh.specialSets["MaxI_VertexSet"]
jWalls = mesh.specialSets["MinJ_VertexSet"] + mesh.specialSets["MaxJ_VertexSet"]
kWalls = mesh.specialSets["MinK_VertexSet"] + mesh.specialSets["MaxK_VertexSet"]
#outerkWall = mesh.specialSets["MinK_VertexSet"]
front = mesh.specialSets["MinI_VertexSet"]
back = mesh.specialSets["MaxI_VertexSet"]
base   = mesh.specialSets["MinJ_VertexSet"]
top    = mesh.specialSets["MaxJ_VertexSet"]
leftWall = mesh.specialSets["MinK_VertexSet"]
rightWall = mesh.specialSets["MaxK_VertexSet"]

allWalls = iWalls + jWalls + kWalls

z2 = -5000. #outflow
z3 = 5000.
meshVz = 5.867
#meshVx = 8.5
#meshVx = 2*meshVz*maxX*maxY/(2*maxY*maxZ-BumpAmplitude*(1/k*np.sin(k*TotalBumpWidth)+TotalBumpWidth))
#Sbump = BumpAmplitude*(zmax-zmin)*(BA1+BA2+BA3+BA4)/(2*2*Amax*(1.0 + 0.5 + 0.25 + 0.125))
#meshVx = meshVz*MODEL_DATA['MAX_X']*(MODEL_DATA['MAX_Y']-bed)/((MODEL_DATA['MAX_Y']-bed)*z2-Sbump)
#print(Sbump,meshVx) #2489279.62623 13.88217000691085
meshV2 = 100
#meshVx = meshVz*MODEL_DATA['MAX_X']/z2
#print(meshVx) #25
velocityField.data[:] = 0.
#velocityField.data[leftWall, 2] = meshVz
#velocityField.data[rightWall, 2] = -meshVz

for h in mesh.specialSets["MinK_VertexSet"]:
    loc = mesh.data[h,1]
    if bed<loc<=iceHeight:
        velocityField.data[h][2] = meshVz

for i in mesh.specialSets["MaxK_VertexSet"]:
    loc = mesh.data[i,1]
    if bed<loc<=iceHeight:
        velocityField.data[i][2] = -meshVz*2
'''
for j in mesh.specialSets["MinI_VertexSet"]:
    loc = mesh.data[j,1]
    if loc<=iceHeight:
        velocityField.data[j][0] = meshVx
'''
for k in mesh.specialSets["MaxI_VertexSet"]:
    z = mesh.data[k,2]
    loc = mesh.data[k,1]
    if z2<z<z3 and loc>bed:
        velocityField.data[k][0] = meshV2
    else:
        velocityField.data[k][0] = 0.

velocityBCs = uw.conditions.DirichletCondition(
                                                variable        = velocityField,
                                                indexSetsPerDof = (iWalls+base, base, kWalls+base),
                                               )
```

```
def c_axis_rotation(dt, steps = 1.):

    dt /= steps

    for i in range(0, int(steps)):

        iceIndices = np.array(np.where(materialVariable.data == materialV)[0])

        velGrad = velocityField.fn_gradient.evaluate(swarm).reshape(swarm.particleLocalCount, mesh.dim, mesh.dim)
        velGrad = velGrad[iceIndices]
        velGradT = velGrad.swapaxes(-1,1)

        # rate of deformation and rate of rotation
        D = 0.5 * (velGrad + velGradT)
        W = 0.5 * (velGrad - velGradT)

        particleDirector.data[iceIndices] = particleDirector.data[iceIndices]
                           + dt * ( np.einsum("ijk,ik->ij", W, particleDirector.data[iceIndices])
                           - np.einsum("ijk,ik->ij", D, particleDirector.data[iceIndices])
                           + np.einsum("ij,ij->i",particleDirector.data[iceIndices],
                np.einsum("ijk,ik->ij",D,particleDirector.data[iceIndices]))[:,None] * particleDirector.data[iceIndices])

        #finally normalize the c-axes
        particleDirector.data[iceIndices] = particleDirector.data[iceIndices] /
                        np.absolute(np.linalg.norm(particleDirector.data[iceIndices], axis=1).reshape(len(iceIndices),1))

        # we want to rotate all directors, if they point towards the negative y-direction
        # this should make it easier to display them
        b = np.where(particleDirector.data[:,1] < 0.)
        particleDirector.data[b] *= -1.


## setup solver and solve

stokes = uw.systems.Stokes(
    velocityField=velocityField,
    pressureField=pressureField,
    voronoi_swarm=swarm,
    conditions=[
            velocityBCs,
            ],
    fn_viscosity=viscosityFn,
    _fn_viscosity2=viscosityFn2,
    #_fn_director=directorField,
    _fn_director=particleDirector,
    fn_bodyforce=buoyancyFn,
)

solver = uw.systems.Solver(stokes)

solver.set_inner_method("mg")
solver.options.scr.ksp_type="cg"
solver.set_penalty(1.0e10) # higher penalty = larger stability + (often) faster calculation
# solver.options.scr.ksp_rtol = 1.0e-3

surfaceArea = uw.utils.Integral( fn=1.0, mesh=mesh, integrationType='surface', surfaceIndexSet=top)
surfacePressureIntegral = uw.utils.Integral( fn=pressureField, mesh=mesh, integrationType='surface', surfaceIndexSet=top)

def calibrate_pressure():

    global pressureField
    global surfaceArea
    global surfacePressureIntegral

    (area,) = surfaceArea.evaluate()
    (p0,) = surfacePressureIntegral.evaluate()
    pressureField.data[:] -= p0 / area

    # print (f'Calibration pressure {p0 / area}')
```

```
def flow(rotate_caxes = True):

    global calibrate_pressure
    global advector1
    global advector2
    global advector3
    global advector4
    global advector5
    global advector6
    global advector7
    global advector8
    global advector9
    global advector10
    global advector11
    global airiceadvector
    global pop_control1
    global snowPlane, airiceSwarm, materialVariable
    global densityFn, particleDensity, buoyancyFn
    #solver.solve(nonLinearIterate=True, nonLinearTolerance=nl_tol, callback_post_solve=calibrate_pressure)
    solver.solve(nonLinearIterate=True, nonLinearMaxIterations = 50, callback_post_solve=calibrate_pressure)

    # Retrieve the maximum possible timestep for the advection system.
    t1=5.
    dt = advector1.get_max_dt()
    if dt>t1:
        dt=t1

    # Advect using this timestep size.
    advector1.integrate(dt, update_owners=True) # the swarm
    advector2.integrate(dt, update_owners=True) # the surface swarm
    advector3.integrate(dt, update_owners=True)
    advector4.integrate(dt, update_owners=True)
    advector5.integrate(dt, update_owners=True)
    advector6.integrate(dt, update_owners=True)
    advector7.integrate(dt, update_owners=True)
    advector8.integrate(dt, update_owners=True)
    advector9.integrate(dt, update_owners=True)
    advector10.integrate(dt, update_owners=True)
    advector11.integrate(dt, update_owners=True)
    airiceadvector.integrate(dt, update_owners=True)

    pop_control1.repopulate()

    if rotate_caxes:

        c_axis_rotation(dt, steps = 100.)
        #c_axis_rotation_mesh(dt, steps = 100.)

    snowfunc = airiceSwarm.data[:,1]
    sfsize = snowfunc.size
    preciRate = 0.15

    if sfsize > 0:
        snowsize = snowPlane.data.size
        xv = np.linspace(0, sfsize-1, snowsize)
        xp = np.arange(sfsize)
        snowfunc_stretch=np.interp(xv, xp, snowfunc)
        snowPlane.data[:] = np.expand_dims(snowfunc_stretch, 1)
        #snowfunc_interp=interp.interp1d(np.arange(snowfunc.size),snowfunc)
        #snowfunc_stretch=snowfunc_interp(np.linspace(0,snowfunc.size-1,snowPlane.data.size))
        #print('sP', np.min(snowPlane.data),np.max(snowPlane.data))

        coord=fn.input()
        conditions = [
                      #(       coord[1] > snowPlane,    materialA    ),
                      (       snowPlane<=coord[1]<=snowPlane+preciRate*dt,    materialV    ),
                      (       True ,           materialVariable                  ),
                     ]

        materialVariable.data[:] = fn.branching.conditional( conditions ).evaluate(swarm)
        densityFn = fn.branching.map(fn_key=materialVariable, mapping=densityMap)
        particleDensity.data[:] = densityFn.evaluate(swarm)
        buoyancyFn = densityFn * z_hat * g
        airiceSwarm.data.setflags(write=1)
        airiceSwarm.data[:,1]+=preciRate*dt

        #if sfsize > 0:
        #    print('airice', np.min(airiceSwarm.data[:,1]),np.max(airiceSwarm.data[:,1]))
    airiceSwarm.update_particle_owners()
    airiceadvector = uw.systems.SwarmAdvector(swarm=airiceSwarm,velocityField=velocityField, order=2)

    return (dt)
```

```
maxSteps = 100001
stepsize = 50.

step = 0
t = 0.

xdmf_mesh    = mesh.save('mesh.h5')

while step < maxSteps:

    #print ("in step " + str(step))

    #snowfallHA(stepsize, mpa, step*stepsize)
    #t += flow(rotate_caxes = True)

    if not step%stepsize: # if multiple of ..

        #print ("in step " + str(step))

        ignore = swarm.save('swarm_' + str(step) + '.h5')

        # eval swarm variables
        particleStrainrate.data[:] = strainRate_2ndInvariantFn.evaluate(swarm)
        particleViscosity.data[:] = viscosityFn.evaluate(swarm)
        particleViscosity2.data[:] = viscosityFn3.evaluate(swarm)
        particleShearstress.data[:] = shearStressFn.evaluate(swarm)
        particleStress.data[:] = devStressFn.evaluate(swarm)
        particleVelocity.data[:]  = velocityField.evaluate(swarm)
        Vgradient= velocityField.fn_gradient
        particleVgradient.data[:] = Vgradient.evaluate(swarm)

        # save swarm variables as xdmf files
        xdmf_swarm = swarm.save('swarm_' + str(step) + '.h5')
        xdmf_surfswarm1 = surfaceSwarm1.save('surf_swarm1_' + str(step) + '.h5')
        xdmf_surfswarm2 = surfaceSwarm2.save('surf_swarm2_' + str(step) + '.h5')
        xdmf_surfswarm3 = surfaceSwarm3.save('surf_swarm3_' + str(step) + '.h5')
        xdmf_surfswarm4 = surfaceSwarm4.save('surf_swarm4_' + str(step) + '.h5')
        xdmf_surfswarm5 = surfaceSwarm5.save('surf_swarm5_' + str(step) + '.h5')
        xdmf_surfswarm6 = surfaceSwarm6.save('surf_swarm6_' + str(step) + '.h5')
        xdmf_surfswarm7 = surfaceSwarm7.save('surf_swarm7_' + str(step) + '.h5')
        xdmf_surfswarm8 = surfaceSwarm8.save('surf_swarm8_' + str(step) + '.h5')
        xdmf_surfswarm9 = surfaceSwarm9.save('surf_swarm9_' + str(step) + '.h5')
        xdmf_surfswarm10 = surfaceSwarm10.save('surf_swarm10_' + str(step) + '.h5')
        xdmf_airiceSwarm = airiceSwarm.save('airice_' + str(step) + '.h5')

        xdmf_surfaceParticle1 = surfaceParticle1.save('surfaceSwarm1_' + str(step) + '.h5')
        xdmf_surfaceParticle2 = surfaceParticle2.save('surfaceSwarm2_' + str(step) + '.h5')
        xdmf_surfaceParticle3 = surfaceParticle3.save('surfaceSwarm3_' + str(step) + '.h5')
        xdmf_surfaceParticle4 = surfaceParticle4.save('surfaceSwarm4_' + str(step) + '.h5')
        xdmf_surfaceParticle5 = surfaceParticle5.save('surfaceSwarm5_' + str(step) + '.h5')
        xdmf_surfaceParticle6 = surfaceParticle6.save('surfaceSwarm6_' + str(step) + '.h5')
        xdmf_surfaceParticle7 = surfaceParticle7.save('surfaceSwarm7_' + str(step) + '.h5')
        xdmf_surfaceParticle8 = surfaceParticle8.save('surfaceSwarm8_' + str(step) + '.h5')
        xdmf_surfaceParticle9 = surfaceParticle9.save('surfaceSwarm9_' + str(step) + '.h5')
        xdmf_surfaceParticle10 = surfaceParticle10.save('surfaceSwarm10_' + str(step) + '.h5')
        xdmf_airiceParticle = airiceParticle.save('airiceSwarm_' + str(step) + '.h5')

        surfaceParticle1.xdmf('surfaceSwarm1_' + str(step) + '.xdmf', xdmf_surfaceParticle1,
                              "surfaceParticle1", xdmf_surfswarm1, "SurfSwarm1", modeltime=step)
        surfaceParticle2.xdmf('surfaceSwarm2_' + str(step) + '.xdmf', xdmf_surfaceParticle2,
                              "surfaceParticle2", xdmf_surfswarm2, "SurfSwarm2", modeltime=step)
        surfaceParticle3.xdmf('surfaceSwarm3_' + str(step) + '.xdmf', xdmf_surfaceParticle3,
                              "surfaceParticle3", xdmf_surfswarm3, "SurfSwarm3", modeltime=step)
        surfaceParticle4.xdmf('surfaceSwarm4_' + str(step) + '.xdmf', xdmf_surfaceParticle4,
                              "surfaceParticle4", xdmf_surfswarm4, "SurfSwarm4", modeltime=step)
        surfaceParticle5.xdmf('surfaceSwarm5_' + str(step) + '.xdmf', xdmf_surfaceParticle5,
                              "surfaceParticle5", xdmf_surfswarm5, "SurfSwarm5", modeltime=step)
        surfaceParticle6.xdmf('surfaceSwarm6_' + str(step) + '.xdmf', xdmf_surfaceParticle6,
                              "surfaceParticle6", xdmf_surfswarm6, "SurfSwarm6", modeltime=step)
        surfaceParticle7.xdmf('surfaceSwarm7_' + str(step) + '.xdmf', xdmf_surfaceParticle7,
                              "surfaceParticle7", xdmf_surfswarm7, "SurfSwarm7", modeltime=step)
        surfaceParticle8.xdmf('surfaceSwarm8_' + str(step) + '.xdmf', xdmf_surfaceParticle8,
                              "surfaceParticle8", xdmf_surfswarm8, "SurfSwarm8", modeltime=step)
        surfaceParticle9.xdmf('surfaceSwarm9_' + str(step) + '.xdmf', xdmf_surfaceParticle9,
                              "surfaceParticle9", xdmf_surfswarm9, "SurfSwarm9", modeltime=step)
        surfaceParticle10.xdmf('surfaceSwarm10_' + str(step) + '.xdmf', xdmf_surfaceParticle10,
                              "surfaceParticle10", xdmf_surfswarm10, "SurfSwarm10", modeltime=step)
        airiceParticle.xdmf('airiceSwarm_' + str(step) + '.xdmf', xdmf_airiceParticle,
                              "airiceParticle", xdmf_airiceSwarm, "airiceSwarm", modeltime=step)
```

```
    xdmf_meshvar = velocityField.save('velocityField_' + str(step) + '.h5')
    velocityField.xdmf('velocityField_' + str(step) + '.xdmf', xdmf_meshvar, "Velocity",
                       xdmf_mesh, "Mesh", modeltime=step)

    xdmf_particleStrainrate = particleStrainrate.save('particleStrainrate_' + str(step) + '.h5')
    particleStrainrate.xdmf('particleStrainrate_' + str(step) + '.xdmf', xdmf_particleStrainrate,
                            "particleStrainrate", xdmf_swarm, "Swarm", modeltime=step)

    xdmf_particleVgradient = particleVgradient.save('particleVgradient_' + str(step) + '.h5')
    particleVgradient.xdmf('particleVgradient_' + str(step) + '.xdmf', xdmf_particleVgradient,
                            "particleVgradient", xdmf_swarm, "Swarm", modeltime=step)

    xdmf_particleDirector = particleDirector.save('particleDirector_' + str(step) + '.h5')
    particleDirector.xdmf('particleDirector_' + str(step) + '.xdmf', xdmf_particleDirector,
                          "particleDirector", xdmf_swarm, "Swarm", modeltime=step)

    #xdmf_particleMeshDirector = particleMeshDirector.save('particleMeshDirector_' + str(step) + '.h5')
    #particleMeshDirector.xdmf('particleMeshDirector_' + str(step) + '.xdmf', xdmf_particleMeshDirector,
    #                        "particleMeshDirector", xdmf_swarm, "Swarm", modeltime=step)

    xdmf_particleViscosity = particleViscosity.save('particleViscosity_' + str(step) + '.h5')
    particleViscosity.xdmf('particleViscosity_' + str(step) + '.xdmf', xdmf_particleViscosity,
                            "particleViscosity", xdmf_swarm, "Swarm", modeltime=step)

    xdmf_particleViscosity2 = particleViscosity2.save('particleViscosity2_' + str(step) + '.h5')
    particleViscosity2.xdmf('particleViscosity2_' + str(step) + '.xdmf', xdmf_particleViscosity2,
                            "particleViscosity2", xdmf_swarm, "Swarm", modeltime=step)

    #xdmf_particleCreationTime = particleCreationTime.save('particleCreationTime_' + str(step) + '.h5')
    #particleCreationTime.xdmf('particleCreationTime_' + str(step) + '.xdmf', xdmf_particleCreationTime,
    #                         "particleCreationTime", xdmf_swarm, "Swarm", modeltime=step)

    xdmf_materialVariable = materialVariable.save('particleMaterial_' + str(step) + '.h5')
    materialVariable.xdmf('particleMaterial_' + str(step) + '.xdmf', xdmf_materialVariable,
                          "materialVariable", xdmf_swarm, "Swarm", modeltime=step)

    xdmf_particleTemperature = particleTemperature.save('particleTemperature_' + str(step) + '.h5')
    particleTemperature.xdmf('particleTemperature_' + str(step) + '.xdmf', xdmf_particleTemperature,
                            "particleTemperature", xdmf_swarm, "Swarm", modeltime=step)

    xdmf_particleDensity = particleDensity.save('particleDensity_' + str(step) + '.h5')
    particleDensity.xdmf('particleDensity_' + str(step) + '.xdmf', xdmf_particleDensity,
                            "particleDensity", xdmf_swarm, "Swarm", modeltime=step)

    xdmf_particleShearstress = particleShearstress.save('particleShearstress_' + str(step) + '_'+ str(t) + '.h5')
    particleShearstress.xdmf('particleShearstress_' + str(step) + '.xdmf', xdmf_particleShearstress,
                            "particleShearstress", xdmf_swarm, "Swarm", modeltime=step)

    xdmf_particleStress = particleStress.save('particleStress_' + str(step) + '_'+ str(t) + '.h5')
    particleStress.xdmf('particleStress_' + str(step) + '.xdmf', xdmf_particleStress,
                            "particleStress", xdmf_swarm, "Swarm", modeltime=step)

    #xdmf_particleInitialYPos = particleInitialYPos.save('particleInitialYPos_' + str(step) + '_'+ str(t) + '.h5')
    #particleInitialYPos.xdmf('particleInitialYPos_' + str(step) + '.xdmf', xdmf_particleInitialYPos,
    #                       "particleInitialYPos", xdmf_swarm, "Swarm", modeltime=step)

    # visualizing the velocityField in paraviewe doesn't work for whatever reason (Paraview just crashes)
    # so we save it as a particle property
    #particleVelocity.data[:]  = velocityField.evaluate(swarm)
    xdmf_particleVelocity = particleVelocity.save('particleVelocity_' + str(step) + '.h5')
    particleVelocity.xdmf('particleVelocity_' + str(step) + '.xdmf', xdmf_particleVelocity,
                  "particleVelocity", xdmf_swarm, "Swarm", modeltime=step)

print (str(t) + ' years, step: ' + str(step))

if step < maxSteps-1:
    t += flow(rotate_caxes = True)

step += 1
```